Adhesion and transendothelial migration of cancer cells

Vinoth Edal Joseph Sundar Rajan

Communauté
UNIVERSITÉ Grenoble Alpes

THÈSE

Pour obtenir le grade de

DOCTEUR DE LA COMMUNAUTÉ UNIVERSITÉ GRENOBLE ALPES

Spécialité : **Biodiversité du développment Oncogenèse**

Arrêté ministériel : 7 août 2006

Présentée par

Vinoth Edal Joseph SUNDAR RAJAN

Thèse dirigée par **Alain DUPERRAY** et
codirigée par **Claude VERDIER**

préparée au sein de **l'Institut Albert Bonniot**
dans **l'École Doctorale : CSV**

Adhesion and transendothelial migration of cancer cells

Thèse soutenue publiquement le **4 Juillet 2016**,
devant le jury composé de :

Pierre-Henri Puech
Chargé de Recherche (Rapporteur)
Isabelle Van Seuningen
Directeur de Recherche (Rapporteur)
Hélène Delanoe-Ayari
Maitre de Conférences (Membre)
Antoine Delon
Professeur (Président)
Alain Duperray
Directeur de Recherche (Membre)
Claude Verdier
Directeur de Recherche (Membre)

This project “Adhesion and transendothelial migration of cancer cell” was performed between two laboratories in Grenoble: 1) Institute for Advanced Bioscience (IAB) and 2) Laboratory for Interdisciplinary Physics (LIPhy).

IAB is an internationally renowned institute in basic biomedical and translational research in the areas of epigenetic, chronic diseases and cancer. The project was conducted in the team of “Analytical Immunology of Chronic Pathologies”. IAB is supported jointly by National Institute of Health and Medical Research (INSERM-U1209), University Grenoble Alpes (UGA) and National Centre for Scientific Research (CNRS-UMR 5309).

LIPhy is another renowned institute that explores the frontiers of physics in different research fields from biology to climate sciences and engineering using three approaches: experimental, computational and theoretical physics. I worked in an interdisciplinary research team DYFCOM and their research focus range from physics, mechanics, biomechanics and applied mathematics. LIPhy is a joint research unit of CNRS (UMR-5588) and UGA.

Acknowledgements

First and foremost I express my praise and thanks to Lord Almighty for the Blessings showered on me to complete my PhD successfully.

With profound respect, I wish to express my deep and sense of gratitude to Dr. Patrice Marche, Team Director, Analytical Immunology of Chronic Pathologies for giving me the opportunity to work in the group. I convey my deep and sincere thanks to my supervisor Dr. Alain Duperray and Dr. Claude Verdier for their constant support throughout my PhD for discussions, questions, suggestions, critical evaluation, motivation, encouragement and valuable advice to the project. Their passion for science and open-minded approach to learn new things has certainly had a positive impact on my PhD work. I also extended my thanks to Dr. Valérie Laurent for introducing me to Atomic Force Microscopy setup and experiments.

I also acknowledge Alexei Grichine, Mylène Pezet and Jacques Mazzega from Imaging and Flow cytometry facility for teaching me the techniques that I have used in the project. Special thanks to Alexei Grichine on his contribution to GMM analysis and useful discussions. I express my sincere thanks to Richard Michel for helping me in TFM analysis for the project.

I acknowledge Dr. Yara Abidine for helping me in optimizing the protocol for gel preparation and patterns. I also extend my hearty thanks to Laure Laforgue for helping me in all French administrative work and being constant support during these years. I would like to thank all my lab members of Team-Marche, LIPhy and Transmig for giving scientific inputs in different domains and made my stay pleasant. Special mention to Zuzana Mackek Jilkova, Daria Tsvirkun, Ayca Zeybek, Keerthi Kurma, Stephanie Traub and Samia Raza for their support and motivation.

I cannot express my gratitude enough to my parents, my brother, my wife, relatives and friends, so I dedicate this PhD dissertation to them.

Special thanks to all my friends in India and Europe, especially to Srikanth, Archana, Mithun, Srinidhi, Saravanan, Jaideep and Gopinath who gave me support and breaks when I needed the most. This PhD work was possible only because of the support from everyone that I mentioned here and also support from those that I might have missed to mention.....

Table of contents

Abstract

Cancer metastasis is associated with 90% cancer-associated deaths, when cancer cells escape from the primary tumor and form metastatic colonies in secondary sites. Extravasation is an important step in cancer metastasis, where cancer cells carried in blood, adhere and transmigrate through the endothelium. Therefore identifying the key molecules involved during the adhesion process could enable to develop new anticancer cancer drugs able to inhibit the adhesion of cancer cells to the endothelium. We have previously shown that InterCellular Adhesion Molecule-1 (ICAM-1) expressed by endothelial cells is involved in the interactions of bladder cancer cells (BCs) with the endothelium. However the ICAM-1 ligands have never been investigated. In this study, we combined adhesion assays and Atomic Force Microscopy (AFM) to identify the ligands involved and to quantify the forces relevant in such interactions. We report the expression of MUC1 and CD43 on BCs and demonstrate that these ligands interact with ICAM-1 to mediate cancer cell-endothelial cell adhesion in the case of the more invasive BCs. AFM experiments were performed to quantify the force ranges involved by MUC1 and CD43 during their interaction with ICAM-1. AFM measurements combined with a Gaussian Mixture Model showed distinct force ranges for the interaction of ICAM-1 with MUC1 and ICAM-1 with CD43. Furthermore, a detailed analysis of the rupture events suggests that CD43 is strongly connected to the cytoskeleton and that its interaction with ICAM-1 mainly corresponds to force ramps followed by sudden jumps. On the contrary, MUC1 seems to be weakly connected to the cytoskeleton as its interactions with ICAM-1 are mainly associated with the formation of tethers. The forces involved during the transmigration of cancer cells through the endothelium was investigated using Traction Force Microscopy (TFM). Preliminary results showed that tractions exerted by cancer cells during transmigration can be studied and quantified using TFM.

Abbreviations

ECM	Extracellular matrix
CAM	Cell adhesion molecules
Ig	Immunoglobulin
ICAM-1	Intercellular adhesion molecule-1
ICAM-2	Intercellular adhesion molecule-2
VCAM-1	Vascular cell adhesion molecule-1
CD	Cluster of differentiation
TNF-α	Tumor necrosis factor - α
PECAM-1	Platelet-endothelial cell adhesion molecule
IAP	Integrin associated proteins
MAdCAM	Mucosal addressin cell adhesion molecule
JAM	Junctional adhesion molecules
LFA-1	Lymphocyte function-associated antigen 1
Mac-1	Macrophage-1 antigen
CRP	Complement regulatory proteins
PSGL-1	P-selectin glycoprotein ligand-1
HCELL	Hematopoietic cell *E*-/L-*selectin ligand*
VNTR	Variable number of tandem repeats
ELISA	Enzyme linked immunosorbent assay
AFM	Atomic force microscopy
SCFS	Single cell force spectroscopy
SMFS	Single molecule force spectroscopy
EMT	Epithelial mesenchymal transition
ATP	Adenosine triphosphate
TFM	Traction force microscopy
BEM	Boundary element method
FTTC	Fourier transform traction cytometry
TRPF	Traction recovery from point force
AM	Adjoint method
PDMA	Polydimethylsiloxane
sulfo-SANPAH	(sulfosuccinimidyl 6-(4'-azido-2'-nitrophenylamino)hexanote)
NHS	N-hydroxysuccinimide
EDC	ethyl(dimethylaminopropyl)carbodiimide
CCD	Charge-coupled device
TEM	Transendothelial Migration
CEA	Carcinoembryonic antigen
VLA	Very late antigen
LAMP	Lysosomal Membrane-Associated Glycoproteins
TCC	Transitional Cell Carcinoma
UC	Urothelial carcinoma
FBS	Fetal bovine serum
HUVECs	Human vascular umbilical endothelial cells
mAb	monoclonal antibody
RT	Reverse transcriptase
PCR	Polymerase chain reaction
shRNA	short hairpin RNA
siRNA	small interfering RNA
GADPH	Glyceraldehyde 3-phoshate dehydrogenase
GMM	Gaussian mixture model
GFP	Green fluorescent protein

BSA	Bovine serum albumin
PBS	Phosphate buffered saline
EDTA	Ethylenediaminetetraacetic acid
GLMM	Generalized linear mixed model
N-HEA	N-hydroxyethylacrylamide
APS	Ammonium persulfate
TEMED	N,N,N',N'-tetramethylethane-1,2-diamine
β-ME	β-mercaptoethanol
PGMEA	Propylene glycol monoethyl ether acetate
HEPES	(4-(2-hydroxyethyl)-1-piperazineethanesulfonic acid)

Table of Figures

List of Tables

Chapter 1 - Introduction to cell adhesion and migration

Cell adhesion and migration are complex multistep processes that are involved in embryogenesis, wound healing, tissue formation and inflammatory responses (Seller, 2001; Ridley *et al.,* 2003; Ladoux and Nicolas, 2012). The aberrant cell adhesion and migration contributes to diseases like tumor metastasis, atherosclerosis, vascular diseases, arthritis etc..(Valster *et al.,* 2005; Khalili and Ahmad, 2015). Chapter 1 focuses on giving an overview of the basic molecules involved in cell adhesion and cell migration. It also describes the role of cell adhesion and migration in different biological processes and introduces various techniques developed to study cell adhesion and migration. Chapter 1 also explains the process of cancer metastasis and the ligands involved in cancer cell-endothelial cell adhesion especially in bladder cancer cells.

1.1 Cell adhesion

Cell adhesion is the ability of cells to interact with a substrate, which can be another cell or extracellular matrix (ECM) in a coordinated manner to form tissues or organs. The ECM is a mixture of matrix molecules like glycoproteins, fibronectin, collagen, laminin, proteoglycans, vitronectin and non-matrix proteins including growth factors. Cell-matrix adhesions mediate direct interaction of cells with their external environment (Seller, 2001; Berrier and Yamada, 2007). Cell adhesion mediates and regulates a range of diverse functions such as cell differentiation, cell proliferation, cell cycle, cell migration, cell survival, cell communication, gene expression and signaling during morphogenesis, tissue homeostasis, wound healing and tumorigenesis. It also plays a central role in embryonic development, tissue development and its maintenance (Huang and Ingber, 1999). Adhesion of cells to one another or ECM is mediated by cell adhesion molecules (CAMs).

1.1.1 Cell Adhesion Molecules

CAMs are transmembrane glycoproteins acting as a molecular link between outside and inside of the cell with three different domains namely, an extracellular domain, a transmembrane domain and a cytoplasmic domain (Lukas and Dvorak, 2004). Apart from sticking the cells together, CAMs are able to transmit both mechanical and chemical signals across the cell membrane (Buckley *et al.*, 1998). CAMs can mediate both homophilic adhesion (binding through the same adhesion molecules between cells) and heterophilic adhesion (binding through different adhesion molecules). The CAMs are divided into 5 major families: the immunoglobulin superfamily, cadherins, selectins, integrins and mucin superfamily as shown in Figure 1.1.

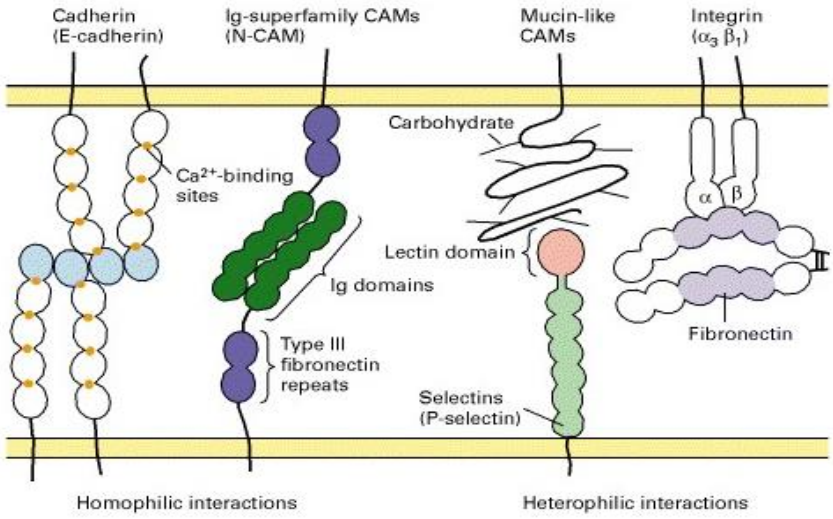

Figure 1.1: Cell Adhesion Molecules. Cadherin and immunoglobulin (Ig) can mediate homophilic adhesion. Calcium binding sites (indicated in orange color) between the domains in the extracellular segment are necessary for cell adhesion of cadherin and the N-terminal domain (blue) causes cadherin to dimerize and to bind cadherin dimers from an opposite cell membrane. The Ig superfamily contains multiple domains (green) similar in structure to Ig and frequently contains type III fibronectin repeats (purple). In a heterophilic interaction, the lectin domain of selectins binds to carbohydrate chains to mucin-like CAMs on adjacent cells in the presence of Ca^{2+}. The lectin domain is separated from the membrane by a series of repeated domains. The main cell-matrix adhesion molecule integrin is a heterodimer of α and β subunits. They bind to the specific domain of fibronectin, laminin or other matrix molecules (Lodish *et al.*, 2000).

1.1.1.1 The Immunoglobulin superfamily and ICAM-1

The immunoglobulin (Ig) superfamily contains many adhesion molecules that are characterized by repeated domains, similar to those found in immunoglobulins. Many Ig of the adhesion molecules superfamily mediate cell-cell adhesion rather than cell-ECM interactions (Seller, 2001). Adhesion molecules in Ig superfamily and their corresponding ligands are listed in Table 1.1.

Adhesion molecule	Expressed on	Ligand
ICAM-1, ICAM-2	Epithelium, endothelium	Leukocyte integrins
VCAM-1	Endothelium	α4β1 integrin on monocyte and lymphocytes
PECAM-1 (CD 31)	Leukocytes, endothelium	
BL CAM (CD22)	Differentiating B cells	
IAP (CD47)	Endothelium, leukocytes, fibroblasts, epithelium, erythrocytes, neurons	αVβ3 integrin
MAdCAM	Mucous membrane	α4β7 integrin, L selectin on Peyer's patch lymphocytes

Table 1.1: Immunoglobulin-like adhesion molecules (Lukas and Dvorak, 2004).

Adhesion molecules like intercellular adhesion molecule-1 (ICAM-1, CD54), intercellular adhesion molecule-2 (ICAM-2, CD102) are expressed on epithelial and endothelial cells and are recognized by leukocyte β2 integrins. Vascular cell adhesion molecule (VCAM-1) is expressed on the surface of activated endothelium and other cell types like dendritic cells, tissue macrophages and some fibroblasts. The expression of VCAM-1 and ICAM-1 on endothelium is low and can be up regulated by several cytokines like interleukins, tumor necrosis factor (TNF-α) and interferon γ (Seller, 2001). VCAM-1 is a ligand for integrin α4β7 expressed on many different cells including monocytes, lymphocytes and certain tumor cells (Seller, 2001; Lukas and Dvorak, 2004). The platelet-endothelial cell adhesion molecule (PECAM-1, CD31) is usually expressed on endothelial cell-cell junctions,

platelets and some leukocytes. PECAM-1 is involved in both homophilic and heterophilic cell adhesion by interacting with itself or integrin αVβ3. Integrin associated proteins (IAP, CD22) is expressed on fibroblasts, platelets, erythrocytes, epithelium, endothelium and leukocytes. PECAM-1 and IAP are involved in leukocyte adhesion and transendothelial migration. Mucosal addressin CAM (MAdCAM) is recognized by α4β7 integrins and L-selectin. A new class of proteins called junctional adhesion molecules (JAMs) belonging to Ig superfamily with two extracellular Ig-like domain has been also reported (Keiper *et al.*, 2005; Barthel *et al.*, 2008). JAMs are expressed at the junctions of endothelial and epithelial cells and are involved in the regulation of leukocyte extravasation via homophilic and heterophilic interactions with other JAMs or integrins expressed on leukocytes. Three different members are reported in JAMs family namely JAM-A, JAM-B and JAM-C (Keiper *et al.*, 2005). The structure of ICAM-1 is described in detail due to its importance in this study.

ICAM-1

ICAM-1 (CD54) is an immunoglobulin (Ig) like cell adhesion molecule expressed by several cell types including leukocytes, endothelial cells, B-cells, T-cells, fibroblasts and some cancer cells (Roland *et al.*, 2007; Lawson and Wolf, 2009). ICAM-1 is a cell-surface transmembrane molecule normally expressed at low levels and can be upregulated by cytokines such as tumor necrosis factor (TNF)-α, interleukin-1β, and interferon-γ (Bella *et al.*, 1998; Seller, 2001). ICAM-1 is a key molecule that mediates the adhesion of leukocytes or cancer cells to endothelial cells (Orr *et al.*, 2000; Roche *et al.*, 2003; Chotard-Ghodsnia *et al.*, 2007; Miles *et al.*, 2008; Strell and Entschladen, 2008; Rahman and Fazal, 2009; Haddad *et al.*, 2010; Laurent *et al.*, 2014). Several ligands for ICAM-1 have been identified including lymphocyte function-associated antigen (LFA-1, CD11a/CD18, αLβ2), macrophage-1 antigen (Mac-1, CD11b/CD18, αMβ2), fibrinogen, rhinoviruses, and plasmodium falciparum-infected erythrocytes (Lawson and Wolf, 2009). Cancer cells lacks the expression of β2 integrins, but MUC1 and CD43 were reported as two potential ligands expressed by some cancer cells for endothelial ICAM-1 (Rosenstein *et al.*, 1991; Regimbald *et al.*, 1996).

Structure of ICAM-1

The extracellular domain of ICAM-1 consists of 453 amino acids, which form five Ig-like domains (D1-D5) as shown in Figure 1.2. All Ig-like domains have a β sheet structure stabilized by disulfide bonds.

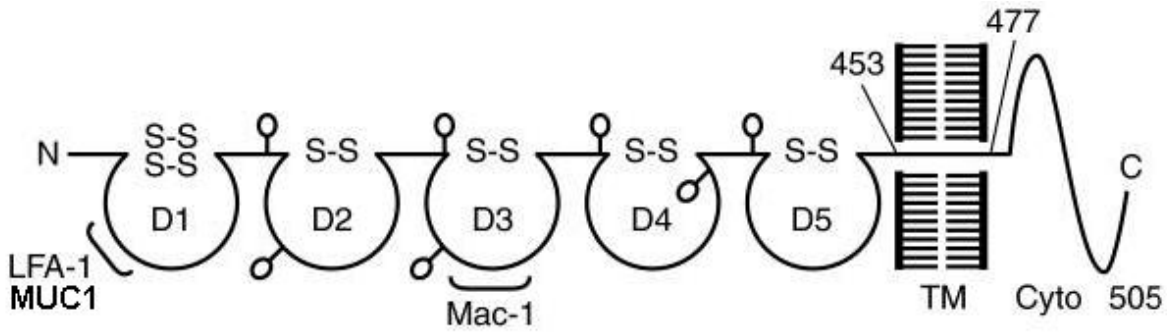

Figure 1.2: Structure of ICAM-1. ICAM-1 contains five extracellular Ig-like domains (D1-D5), a hydrophobic transmembrane domain (TM) and a short cytoplasmic domain (Cyto). The binding sites for LFA-1, Mac-1 and MUC1 are shown (Rahman and Fazal, 2009).

The leukocytes ligands LFA-1 and Mac-1 bind to domain 1 and domain 3 of ICAM-1 respectively as shown in Figure 1.2. It has been reported that MUC1 binds to domain 1 of ICAM-1 (Hayashi *et al.*, 2001) as indicated in Figure 1.2. The exact binding domain for CD43 on ICAM-1 is not reported so far. ICAM-1 has a hydrophobic transmembrane domain (TM) with 24 amino acids and a cytoplasmic domain of 28 amino acids which interacts with the actin cytoskeleton via α-actinin, ezrin and moesin and activates many signaling pathways (Rahman and Fazal, 2009).

1.1.1.2 The Cadherins

Cadherins belong to the group of cell adhesion molecules that mediate calcium dependent cell-cell adhesion in all tissues of the organism (Ivanov *et al.*, 2001). Cadherins are responsible for the formation of stable cell-cell junctions and play a key role in tissue and organ development during embryogenesis or in maintenance of normal tissue structure (Buckley *et al.*, 1998; Ivanov *et al.*, 2001; Maître and Heisenberg, 2013). Cadherin-mediated cell-cell junctions are formed due to the interactions between extracellular domains of identical cadherins, located on the membranes of neighboring cells (homophilic adhesion). However, cadherins can also interact with other CAMs like integrins (αEβ7) and proteoglycans (Seller, 2001). The cadherin molecule consists of a N-terminal long extracellular domain with variable repeats with each containing the calcium binding site (Figure 1.3), a transmembrane segment and a C-terminal cytoplasmic domain that is highly conserved between cadherin molecules. The cytoplasmic domain of cadherins is associated with cytoplasmic proteins like catenins (α, β and γ) and plakoglobin, which in turn, serve as linkers between cadherins and actin filaments (Figure 1.3).

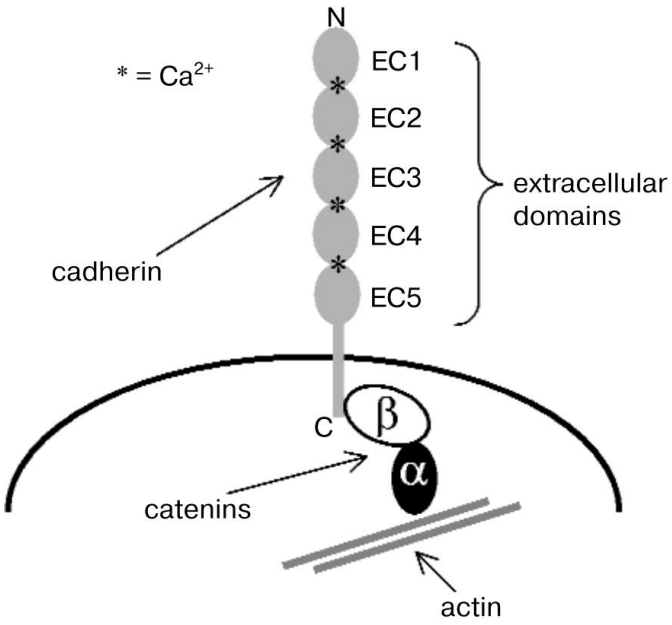

Figure 1.3: Structure of a cadherin. The extracellular domain is composed of variable domains with calcium binding sites (marked as *). The cytoplasmic tail interacts with actin filaments through catenins (Ivanov *et al.*, 2001).

The interaction of cadherins with catenins is essential to form cell junctions, which are important for epithelial cell polarity. Cadherins are subgrouped as neural cadherin (N-cadherin), placental cadherin (P-cadherin), vascular endothelial cadherin (VE-cadherin), retinal cadherins (R-cadherin) and epithelial cadherin (E-cadherin) which are expressed in specific tissues during their development. E-cadherin is concentrated at cell-cell junctions and is involved in the formation of strong cell-cell adhesion. Furthermore, the loss of E-cadherin expression has been linked to the invasive behavior of tumour cells (Seller, 2001).

1.1.1.3 The Selectins

Selectins are a family of calcium dependent carbohydrate-binding proteins involved in mediating the initial attachment of leukocytes and some cancer cells to the endothelium during inflammation and metastasis (Barthel *et al.*, 2008). Selectins bind to carbohydrate ligands, mainly sialyl Lewis X (sLe^x) and sialyl Lewis A (sLe^a), which are expressed on leucocytes. It has been reported that selectin/carbohydrate binding helps the leukocytes to roll on the endothelium in the direction of flow (Seller, 2001). The extracellular part of selectins comprises a N-terminal lectin-like domain, which determines the specificity towards carbohydrate ligands, an epidermal growth factor-like region and a variable number of repeat sequences similar to those found in complement regulatory proteins (CRP) (Figure 1.4). This

is followed by a transmembrane domain and a short cytoplasmic tail (Seller, 2001; Ley, 2003; Barthel *et al.*, 2008).

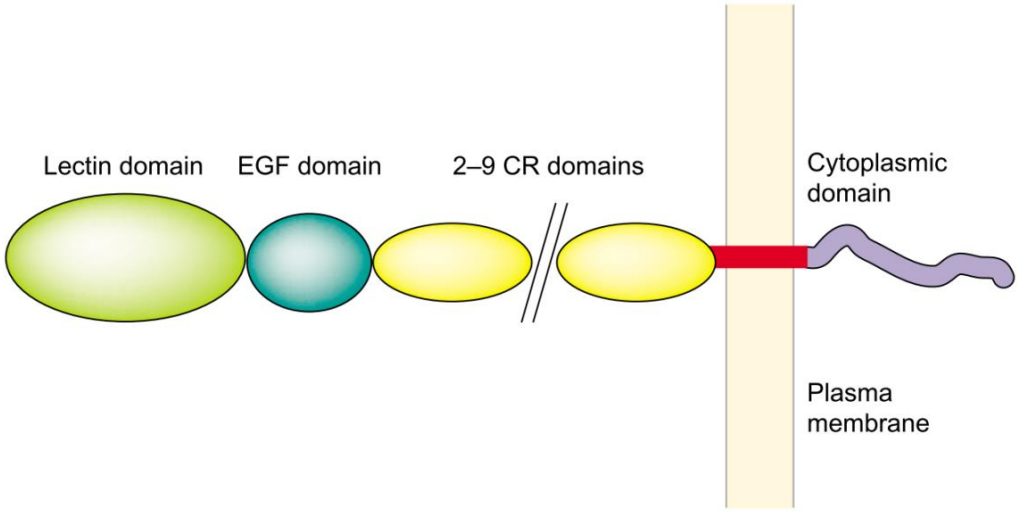

Figure 1.4: Selectin structure. They are composed of one lectin domain (light green), an epidermal growth factor (EGF domain) in dark green, two (L-selectin), six (E-selectin) or nine (P-selectin) repeats similar to complement regulatory proteins (yellow) and a cytoplasmic domain (purple), (Ley, 2003).

There are three main groups of selectins: endothelial selectin (E-selectin, CD62P), leukocyte selectin (L-selectin, CD62L) and platelet selectin (P-selectin, CD62P). E-selectin is a heavily glycosylated protein expressed at low levels on resting endothelial cells and this expression can be stimulated by cytokines like TNF-α or IL-1 (Lukas 2004). Cancer cells and leukocytes express various E-selectin specific ligands like P-selectin glycoprotein ligand-1 (PSGL-1), HCELL (a CD44 glycoform), CD43, MUC1 and β2 integrin (Barthel *et al.*, 2008). E-selectin plays a major role in the initial attachment of cancer cells to the endothelium.

P-selectin is expressed only on platelets and endothelial cells, where it is stored in cytoplasmic granules like α-granules or Weibel-Palade bodies. P-selectin is recruited to the cell surface of endothelial cells in response to activation with thrombin. The binding of some tumor cells to platelets expressing P-selectins helps tumor cells to escape from the immune system (Seller, 2001).

L-selectin is only expressed on leukocytes and is important for leukocyte homing.

1.1.1.4 The Integrin family

Integrins are one of the major families of cell surface receptors mediating cell-matrix and cell-cell adhesion. Integrins are called so as they integrate the extracellular and intracellular environments by binding to ligands outside the cell and cytoskeletal components inside the cell (Luo *et al.*, 2007). Integrins play important roles in development, fertilization, tissue organization and inflammation through mediating cell migration, proliferation, differentiation and gene expression (Buckley *et al.*, 1998; Seller, 2001). They also play a key role in leukocyte recirculation and recruitment, with specific integrins expressed on leukocyte participating in many important areas of immune regulation including antigen presentation, cytotoxicity and phagocytosis (Buckley *et al.*, 1998). Integrins are non-covalently associated heterodimeric cell surface adhesion molecules with one α-subunit and one β-subunit. This family comprises 18 α-subunits and 8 β-subunits, combined to form 24 distinct integrin receptors that bind to different ECM ligands (Figure 1.5). Integrins can be classified into four subfamilies based on the β-subunit: β1 integrin (very late activated antigen), β2 integrin (leukocytes cell adhesion molecules), β3 integrin (cytoadhesion) and β7 integrin (homing). The β1 and β3 subfamilies are mostly involved in cell-matrix interaction, while the members of β2 are involved in cell-cell adhesion (Lukas and Dvorak, 2004).

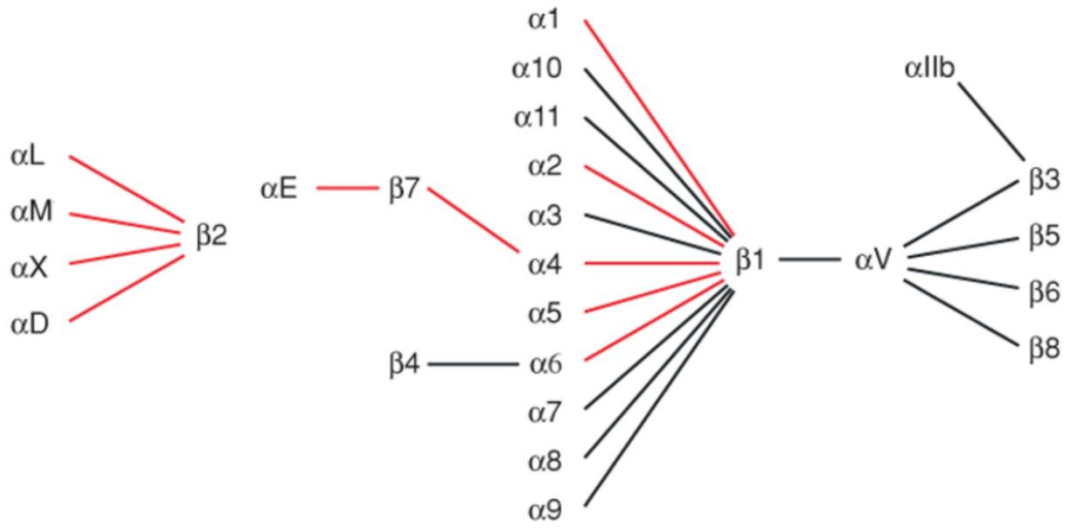

Figure 1.5: 24 integrins heterodimers. Possible αβ combinations are shown with integrins expressed on immune cells shown with red lines (Luo *et al.*, 2007).

Both α and β subunits of integrins are transmembrane glycoproteins with a large extracellular domain, a transmembrane domain and a short cytoplasmic domain. The extracellular domain binds to ECM ligands, divalent cations and also to other proteins at the

cell surface (Berrier and Yamada, 2007). The integrin cytoplasmic domains form multi-molecular complexes with cell signaling and adaptor proteins that can activate various downstream signaling cascades (cell proliferation, migration, differentiation, adhesion, survival etc.) as shown in Figure 1.6. Their cytoplasmic domains interact with the actin cytoskeleton through many different proteins like talin, vinculin and tensin (Figure 1.6). Integrin subunits can transmit signals from the extracellular matrix to the cell interior (outside-in) and from the inside of the cell to the outside of the cell (inside-out) (Seller, 2001; Lukas and Dvorak, 2004).

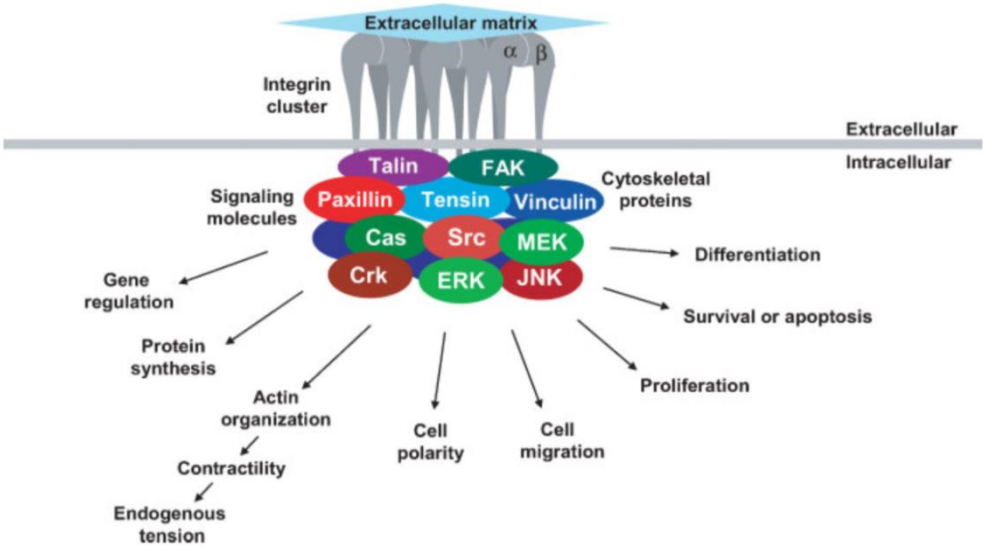

Figure 1.6: Cell-Matrix adhesion and downstream regulation. The cytoplasmic tail of integrins binds to various cytoplasmic proteins to control different cellular processes (Berrier and Yamada, 2007).

The β1 integrin is involved in adhesion to connective tissue macromolecules such as fibronectin, laminin and collagen, while the β3 binds to vascular ligands such as fibrinogen, von Willebrand factor, thrombospondin and vitronectin (Lukas and Dvorak, 2004)). Integrin-mediated signaling has been reported in the context of cancer cell growth and behavior (Seller, 2001). Cells transmit extracellular or intracellular forces through localized adhesion sites called focal adhesion (FA) complex (Figure 1.7). Integrins are attached to the cytoskeleton through FA complex. Active integrins play an important role in mechanotransduction (i.e converting mechanical signal into bio-chemical response) through FA proteins connecting integrin domains to actin filaments to form adhesion complex that transmit adhesive and traction forces (Figure 1.7). The formation of FA is important in cell signaling, cell migration and proliferation (Khalili and Ahmad, 2015).

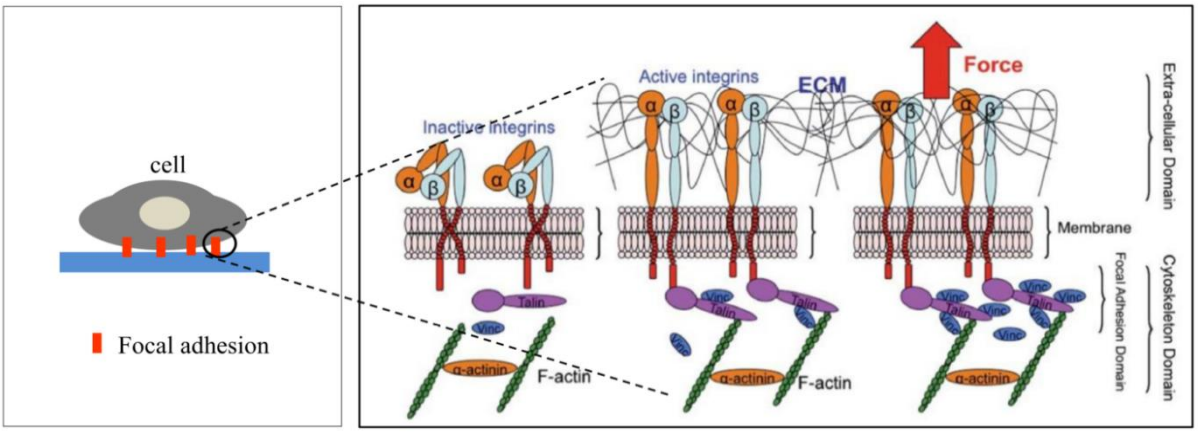

Figure 1.7: Focal adhesion (FA) complex. Schematic representation of activated integrins and formation of ECM-integrin-cytoskeleton linkage in the FA site to transmit forces (Khalili and Ahmad, 2015).

1.1.1.5 The Mucin superfamily

Mucins are high molecular weight glycoproteins either expressed or secreted from epithelial cells that protect and lubricate the epithelial surface (Senapati *et al.*, 2010; Rivalland *et al.*, 2015). Mucins are expressed by a variety of tissues including eye, mammary glands, gastrointestinal tracts and genitourinary tracts (Linden *et al.*, 2008). Mucins are divided into two groups: Transmembrane Mucins (MUC1, MUC3, MUC4, MUC12-17 and MUC20) and Secreted Mucins (MUC2, MUC5AC, MUC5B, MUC6-8 and MUC19) (Gendler, 2001; Jonckheere and Van Seuningen, 2008; Senapati *et al.*, 2010; Rivalland *et al.*, 2015). Secreted mucins form a layer of mucus gel on the epithelial surfaces that serves as a protection against the entry of pathogens. Transmembrane mucins act as sensors to transport signals from the environment to the interior of the cell (Gendler, 2001; Jonckheere and Van Seuningen, 2008). The transmembrane mucins were reported to play important biological roles by mediating cell-cell and cell-matrix interactions (Jonckheere *et al.*, 2010). This superfamily also includes some mucin-like glycoproteins such as CD34 (L-selectin ligand), CD43 (leukosialin), CD162 (PSGL-1), CD164 (glycosylated-dependent CAM 1, GlyCAM1) and mucosal MAdCAM-1 (Apostolopoulos *et al.*, 2015). The structure and expression of MUC1 and CD43 are described in detail due to their importance in this study.

MUC1

MUC1 (episialin, human milk fat globule membrane antigen, CD227, Epithelial membrane antigen) is a large, transmembrane protein with a heavily glycosylated extracellular domain that extends 200-500 nm beyond the plasma membrane as shown in Figure 1.8 (Gendler, 2001; Jonckheere and Van Seuningen, 2008; Nath and Mukherjee, 2014;

Rivalland *et al.*, 2015). MUC1 is normally expressed on the apical surface of secretory epithelial cells including mammary gland, esophagus, stomach, duodenum, pancreas, uterus, prostate and lungs and to a lesser extent in hematopoietic cells (Gendler, 2001; Jonckheere and Van Seuningen, 2008; Nath and Mukherjee, 2014). MUC1 provides protection and lubrication to the epithelia surface and acts as a barrier against pathogen infection and pollutants (Nath and Mukherjee, 2014). MUC1 generally has an anti-adhesive property due to the extended negatively charged sugars on its surface that can block cell-cell and cell-matrix interactions (Gendler, 2001). Alternatively, MUC1 can act as an adhesive molecule for different ligands like E-selectin, ICAM-1 and few other molecules (Senapati *et al.*, 2010; Geng *et al.*, 2012). MUC1 also regulates intracellular signal transduction through numerous pathways including Grb2/SOS, MAP-kinase, EGFR and β-catenin (Rivalland *et al.*, 2015).

MUC1 structure

The structure of MUC1 is shown in Figure 1.8. The MUC1 gene encodes a single polypeptide chain, which is proteolytically cleaved in the endoplasmic reticulum into N-terminal and C-terminal subunits. Extracellularly, these subunits remain associated through stable hydrogen bonds between glycine and serine residues (Nath and Mukherjee, 2014; Rivalland *et al.*, 2015). MUC1 is composed of an extracellular domain, a transmembrane domain and a cytoplasmic domain. The extracellular domain contains a N-terminus region (104 amino acids), followed by tandem repeats of 20 amino acids (PAPGSTAPPAHGVTSAPDTR) repeated 25-125 times (variable number of tandem repeats, VNTR) depending on the individual polymorphism. VNTR domain is heavily glycosylated since it is rich in amino acids (serine and threonine residues) that have O-glycosylated sites giving the rod-like shape (Gendler, 2001; Jonckheere and Van Seuningen, 2008; Nath and Mukherjee, 2014). The transmembrane domain (28 amino acids) anchors MUC1 to the apical surface of epithelial cells. The cytoplasmic domain (72 amino acids) can bind to different cytoplasmic proteins and activates many intracellular pathways (Senapati *et al.*, 2010; Haddon and Hugh, 2015). Several isoforms of MUC1 have been reported due to alternative splicing during gene expression (Hanisch and Müller, 2000; Apostolopoulos *et al.*, 2015).

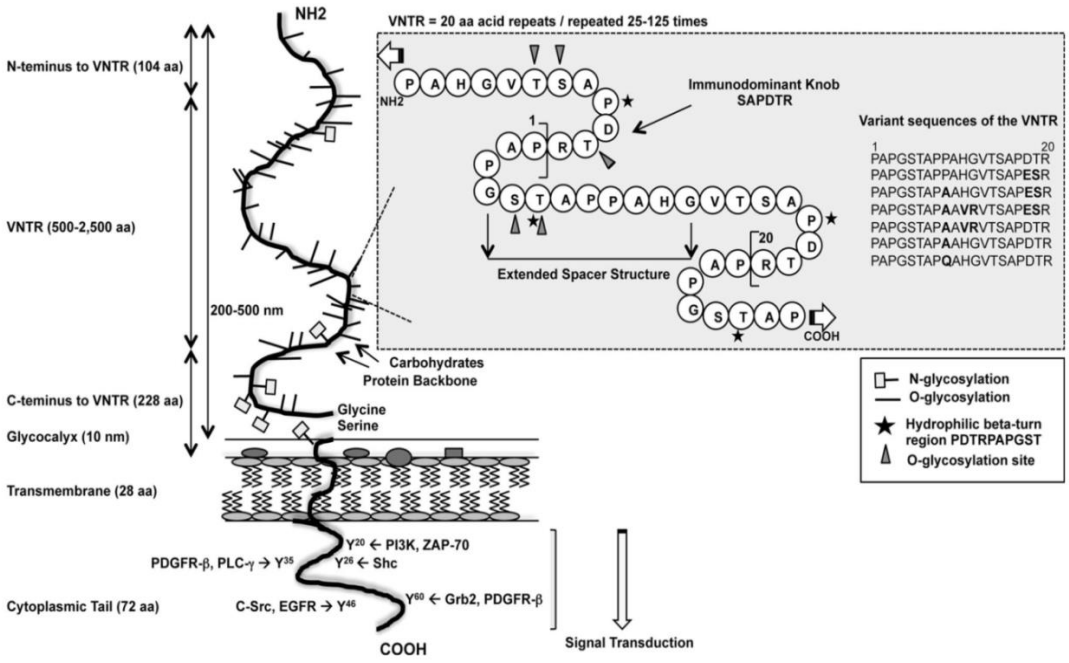

Figure 1.8: Structure of MUC1: The extracellular region contains a large variable number of tandem repeats (VNTR) region that contains O- and N- glycosylation sites with 20 amino acids identical sequence repeated 25-125 times. MUC1 extends 200-500 nm from the cell surface. The extracellular and intracellular subunits are connected by the glycine and serine residues and proteolysis at these sites shed the extracellular domain of MUC1. Intracellular subunits include a transmembrane region and a cytoplasmic tail. The cytoplasmic tail contains tyrosines that can be phosphorylated, leading to signal transduction events (Apostolopoulos *et al.*, 2015).

MUC1 expression in tumor cells

In several cancer cells including breast, lung, colon, ovary and bladder, the expression of MUC1 significantly differs from their normal counterparts (Simms *et al.*, 1999; Nath and Mukherjee, 2014; Apostolopoulos *et al.*, 2015; Haddon and Hugh, 2015; Rivalland *et al.*, 2015). MUC1 is overexpressed over the entire cell surface and within the cytoplasm due to loss of cellular polarity. This overexpression and aberrant localization is associated with the increased metastatic potential of cancer. In addition, cancer cells exhibit abnormal O-glycosylation (underglycosylated) to expose the peptide core of MUC1 especially, 7 amino acid epitopes (PDTRPAP) in VNTR segment of MUC1. Thus several monoclonal antibodies that bind to these normally hidden epitopes can be used to distinguish normal and cancer cells (Rivalland *et al.*, 2015). Expression of MUC1 from cancer cells was first reported in breast cancer cells. It has been also reported that MUC1 is a ligand for endothelial ICAM-1 (Regimbald *et al.*, 1996). The peptide core of MUC1 binds to domain 1 of ICAM-1 to mediate the adhesion of cancer cells to endothelial cells (Hayashi *et al.*, 2001; Rahn *et al.*, 2004).

In cancer cells, the extracellular domain of MUC1 is cleaved by proteolysis and shed into the surface of normal epithelia. The secreted MUC1 can be detected in normal plasma and used as a tumor marker (Hayes *et al.*, 1985). MUC1 is a potential target for immunotherapy, as it is overexpressed and underglycosylated, revealing tumor-specific epitopes. It has been reported that tumor cells expressing MUC1 exhibit an increased capacity to resist the effects of chemotherapeutic drugs. MUC1 directed immunotherapeutic strategies are classified into three classes: vaccination, MUC1 monoclonal antibodies and antibody conjugates (Yang *et al.*, 2007; Jonckheere and Van Seuningen, 2008; Park and Seov, 2009; Rivalland *et al.*, 2015). MUC1 based immunotherapies in different phases of clinical trials are listed in Table 1.2 and this exemplifies the importance of MUC1 in cancer immunotherapy.

Type of product	Agent	Stage of development	Disease setting	Main results	References
Monoclonal MUC1-specific antibodies	MAb-AR20.5 (Brevarex®)	Phase I	Adenocarcinomas	Antibody response	De Bono et al. (2004, 354)
	AS1402	Phase I	Breast cancer, metastatic	Correct tolerance	Pegram et al. (2009, 356)
		Randomized Phase II	Breast cancer, metastatic, with letrozole	No improvement	Ibrahim et al. (2011, 357)
Radiolabeled MUC1-specific antibodies	C595-^{67}Cu	Phase I	Bladder cancer	Tumour uptake	Hughes et al. (2001, 359)
	C595-^{111}In	Phase I	Bladder cancer	Tumour uptake	Hughes et al. (2001, 359)
	NCRC48-^{111}In	Phase I	Bladder cancer	tumoral uptake	Kunkler et al. (1995, 362)
MUC1 VNTR peptides vaccines	MUC1-MFP (mannan fusion protein)	Phase I	Adenocarcinomas	Antibody and T cell immune response	Karanikas et al. (2001, 366)
		Randomized Phase III	Breast cancer	Decreased recurrence rate	Apostolopoulos et al. (2006, 371)
	L-BLP25 (Stimuvax®)	Randomized Phase II	Non-small-cell lung cancer, advanced	Improved overall survival in stage III patients	Butts et al. (2005, 372, 2011, 374)
		Phase III	Non-small-cell lung cancer, non-resectable stage III	Improved survival in patients who received concurrent chemoradiothaerpy	Butts et al. (2014, 375)
	MUC1-KLH	Phase I	Breast cancer, high risk	Antibody response	Gilewski et al. (2000, 376)
Vaccines based on poxviruses encoding MUC1 DNA sequence	PANVAC (CV 301)	Randomized Phase II	Colorectal, cancer after surgical resection of metastases (treated with vaccine + DC)	Improved overall survival	Morse et al. (2013, 377)
		Phase III	Pancreatic cancer, advanced, after failure of gemcitabine	No improvement of survival	Therion Biologics press release (2006)
		Randomized Phase II	Breast cancer, metastatic, combination with chemotherapy	Improved progression-free survival	Heery et al. (35th CTRC-AACR San Antonio Breast Cancer Symposium)
	TG4010	Phase II	Kidney cancer, metastatic	Favourable overall survival	Oudard et al. 2011, 88)
		Randomized Phase II	Prostate cancer, PSA failure	Improvement in PSA-doubling time	Dreicer et al. (2009, 378)
		Randomized Phase II	Lung cancer, advanced, combination with chemotherapy	Improved response rate	Ramlau et al. (2008, 90)
		Randomized Phase II	Lung cancer, advanced, combination with chemotherapy	Improved 6-month PFS and response rate, TrPAL biomarker	Quoix et al. (2011, 379)
MUC1 mRNA vaccines	In vitro-transcribed naked RNA	Phase I/II	Kidney cancer, metastatic	Stabilizations/response	Rittig et al. (2011, 380)
Adoptive cell therapy	MUC1-stimulated PBMCs	Phase I/II	Breast cancer, advanced	Change tumour burden	Wright et al. (2009, 381)
		Phase I	Ovarian cancer	One complete clinical response	Dobrzanski et al. (2009, 382), Corbiere et al. (2011)
		Phase I/II	Pancreatic cancer	Long-term survival	Lepisto et al. (2008, 383)
	MUC1-MFP-pulsed DCs	Phase I	Adenocarcinomas	Cellular immune response, two long stabilizations	Loveland et al. (2006, 385)
	Dendritic cells and CTL transfer	Phase I	Pancreatic cancer	Clinical response	Kondo et al. (2008, 408)

Table 1.2: Summary of MUC1 based immunotherapies (Acres *et al.*, 2015).

CD43

CD43 (Leukosialin, Sialophorin or gp115) is a major sialoglycoprotein expressed on the surface of leukocytes such as T-lymphocytes, thymocytes, monocytes, neutrophils, platelets and some B lymphocytes (Shelley *et al.*, 1990). CD43 is a highly glycosylated membrane protein that has a mucin type extracellular domain with extended rod-like structure that protrudes about 45 nm from the cell surface (Takai *et al.*, 2008; Park *et al.*, 2012; Tuccillo *et al.*, 2014b). CD43 also has both anti-adhesive property and pro-adhesive property like MUC1. CD43 has been reported as a ligand for ICAM-1, Galectin-1, and E-selectin (Ziprin *et al.*, 2004; Alkhamesi *et al.*, 2005, 2007; Matsumoto *et al.*, 2005).

CD43 structure

CD43 consists of 1) an extracellular domain of 235 amino acids, that contains five tandem repeats of 18 amino acids sequence which is extremely rich in serine, threonine and proline residues that are O-glycosylation sites, 2) a transmembrane domain of 23 amino acids that links the other two domains and 3) a cytoplasmic domain of 124 amino acids that binds to ERM proteins (ezrin/radixin/moesin). The ERM proteins serve as linkers between CD43 and the cytoskeleton to activate different signaling cascades (Takai *et al.*, 2008; Tuccillo *et al.*, 2014b).

CD43 expression in tumor cells

CD43 is expressed in solid tumors such as breast, colon, gastric, cervical, lung, bladder and pancreatic cells, whereas it was undetected in the relative normal tissue and benign lesions (Santamaría *et al.*, 1996; Hurford *et al.*, 1999; Fernandez-Rodriguez *et al.*, 2002; Tuccillo *et al.*, 2014b). Rosenstein in 1991 first reported that CD43 is a ligand for ICAM-1 (Rosenstein *et al.*, 1991). It has been demonstrated that CD43 is involved in tumor-mesothelial cell adhesion via interaction with ICAM-1 (Ziprin *et al.*, 2004; Alkhamesi *et al.*, 2005, 2007).

CD43 is expressed by a variety of cancer cells and tumor tissues, whereas it is undetected in normal tissue and for this reason it can be used as a tumor marker. Various monoclonal antibodies are used to identify CD43 expression in cancer cells and it is also a potential target for cancer immunotherapy (Tuccillo *et al.*, 2014a, 2014b).

1.2 Assays to measure the surface expression of CAMs

The surface expressions of CAMS or other proteins are usually measured by extracellular labeling of proteins using biotinylation or antibodies. In biotinylation assays, the proteins on the surface are labeled with biotin and purified using streptavidin affinity and visualized through western blotting. Whereas, enzyme linked immunosorbent assay (ELISA) and flow cytometry works by labeling the proteins with primary antibodies specific to an extracellular epitope and subsequently with a secondary antibody that is either enzyme-linked (ELISA) or fluorescent (flow cytometry) (Lam *et al.*, 2013). In this study, we used flow cytometry to detect the surface expression of proteins (receptors) and the principle and method of detection is explained in detail.

Flow cytometry measures and then analyzes the multiple physical characteristics of single cells (or any other particles - including nuclei, micro-organism, chromosomes and latex beads), as they flow in a stream of fluid (Brown and Wittwer, 2000). It measures the optical and fluorescence characteristics of single cells that include relative particle size, relative granularity or internal complexity and relative fluorescence intensity. The flow cytometry is made up of three main components 1) fluidics - that is used to transport the particles, 2) optics - consists of lasers to illuminate the particles in the stream and 3) electronics - to convert the detected light signals into electronic signals that can be processed by the software (Figure 1.9). The fluidics system helps to create a laminar flow, allowing the single cells to pass through the laser beam for detection. When a cell interacts with the laser, light is scattered in all directions depending on the physical properties of the cell (size and internal complexity).

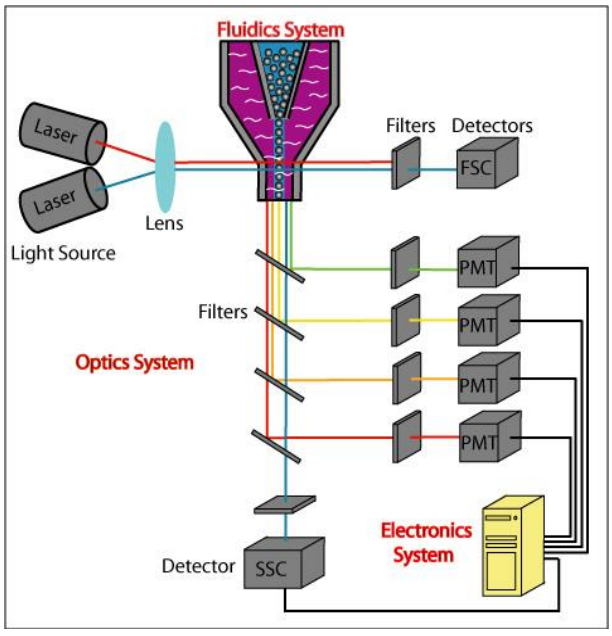

Figure 1.9: Schematic representation of a flow cytometer. Three main systems of the flow cytometer 1) fluidics 2) optics and 3) electronics are shown. (Source: selectscience.net).

Scattered light is collected at two angles: forward scatter (FSC) and side scatter (SSC). Forward scatter measures the diffracted light in the direction of laser path (Figure1.10) and is proportional to the cell surface area or size. FSC provides a method to detect the particles based on their size. Side scattering measures the reflected light at an angle of 90° (Figure1.10) and is proportional to the internal complexity.

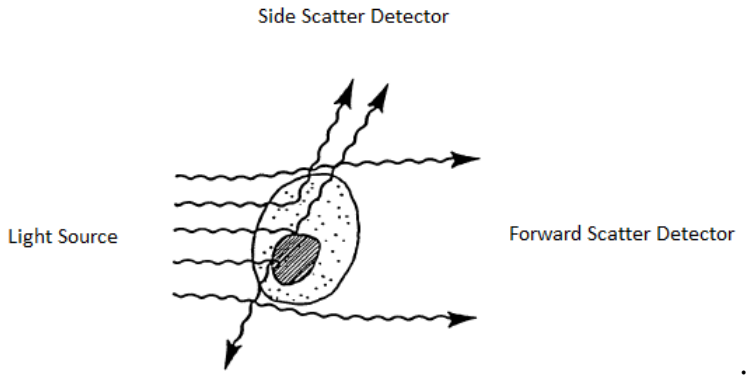

Figure 1.10: Scattering properties of a cell. The light from a cell is forward scattered and side scattered during their interaction with the light source. (Source: BD bioscience).

Correlated measurements of FSC and SSC can be used to separate the cell types from a heterogeneous cell population. For example, the leukocyte subpopulations (lymphocytes, monocytes and neutrophils) in blood samples are separated based on size distinction and cell granularity when plotting forward scatter (x-axis) data against side scatter data (y-axis) as shown in Figure 1.11.

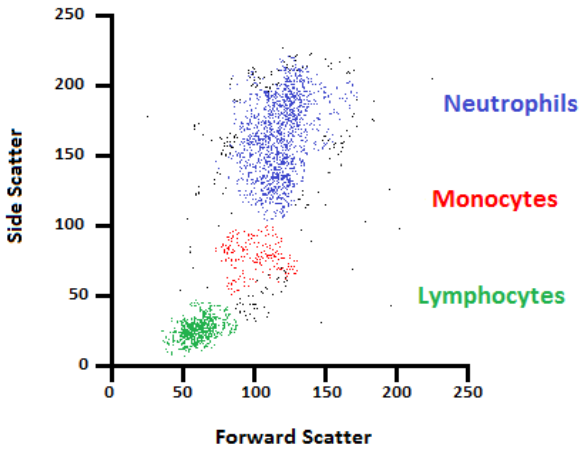

Figure 1.11: 2-D scatter plot of leukocytes from blood sample. Flow cytometry analysis showing the subpopulations from the blood sample while plotting FSC Vs SSC (Source: BD Bioscience).

The flow cytometer also detects the signals from cells when they are labeled with fluorescent dyes. Monoclonal antibodies conjugated with fluorescent dyes can be used to identify the expression of specific proteins on cell membrane or inside the cells. The fluorescence signals from protein are separated and detected using the optical system. Combining fluorescence, FSC and SSC data allows researchers to identify multiple subpopulations of cells in a sample and to count their relative percentage. The experiments performed in this study were performed using an Accuri C6 flow cytometer from BD bioscience (Figure 1.12).

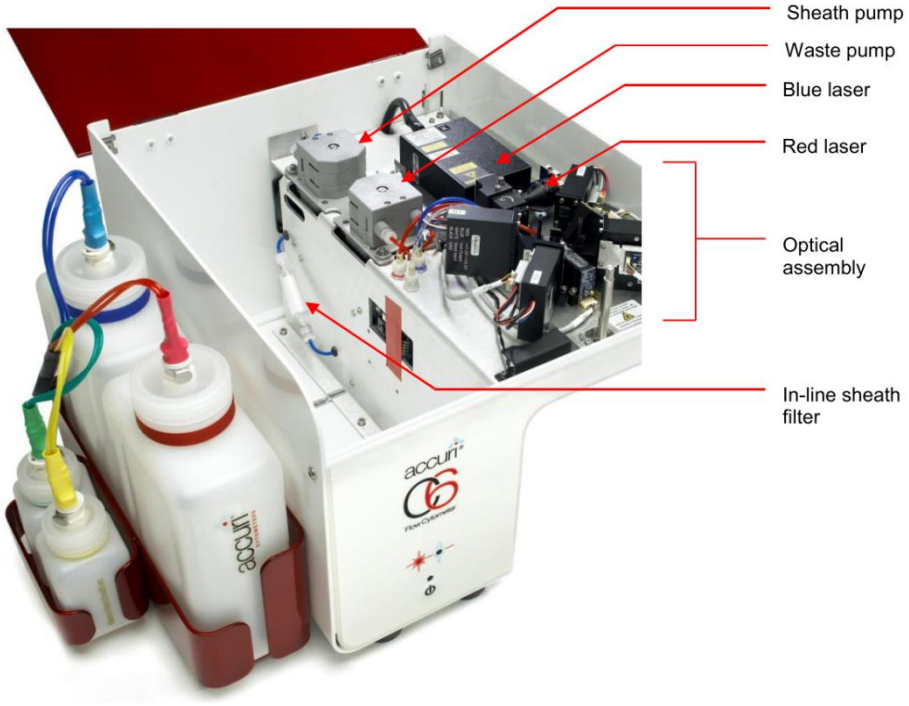

Figure 1.12: BD Accuri C6 Flow Cytometer Optics and Fluidics: Main components in Accuri C6 are shown in top view and lid open. (Source: BD Bioscience).

1.3 Methods to study cell adhesion

Cell adhesion plays an important role in regulating some basic functions of cells such as cell differentiation, cell cycle, cell migration, cell survival, cell communication and is fundamental for the development and maintenance of tissues (Huang and Ingber, 1999). Controlled cell adhesion is required in many biological processes including embryonic development, inflammation and wound healing. Aberrant cell adhesions are related to diseases like arthritis (Szekanecz and Koch, 2000), osteoporosis (Perinpanayagam *et al.*, 2001), atherosclerosis (Simon and Green, 2005) and most importantly tumor metastasis (Huang and Ingber, 1999; Hirohashi and Kanai, 2003). All these indispensable functions of cell adhesion have motivated interest to develop methods to study cell adhesion ranging from

cell binding assays to various techniques for quantifying adhesion strength and the forces involved in cell-cell and cell-matrix adhesion.

Cell adhesion studies can be divided into cell attachment and detachment events. Both attachment and detachment events are divided again into single cell or cell population approach. Cell attachment studies focus on adhesion mechanisms between the cells and the substrates as shown in Figure 1.13A-C. On the contrary, detachment events involve the application of forces to detach the adherent cells from the substrates as shown in Figure 1.13D-F. Different methods used to study the attachment and detachment events are shown in Figure 1.14. Methods like adhesion assay, flow chamber assay and centrifugation assays are used to measure the adhesion strength of large population of cells. Whereas, surface force apparatus, optical tweezers, biomembrane force probe and atomic force microscopy (AFM) are used to measure the adhesion strength at the single cell level. The principle and methodologies of adhesion assays and AFM are discussed below.

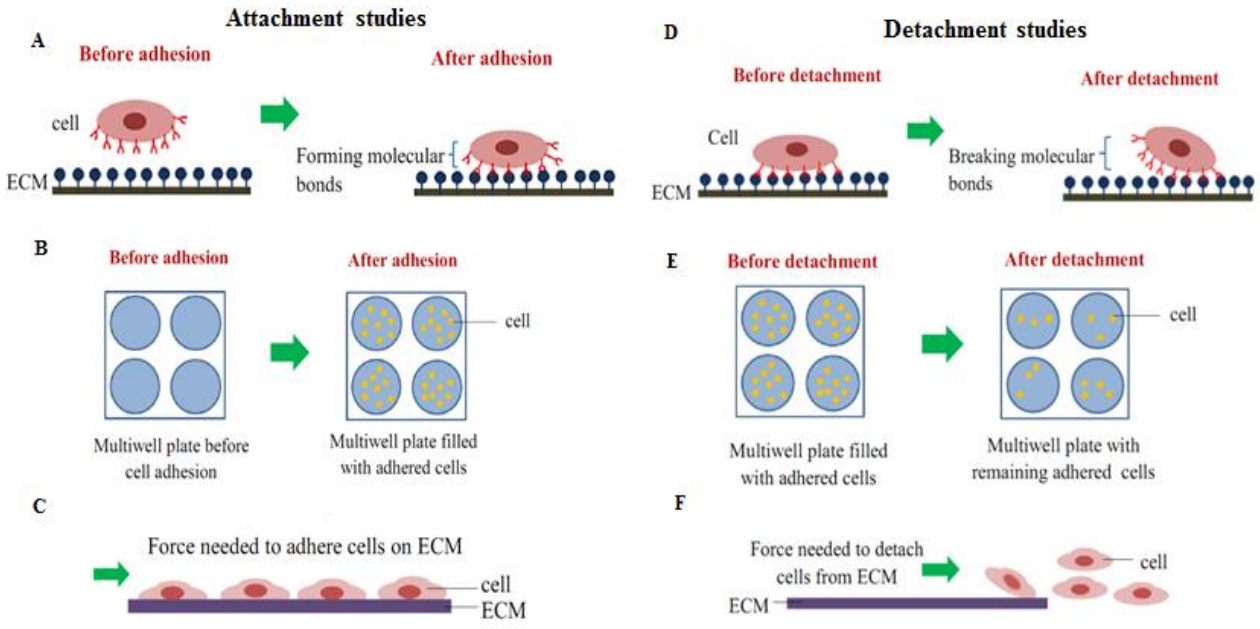

Figure 1.13: Schematic representation of cell attachment and detachment studies. (A) Single cell attachment studies via the formation of molecular bonds and (B,C) cell population attachment studies. (D) Single cell detachment studies by breaking of bonds and (E,F) cell population detachment studies, (Khalili and Ahmad, 2015).

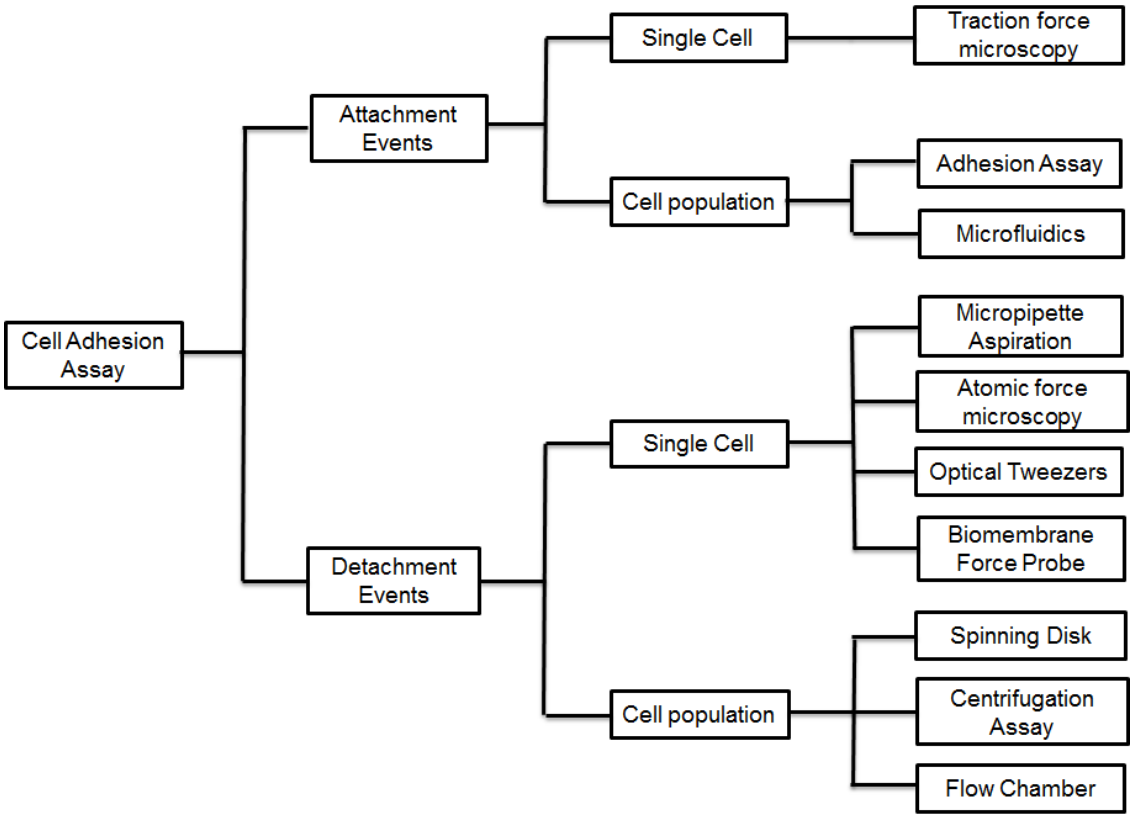

Figure 1.14: Summary of techniques involved in cell adhesion studies classified by attachment and detachment events (modified from Khalili and Ahmad, 2015).

1.3.1 Adhesion Assay or plate and wash assay

The adhesion assay is based on calculation of the percentage of cells adhered to a substrate or a cell monolayer after a period of time. For adhesion assay the cells are cultured in multiwell plates (96 or 48 or 24 wells) with different substrates like ECM proteins or cells and incubated. The non-adherent cells are removed by washing and then the remaining cells are quantified. Adhering cells are quantified by manual counting or by radiolabelling, staining with fluorescent agents or by enzymatic techniques in which a substrate is cleaved, resulting in a signal proportional to the number of cells present (Connors and Heino, 2005; Khalili and Ahmad, 2015). The signal is then detected using an automated plate reader. This method enables the identification of key adhesion molecules involved in cell attachment and generates valuable insights into the proteins regulating adhesion (Ziprin *et al.*, 2004; Alkhamesi *et al.*, 2005; Friedrichs *et al.*, 2013). However, this assay is only qualitative and does not provide any information on adhesion strength and binding forces involved by the molecules during the adhesion process.

1.3.2 Atomic Force Microscopy

Atomic force microscope is one of the important tool for imaging the surfaces of objects at nanometer scale resolution. Initially this technique has been widely used to characterize the surface of non-biological structures such as polymers, films or fibers, powders, adsorbed molecules, microcircuits and nanostructures (Chang *et al.*, 2012; Vahabi *et al.*, 2013). The application of AFM in biology has increased rapidly due to its ability to study biological objects in their physiological buffer solutions and conditions. For the past twenty years AFM has been applied to provide topographical information on cells such as bacteria, virus and mammalian cells, down to individual molecules of nucleic acids and proteins with sub molecular resolution (Sokolov, 2007). The role of AFM in drug discovery is increasing rapidly and AFM is used to test the interactions of drugs with model receptors or with target cell membranes (Maver *et al.*, 2016). AFM can also be used to study the biomechanical properties of cells like stiffness and viscoelasticity, especially in cancer cells. The mechanical properties of cancer cells differ from its non-malignant cells, so these properties can be used as marker in cancer cell identification. Lekke at al. studied the elasticity of normal cells (Hu609 and HCV 29) and cancer cells (Hu 456, T24 and BC 3726) from bladder using AFM and reported that normal cells are stiffer (higher Young's modulus) then cancer cells (Lekka *et al.*, 1999; Ramos *et al.*, 2014; Lekka, 2016). Studies performed on cancer cells from different origin also showed similar results and thereby stiffness of cells can be used as a biomarker in cancer studies (Xu *et al.*, 2012; Abidine *et al.*, 2015). The morphological changes in cancer cell membrane after treatment with anticancer agents such as paclitaxel, colchicine or cytarabine can be also studied using AFM (Chang *et al.*, 2012; Li *et al.*, 2015). In recent years, Atomic Force Microscopy (AFM) emerged as an potential tool to study adhesive interactions of cells with other cells, proteins or functionalized surfaces (Franz *et al.*, 2007; Friedrichs *et al.*, 2010; Zhang *et al.*, 2002, 2004). In particular, AFM is a powerful tool to identify and quantify ligand-receptor interactions (Puech *et al.*, 2005; Sulchek *et al.*, 2005; Alsteens *et al.*, 2010; Taubenberger *et al.*, 2014; Pfreundschuh *et al.*, 2015). The magnitude of various ligand-receptor interactions is usually in the range of 30-80 pN and it varies with the velocity. The non-linear increase in unbinding forces with velocity is explained by Evans and Richtie model that predicts 3 different regimes. In the first regime the forces increases slowly, then the forces increases linearly at intermediate velocity and finally, we move into ultrafast regimes (Evans and Ritchie, 1997). Other techniques like biomembrane force probe (BFP), surface probe apparatus (SFA) and optical tweezers can be used to study ligand-receptor

interactions but these techniques have some limitations in the range of detachable adhesion forces (Friedrichs *et al.*, 2013; Taubenberger *et al.*, 2014). In our study we used the Single Cell Force Spectroscopy (SCFS) mode of AFM because it offers a large range of detachable forces from 10 pN to 1 µN and offers precise spatial and temporal control over experiments. The principle of AFM and its application in force measurements are described in details below.

1.4 Development of AFM

AFM is an important tool to characterize the surface of non-biological materials and also for studying biological structures and processes at cellular and molecular scales. AFM is an extension of the scanning probe microscope (Binnig *et al.*, 1986) that detects the forces between a probe and a sample surface. AFM is compatible to operate both in air as well as in liquid which is required for live cell imaging.

1.4.1 AFM principle

AFM operates based on the principle of flexible cantilevers as a spring to measure the local attractive or repulsive forces between the cantilever tip and the sample based on the bending or deflection of the cantilever. The cantilever attached to a rigid substrate is deflected towards or away (attractive or repulsive) from the surface depending on the interaction. The cantilever deflection is known from the laser beam deflection on the back of the cantilever which is detected by a 4-quadrant photodiode detector (Figure 1.15). When the tip approaches the sample the forces on the cantilever (i.e deflection and bending angle) cause the reflected laser beam to fall onto a certain spot on the photodiode. The signal coordinates on the four quadrants of the photodiode are compared to calculate the signal deflection. As the photodiode consists of four quadrants, laser spot positions can be calculated in two directions. Vertical deflection, measures the interaction force calculated by comparing the amount of signal from top and bottom halves of the photodiode. Lateral twisting of the cantilever can also be calculated by comparing the left and right halves of the photodiode.

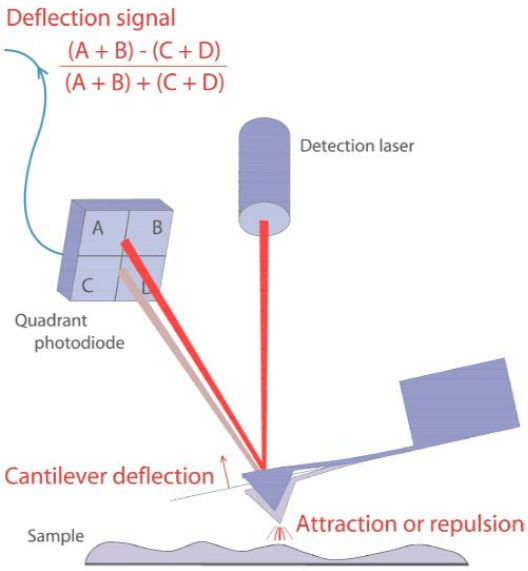

Figure 1.15: Principle of AFM. The cantilever deflection is measured from the laser reflected on the surface of the cantilever to the photodiode. (Source: NanoWizard AFM Handbook).

1.4.2 AFM Modes

The forces between the tip and the sample can be attractive or repulsive based on their distance. When the tip approaches the sample, the long range forces (i.e van der Waals forces and capillary forces) are attractive, and the forces become repulsive when they are at short ranges (electrostatic forces or other interactions). AFM has four different modes: 1) contact mode, 2) non-contact mode, 3) intermittent mode and 4) force modulation mode. These modes operate in different force regimes as shown in Figure 1.16.

Contact mode: The cantilever is in direct contact with the surface, and therefore the interaction is repulsive as shown in Figure 1.16. This mode can be used for obtaining surface topography of nanostructures and to make high resolution imaging of organic or protein crystals by maintaining a constant cantilever deflection using a feedback loop. Contact mode works well for rough samples but the direct contact can damage soft biological samples like cells.

Non-contact mode: The cantilever oscillates (5-15 nm) above the sample surface, but without making contact with the surface and generates attractive forces between the tip and the sample (Figure 1.16). This mode is not so widely used, as there is a possibility of the tip coming into contact with the surface. Operation in non-contact mode is very difficult under ambient conditions. Non-contact mode might be useful for imaging soft-substrates, but its sensitivity to external vibration is often reported as a problem.

Intermittent mode or tapping mode: The cantilever is oscillated up and down at its resonant frequency with tip making intermittent contact with the surface for a brief period of time. Intermittent mode moves between the attractive and repulsive regime of the curve (Figure 1.16) and is mainly used to image samples with structures that are weakly bound to the surface or samples that are soft (polymers, thin films). This mode is especially used for biological samples because it does not damage them.

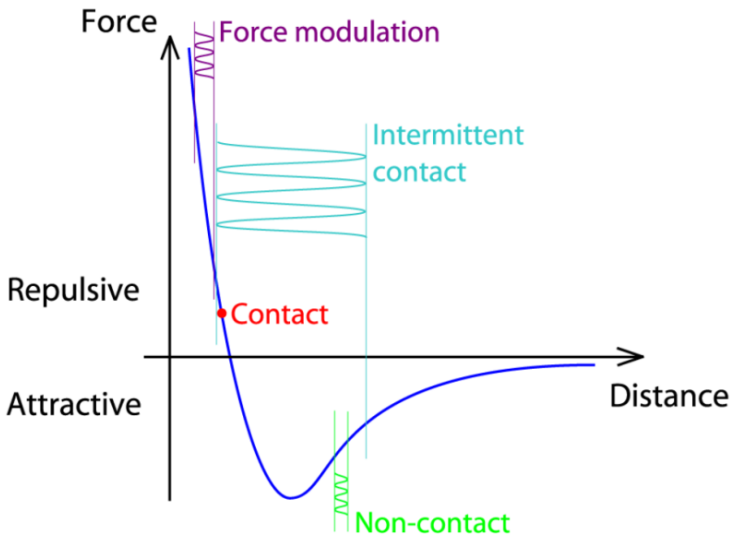

Figure 1.16: Different modes of AFM in relation with the force between the tip and the sample. (Source: NanoWizard AFM Handbook).

Force modulation mode: The cantilever is indented into the sample, and then it is oscillated at a constant force inside the sample with smaller amplitude. This mode is in repulsive regime (Figure 1.16) and is used to detect variations in mechanical properties of the sample like visco-elasticity, adhesion and friction.

1.4.3 The cantilever

The cantilever is the heart of the AFM, since it deflects the laser onto the photodiode. The cantilever is usually made of silicon nitride or crystalline silicon and mounted on a probe with pointed tip as shown in Figure 1.17, left. The tip interacts with the sample and the deflection of the cantilever is measured. The probe can have cantilevers of different sizes and shapes that vary in resonant frequency, spring constant, length and width (Figure 1.17, right).

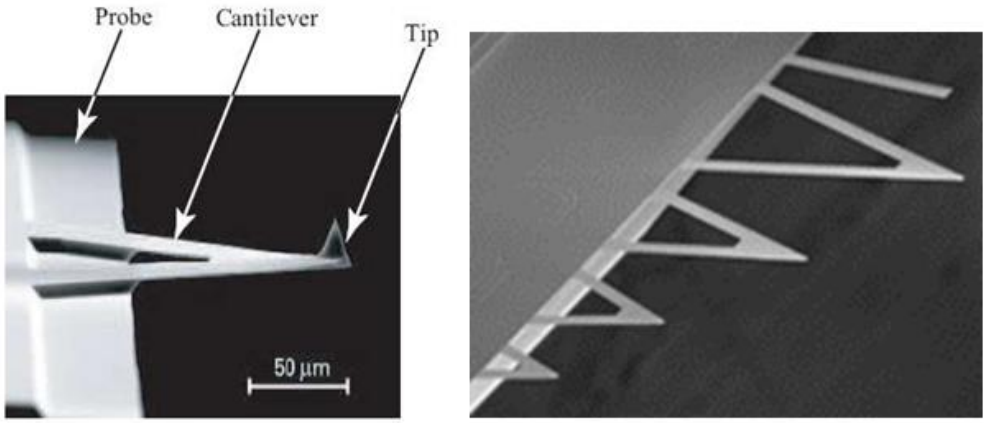

Figure 1.17: Image of the triangular cantilever with a pyramid shaped tip (left). Different sizes and shapes of the cantilever attached to a single probe (right). (Source: burkerafmprobes.com).

The AFM cantilever behaves like a spring and its deflection can be related to force using Hooke's law,

$$\mathbf{F = ks}$$

where, F = Force, k = spring constant, s = distance or cantilever deflection.

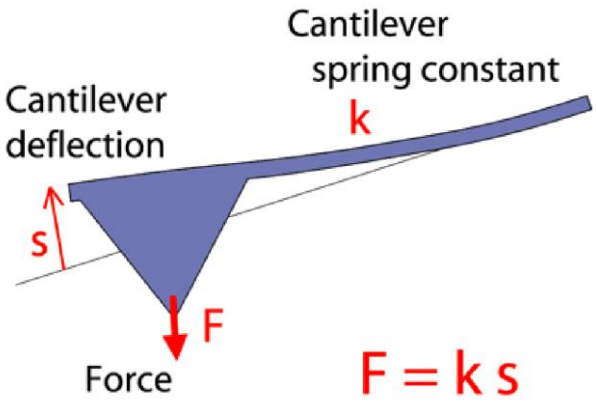

Figure 1.18: Forces are measured from the deflection (s) and spring constant (k) using Hooke's law. (Source: NanoWizard AFM Handbook).

The force between the tip and the sample depends on the spring constant (stiffness) of the cantilever and the deflection of the cantilever as shown in Figure 1.18. The mass of a cantilever influences its resonant frequency ($f_0=\frac{1}{2\pi}\sqrt{\frac{k}{m}}$), where m = mass, k = spring constant. A light cantilever with a high spring constant will have a high resonant frequency. The spring constant of the cantilever strongly depends on the thickness and material properties.

1.4.4 Force Spectroscopy

AFM is a powerful technique for force measurements apart from imaging the structures at high-resolution. The forces between the tip and sample are measured using force spectroscopy as described below. The tip of the cantilever is approached towards the surface using a piezo actuator and then retracted again as shown in Figure 1.19. The deflection of the cantilever and other signals, such as the amplitude or phase can be measured. This technique is called force spectroscopy.

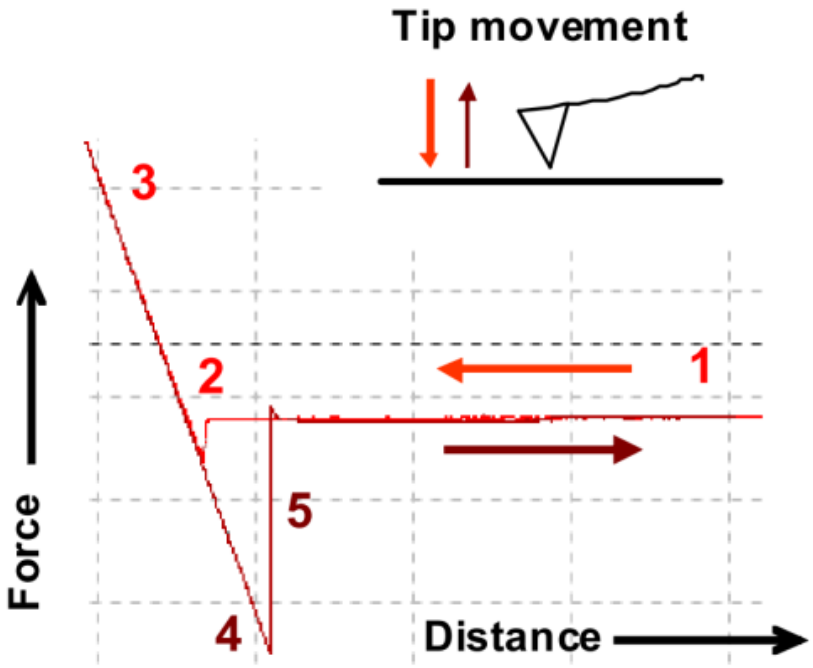

Figure 1.19: Force-distance curve. (1) The cantilever tip is approaching the surface, (2) contact of the tip with the surface, (3) increase in repulsive force when the tip is in contact with the surface, (4) retraction of the cantilever while the tip is still in contact with the surface and (5) tip is pulled off from the surface. (Source: JPK NanoWizard II user manual).

The data from force measurements are displayed as x-y plots, where distance of the cantilever while approaching and retracting corresponds to x-axis. The Y-axis represents the vertical deflection of the cantilever, which gives a direct measure of the interaction force. The force-distance plots are also referred to as force curves. A Simple force curve shown in Figure 1.19 indicates different steps (1-5) involved in force measurements and their associated interactions are shown in Table 1.3.

Approach	
Tip far away (10 - 100 microns)	No interaction
Tip approaching (few microns)	• Electrostatic forces • Long-range interactions from adsorbed molecules, e.g. polymer brush
Tip close to surface (nanometers to atomic distances)	• Van der Waals • Capillary forces (in air) • DLVO/screened electrostatics (in aqueous solutions) • Chemical potential • Magnetic • Solvation forces (water layering) 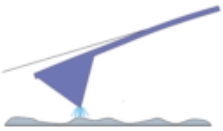
Contact	
Tip indenting sample	• Stiffness (Young's modulus, elastic response) • Viscoelastic response (variable rates or indentation depth) • Measurement of active forces (e.g. generated by cells) 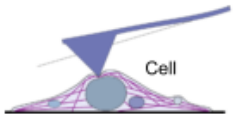
Retract	
Tip lifting off surface (few atomic distances to nanometers)	Adhesion: • Non-specific (including chemical affinity, surface coatings) • Ligand-receptor (e.g. antibody-antigen) • DNA hybridisation (e.g. matched or mismatched pairs) • Cell surface interactions 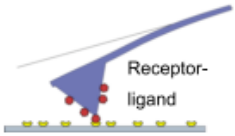
Tip further away (nanometers to hundreds of nanometers)	Stretched molecules between tip and surface: • Protein unfolding, pulling out of membranes • Entropic elasticity • DNA stiffness, structural transitions and "melting" • Other conformational changes in stretched molecules, e.g. chair-to-boat transition in sugar rings Other stretched attachments e.g. membrane tethers formed on cells 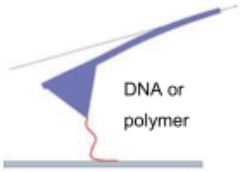
Tip far from surface (1-5 microns)	Connections broken between the tip and surface, no further interaction. Adhesion strength can be measured between attached molecules and the surface when the attachments break.

Table 1.3: An overview of interactions measured during a force spectroscopy cycle. (Source: NanoWizard AFM Handbook).

1.4.5 Single cell force spectroscopy (SCFS)

AFM based force spectroscopy is used in various important applications like nano-mechanical investigations of elastic properties, studying protein unfolding dynamics, quantifying ligand-receptor interactions and cell adhesion strength. Regarding cell-cell interactions, the technique is capable of resolving individual detachment events, as well as the overall force required to detach a cell and therefore is widely used to quantify the forces involved during cell adhesion. Single cell force spectroscopy (SCFS) is the most versatile

method to study the adhesive interactions of cell with other cells, or cell and a functionalized substrate. A living cell is attached to an AFM cantilever and the interactions of cell with other cells, surfaces (extracellular matrix) or proteins can be studied and forces in the range of 10 pN to 200 pN can be detected (Helenius *et al.*, 2008; Friedrichs *et al.*, 2013).The interactions of isolated receptor and ligand complexes can be studied using single molecule force spectroscopy (SMFS) (Friedrichs *et al.*, 2013). For SMFS experiments the tip of the AFM cantilever is modified with a ligand (or receptor) of interest and the surface is coated with a receptor (or ligand) and detachment of single ligand-receptors can be studied. SMFS have some limitations; the receptors isolated from the cell surface can be in different functional state than in their native environment. The transmembrane receptors are purified in truncated forms and therefore the regulation with cytoplasmic factors are neglected (Helenius *et al.*, 2008). In contrast to SMFS, SCFS enables us to study ligand-receptor interactions in their cellular environment.

Zhang et al. studied the interaction of LFA-1 with ICAM-1 using this technique and demonstrated that the mean unbinding force increases with the loading rate (Zhang *et al.*, 2002). Wojcikiewicz et al. investigated the interaction of 3A9 cells expressing LFA-1 with recombinant ICAM-1 while stimulating the cells using phorbol myristate acetate (PMA). It has been reported that adhesion got enhanced after PMA stimulation as compared to non-stimulated cells but that the unbinding forces were not between these two conditions (Wojcikiewicz *et al.*, 2003). Taubenberger et al. studied the interaction of α2β1 integrin with collagen type 1 matrix. SCFS experiments were performed with cells expressing α2β1 with collagen type I coated substrate at two different contact time (<60s and >60s) and reported that cells switch to an activated state for the contact time >60s. The mean unbinding force increased from 47±13 pN (contact time <60 s) to 159±132 pN (contact time >60s) suggesting a change from single to cooperative receptor binding (Taubenberger *et al* ., 2007). The mean unbinding forces obtained for various ligand-receptor interactions that have been measured using SCFS and SMFS is shown in Table 1.4.

Receptor	Ligand(s)	SCFS rupture force [pN]*	SMFS rupture force [pN]	Cell type
Integrin α2β1	Collagen I and IV	65 (collagen I)	Not determined	CHO
Integrin α4β1	VCAM1	20	Not determined	U937
Integrin α5β1	Fibronectin	60 (80), 35, 40	Not determined	Epithelial, K562
Integrin αLβ2 (LFA-1)	ICAM1	35, 40 (80), 70	Not determined	Jurkat and 3A9 HUVEC
Integrin αLβ2 (LFA-1)	ICAM2	40 (50)	Not determined	Jurkat
Integrin αVβ3	RGD peptide	42	Not determined	Bone
E-cadherin	E-cadherin	73	25	CHO
N-cadherin	N-cadherin	30	Not determined	CHO
VE-cadherin	†	50	45	HUVEC
PMN‡	E-selectin	140	Not determined	PMN
PMN‡	L-selectin	80	Not determined	PMN
PSGL-1 (SELPLG)	P-selectin	130	150	PMN and LS174T
NIH3T3 cell‡	Concavalin A	80	95	NIH3T3
Surface-expressed mannose residues	Concavalin A	86	Not determined	NIH3T3
Saccharides from blood types A and O	Helix pomatia lectin	65	Not determined	Red blood cells
Galectin 3, galectin 9	Collagen I and laminin 3	Not determined	Not determined	MDCK
SGLT1 (SLC5A1)	Monosaccharides	51 (glucose)	Not determined	CHO
hbhA	Heparin	53	50	*Mycobacterium tuberculosis*
csA	csA	20	Not determined	*Dictyostelium discoideum*
D-Ala-D-Ala peptide terminal‡	Vancomycin	83	98	*Lactococcus lactis*

Table 1.4: Ligand-receptor interactions studied using SCFS and SMFS (Helenius *et al.*, 2008).

1.4.6 Studying cell adhesion using SCFS

There are a number of technical considerations to conduct experiments using SCFS. Some of the important ones are discussed below.

1.4.6.1 Cantilever selection

For SCFS, soft and tipless AFM cantilevers are used to detect single adhesive bonds in the range of 20 pN to 100 pN. The soft cantilevers with low spring constant (0.01-0.06 N/m, very flexible cantilever) are used for experiments. Tipless cantilevers from Bruker (MLCT-O10) were used in our study and specifications for different tips on the cantilever are shown Figure 1.20. A cantilever with different tips (B-F) is shown in Figure 1.20 and tip A is placed at the other end of the cantilever.

Shape	Resonant frequency (kHz)	Spring constant (N/m)	Length (µm)	Width (µm)
A Triangular	22	0.07	170	22
B Rectangular	15	0.02	200	20
C Triangular	7	0.01	300	20
D Triangular	15	0.03	215	20
E Triangular	38	0.1	130	18
F Triangular	125	0.6	75	18

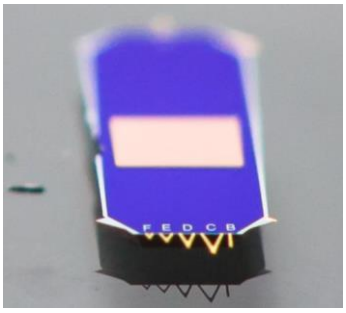

Figure 1.20: Picture of tipless cantilevers from Bruker (MLCT-O10) and specifications of tipless cantilevers (MLCT-O10). (Source: brukerafmprobes.com).

1.4.6.2 Coating and calibration of the cantilevers

To attach a cell to the cantilever, it has to be coated with a molecule that aids binding of the cell with a bond-strength greater than the bonds involved in cell-cell or cell-surface adhesion. There are different cell adhesive agents used for coating the cantilevers like CellTak (a polyphenolic protein that anchor itself to solid structures), lectins such as Concanavalin A and wheat germ agglutinin (which specifically recognizes sugar groups on the cell surface). Antibodies that specially bind to target motif on cell surface, poly-lysine (binds to negative charges on the cell surface) and ECM proteins can be also used for attaching the cell to the cantilever (Friedrichs *et al.*, 2013).

The coated cantilever is calibrated to find the sensitivity and spring constant using built-in routines in the JPK software. Sensitivity and spring constant convert the photodetector signal in volts to a quantitative force value in Newton. The calibration of sensitivity and spring constant are described in detail in Appendix C.

1.4.6.3 Cell attachment and force measurements

The single cell attached to the cantilever is approached to the surface at constant speed and put in contact with another cell at a certain force for a few seconds. Then, the cantilever is retracted and the force curve obtained is analyzed to obtain different parameters like adhesion strength, detachment force and mean rupture force. Cell attachment to the cantilever, force measurements and data analysis are explained in chapter 3.

1.4.6.4 Parameter selection

There are some critical parameters that need to be optimized for SCFS experiments. These include pulling distance, contact force, contact time, approach and retracting velocity and sampling rate. SCFS measurements are performed with long pulling distance (>60 µm) using the CellHesion module (JPK instruments, Berlin). The force applied by the cantilever

(contact force) when the cell is in contact with the surface and the contact time determine initial cell spreading and the number of bonds involved in the interaction. The approach and retract velocity must be carefully controlled in order to avoid an excess hydrodynamic drag. Higher sampling rate can be used during acquisition to detect weak bonds and to discriminate very close bonds in the curve (Friedrichs *et al.*, 2013). If a cell attached to the cantilever is used for multiple measurements, then a relaxation time is necessary. The relaxation time for the cells between each force curves has to be greater than the contact time used in the experiments (Friedrichs *et al.*, 2010). In addition, the force measurements can be conducted either in constant height or constant force mode. Constant height and constant force refer to how the piezo responds to cantilever movement after the cell has come in contact with the surface.

1.4.6.5 Temperature control

SCFS measurements can be performed under physiological conditions using Petri Dish Heater (JPK instruments) for controlling the temperature.

1.4.6.6 Limitations of SCFS

In SCFS, with a single cell attached to the cantilever only a few force measurements can be recorded, so that many experiments need to be performed to obtain good statistics. The parameters for SCFS experiments have to be optimized and selected for addressing each objectives (SMFS, cooperative studies etc) and this might be time consuming. Calibration of sensitivity and spring constant needs to be performed for each cantilever and these values might change between the cantilevers (10-15%) inducing an error in the measurements. So the data obtained from the force measurements that have optimum sensitivity and spring constant values can be considered. In addition, thermal drift in AFM complicates long time contact experiment (>20min). Thus, SCFS is mostly used in short contact time that ranges from milliseconds to 20 min (Helenius *et al.*, 2008). SCFS measures both specific and nonspecific interactions between the cells, and the data must to be treated carefully to eliminate the nonspecific interactions. Also with AFM, only the vertical forces can be measured (force between the tip and the sample) and this method is not suitable for studying forces on horizontal direction.

1.5 Cell migration

Cell migration is defined as the movement of individual cells, cell sheets and cell clusters from one location to another. Cell migration is a complex and highly integrated multistep process that plays a central role in embryogenesis, morphogenesis, development of the nervous system, tissue formation, vascular sprouting, placental development and immune cell trafficking (Lauffenburger and Horwitz, 1996; Valster *et al.*, 2005; Friedl and Wolf, 2010; Hulkower and Herber, 2011; Kramer *et al.*, 2013). Cell adhesion and migration are highly dependent on each other since they share many common features including surface receptors, signaling elements and the cytoskeleton (Ladoux and Nicolas, 2012). Cell migration orchestrates many stages of embryonic development. For example, during gastrulation, cells migrate collectively as sheets to form three-layer embryo. Also, cells migrate from epithelial layers to target locations, where they differentiate into specialized cells to form different tissues and organs (Ridley *et al.*, 2003). Cell migration is also critical in tissue repair and immune surveillance, where leukocytes in the circulation migrate into the surrounding tissue to destroy invading micro-organisms and infected cells (Ridley *et al.*, 2003; Ladoux and Nicolas, 2012).

1.5.1 Modes of migration

Cell migration requires the dynamic interactions between a cell and the substrate, where a cell will adhere, spread and then migrate. The mode of cell migration is classified based on the morphology of cell migration patterns. These modes can be influenced by various molecular parameters such as cytoskeletal reorganization, cell-matrix interaction, force generation and other external cues (Friedl and Wolf, 2010; Huttenlocher and Horwitz, 2011; Kramer *et al.*, 2013). Two main cell migration patterns are single cell and collective cell migration. Single cell migration can further be subdivided into amoeboid and mesenchymal types of migration. Amoeboid migration is characterized by the movement of rounded or ellipsoidal cells without the involvement of focal adhesion and stress fibers. They are two subtypes in the amoeboid movement. The first is the rounded, blebby migration of cells that use a propulsive, pushing migration mode used by embryonic cells, leukocytes migrating through the ECM or by some cancer cells (Figure 1.21). The second form is characterized by more elongated cells with actin-rich filopodia at the leading edge and weak adhesive interactions with the substrate (Figure 1.21). This type of migration is observed in moving neutrophils, dendritic cells and some cancer cells (Friedl and Wolf, 2010; Kramer *et al.*, 2013). Mesenchymal cell migration is characterized by the movement of cells with strong

adhesion to the ECM, cytoskeletal contractility and elongated spindle-like cell bodies as shown in Figure 1.21. Cells like fibroblasts, sarcoma and cancer cells that have undergone epithelial to mesenchymal transition (EMT), use this mode of migration. Sometimes individual cells form cell-cell contacts while moving in a common track termed as chain migration or multicellular streaming (Figure 1.21). Single cell migration is important for cells to integrate into tissues or to move from one location to another for different functions (immune cell trafficking). Collective cell migration is characterized by the movement of cells in the form of multicellular tubes, sheets, strands through the ECM maintaining their cell-cell junctions as shown in Figure 1.21. Collective cell migration occurs on 2D surfaces, when epithelial sheets travel collectively across basal membrane for wound healing. Collective cell migration of cells is mainly observed during embryonic development or during the development of glands and ducts (Friedl and Wolf, 2003). Collective migration in 3D occurs as branches, tubes, strands or clusters in case of cancer cell invasion. It also plays an essential role in building, shaping and remodeling of tissues and tissue compartments.

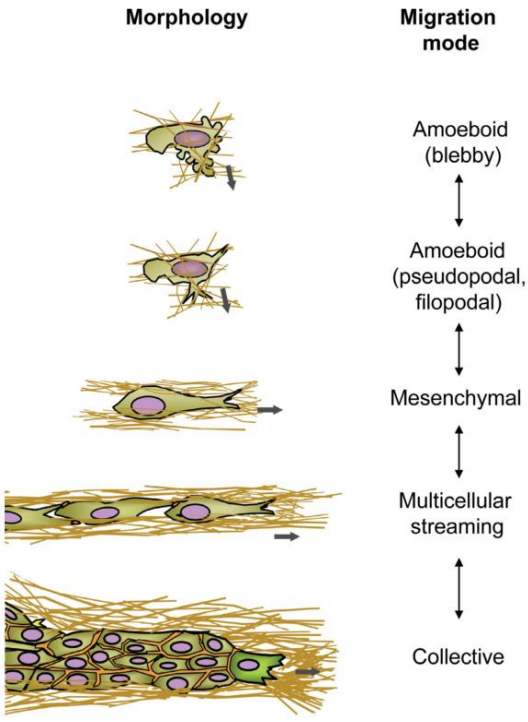

Figure1.21: Modes of cell migration with their morphologies. The cells show different morphology (rounded, actin rich filopodia or spindle shaped) and collective during the migration. The thick grey arrows indicate the direction of cell migration (Friedl and Wolf, 2010).

1.5.2 Cell migration in 2D

Single cell adhesion and migration have been extensively studied in 2D culture systems, either on plastic or glass surfaces. Cell migration in 2D is described as a multistep cyclic process involving cell-substrate adhesion, extension of the leading edge and retraction of the trailing edge of a cell. Different steps involved in the cell migration are shown in Figure 1.22. First, a moving cell becomes polarized and extends protrusions in the direction of migration. These protrusions can be lamellipodia or spike-like filopodia and they are driven by actin polymerization (Figure 1.22-1). Actin polymerization at the leading edge of the cell directly provides the force necessary for protrusion. Following the protrusion of the leading edge, adhesion molecules gather in the extending region help to attach the leading edge to the substrate. Cell-substrate attachments are created at the leading edge when actin bundles link the cell to the substrate via focal adhesion complexes (Figure 1.22-2). These attachments prevent the leading edge from retracting. When the cell adheres at the leading edge, it also detaches the rear of the cell, due to contraction of actin bundles. Finally, the rest of the cell is pulled forward (Figure 1.22-3), by contractile forces (traction forces) that are produced by actomyosin contraction at the cell body and the rear (Lee *et al.*, 1993; Friedl and Brocker, 2000; Friedl and Wolf, 2003; Ridley *et al.*, 2003; Ananthakrishnan and Ehrlicher, 2007; Ladoux and Nicolas, 2012).

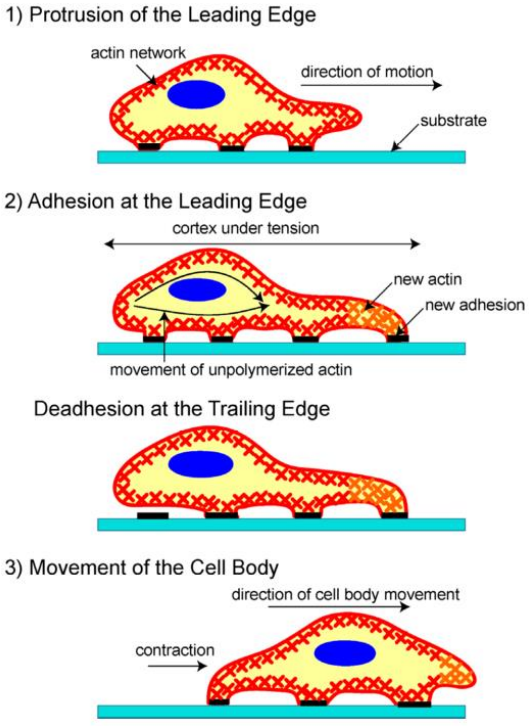

Figure 1.22: Schematic representation of the different steps involved in cell migration on 2D substrates. 1. Cell extends a protrusion in the direction of actin polymerization at the leading edge. 2. Then the cell attaches its leading edge to the surface using transmembrane cell surface receptors and de-adheres at the cell body and rear. 3. Finally, it pulls the whole body forward by contractile forces generated at the cell body and rear of the cell (Ananthakrishnan and Ehrlicher, 2007).

1.5.3 Molecular mechanism involved in 2D Cell migration

Many different molecules and signaling pathways coordinate cell migration, but the actin cytoskeleton and Rho family GTPases play very prominent roles as shown in Figure 1.23 (Ridley *et al.*, 2003; Burridge and Wennerberg, 2004; Reig *et al.*, 2014). For a cell to migrate, it must be polarized, which means that the molecular processes at the front and the back of a cell has to be different, developing a front-to-back polarity. The protrusions are driven by actin polymerization and the organization of actin depends on the type of protrusions. Lamellipodia contain a highly branched dendritic network of actin filaments, whereas filopodia are formed by long parallel actin filament bundles (Figure 1.23, left). Branched actin networks termed as cortical actin and elongated cables of actin fibers called stress fibers are formed during the attachment of cells to the substrate. Acquisition of front-to-back polarity is fundamental to initiate locomotion and it depends on the activity of small GTPases such as Cdc42, Rac and Rho, which regulate actin dynamics, adhesion and protrusion formation (Figure 1.23, right). Cdc42 is active at the front of a migrating cell and its main role is to activate Rac1. Cdc42 along with Rac1 mediate the actin polymerization in protrusions. The back of a migrating cell is defined by the activity of Rho, myosin II and Ca^{2+} - activated proteases. The contraction of actin filament is controlled by myosin II and they are induced by Rho and ROCK kinase (Ridley *et al.*, 2003; Reig *et al.*, 2014).

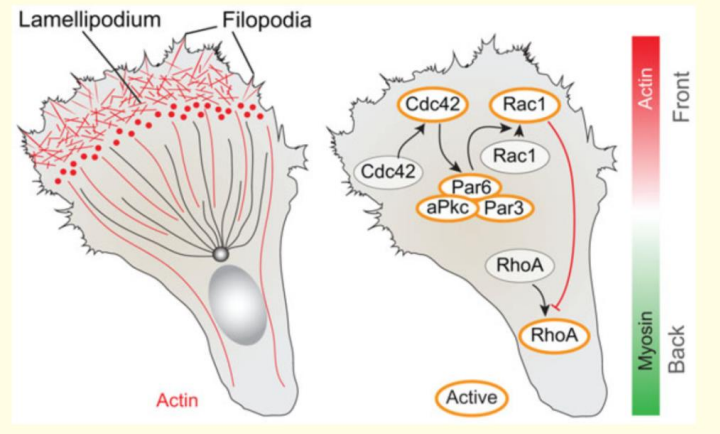

Figure 1.23: Front-to-back polarity in a migrating cell. The figure shows different types of actin filaments observed in a migrating cell and presents important signaling molecules involved in the migration (Reig *et al.*, 2014).

1.5.4 The Cytoskeleton

Cell adhesion and migration are tightly coupled and both processes require constant remodeling of the cytoskeleton. In most cells, the cytoskeleton is essential for creating motility-driving forces and in coordinating the process of cell migration. The cytoskeleton is comprised of three types of filaments: actin filaments, microtubules and intermediate filaments. The important component of the cytoskeleton that is involved in all the steps of cell migration is actin filaments (microfilaments), which are 7 nm in size. The globular actin monomers (G actin) polymerize to form filamentous actin (F-actin) that are linked together to form the actin filament with a right-handed helix structure (Figure 1.24B). Within the cells, actin filaments are organized into highly-ordered structures forming bundles or 3-D networks. Actin filaments are dynamic in nature with constant assembly and disassembly of actin monomers. They have two distinct ends: a fast growing end (plus end) and a slow growing end (minus end) (Figure 1.24B). Actin filament will bind monomers at one end and grows by polymerization when the concentration of monomeric actin is above its critical concentration. On the other hand, when the concentration falls below, the monomers detach from the filament at minus end and they shrink by depolymerization. By having two different critical actin concentrations at the opposing ends of filament, actin filaments can grow in the plus end and shrinks in the minus end and this process is termed as treadmilling. This process helps actin filaments to move inside the cytosol and generate forces. Actin self-assembles in the presence of cross-linker proteins and molecular motors like myosin II. Actin filaments provide mechanical support to the cells and are remodeled constantly to perform specific cellular functions like cell adhesion and cell migration (Cooper, 2000; Alberts *et al.,* 2002; Ananthakrishnan and Ehrlicher, 2007; Wickstead and Gull, 2011).

A second member of the cytoskeleton is microtubules. Microtubules are hollow, straw shaped rigid rods with an outer diameter of 25 nm. They are made up of tubulin heterodimers (α-tubulin and β-tubulin) and they polymerize to form protofilaments. Then, typically 13 protofilaments align together to form microtubules. Microtubules exhibit similar dynamics to those of actins: the tubulin dimers can polymerize and depolymerize constantly, treadmill, and can impact the force through polymerization. They are required for various cellular functions like cell division, organization of intracellular structures and intracellular cargo transport.

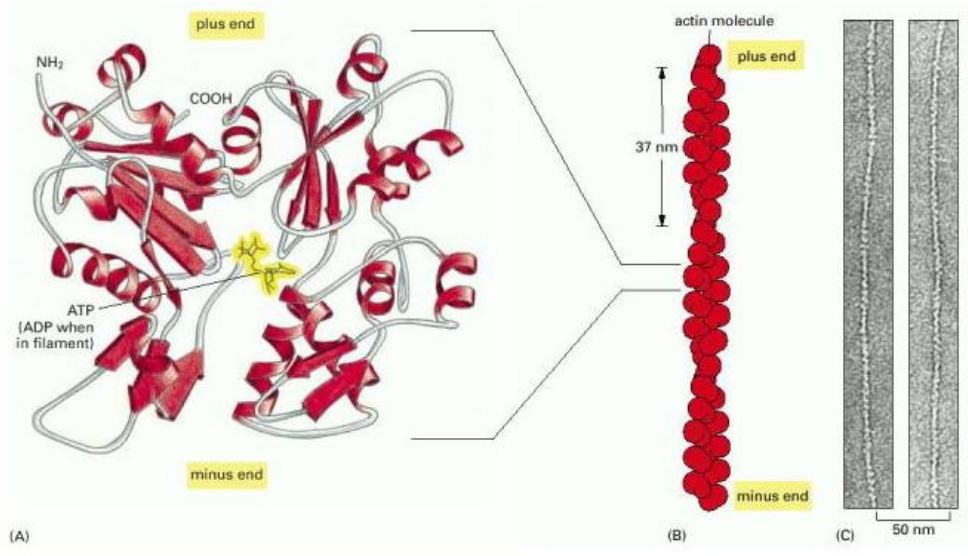

Figure 1.24: Structure of actin filament. The actin monomer structure (A). Assembly of actin monomers in a filament showing plus and minus end (B).Electron micrograph of actin filaments (C) (Alberts *et al.*, 2002).

Intermediate filaments are the third member of the cytoskeleton. They are about 10 nm in diameter. They are stable structures comprising of more than 50 different proteins that are categorized into six groups: 1) type 1 keratins (acidic) 2) type II keratins (basic/neural) 3) vimentin and desmin 4) neurofilament proteins 5) nuclear lamins and 6) nestin. Intermediate filaments are not dynamic structures like microtubules and actin. Intermediate filaments give structural integrity to cells by providing mechanical strength to cells and tissues (Cooper, 2000; Alberts et al., 2002; Wickstead and Gull, 2011).

1.6 Methods to study cell migration

Cell migration is an integrated multistep process that regulates embryo morphogenesis, contributes to tissue repair and regeneration. Deregulation of migration contributes to several important pathological processes, including vascular disease, osteoporosis, chronic inflammatory diseases (rheumatoid arthritis and multiple sclerosis), cancer and mental retardation. Thus, understanding the process of cell migration is essential for effective drug development (Ridley *et al.*, 2003; Valster *et al.*, 2005). Various methods used to study cell migration are shown in Figure 1.25. Two widely used methods to study cell migration such as Boyden chamber assay and wound healing assay are discussed below.

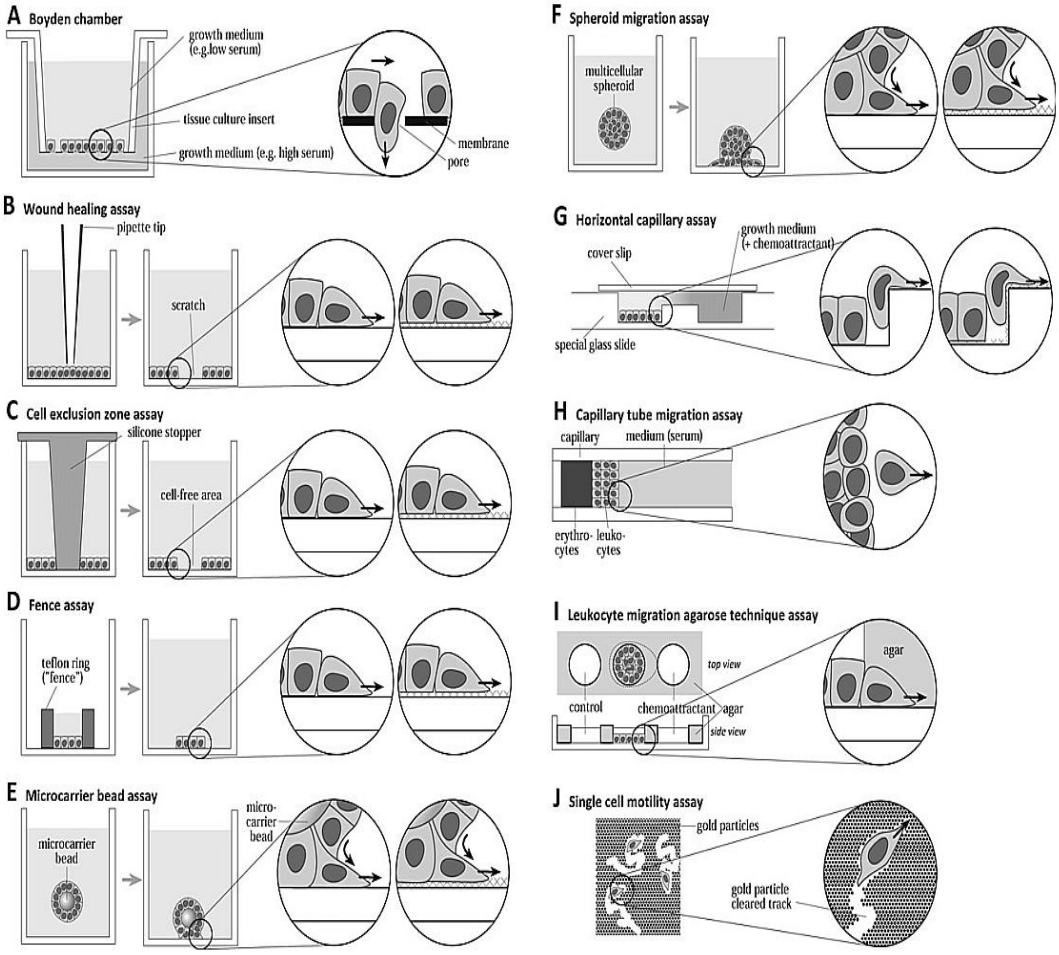

Figure 1.25: Schematic representation of commonly used migration assays (Kramer *et al.*, 2013).

1.6.1 Transwell migration assay (Boyden chamber)

This assay was introduced by Boyden to analyze chemotactic responses of leukocytes (Boyden, 1962). This assay is based on a chamber separated into two compartments by a porous membrane filter through which the cells migrate in response to a chemotactic agent (Figure 1.25A). In this assay, cells are seeded in the upper part of the compartment above the membrane and they migrate through the pores of the membrane into the lower compartment that contains medium with an attractant. After the incubation period, migrated cells can be detected and quantified. Two types of methods can be used to detect and quantify these cells. First, the cells that passed through the membrane can be quantified by fixing and staining the membrane and then counting the number of cells on the underside of the membrane using a microscope. Second, the migrated cells can be stained with fluorescent dyes and detached from the membrane which then can be quantified using a fluorescent reader (Hulkower and Herber, 2011; Kramer *et al.*, 2013). In this assay, it is critical to choose the right pore size,

which allows the cells to migrate. The advantages are easy experimental setup, availability of membranes with different pore sizes, ability to analyze migration of adherent as well as non-adherent cells. The main disadvantage is all the parameters like pore size, time for migration needs to be optimized for each cell types.

1.6.2 Scratch assay (wound-healing assay)

This assay is widely used to study the migration of cells on 2D surfaces. In this assay, cells are seeded on a multiwell plate. The cells are allowed to attach, spread and form a confluent monolayer. Then, a plastic pipette tip is used to scratch and remove the cells (wound formation) from the monolayer (Figure 1.25B). Cell migration can be subsequently monitored by microscopy, as cells travel from the intact zones into the wounds. Cell movement can be calculated by measuring the decrease of wound area at different time points until the wound is closed. This assay allows the possibility to study cell migration on different substrates (cells can be seeded on substrate with collagen I, fibronectin or Matrigel). Scratch assays were used as models of wound healing for epithelial or mesenchymal cells. Simple setup and easy readout are the main advantage of this assay. Drawback of this assay is that the scratch made in the monolayer is uneven between the wells and they can also damage the ECM and cells (Hulkower and Herber, 2011; Kramer *et al.*, 2013).

1.7 Force generation during cell migration

Cell migration occurs through complex interactions involving actin polymerization, matrix degradation, chemical signaling and formation of focal adhesion complexes. In this multi-step process, two distinct types of forces are generated as shown in Figure 1.26. First, is the protrusive force essential to extend the membrane (lamellipodia or filopodia) and this force is provided by actin polymerization. The second force is the contractile force (traction force) exerted by cells which is important to move the cell body forward. Actin filaments generate motility forces through their interaction with myosin motors. A Myosin motor consists of a head, a neck and a tail region, where head and neck are responsible for the attachment and force production. Myosin motors walk on actin filament through a three step process: binding, power stroke and unbinding. This ATP dependent process is continuously repeated and leads to the generation of traction forces (acto-myosin contractile force) and helps in the forward cell movement (Lauffenburger and Horwitz, 1996; Ananthakrishnan and Ehrlicher, 2007).

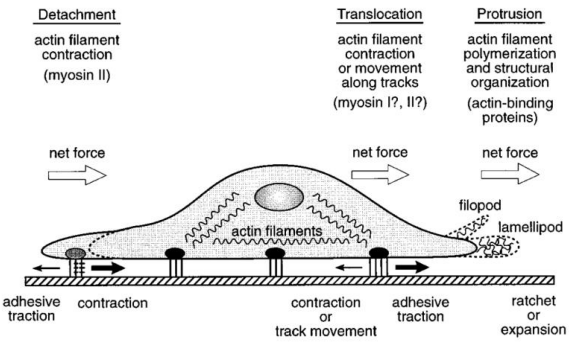

Figure 1.26: Different forces involved in cell migration. Protrusion of membrane lamellipodia or filopodia requires force generated by actin polymerization that is explained by ratchet or cortical expansion mechanism. Translocation of the cell body forward occurs by myosin interaction with the actin filaments (Lauffenburger and Horwitz, 1996).

1.7.1 Methods to study traction forces during cell migration

Forces produced by the cell itself are generated by various cytoskeletal elements and they are transmitted through the cytoplasm. Traction forces exerted by the cells are transmitted to the underlying substrate via focal adhesion sites. Traction forces are correlated with the remodeling of internal cellular structures such as focal adhesion and the cytoskeleton. Measuring the traction forces remains challenging due to the small dimension of focal adhesion sites and the inverse nature of the problem. However, methods to visualize traction forces during cell migration were developed and then modified into quantitative tools for measuring the traction forces.

Haris and co-workers in 1980 were the first to qualitatively visualize cellular tractions as visible wrinkles on a deformable silicone rubber substrate (Harris *et al.*, 1980). They compared and estimated the traction forces generated by different cell types, according to the degree of wrinkling. This technique has been used to study the forces exerted by fibroblasts. Lee and co-workers modified the above assay, by introducing stretchable silicone substrate with beads to measure the traction forces (Lee *et al.*, 1994; Oliver *et al.*, 1995). This method was used to study the traction forces exerted by keratocytes. In 1999 Dembo and Wang used smaller fluorescent beads (200 nm) embedded in polyacrylamide (PA) gel as substrate and determined the position of beads as compared to the initial one, to obtain beads displacements (Figure 1.27A). The displacement of beads can be followed in time with the microscope and hence this technique is termed as traction force microscopy (TFM). During migration, the cells exert some forces on the PA substrate that cause the beads to displace (Figure 1.27B). The bead movements are translated into a strain map, and these strains are used to calculate the forces exerted by the cells through mathematical computations (Dembo and Wang, 1999).

This is an inverse elasticity problem and it is very sensitive to noise, which originates from the limited spatial resolution of the measured deformation field. Several methods have been developed to solve this inverse problem namely, 1) the boundary element method (BEM), 2) the Fourier Transform Traction Cytometry (FTTC), 3) the Traction Recovery from Point Force (TRPF) and 4) the Adjoint Method (AM) (Ladoux and Nicolas, 2012).

Some alternative methods were also developed and used to determine the traction forces exerted by individual focal adhesion sites. Galbraith and Sheetz developed a microsystem allowing the deflections of small pillars/needles to give access to the local forces exerted by the cells at the focal adhesion (Galbraith and Sheetz, 1997). This method was further improved to measure stresses at focal adhesion sites on micropatterned surfaces (Balaban *et al.*, 2001). Another approach has been developed using a substrate composed of flexible arrays of micropillars (Tan *et al.*, 2003) that were made of polydimethylsiloxane (PDMS). In this case, the deflection of each post gives a direct measurement of the local forces exerted by the attached cells independently of the forces acting on the neighboring cells (Figure 1.27C-D).

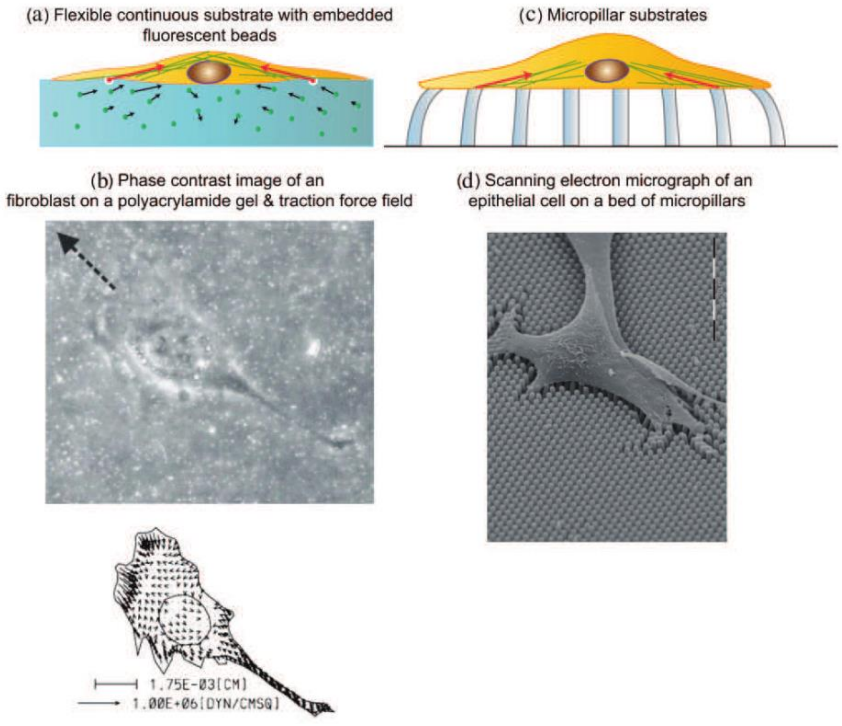

Figure 1.27: Traction force microscopy (TFM) technique to measure the forces generated by cells. Schematic representation of TFM using the fluorescent beads embedded on the gel (a) and picture of cell deforming the substrate and the resulting forces (b). Schematic representation of the TFM using the micropillar method (c) and example of a cell adhered on micropillars (d), (Ladoux and Nicolas, 2012).

These different approaches have been used to study the traction forces involved in single cell migration (Balaban *et al.*, 2001; Tan *et al.*, 2003; Sabass *et al.*, 2008; Delanoe-Ayari *et al.*, 2010; Rieu *et al.*, 2015), cell-cell interactions (Ladoux and Nicolas, 2012), stem cell differentiation (Fu *et al.*, 2010) and multicellular systems (Nelson *et al.*, 2005; Trepat *et al.*, 2009).

1.7.2 Polyacrylamide (PA) gel Traction Force Microscopy

PA gels are widely used to study the traction forces exerted by different cell types because they have interesting physico-chemical properties. They are optically transparent, low cost and chemically simple compounds. PA gels are prepared by mixing acrylamide and bis-acrylamide and inducing free radical polymerization. The elasticity or stiffness (measured as Young's modulus, E) of the substrate can be easily tuned by changing the relative concentration of acrylamide and bis-acrylamide over several orders of magnitude from extremely soft to stiff (1 kPa to 100 kPa) gels. The expected modulus of elasticity by changing the relative concentrations of acrylamide and bis-acrylamide is provided in Table 1.5 (Tse and Engler, 2010) with rigidity of gel that were used in the experiments indicated in box. The surface chemistry of PA gels can be kept constant while changing mechanical properties (Pelham and Wang, 1998). PA gels have antifouling properties, meaning that the adsorptions of serum proteins or the nonspecific binding of cell surface receptors are negligible. Henceforth, only adhesive molecules can be covalently attached to the surface of the gel that serve as the ligands for the attachment of cells (Vignaud *et al.*, 2014). PA gels are non-adhesive and different methods are used to deposit the protein of interest (collagen or fibronectin) on their surface. Most of the methods require chemical crosslinkers such as (sulfosuccinimidyl 6-(4'-azido-2'-nitrophenylamino)hexanote(sulfo-SANPAH) or N-Hydroxysuccinimide(NHS) and ethyl(dimethylaminopropyl)carbodiimide(EDC) (Damljanovic *et al.*, 2005) to bind the proteins on PA gels. These reagents are poorly stable in presence of water and the efficiency of the crosslinking is variable between the experiments. Few other methods like deep UV (Tseng *et al.*, 2011) exposure or adding the NHS ester during the polymerization (Polio *et al.*, 2012) were developed to overcome the disadvantages of the above methods that involve chemical crosslinking. But these methods have difficulties to control the cell-ligand density (Grevesse *et al.*, 2013). So, Grevesse and co-workers in 2013 developed a very simple strategy to functionalize PA gels by incorporating hydroxyl groups in acrylamide hydrogels that are called as hydroxy-PAAm hydrogels. The hydroxyl groups on

the surface permit us to attach the protein of interest directly and this avoids the use of chemical compounds (Grevesse *et al.*, 2013).

Acrylamide %	Bis-acrylamide%	Acrylamide from 40% stock solution (ml)	Bis-acrylamide from 2% stock solution (ml)	Water (ml)	$E \pm$ St. Dev. (kPa)
3	0.03	0.75	0.15	9.1	0.20 ± 0.03
3	0.06	0.75	0.3	8.95	0.48 ± 0.16
3	0.1	0.75	0.5	8.75	1.10 ± 0.34
3	0.15	0.75	0.75	8.5	1.37 ± 0.22
3	0.225	0.75	1.125	8.125	1.67 ± 0.14
3	0.3	0.75	1.5	7.75	1.78 ± 0.19
4	0.03	1	0.15	8.85	0.71 ± 0.24
4	0.06	1	0.3	8.7	1.16 ± 0.54
4	0.1	1	0.5	8.5	2.01 ± 0.75
4	0.15	1	0.75	8.25	2.55 ± 0.17
4	0.225	1	1.125	7.875	3.13 ± 0.42
4	0.3	1	1.5	7.5	3.24 ± 0.58
5	0.03	1.25	0.15	8.6	1.00 ± 0.31
5	0.06	1.25	0.3	8.45	1.80 ± 0.44
5	0.1	1.25	0.5	8.25	3.15 ± 0.85
5	0.15	1.25	0.75	8	4.47 ± 1.19
5	0.225	1.25	1.125	7.625	8.44 ± 0.82
5	0.3	1.25	1.5	7.25	8.73 ± 0.79
8	0.048	2	0.24	7.76	2.61 ± 0.82
8	0.264	2	1.32	6.68	19.66 ± 1.19
8	0.48	2	2.4	5.6	40.40 ± 2.39
10	0.03	2.5	0.15	7.35	2.83
10	0.06	2.5	0.3	7.2	7.43
10	0.1	2.5	0.5	7	10.61
10	0.15	2.5	0.75	6.75	16.70
10	0.225	2.5	1.125	6.375	23.43
10	0.3	2.5	1.5	6	34.88

Table 1.5: Expected modulus of elasticity after polymerization of relative concentrations of acrylamide and bis-acrylamide and rigidity of gel used in the experiments is indicated in box (Tse and Engler, 2010).

1.7.3 Elasticity of Polyacrylamide gels

The elasticity (stiffness or rigidity) is a characteristic of the ECM that anchorage dependent cells can sense and respond to with a variety of cellular processes. The changes in substrate elasticity influences several cellular behaviors including cell proliferation, locomotion, adhesion, spreading, morphology and even differentiation of stem cells (Tse and Engler, 2010). Most of the experiments performed to understand cell adhesion and migration were performed with plastic or glass surfaces, which represent a physiologically inappropriate

environment. For this reason, several synthetic materials that can replicate the range of ECM rigidities were developed to study cell adhesion and migration (Versaevel *et al.*, 2014). Many cellular functions have been shown to depend on the rigidity of the environment. It has been reported that cell migration were directed towards increased substrate adhesiveness and stiffness (Lo *et al.*, 2000). Engler and co-workers in 2006 reported that the changes in the ECM stiffness can drive the differentiation of mesenchymal stem cells into specific lineages as shown in Figure 1.28. The mesenchymal stem cells seeded on PA gels with different rigidity with 0.1-1 kPa, 8-17 kPa and 25-40 kPa differentiated into primary neurons, myoblasts and osteoblasts respectively (Engler *et al.*, 2006).

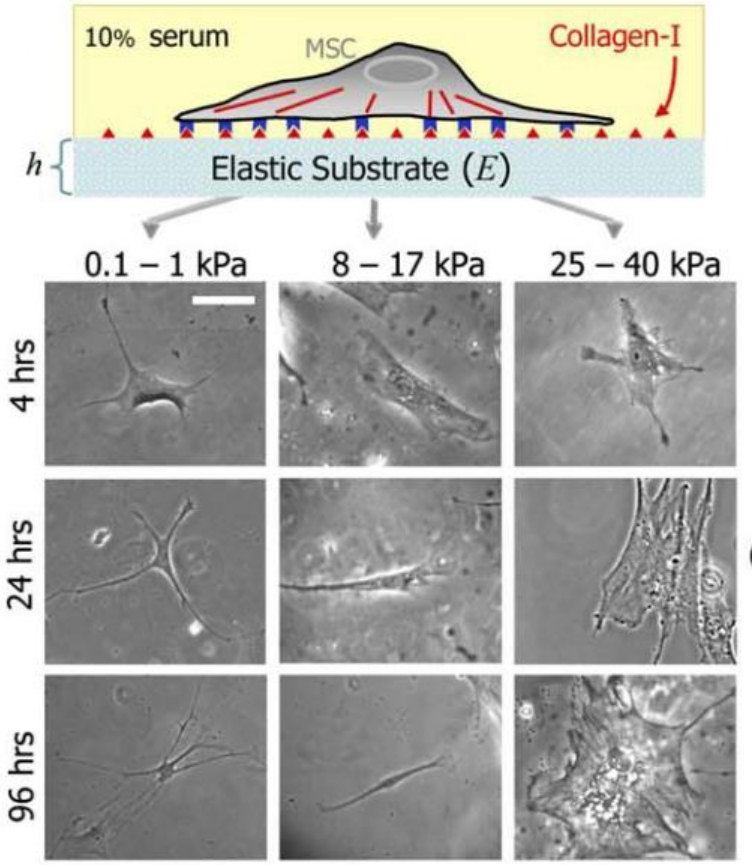

Figure 1.28: Differentiation of mesenchymal stem cells. The PA gel with different rigidity were seeded with mesenchymal stem cells and then followed during spreading and differentiation of cells. Scale bar = 20µm (Engler *et al.*, 2006).

Different tissues and organs also exhibit a wide range of elasticity from 10^3 Pa to 10^6 Pa as shown in Figure 1.29. However, only very few materials like PA gels have been reported to cover the entire range of elasticity (from kPa to MPa) that can be found in the human body.

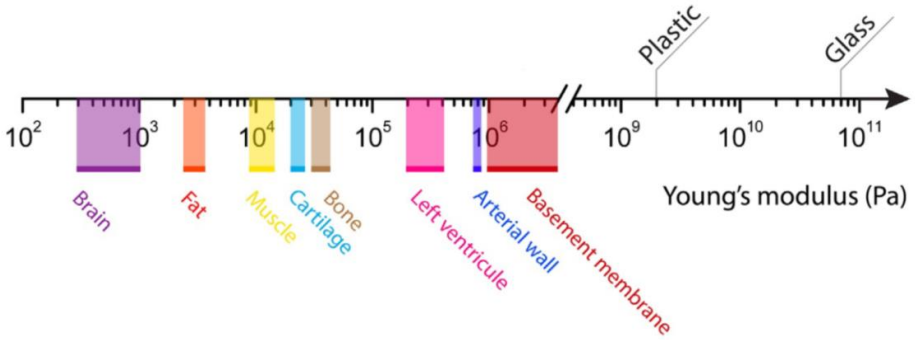

Figure 1.29: Elasticity of different cell types in our body. The elasticity of different tissues was compared with culture surfaces such as plastic dishes and glass coverslips (Versaevel *et al.*, 2014).

Few studies reported that the elasticity of cells can be used to differentiate cancer cells from normal cells. They showed that the normal cells are stiffer as compared to the cancerous cells using AFM (Lekka *et al.*, 1999; Ramos *et al.*, 2014; Abidine *et al.*, 2015; Lekka, 2016).

1.7.4 Polyacrylamide gel micropatterning

Cells *in situ*, within organs or tissues are embedded into a highly structured microenvironment. The cell microenvironment geometry and mechanics can strongly impact the cell morphology and their functions. The *in vivo* microenvironment geometry and architecture can be mimicked and controlled using micropatterning techniques. It allows the creation of ECM protein islands of controlled size and shape, called micropatterns, surrounded by antifouling polymers preventing nonspecific protein and cell adhesion. Recently, micropatterning technique has been used to study the role of microenvironment geometry in regulation of many physiological processes like cell shape, cell architecture, internal cell organization, cell migration, cell division, cell differentiation, tissue architecture etc. (Théry, 2010; Vignaud *et al.*, 2014). Different micropatterning methods like microcontact printing, photo-patterning and laser-patterning have been developed and used to create protein islands on glass or plastic culture substrates (Théry, 2010). Similarly, many experimental methods have been achieved to micropattern proteins on PA hydrogels (Rape *et al.*, 2011; Tseng *et al.*, 2011; Grevesse *et al.*, 2013; Polio and Smith, 2014; Vignaud *et al.*, 2014). Most of these methods involve a microcontact printing (μCP) step to physically transfer the proteins onto the PA hydrogels (Vignaud *et al.*, 2014). Micropattering of hydrogels allows us to measure the cell traction forces through the deformation of the patterned cell contact area (Tseng *et al.*, 2011). In our current study we used microcontact printing on modified polyacrylamide hydrogels (hydroxyl-PAAm hydrogels) to measure the traction forces exerted by the cells (Grevesse *et al.*, 2013).

1.7.5 Microcontact printing on hydroxy-PAAm hydrogels

A simple method to functionalize soft polyacrylamide hydrogels by microcontact printing was developed by Grevesse et al. in 2013. They added N'hydroxyethylacrylamide monomers to standard acrylamide and bisacrylamide to provide hydroxyl groups to the gels. The ECM proteins can directly bind to these hydroxyl groups and no chemical treatments are necessary in this case. Important steps involved in this process are shown in Figure 1.30. The PDMS microstamps are incubated with fibronectin and dried after functionalization. Fibronectin functionalized PDMS microstamps are microcontact printed on the prepared hydroxy-PAAm hydrogels. The fibronectin is transferred from PDMS to hydrogels and then gels are passivated with BSA before seeding cells.

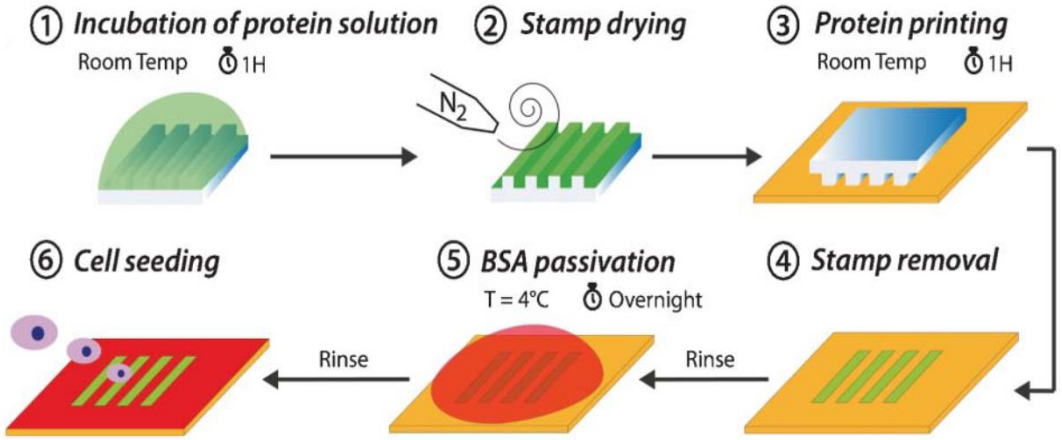

Figure 1.30: Schematic representation of micropatterning process on hydroxy-PAAm hydrogels. (1) PDMS stamp is incubated with protein solution for 1 h, (2) stamp is dried with N_2 gas, (3) protein is transferred to the gel using microcontact printing, (4) PDMs stamp is removed from the gel, (5) gel is passivated with BSA and (6) finally cells are seeded on the gel (Grevesse *et al.*, 2013).

1.7.6 Traction forces and migration of cancer cells

Metastasis involves the migration of cancer cells and for this process cancer cells must generate forces to reorganize the basement membrane and invade into the surrounding stroma (Kraning-rush *et al.*, 2012). TFM has brought a wealth of new insights into the mechanobiology of normal and cancer cell migration (Mierke *et al.*, 2008a). Paszek (2005) showed that the magnitude and organization of traction stresses differ between the cancerous cells and untransformed mammary epithelial cells, suggesting the inherent difference in cell force generation in cancer cells (Paszek *et al.*, 2005). The effect of metastatic potential on force generation was studied by Kraning and co-workers in 2012. They reported that the

metastatic cancer cells exert increased forces as compared to the non-metastatic cells in lung, breast and prostate as shown in Figure 1.31.

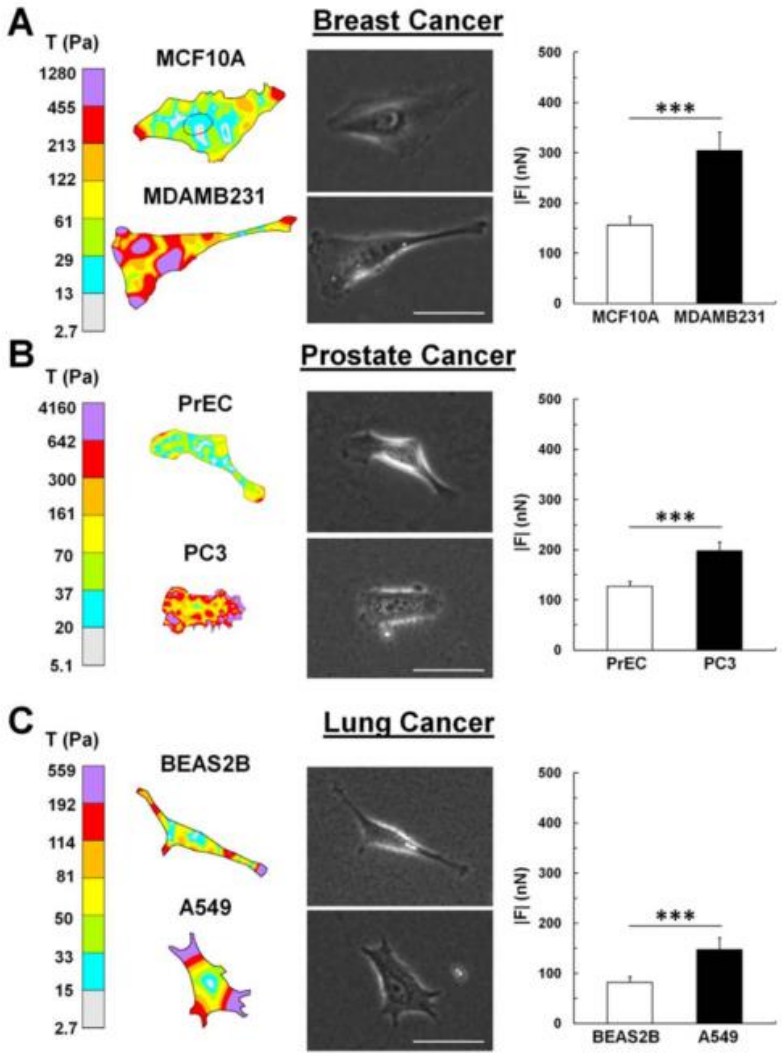

Figure 1.31: Cancer cells exert larger traction forces than non-metastatic cells. Traction maps and corresponding phase contrast images of metastatic cells (MDAMB231, PC3 and A595) and non-metastatic cells (MCF10A, PrEC and BEAS2B) from (A) breast, (B) prostate and (C) lung, Scale bar = 50 µm (Kraning-rush *et al.*, 2012).

In another study involving normal 3T3 fibroblast and H-ras transformed 3T3 (metastatic cell line), Munevar et al., reported that normal 3T3 cells exert strong and dynamic propulsive forces near the leading edge. In contrast, H-ras transformed 3T3 cells display weak traction forces and are distributed all along the cell edges (Munevar *et al.*, 2001). Peschetola and co-workers performed TFM to compare the traction forces exerted by bladder cancer cells of different invasiveness. They showed that the invasive cell line (T24) exerted less traction forces as compared to a less invasive cell line (RT112), suggesting higher traction forces for

less invasive cells (Peschetola *et al.*, 2013). These results suggest that traction stresses exerted by cells can be used as a biomarker for metastasis.

In metastasis, the extravasation is an important process where cancer cells cross the endothelial barrier and migrate to form secondary tumor at distant loci. Cancer cells have to modify their cytoskeleton and exert forces to migrate through the endothelium. TFM can be used to study the traction forces exerted by the cancer cells during the transendothelial migration. The transmigration of neutrophil through the endothelium has been already studied using different rigidities (0.42-280 kPa) of PA gels combined with TFM (Figure 1.32). Stroka et al. reported that neutrophil transmigration increased with increasing substrate stiffness (Stroka and Aranda-Espinoza, 2011). A similar approach can be used to compute the traction forces exerted by cancer cells during transendothelial migration.

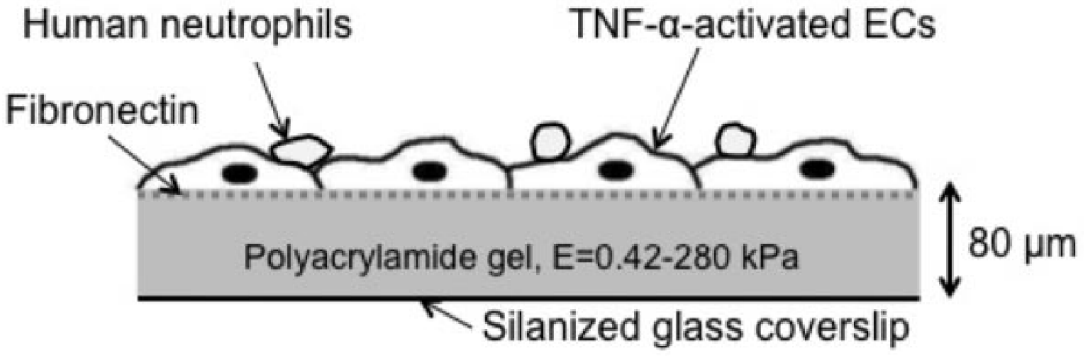

Figure 1.32: Schematic representation of neutrophil transmigration setup. ECs were plated on fibronectin coated PA gels. Neutrophils were added onto the ECs monolayer activated with TNF-α (Stroka and Aranda-Espinoza, 2011).

1.7.7 Laser scanning confocal microscopy

Confocal microscope is used to visualize cells (phase contrast or fluorescence mode) and to record the position of beads in PA gels. Time lapse imaging is performed and the displacement of beads can be calculated. Confocal microscopy offers better optical resolution by placing a pinhole to eliminate the out-of-focus light originating from the specimen. It also enables us to reconstruct the 3-D structures from the obtained slices of images. The optical path of the confocal microscope along with its important components is shown in Figure 1.33. In confocal microscopy, the sample is illuminated by a single point of light from the laser. The laser beam scans the sample in a raster pattern (point by point). The signal is detected sequentially from each point by a photomultiplier tube after passing through the pin hole and an entire image is created. The single-beam laser scanning confocal microscope is limited in

image acquisition speed and this can be overcome by using a Spinning Disk Microscope. In the spinning disk method, the specimen is illuminated at many spots through multiple pinholes. The spots are moved by the rotating disk and the light is collected on the CCD camera. The entire image is acquired faster so that photo bleaching and damage to the sample is limited.

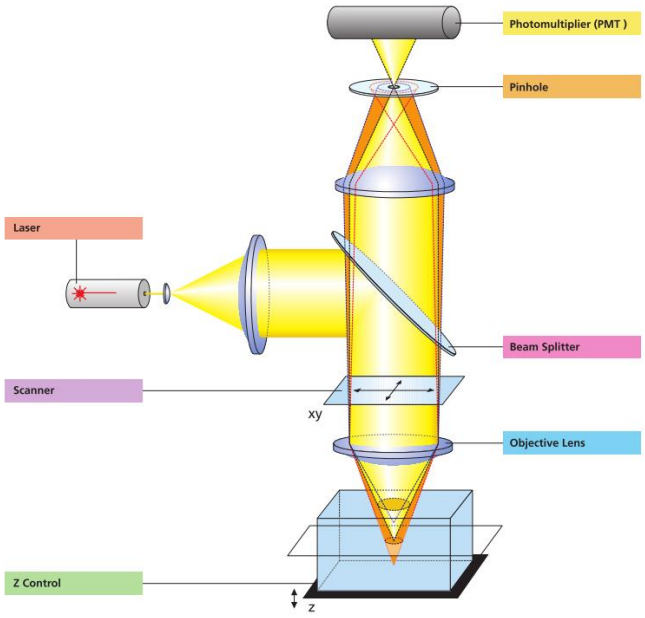

Figure 1.33: Setup of Laser Scanning Microscope (Source: Carl Zeiss).

1.7.8 Cell migration in 3D

Cell migration *in vivo* occurs in the context of 3D tissue environments. Force generation, migratory behavior, cell adhesion, focal adhesion formation, cytoskeleton organization and dynamics of cells in 2D culture have been shown to differ from those observed in 3D environment (Mierke *et al.*, 2008a). In 3D matrices, greater range of protrusive structures such as filopodia, blebs, lobopodia and pseudopods are observed. Physical properties like stiffness, crosslinking and pore size can also affect the 3D migration (Even-Ram and Yamada, 2005; Friedl *et al.*, 2012; Reig *et al.*, 2014). Several gel models have been developed to study cell adhesion and migration in 3D microenvironment like 3D collagen matrix model and basement membrane like matrices (Matrigel) to get more insights on cell migration in 3D environment.

1.8 Cancer

Cells are the basic units that make up the entire human body. Cells undergo growth and division in a spatio-temporally regulated fashion. Cancer is defined as the uncontrolled

proliferation of cells resulting in the formation of a mass called tumor that can be benign or malignant. A benign tumor is confined to its original location and does not spread. However, a malignant tumor is capable of both invading the tissue and spreading to a distant body site. Both benign and malignant tumors are classified into four main groups according to the type of cell from which they arise (Table 1.6).

Cancer	Source of origin
Carcinomas	Epithelial cells (skin or tissues that cover the surface or glands)
Sarcomas	Connective tissues (muscle, bone, cartilage, nerves etc)
Leukemias	Blood cells (WBC, RBC etc)
Lymphomas	Immune cells (T-cells or B-cells)

Table 1.6: Types of cancer. Common types of cancer and the origin (Cooper, 2000).

1.8.1 The Metastatic process

Cancer metastasis is the primary cause for 90% of cancer-associated deaths. The malignancy of cancer strongly depends upon the ability of primary tumors to spread (metastasize) to distant organs mostly via the blood stream (Jeon *et al.*, 2013; Reymond *et al.*, 2013; Shenoy and Lu, 2014). During metastasis, cancer cells manage to escape from primary tumors and penetrate in the flood flow (intravasation). Cancer cells that are carried in the blood flow can interact with the endothelium lining the walls of the blood vessels, adhere and eventually migrate (extravasation or diapedesis) through the endothelium to form secondary tumor at distant site (Mierke, 2013; Bersini *et al.*, 2014). This multi-step cascade has been divided into three major steps (1) epithelial to mesenchymal transition (2) intravasation and (3) extravasation. Firstly, the epithelial cancer cells in the primary tumor undergo epithelial to mesenchymal transition (EMT) where epithelial cells lose their cell-cell contacts and reorganize their cytoskeleton. They also lose apical-basal polarity and become highly motile and invasive (Thiery *et al.*, 2009; Nieto, 2011). Thus the process of EMT is a prerequisite for cancer cell invasion, migration and metastasis. Secondly, the cancer cells enter the blood stream (intravasation) migrating through the endothelium and the process is known as transendothelial migration (TEM). Both intravasation and extravasation process follow TEM but they are different processes because cancer cells approach the endothelium in the opposite site (Reymond *et al.*, 2013). Finally, the circulating cancer cells attach to the endothelium and

extravasate to complete the metastatic process. The process involves: 1) rolling of cells on the endothelium, 2) adhesion of cells to the endothelium, and 3) spreading and transmigration of cells through the endothelium as shown in Figure 1.34 (Strell and Entschladen, 2008; Mierke, 2013; Reymond *et al.*, 2013; Shenoy and Lu, 2014).

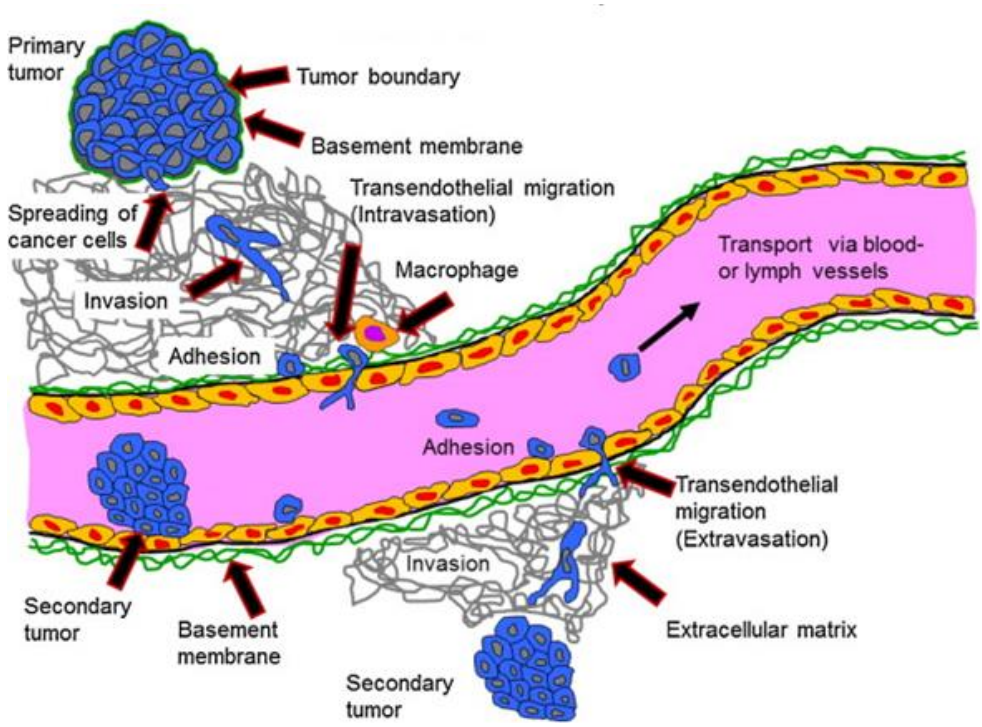

Figure 1.34: Steps involved in the metastasis process. Cancer cells from the primary site of origin invade through the ECM to reach the basement membrane lining the blood vessel. Then, cancer cells transmigrate through the endothelium lining the blood vessels or lymph vessels (intravasation) with the help of macrophages. Within the blood vessels cancer cells are transported through the whole body and adhere at specific site and eventually transmigrate through the endothelium (extravasation) to form secondary tumors (Mierke, 2013).

1.8.2 The seed and soil hypothesis

Cancer cells from the primary site of origin tend to metastasize to specific organs and the mechanisms governing this aspect were studied and hypothesized. The seed and soil hypothesis proposed by Steven Paget (Stephen Paget, 1889) suggested that the outcome of metastasis was not due to a random chance. He proposed that certain tumor cells (seeds) have specific affinity for certain organs (soil). Therefore cancer cells would metastasize only when seed and soil are compatible. James Ewing (1929) proposed that the main factor responsible for metastases is the anatomy of blood and lymphatic vessels and the circulatory patterns between the primary tumors and specific secondary sites (Psaila and Lyden, 2009). Scientists have reported that cancer cells from the primary tumor target subset of organs specific for each cancer type. This mechanism is partially due to the anatomy of the circulatory system

and also influenced by the interaction between 'seed cells' and 'receptive soil' (Chambers *et al.*, 2002; Jeon *et al.*, 2013; Bersini *et al.*, 2014).

1.8.3 Comparison of cancer cell and leukocyte transmigration

Leukocytes and cancer cells follow similar mechanisms for extravasation. Insights into the process of tumor cell extravasation have been deduced from leukocytes extravasation during inflammation. Inflammation is a defense mechanism caused during tissue damage or injury characterized by heat, redness, swelling and pain. Leukocytes transported in the blood, adhere and extravasate to the site of injury for repair. Cancer cells follow similar mechanisms, but the molecules involved in each step of the processes can be different (Orr *et al.*, 2000; Miles *et al.*, 2008; Strell and Entschladen, 2008). The molecules involved in the three main steps of the process (rolling, adhesion and transendothelial migration) for leukocytes and cancer cells are shown in Table 1.7 and discussed in detail.

	Rolling	**Adhesion**	**Diapedesis or Transmigration**
Leucocytes	PSGL-1 – E-selectin	LFA-1 – ICAM-1/2	**Paracellular**
	HCELL – E-selectin	Mac-1 – ICAM-1/2	JAM-C – JAM-B
	CD24 – E-selectin	LFA-1 – JAM-A	LFA-1 – JAM-A
	L-selectin – MadCAM	Mac-1 – JAM-C	VLA-4 – JAM-B
	N-cadherin – N-cadherin	VLA-4 – VCAM-1	Mac-1 – JAM-C
	L-selectin – peripheral lymph node adressin	Glycosylated proteins – galectins	VE-cadherin – VE-cadherin
		L1-CAM – VLA-5	PECAM-1 – PECAM-1
			CD99 – CD99
			Transcellular
			LFA-1 – ICAM-1
			PECAM-1 – PECAM-1
Cancer Cells	PSGL-1 – E-selectin	α4β1/β7 – VCAM-1	N-cadherin – N-cadherin
	HCELL – E-selectin	CD44v6 – galectin-3	αvβ3 – PECAM-1
	CD24 – E-selectin	Lamp1/2 – galectin-3	
	CEA – E/L-selectin	MUC1 – galectin-3	
	MUC1 – E-selectin	αvβ3 – L1-CAM	
	CD43 – E-selectin	MUC1 – ICAM-1	
	Galectin-3 – E-selectin	CD43 – ICAM-1	
	N-cadherin – N-cadherin		
	ICAM-1/LFA-1 via leukocytes		

Table 1.7: Comparison of molecules involved in different steps of metastasis and leukocytes extravasation (modified from Strell and Entschladen, 2008).

1.8.3.1 Rolling

Rolling of leukocytes or cancer cells on the endothelium is the first step of extravasation. The possible ligand-receptor interactions mediating the rolling of leukocytes (blue) on endothelium (green) and cancer cells (orange) on endothelium (green) are shown in Figure 1.35 and Table 1.7 and described below.

Rolling of leukocytes on the endothelium is mediated by selectins (lectin cell adhesion molecules) that are expressed on the surface of both leukocytes and endothelial cells as shown in Figure 1.35. P-selectin and L-selectin help in rolling and initial attachment of leukocytes, whereas E-selectin enhances the recruitment of leukocytes. PSGL-1 expressed on leukocytes acts as the ligand for P-selectin and E-selectin (Elangbam et al., 1997; Strell and Entschladen, 2008). Often E-selectin ligands like CD43 and PSGL-1 are decorated with tetra-saccharide sialyl Lewis X (sLe^x) or sialyl Lewis A (sLe^a) (Barthel *et al.*, 2008). Cadherin is also known to assist the rolling of cells on the endothelium (Ivanov *et al.*, 2001). The involvement of N-cadherin in the rolling process of neutrophil granulocytes on pulmonary microvasculature has also been reported (Strell *et al.*, 2007).

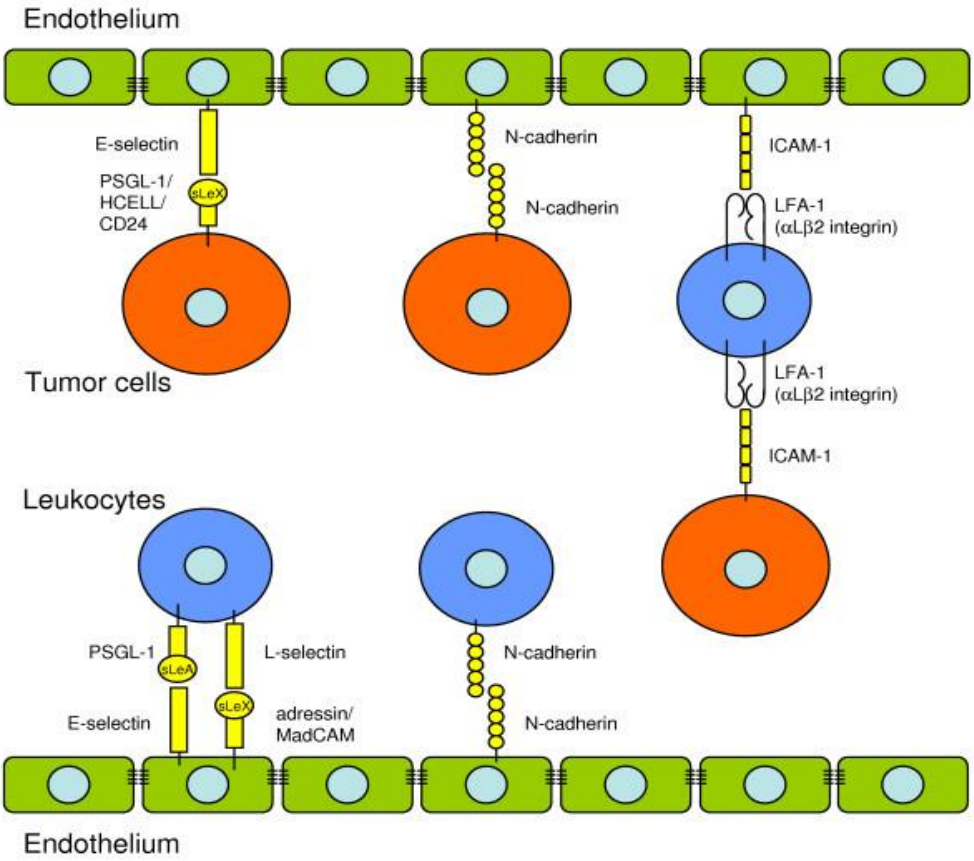

Figure1.35: Receptors involved in the rolling of leukocytes and tumor cells. The endothelium is shown in green, leukocytes in blue and tumor cells in red (Strell and Entschladen, 2008).

In contrast to leukocytes, the rolling behavior of cancer cells has been reported only in vitro but has not yet been described in vivo (Reymond *et al.*, 2013). Depending on cancer type, cancer cells express various E-selectin specific ligands like HCELL, PSGL1 and carcinoembryonic antigen (CEA) as shown in Table 1.7. Apart from these mentioned ligands few more E-selectin specific ligands like MUC1, CD43, and Galectin-3-binding protein have also been reported in the literature (Matsumoto *et al.*, 2005; Geng *et al.*, 2012; Reymond *et al.*, 2013). Also, N-cadherin expressed by endothelial cells and some cancer cells is involved in the rolling of cancer cells on the endothelium. A few articles have also reported that the leukocytes can act as a bridge or linker to facilitate the adhesion between cancer cells and the endothelium as shown in Figure 1.35. Cancer cells expressing ICAM-1 can bind to leukocytes via LFA-1, which then can adhere to the endothelial cells (Strell and Entschladen, 2008).

1.8.3.2 Adhesion

After rolling, leukocytes or cancer cells adhere strongly to the endothelium and this is reported as a key step in extravasation. The possible ligand-receptor interactions mediating the adhesion of leukocytes (blue) on endothelium (green) and cancer cells (orange) on endothelium (green) are shown in Figure 1.36 and Table 1.7 and described below.

Leukocytes adhere to the endothelial cells primarily via integrins that are activated during the rolling step. ICAM-1/2 and VCAM-1 expressed by endothelial cells mediate the strong adhesion of leukocytes. As shown in Figure 1.36, leukocytes express LFA-1 (αLβ2 intergin) and Mac-1 (αMβ2 integrin), which are well known ligands of ICAM-1/2 (Simon *et al.*, 1995, 2000). LFA-1 and Mac-1 also bind to JAM-A and JAM-C respectively (Ostermann *et al.*, 2002; Strell and Entschladen, 2008). The very late activation antigen-4 (VLA-4, α4β1 intergrin) acts as a ligand for VCAM-1 and helps in the leukocyte adhesion (Ibbotson *et al.*, 2001). It has to be noted that endothelial cells also express VLA-5 (α5β1integrin) that binds to L1-CAM (Ruppert *et al.*, 1995) as shown in Figure 1.36.

The expression of several integrins, especially the β2 subgroup, is restricted to leukocytes. Thus, cancer cells involve different receptors for mediating the strong adhesion to the endothelium. VLA-4 on melanoma cells was shown to interact with VCAM-1 to mediate adhesion (Klemke *et al.*, 2006). β1 and β4 integrins in combination with several α-integrins including αVβ3 contribute to the strong adhesion between prostrate cancer cell and endothelial cells in vitro (Barthel *et al.*, 2014). Galectin-3 expressed on the endothelium binds to Thomsen-Friedenreich antigen like MUC1 and CD44v6 (Figure 1.36) to promote adhesion

in breast and prostate carcinoma cell lines (Glinsky *et al.*, 2001; Khaldoyanidi *et al.*, 2003; Yu *et al.*, 2007). Futhermore, lysosomal membrane-associated glycoproteins (Lamp) 1 and 2 expressed by some tumor cells can bind to galectins-3 (Sarafian *et al.*, 1998). Tumor cells do not express LFA-1 and Mac-1 (β2-integrins), the well-known ligands for endothelial ICAM-1 on leukocytes. However it has been reported that some cancer cells express MUC1 (Regimbald *et al.*, 1996) and CD43 (Rosenstein *et al.*, 1991) that mediate the strong adhesion with endothelial ICAM-1.

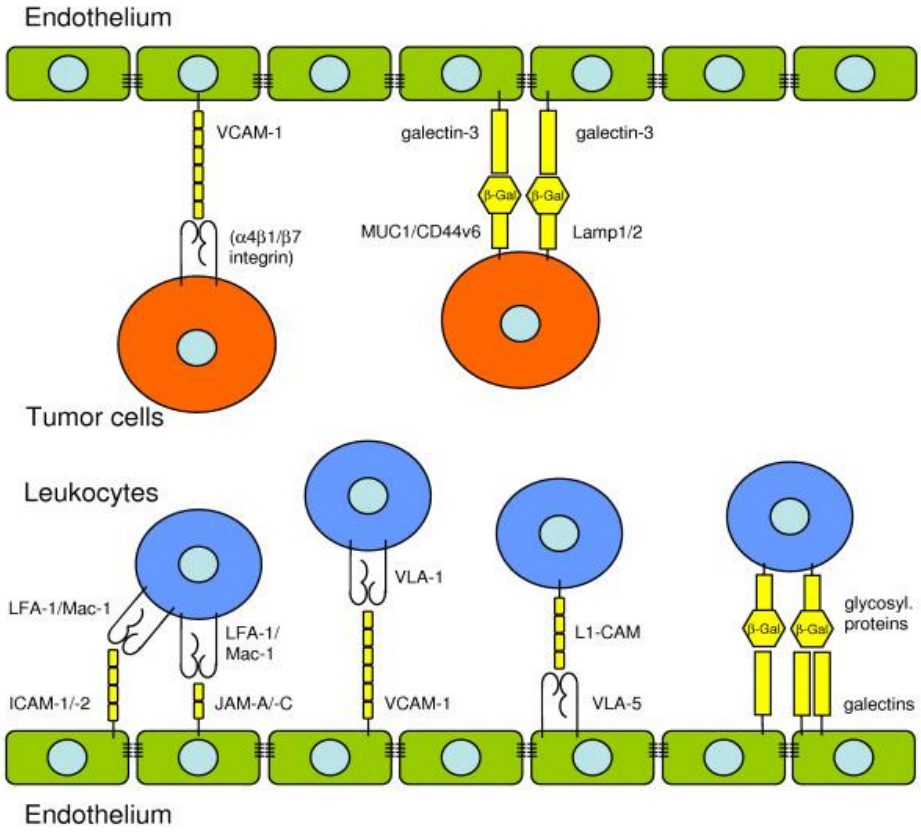

Figure 1.36: Receptors involved in the adhesion of leukocytes and tumor cells to endothelial cells. The endothelium is shown in green, leukocytes in blue and tumor cells in orange (Strell and Entschladen, 2008).

1.8.3.3 Extravasation

Finally, leukocytes or cancer cells transmigrate through the endothelium. The possible ligand-receptor interactions mediating the transmigration of leukocytes (blue) through the endothelium (green) are shown in Figure 1.37 and Table 1.7 and described below.

Leukocytes transmigrate through the endothelium using two different routes: paracellular and transcellular. Paracellular TEM is defined as migration of cancer cells through endothelial junctions by disruptions of junctions between adjacent endothelial cells

(Vestweber, 2012). Transcellular TEM is defined as the migration of leukocytes directly through the endothelial cell body (Carman and Springer, 2008). The different receptors involved in paracellular TEM and transcellular TEM of leukocytes are shown in Figure 1.37 and in Table 1.7 (Strell and Entschladen, 2008).

Cancer cells have often been reported to use a paracellular route *in vitro* without damaging the integrity of the endothelium (Mierke *et al.*, 2008; Reymond *et al.*, 2013). It has been reported that colorectal cancer cells can use the transcellular route *in vitro* (Tremblay *et al.*, 2008). It has been reported that most of the receptors mediating strong adhesion can also promote extravasation in tumor cells (Miles *et al.*, 2008; Reymond *et al.*, 2013). In contrast to leukocytes, the specific receptors involved in paracellular TEM and transcellular TEM of cancer cells have not been elucidated so far.

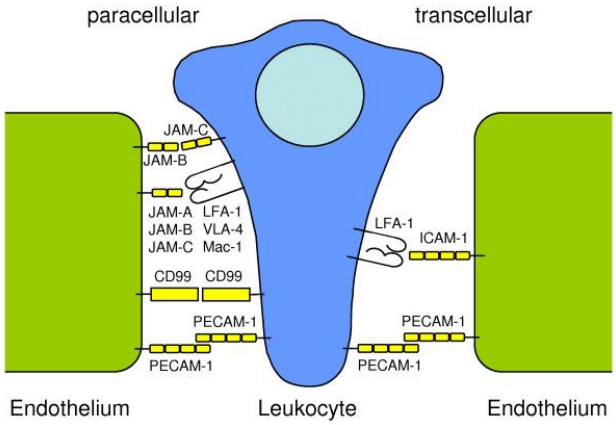

Figure 1.37: Transmigration of leukocytes through the endothelium. Receptors involved in the paracellular route are shown on the left side and receptors involved in the transcellular route are shown on right side. The endothelium is shown in green, leukocytes in blue (Strell and Entschladen, 2008).

1.9 Bladder cancer

The bladder is a hollow organ in the pelvis with flexible, muscular walls and its main function is to store and release the urine made in the body. Urine produced in the kidneys is carried to the bladder through tubes called ureters. During urination, muscles in the bladder contract and urine is forced out of the bladder through a tube called the urethra (Figure 1.38). The wall of the bladder is composed of several layers of cells as shown in Figure 1.38, zoomed region. Bladder cancer originates at the innermost lining of the bladder, which is called the transitional epithelium and grows through other layers in the bladder wall. Finally the cancer cells metastasize to distant lymph nodes, bones, the lungs, or the liver.

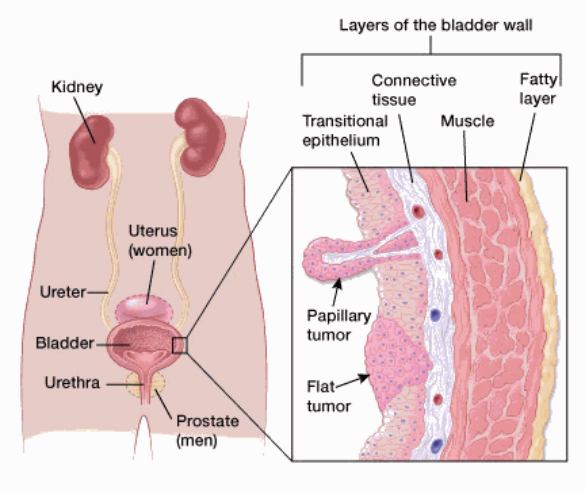

Figure 1.38: Scheme of bladder connected to other parts of the body. Different layers of tissues on the walls of the bladder are shown in the zoomed region. (Source: Cancer.org).

Common types of bladder cancer are urothelial carcinoma (UC) or as transitional cell carcinoma (TCC), squamous cell carcinoma, adenocarcinoma and other subtypes (Mitra and Cote, 2009). Bladder cancer is the most common cancer of urinary tract with ~38,000 new cases and ~150,000 deaths per year worldwide. It ranks fifth among the cancers in men with an incidence being four times higher compared to women (Ploeg *et al.*, 2009; Cheung *et al.*, 2013; Knowles and Hurst, 2015). The alterations in molecular pathways responsible for the bladder cancer tumorigenesis and progression are displayed in Figure 1.39. These include five cellular processes: cell death, cell growth, cell-cycle regulation, gene regulation and signal transduction that can respond to external carcinogenic cues or due to genetic alterations. Angiogenesis and tumor cell invasion are two processes that aids in tumor maintenance and progression (Mitra and Cote, 2009).

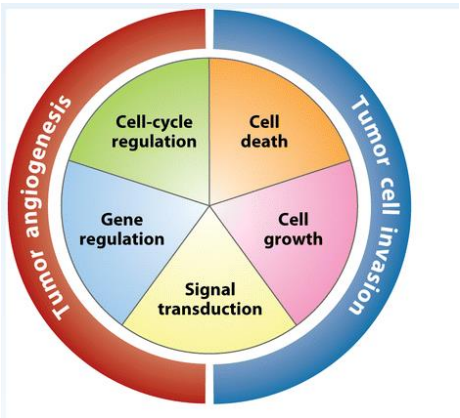

Figure 1.39: Aberrant cellular process contributing to bladder tumorigenesis. Malignant transformation of the bladder involves alteration in five cellular process (central pie) that can respond to carcinogenic cues or genetic alterations. Tumor maintenance, progression and metastasis depend on angiogenesis and invasion (Mitra and Cote, 2009).

The tumors are classified using the Tumor-Node-Metastasis system (TNM system - UICC 2009), where T describes how far the primary tumor has grown into the walls of bladder (T0-T4), N describes the spread to lymph nodes near the bladder (N0-N3) and M describes the spread of tumor to other body parts (M0, M1). The majority of the bladder cancers are non-invasive papillary tumors of lower grade (Ta). Stage T1 tumors have penetrated the epithelial basement membrane while higher stages (T2-T4) have invaded the muscle as shown in Figure 1.40.

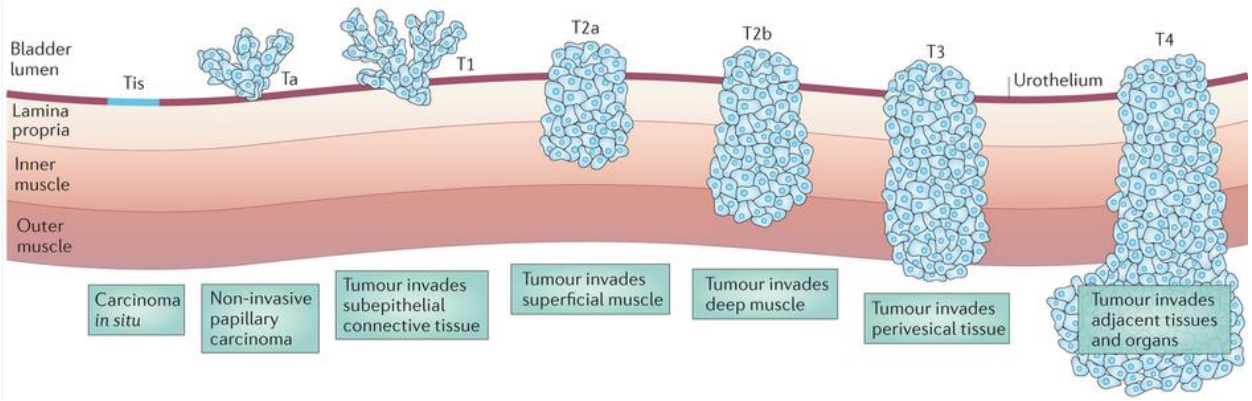

Figure 1.40: Staging of bladder cancer: The invasion of cells on the walls of the bladder is related to its stage (Ta, T1,T2a, T2b, T3 and T4), (Knowles and Hurst, 2015).

Once the T, N, and M categories have been determined, this information is combined to find the overall cancer stage (G0-G4). Tumors are also categorized into different stages based on their morphological and pathological features such as growth rate and extent of differentiation as reported in Table 1.8.

Grading	Pathological Characteristics
G0	Cannot be assessed.
G1	Well differentiated, low grade
G2	Moderately differentiated, intermediate grade.
G3	Poorly differentiated , high grade
G4	Undifferentiated, high grade

Table 1.8: Grading of tumor cells (Source: Cancer.ca).

1.10 Objectives of my thesis

The primary aims of my PhD thesis are,

1. To identify the key adhesion molecules involved and to study the role of the molecules in bladder cancer cell-endothelial cell adhesion.
2. To quantify the forces involved by the adhesion molecules in bladder cancer cell-endothelial cell adhesion using SCFS mode of AFM.
3. To investigate the forces involved by cancer cells during the transmigration using Traction Force Microscopy (TFM).

Chapter 2 - Characterization of the molecules involved in bladder cancer cell-endothelial cell adhesion

The adhesion of cancer cells to endothelial cells (ECs) is an important step in cancer metastasis, therefore identifying the key molecules involved during this process promises to help blocking the metastatic cascade (Bersini *et al.*, 2014). The adhesion is mediated by several cell adhesion molecules (CAMs) like β1 integrins (Heyder *et al.*, 2005), Vascular Cell Adhesion Molecule-1 (VCAM-1) (Klemke et al., 2006), L-selectin (Yamada *et al.*, 2006) and Intercellular Adhesion Molecule-1 (ICAM-1) (Roche *et al.*, 2003; Chotard-Ghodsnia *et al.*, 2007; Haddad *et al.*, 2010; Laurent *et al.*, 2014). In a recent publication (Laurent *et al.*, 2014) we showed that ICAM-1 expressed by ECs is involved in the adhesion of bladder cancer cells (BCs). MUC1 (Regimbald *et al.*, 1996) and CD43 (Rosenstein *et al.*, 1991) expressed by some cancer cells have been identified as the ligands for ICAM-1. However, the ligands for ICAM-1 on BCs are not identified clearly as for leukocytes but MUC1 and CD43 may be two potential candidates that could be involved in bladder cancer cell-endothelial cell adhesion. In this chapter, we used flow cytometry to check the surface expression of MUC1 and CD43 on different BCs. Adhesion assays provided us the quantitative information regarding the involvement of these molecules (ICAM-1, MUC1, and CD43) in bladder cancer cell-endothelial cell adhesion.

2.1 Materials and Methods

2.1.1 Cell lines and cell culture

Four human BCs RT4, T24 and J82 (ATCC, Rockville, MD) and RT112 (German tumor bank, Heidelberg, Germany) were cultured in RPMI 1640 medium (Gibco, Saint Aubin, France) supplemented with 10% fetal bovine serum (FBS) and 1% penicillin/streptomycin mix (complete RPMI medium). TCCSUP BCs were cultured in DMEM high glucose medium (Gibco, Saint Aubin, France) supplemented with 10% fetal bovine serum and 1% penicillin/streptomycin mix. These cell lines represent progression from well to poorly differentiated phenotypes and arise from superficial to invasive epithelial human bladder cancer as shown in Table 2.1 (Masters *et al.*, 1986; Champelovier *et al.*, 2003). Chronic myelogenous leukemia cells K562) were cultured in RPMI 1640 supplemented with 10% FBS, 1% penicillin/streptomycin mix, 1% non-essential amino acids and 1% sodium pyruvate. Human Vascular Umbilical Endothelial Cells (HUVECs) were purchased from Promocell (Heidelberg, Germany). HUVECs were grown on culture dishes coated with 100 µg/ml collagen I (BD Bioscience, Le Pont de Claix, France) in complete endothelial growth medium (Promocell) supplemented with 1% antibiotic/antimycotic mix. HUVECs subcultures from passage 2-6 were selected for our experiments. Cultures were grown at 37°C in a 5% CO_2 humidified atmosphere.

Cell line	Orgin of tumor	Stage and Grade of tumor	Cell line origin
RT4	Bladder	pTa G1	ATCC-HTB-2
RT112	Bladder	pTa G2	German tumorbank
T24	Bladder	pT2-3 G3	ATCC-HTB-4
J82	Bladder	pT3G3	ATCC- HTB-1
TCCSUP	Bladder	pT4 G4	ATCC-HTB-5

Table 2.1: Stage and grade of bladder cancer cells: RT4, RT112, T24, J82 and TCCSUP.

2.1.2 Flow cytometry

BCs grown on tissue culture flask were detached using a cell dissociation solution (Sigma-Aldrich, Lyon, France). The cell suspension was incubated with primary antibodies (10 µg/ml) against MUC1 or CD43 or appropriate isotype control in ice for 45 min. Mouse immunoglobulin (IgG) (Vector Laboratories, CA, USA) used as the isotype control. After washing, the cells were then incubated with Alexa-488 (goat anti-mouse IgG) secondary

antibody (Life Technologies, Saint Aubin, France) in ice for 30 min. Expression levels of MUC1 and CD43 were analyzed using an Accuri C6 flow cytometer (BD Bio-sciences, USA). Specifically, mouse anti-human MUC1 monoclonal antibody (mAb) clone E29 (DAKO, Glostrup, Denmark), mouse anti-human MUC1 C595 mAb (Santa Cruz, Heidelberg, Germany), mouse anti-human CD43 mAb clone L10 (Invitrogen, Saint Aubin, France) and anti-ICAM-1 2D5 mAb (Languino *et al.*, 1995) were used in this study. The anti–ICAM-1 mAb recognizes the domain I of ICAM-1 and ICAM-1 expression can be stimulated by cytokines like TNF-α (Sans *et al.*, 2001; Roland *et al.*, 2007; Lawson and Wolf, 2009). Both anti-MUC1 mAb (Hayashi *et al.*, 2001) and anti-CD43 mAb (Fernandez-Rodriguez *et al.*, 2002) recognize an extracellular domain of the protein and were reported to inhibit the adhesion (Hayashi *et al.*, 2001; Ziprin *et al.*, 2004).

The level of expression of MUC1 and CD43 were quantified by taking the ratio of median fluorescence of sample (M_{sample}) over the control ($M_{control}$). We used this ratio to separate the level of expression into four categories: no expression, weak expression, moderate expression and strong expression as shown in Table 2.2.

Expression	$M_{sample}/M_{control}$	Symbol
No expression	<1.2	-
Weak expression	1.2 to 4	+
Moderate expression	4.1 to 10	++
Strong expression	>10	+++

Table 2.2: Quantifying the levels of expression. Ratio of Median fluorescence of sample (M_{sample}) over the median fluorescence of control ($M_{control}$) is used to group the levels of expression of receptors on the cell surface.

2.1.3 Bladder cancer cell-endothelial cell adhesion assay

ECs ($2x10^4$) were seeded in 48 well plates (Nunc, Saint Aubin, France) coated with 100 µg/ml collagen I and grown to confluence for 3 days. BCs were detached with a cell dissociation solution and labeled with calcein (Life Technologies, Saint Aubin, France) for 30 min at 37°C. Calcein is a cell-permeable, non-fluorescent dye that is converted to green fluorescence after hydrolysis by cytoplasmic esterases. $2x10^5$ labeled BCs were added per well and incubated for 30 min at 37°C. Non-adherent BCs were removed by gentle washing with complete RPMI medium. The remaining adherent cells were then lysed with detergent (10% SDS) and the signal was quantified using Victor3 multilabel counter (Perkin Elmer, Waltham, MD). For blocking experiments, ICAM-1 on ECs and MUC1 or CD43 on BCs

were blocked with specific antibodies (20 µg/ml) and control with mouse IgG for 15 min at 37°C prior to the addition of cancer cells. The adhesion percentage was calculated as:

$$\% \text{ Adhesion} = \frac{100^* \text{ fluorescence of adhered cells}}{\text{Total fluorescence}}$$

Total fluorescence corresponds to the fluorescence of added cells ($2x10^5$) and fluorescence of adhered cells corresponds to the fluorescence value obtained after washing while blocking the different receptors involved in the interaction.

2.1.4 Isolation of Total RNA and Reverse Transcriptase-Polymerase Chain Reaction

Cellular RNA from the cultured cells (T24 and J82) was extracted by RNeasy Kit according to the manufacturer instructions (Qiagen, Courtaboeuf, France). The concentration of RNA was measured from the absorbance (A260/A280) using Nano drop (Nanodrop 2000, Thermo Scientific, Courtaboeuf, France) and stored at -80°C. 12.5 µg of total RNA from T24 and J82 BCs were reverse transcribed using the first-strand cDNA synthesis (SuperScript II Reverse Transcriptase, Invitrogen, Saint Aubin, France) according to the protocol from the manufacturer. The real time PCR (Bio-Rad CFX96 Touch, France) was performed for MUC1 using the following primer pairs: MUC1 (forward primer 5'-ACAATTGACTCTGGCCTTCC-3' and reverse primer 5'-GAAATGGCACATCACTCACG-3') (Eurogentec, Angers, France) and using iTaq Universal SYBR Green supermix (BioRad, France). PCR conditions were 95°C for 10 s followed by 60°C for 20 s, for a total of 40 cycles. The complete protocol for RNA extraction and Reverse Transcriptase-PCR was described in Appendix A. The expression of mRNA was quantified by relative quantification normalized against unit mass. When comparing the expression of two samples using relative quantification, one sample was usually chosen as calibrator (control) and the expression of other sample was expressed as an increase or decrease relative to the control. The C_T (Threshold cycle – cycle that gives detectable signal from the amplified product) values for the sample and the control were then used to calculate the relative expression using the following equation:

$$\textbf{Ratio}_{\textbf{(sample/control)}} = 2^{\Delta CT}$$

where, $\Delta CT = C_T(\text{sample}) - C_T(\text{control})$.

2.1.5 Knock down of MUC1 using short hairpin RNA

To knockdown the expression of MUC1 in T24 and J82 BCs, a short hairpin RNA (shRNA) sequence targeting MUC1 was designed from the mRNA sequence of MUC1 using Designer of small interfering RNA software (DSIR, CEA, Grenoble). The clone containing the specific target sequence (5 -CCGGGCTCAAAGATGTACACCACTTCTCGAGAAGTG GTGTACATCTTTGAGCTTTTTTG -3') was selected and purchased from Sigma-Aldrich (Mission Lentiviral Transduction Particles). The target sequence was cloned in pLKO.1 vector with puromycin selection and transfected into lentiviruses. Also, non-targeted shRNA control lentiviral transduction particles (sequence that will not target any mammalian genes) cloned in pLKO.1 vector with puromycin selection (SHC002V) was purchased from Sigma-Aldrich (Lyon, France). Puromycin selection allows us to obtain the transfected cells by growing them in the complete RPMI medium containing puromycin. Around 10^5 BCs (T24 and J82) were cultured in 6 well plates (Nunc, Saint Aubin, France) and incubated overnight at 37°C. T24 and J82 cells were transfected with lentiviral particles containing shRNA sequence specific for MUC1 (sh-MUC1) and non-targeted sh-control in the ratio 1:3 (BCs:lentiviral particles) in the presence of polybrene (8 µg/ml). After 48 h of transfection, complete RPMI medium with puromycin (5 µg/ml) was added to select the transfected cells. The cells were feeded with fresh medium containing puromycin for 2 to 3 days to obtain only the transfected cells.

RNA was isolated from the transfected cells and reverse transcriptase - q-PCR was performed with the protocol mentioned above. The C_T value for sh-control cells and sh-MUC1 transfected cells were obtained by performing q-PCR with cDNA template using the primers specific for MUC1. Glyceraldehyde 3-phoshate dehydrogenase (GADPH) or β-actin was used as the reference gene and their C_T Values were obtained by performing q-PCR with cDNA template using primers specific for GADPH or β-actin. The level of knock down in MUC1 expression was quantified by comparing the expression in sh-control and sh-MUC1 using the Livak method. This method gives the relative expression of MUC1 in sh-MUC1 transfected cells as compared to sh-control by normalizing the expression to a reference gene (GADPH or β-actin). Since the expression of a reference gene was not supposed to change between sh-control and sh-MUC1 cells, it was used in the quantification. The level of knock down was quantified by using the C_T values of sh-control and sh-MUC1 for target and reference genes as shown below:

Sample	C_T (Target)	C_T (Reference)
sh-control (control)	X1	Y1
sh-MUC1 (sample)	X2	Y2

First, the C_T of target gene was normalized to the C_T of reference gene for both control and sample,

ΔC_T (control)= X1-Y1

ΔC_T (sample)= X2-Y2

Second, the ΔC_T of the sample was normalized to the ΔC_T of the control

$\Delta\Delta CT = \Delta C_T$ (sample) - ΔC_T (control)

Finally, the relative expression was quantified using the formula: $2^{-\Delta\Delta CT}$

The relative expression of sample was reported by normalizing the expression of control to 1.

2.1.6 Statistical Analysis

All the data for adhesion assays were generated from at least three independent experiments performed in triplicates. The data are reported as mean with standard error of the mean (SEM) as error bars. The significance of the data was calculated with one-way ANOVA and unpaired t-test using GraphPad Prism (GraphPad Software Inc, San Diego, CA, USA).

2.2 Results

2.2.1 Expression of MUC1 by bladder cancer cells

BCs (RT4, RT112, T24, J82 and TCCSUP) were analyzed for the expression of MUC1 by flow cytometry using MUC1 mAb E29. The scatter plot obtained for RT4 BCs when blocking MUC1 is shown in Figure 2.1A. This plot shows that approximately 50% of the cells were gated to analyze the fluorescence signals. Control IgG was used to detect the background level (Figure 2.1: black curves) in the measurements. As shown in Figure 2.1, MUC1 (red curves) were expressed by all the cell lines at different levels. A weak expression of MUC1 was observed on RT4 (Figure 2.1B), RT112 (Figure 2.1C) and T24 (Figure 2.1D), while J82 showed a stronger expression (Figure 2.1E) and TCCSUP showed a moderate expression of MUC1 (Figure 2.1F) as shown in Table 2.3.

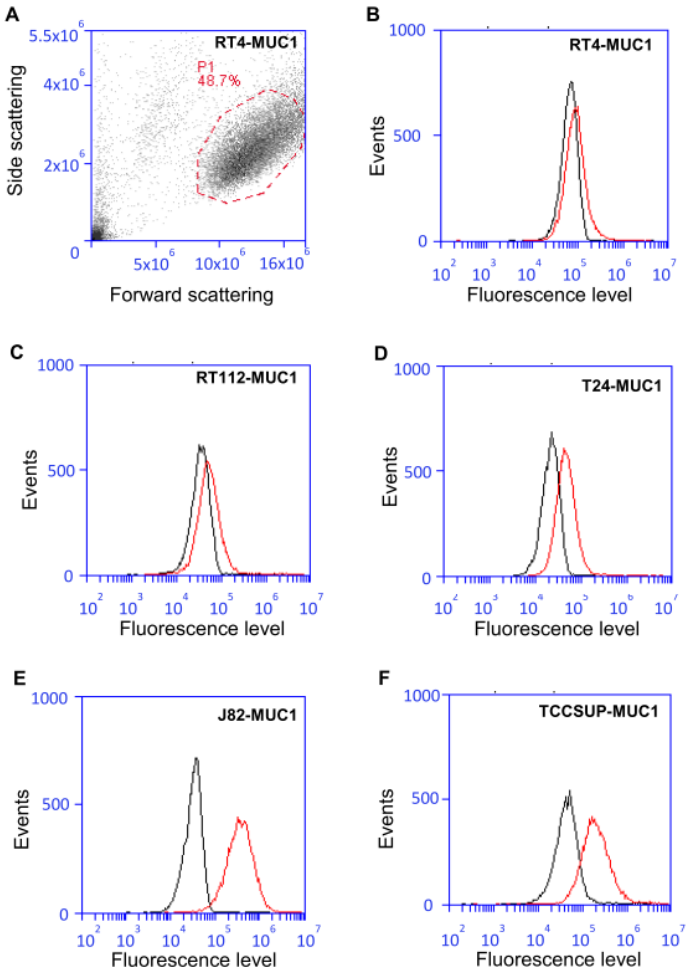

Figure 2.1: Flow cytometry analyses of MUC1 expression in BCs. (A) Scatter plot of RT4 showing the gate. Expression levels of MUC1 (red curve) by flow cytometry analysis in comparison with an irrelevant antibody (black curve): (B) RT4, (C) RT112, (D) T24, (E) J82 and (F) TCCSUP.

2.2.2 Expression of CD43 by bladder cancer cells

BCs (RT4, RT112, T24, J82 and TCCSUP) were analyzed for the expression of CD43 by flow cytometry using CD43 mAb L10. Control IgG was used to detect the background level (Figure 2.2: black curves) in the measurements. As shown in Figure 2.2, CD43 (red curves) were expressed by these cell lines at different levels. A weak expression of CD43 was observed on RT4 (Figure 2.2A), RT112 (Figure 2.2B), T24 (Figure 2.2C) and TCCSUP (Figure 2.2E), while J82 showed a moderate expression of CD43 (Figure 2.2D) as shown in Table 2.3.

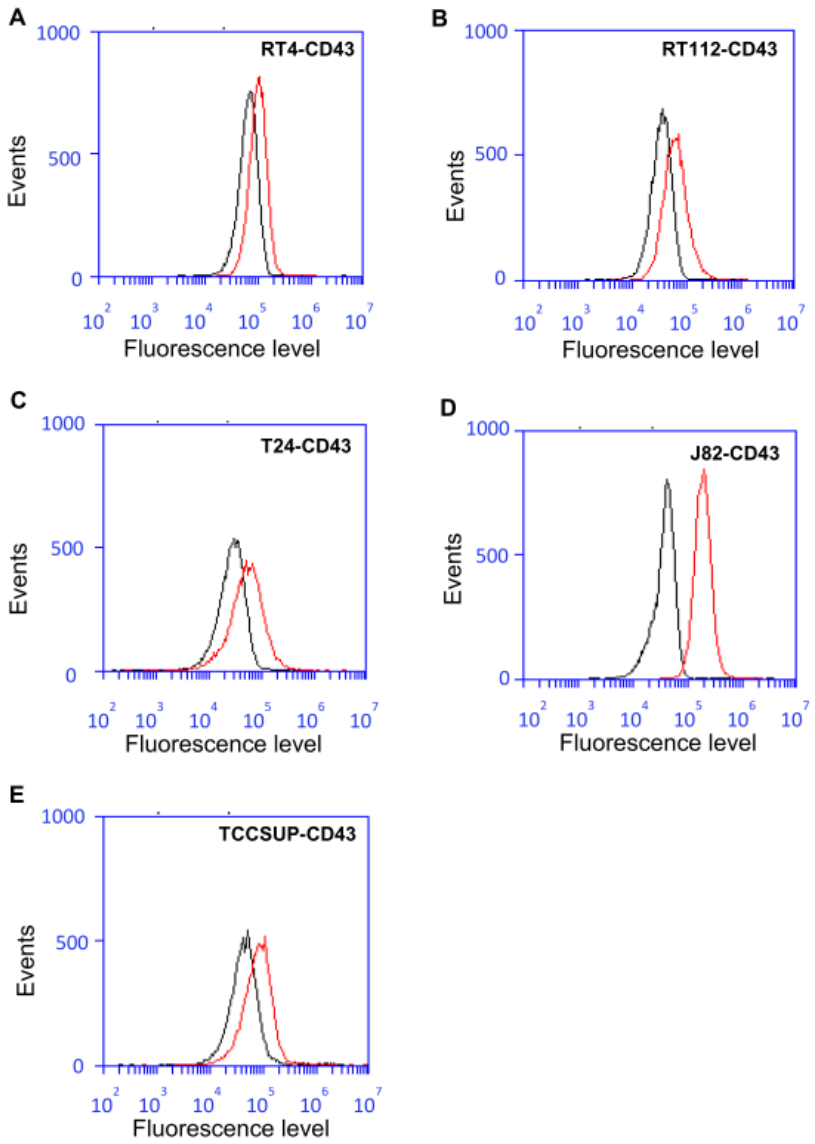

Figure 2.2: Flow cytometry analyses of CD43 expression in BCs. Expression levels of CD43 (red curve) by flow cytometry analysis in comparison with an irrelevant antibody (black curve): (A) RT4, (B) RT112, (C) T24, (D) J82 and (E) TCCSUP.

Invasivity

Cells	MUC1 expression	CD43 expression
RT4	+	+
RT112	+	+
T24	+	+
J82	+++	++
TCCSUP	++	+

Table 2.3: Expression level of MUC1 and CD43 analyzed by flow cytometry. Five BCs were screened for the expression of MUC1 and CD43 using specific antibodies and the expression levels were indicated here: + (weak expression), ++ (moderate expression), +++ (Good expression). [Refer to Table 2.2 for classification of expression]. The arrow indicates the trend of invasivity.

2.2.3 Expression of MUC1 at mRNA level

The expression of MUC1 at the cellular level was analyzed for T24 and J82 using reverse transcriptase and q-PCR from RNA and analyzed by relative quantification method. In our case, MUC1 expression from T24 was used as the control and the expression was considered as 1 and the relative expression of MUC1 by J82 was quantified. J82 BCs express ~30 times more MUC1 as compared to T24 at the mRNA level (Figure 2.3).

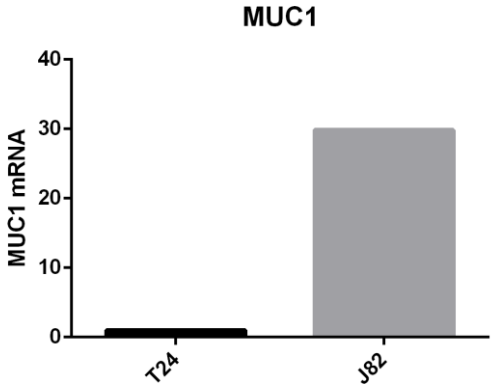

Figure 2.3: Expression of MUC1 at mRNA level. The analysis showed that J82 express ~30 fold more MUC1 compared to T24.

2.2.3 Expression of ICAM-1 by endothelial cells

HUVECs were analyzed for the expression of ICAM-1 on normal cells (N) and cells stimulated overnight (St) with TNF-α (10^2 TU/ml). HUVECs showed moderate expression of ICAM-1 on normal cells and the expression was increased ~15 fold after the stimulation as

shown in Figure 2.4. HUVECs without stimulation were used for adhesion assay, as they already express good level of ICAM-1.

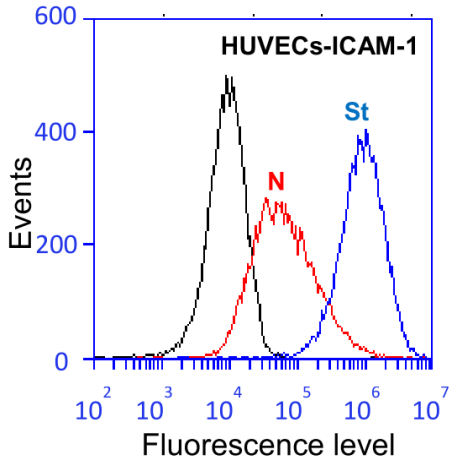

Figure 2.4: Flow cytometry analyses of ICAM-1 on ECs. Expression levels of ICAM-1 on normal ECs (red curve) and TNF-α stimulated ECs (blue curves) by flow cytometry analysis in comparison with an irrelevant antibody (black curve).

2.2.4 MUC1 and CD43 mediate bladder cancer cell-endothelial cell adhesion

We have shown that BCs express MUC1 and CD43, which are ligands for ICAM-1. To verify if this expression mediates the adhesion of BCs to ECs via interaction with ICAM-1, adhesion assays were performed. Three BCs (RT112, T24 and J82) with different stages and grades were selected to study the role of adhesion molecules with respect to their invasiveness (RT112<T24<J82). Specific monoclonal antibodies were used to inhibit ICAM-1 expressed on ECs and MUC1 or CD43 expressed on BCs (RT112, T24 and J82) prior to the adhesion assay. The percentage of adhesion after blocking ICAM-1 on ECs and MUC1 or CD43 or MUC1+CD43 on BCs was calculated and compared to the adhesion obtained using a control antibody (mouse IgG). The percentage of cells adhered in the control versus the total number of cells added were 75%, 55%, 66% respectively for RT112, T24 and J82 (Figure 2.5). The percentage of adhered cells in the control for three different invasive BCs was compared to understand if there was any correlation between the percentage of adhesion and the invasiveness. T24 BCs showed a significant decrease in adhesion as compared to the less invasive BCs RT112, while J82 BCs showed non-significant decrease in adhesion as compared to RT112. These results suggest that there was no correlation between the percentage of adhesion and the invasiveness of BCs under our experimental conditions.

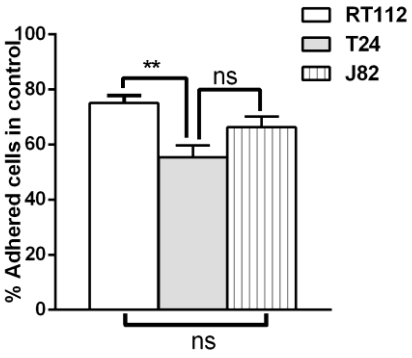

Figure 2.5: Percentage of cells adhered in the control. The percentage of adhered cells were calculated from the total number of cells remained in the control taking into account the total number of cells added initially for RT112, T24 and J82.

We normalized the control to 100% and calculated the inhibition when blocking receptors on different cell lines. Blocking ICAM-1 on ECs showed a ~36% decrease in adhesion for T24 and J82 (Figure 2.6B,C) and a ~18% decrease in adhesion for RT112 (Figure 2.6A). Likewise, blocking MUC1 or CD43 on T24 and J82 showed a ~50% decrease in adhesion (Figure 2.6B,C) and RT112 showed only a ~25% decrease in adhesion (Figure 2.6A). Blocking both (MUC1+CD43) induced an additional decrease in adhesion compared to blocking them separately in all three BCs (Figure 2.6A-C).

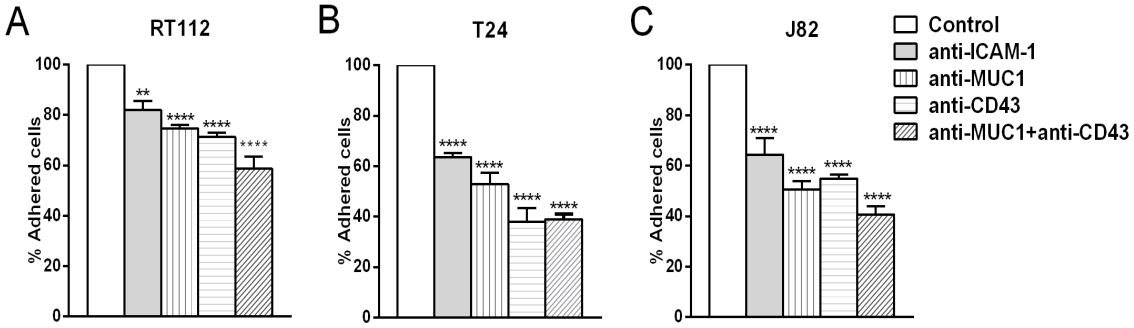

Figure 2.6: Quantification of bladder cancer cell-endothelial cell adhesion. In adhesion assay, the percentage (Mean±SEM) of three BCs (A) RT112, (B) T24 and (C) J82 adhering to ECs was quantified while blocking ICAM-1 on ECs and blocking MUC1, CD43 or MUC1+CD43 on cancer cells. One-way ANOVA was performed to check the significance with respect to the control, ****$p \leq 0.0001$, ** $p \leq 0.01$.

The decrease in adhesion when blocking ICAM-1, MUC1 or CD43 was 50% less in RT112 as compared to T24 and J82 (Table 2.4). These results suggest that bladder cancer cell-endothelial cell adhesion is mainly mediated by the interaction of MUC1 and CD43 with endothelial ICAM-1 for invasive cells (T24 and J82). In contrast, RT112 adhesion on ECs is less dependent on ICAM-1.

Cells	anti-ICAM-1 Mean±SEM	anti-MUC1 Mean±SEM	anti-CD43 Mean±SEM	anti-MUC1+anti-CD43 Mean±SEM
RT112	**18.0±3.7**	**25.4±1.4**	**28.7±1.8**	**41.2±4.6**
T24	**36.4±1.7**	**47.3±4.8**	**62.1±5.5**	**61.0±2.0**
J82	**35.6±6.6**	**49.3±3.2**	**45.0±1.5**	**59.4±3.4**

Table 2.4: Quantification of cancer cell-endothelial cell adhesion. The percentage of inhibition of adhesion (Mean±SEM) while blocking different receptors on endothelial cells (ICAM-1) and cancer cells (MUC1, CD43 or both) for three different bladder cancer cells (RT112, T24 and J82) is shown. The arrow indicates the trend of invasivity.

2.2.5 Silencing of MUC1 expression in T24 and J82

In order to validate the involvement of in bladder cancer cell-endothelial cell adhesion we generated stable bladder cancer cells (T24 and J82) knockdown for MUC1 using a shRNA approach. Our goal was to perform adhesion assays using MUC1 silenced T24 and J82 BCs and to compare with the results obtained using antibodies.

First, the decrease in the expression of MUC1 in sh-MUC1 transfected T24 and J82 cells compared to sh-control was quantified using q-PCR. As shown in Figure 2.7, T24 showed a ~10 fold decrease in MUC1 expression as compared to control. Meanwhile, J82 showed a ~25 fold decrease in MUC1 expression at the mRNA level.

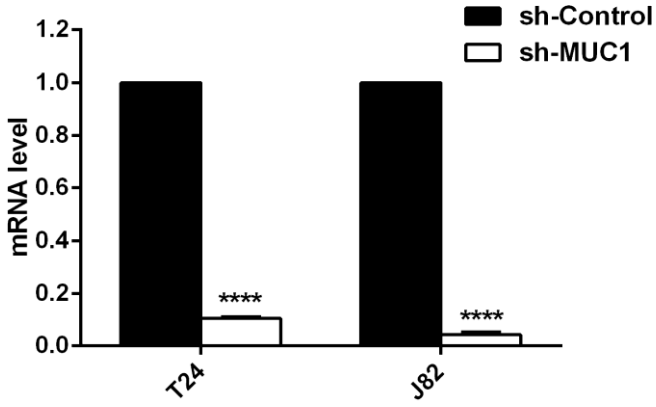

Figure 2.7: Knockdown of MUC1. MUC1 mRNA expression was analyzed in T24 and J82 BCs in control and MUC1-shRNA by q-PCR. The expression of MUC1 was normalized to that of GADPH and β-actin (reference gene). The amount is represented as relative to that of sh-control (set as one fold). The results indicate the Mean±SEM from two different experiments and student t-test was performed to check the significance with respect to control, ****$p \leq 0.0001$.

Then, the decrease in surface expression of MUC1 was analyzed by performing flow cytometry on sh-control and sh-MUC1 transfected cells (T24 and J82). MUC1 mAb E29 was used to identify the expression of MUC1. Control IgG was used as a control in the measurements (black curve). The surface expression of MUC1 was decreased in T24-sh-

MUC1 (Figure 2.8B) and J82-sh-MUC1 (Figure 2.8D) as compared to their respective control. These results indicate that the expression of MUC1 was decreased both on surface and at the mRNA level.

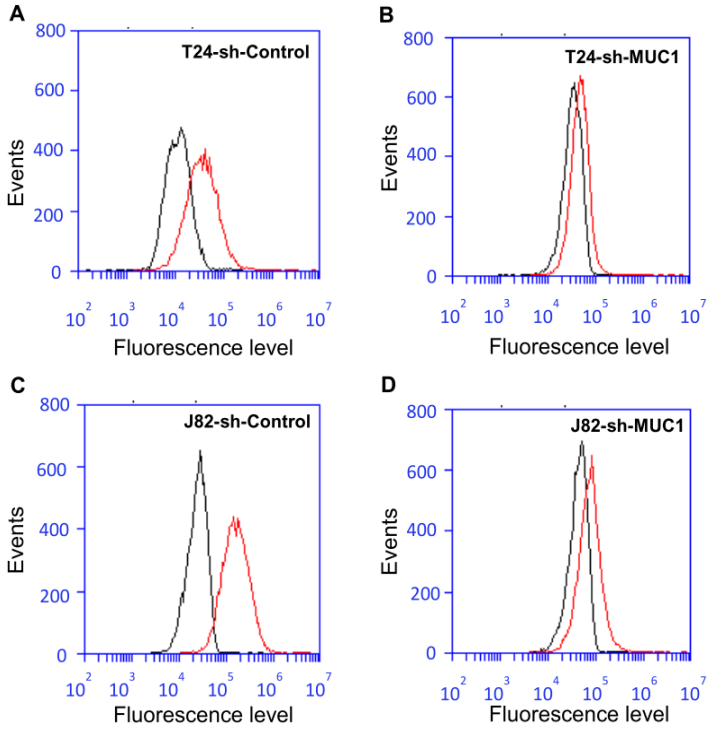

Figure 2.8: Flow cytometry analyses of MUC1 in transfected cells. Expression levels of MUC1 in control (sh-Control) and cells knockdown for MUC1 (sh-MUC1) using E29 mAb (red curve) in comparison with an irrelevant antibody (black curve): (A,B) T24, (C,D) J82 cells.

The above analysis was performed with the entire population of transfected cells obtained after selection. In order to have a less heterogeneous population, these transfected cells were cloned by limited dilution. J82 BCs (sh-control and sh-MUC1) were expanded in complete medium with 2.5 µg/ml of Puromycin. Two colonies selected from the transfected cells (sh-control and sh-MUC1) were analyzed for the surface expression of MUC1 using flow cytometry. As shown in Figure 2.9, control cells from both colonies express stronger level of MUC1 (Figure 2.9A,B), whereas the sh-MUC1 cells from both colonies showed almost no expression for MUC1 (Figure 2.9C,D). The stable J82 cells with almost no expression of MUC1was generated. These transfected cells (sh-MUC1) can be used to perform adhesion assays and the results can be compared with adhesion assays using antibiotics. Adhesion assays using transfected cells were not performed due to time limitation.

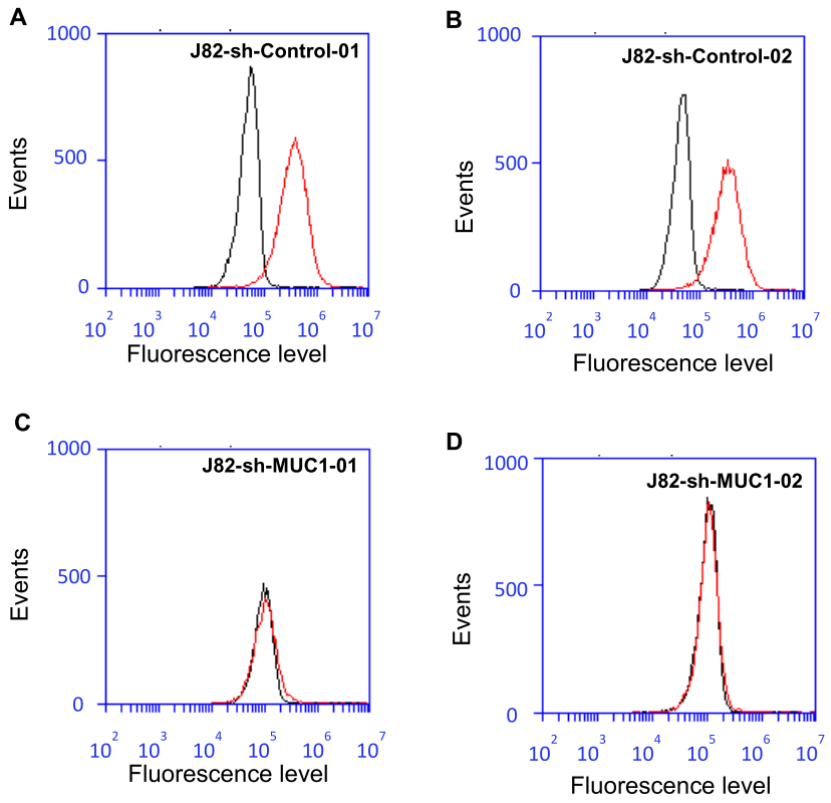

Figure 2.9: Flow cytometry analyses of MUC1 in J82 cloned from single cells. Expression levels of MUC1 in control (sh-Control) and cells knockdown for MUC1 (sh-MUC1) cloned from single cells using E29 mAb (red curve) in comparison with an irrelevant antibody (black curve): (A) J82-sh-Control-01, (B) J82-sh-Control-02, (C) J82-sh-MUC1 and (D) J82-sh-MUC1.

2.3 Discussion

Five BCs of different invasiveness were used in this study, expressing MUC1 and CD43 at various levels. RT4, RT112 and T24 showed a weak expression of MUC1, whereas J82 and TCCSUP showed good and moderate expression of MUC1 respectively (Figure 2.1 and Table 2.3). It has been reported that in bladder carcinomas the expression of MUC1 was stronger in high grade tumors (grade 2/3) than in low grade tumors (grade 1/2) and stronger in muscle invasive tumors (T2-T4) than in superficial (Ta-T1) one (Cardillo *et al.*, 2000). Few other publications also suggested that the expression of MUC1 increases with metastatic potential of cancer cells (Nakamori *et al.*, 1994; Simms *et al.*, 1999; Cardillo *et al.*, 2000; Kaur *et al.*, 2014; Rivalland *et al.*, 2015). In our study we also observed the increase in MUC1 expression in relation to their invasiveness (RT4<RT112<T24<J82) as shown in Figure 2.1. But the highly invasive cell line TCCSUP showed less MUC1 expression than J82 cells.

It has to be noted that in our previous publication (Laurent *et al.*, 2014), no expression of MUC1 was detected on RT112 and T24, while J82 showed a weak expression of MUC1. In contrast, in the present work a weak expression of MUC1 on RT112 and T24 is observed and a stronger expression of MUC1 on J82 is found (Figure 2.1). This difference in MUC1 expression might be due to the use of different antibodies in the experiments. In the present work, E29 mAb is used to analyze MUC1 expression, while C595 mAb was used in our previous publication (Laurent *et al.*, 2014). To verify this, the MUC1 expression was analyzed on five BCs using C595 mAb and the results are shown in Figure 2.10.

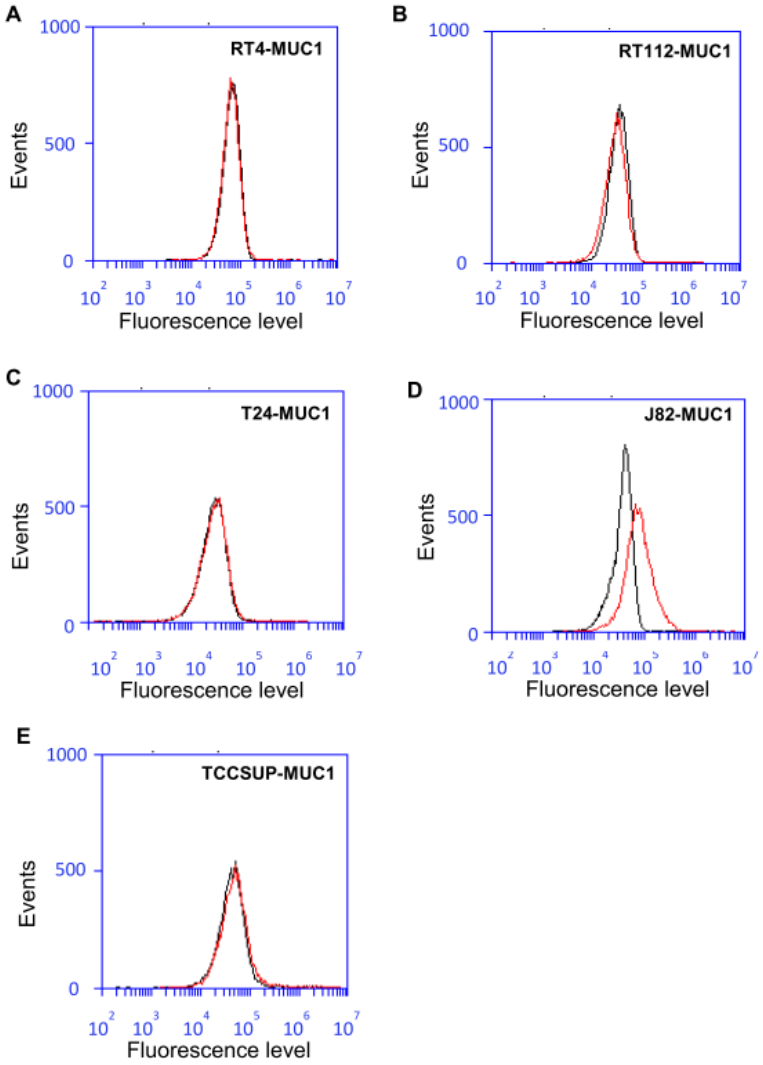

Figure 2.10: Flow cytometry analyses of MUC1 expression in BCs using C595 mAb. Expression levels of MUC1 (red curve) by flow cytometry analysis in comparison with an irrelevant antibody (black curve): (A) RT4, (B) RT112, (C) T24, (D) J82 and (E) TCCSUP.

Flow cytometry analysis indicated a weak expression of MUC1 on J82, while MUC1 expression was not observed on other BCs like RT4, RT112, T24 and TCCSUP (Figure 2.10). From the literature, we know that the antibodies (E29 and C595) recognize the same region

(PDTRP motif) in VNTR segment of MUC1 which is repeated 25-125 times, allowing the mAb to bind to multiple repeats. It has been reported that binding to multiple repeats of MUC1 was not observed with C595 mAb (Karsten *et al.*, 2004). In contrast, E29 mAb was shown to bind to multiple repeats on MUC1 (Karsten *et al.*, 1998, 2004) thereby increasing the sensitivity to detect the expression of MUC1. This might explain the weak expression of MUC1 detected in RT4, RT112, T24 and moderate expression in TCCSUP observed in our present work when using E29 mAb (Figure 2.1). These results indicated that the sensitivity to detect MUC1 expression increases when using E29 mAb and this might be due to its binding to multiple repeats.

This is better illustrated in Figure 2.11A where we can see a ~6 fold increase in MUC1 expression for J82 cells while using E29 mAb when compared to C595 mAb. This increase in MUC1 expression while using E29 was also observed in another cell line K562 (chronic myelogenous leukemia) as shown in Figure 2.11B.

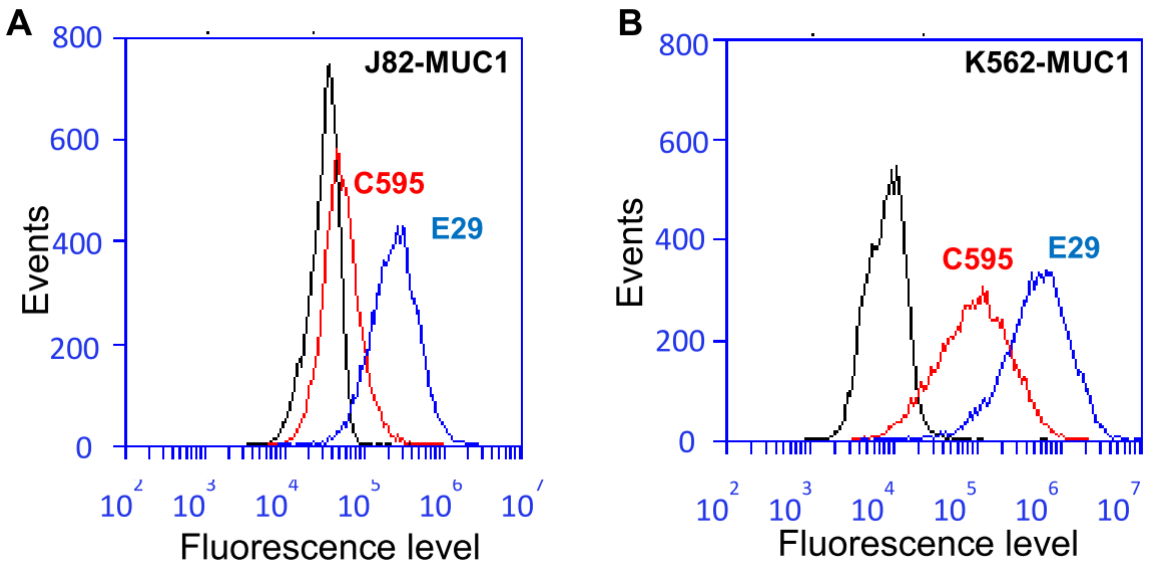

Figure 2.11: Flow cytometry analyses of MUC1 comparing C595 and E29 mAb. Expression levels of MUC1 using C595 mAb (red curve) and E29 mAb (blue curves) by flow cytometry analysis in comparison with an irrelevant antibody (black curve): J82 (A) and K562 (B).

The mRNA analysis also indicated that J82 express ~30 fold higher amount of MUC1 as compared to T24 (Figure 2.3). This validates our findings from flow cytometry, that J82 and T24 express strong and weak expression of MUC1 respectively. A weak expression of MUC1 was already observed in T24 at the mRNA level (Fujii *et al.*, 2013) while another study reported no detectable level of MUC1 mRNA in T24. By cons, J82 cells showed a moderate expression of MUC1 (Kaur *et al.*, 2014), as observed in our current study (Figure

2.1E). MUC1 expression was also reported in RT4 (Retz *et al.*, 1998), TCCSUP and few other BCs like KU7, UMUC2, SCaBER, 647V, 486P and HT-1367 (Retz *et al.*, 1998; Fujii *et al.*, 2013; Kaur *et al.*, 2014). A weak expression of CD43 was observed in RT4, RT112, T24 and TCCSUP, while J82 expressed moderate levels of CD43 (Figure 2.2 and Table 2.3). The expression of CD43 has not been studied extensively, but some works showed a *de novo* expression of CD43 in cancer tissues and in particular in bladder cancer tissues (Santamaría *et al.*, 1996; Hurford *et al.*, 1999).

It has been already shown that MUC1 mediates the adhesion of breast cancer cells to ECs via ICAM-1 and this adhesion is decreased when blocking MUC1 or ICAM-1 (Regimbald *et al.*, 1996; Rahn *et al.*, 2005). The interaction of MUC1 with ICAM-1 mediates the transendothelial migration of breast cancer cells (Rahn *et al.*, 2005) and also initiates calcium signaling (Rahn *et al.*, 2004). Likewise, CD43 expressed by some cancer cells plays a role in tumor-mesothelial cell adhesion via its interaction with ICAM-1 (Rosenstein *et al.*, 1991; Ziprin *et al.*, 2004; Alkhamesi *et al.*, 2005, 2007). Our results show that the adhesion of BCs (T24 and J82) to ECs was greatly reduced when blocking ICAM-1, MUC1 or CD43, whereas the adhesion of RT112 to ECs was not much affected by blocking these receptors (Table 2.4). Our present results from adhesion assays indicate that bladder cancer cell-endothelial cell adhesion is mainly mediated through ICAM-1 for invasive cells (T24 and J82). Similar results were obtained in our previous study using AFM (Laurent *et al.*, 2014), demonstrating that endothelial ICAM-1 interacts with tumor cell ligands and mediates the adhesion process for invasive cells (T24 and J82) while ICAM-1 does not seem to play a major role in the adhesion process of a less invasive cell line (RT112).

The functional role of a protein can be studied by generating stable cell lines knockdown for specific proteins by shRNA approach and comparing it with control cells. T24 and J82 BCs were knocked-down for MUC1 to validate the role of MUC1 in bladder cancer cell adhesion. Our preliminary results showed that MUC1 expression was decreased at the surface and cellular level as reported in other publications using this approach (Pochampalli *et al.*, 2007; Fujii *et al.*, 2013; Tréhoux *et al.*, 2015). Our results also indicated that MUC1 transfected cells expanded from single cells showed almost no expression for MUC1. The sh-RNA approach combined with cloning from single cells can be a good approach to create stable cell lines knockdown for specific proteins. The adhesion assays using sh-MUC1 transfected cells were not performed due to our time constraints.

2.4 Conclusions

From chapter 2, we showed that a weak expression of MUC1 and CD43 was observed on RT4, RT112 and T24 BCs. TCCSUP showed moderate and weak expression of MUC1 and CD43 respectively. Comparing to other BCs, J82 showed a strong expression of MUC1 and a moderate expression of CD43. As MUC1 and CD43 are the ligands for ICAM-1, we studied the role of these molecules in bladder cancer cell-endothelial adhesion by performing adhesion assays. Our results showed that ICAM-1 plays an important role in bladder-cancer endothelial cell adhesion via its interactions with MUC1 and CD43 mainly for invasive cells (T24 and J82). For the less invasive cell (RT112), endothelial ICAM-1 does not seem to play a role in the adhesion process. In this chapter, we showed the involvement of MUC1 and CD43 in cancer cell-endothelial cell adhesion. The AFM study involving the quantification of forces mediated by MUC1 and CD43 during their interactions with ICAM-1 is complementary and will be discussed in detail in chapter 03.

Chapter 3 - Study of the forces involved in bladder cancer cell–endothelial cell adhesion

In chapter 2, we showed that MUC1 and CD43 were playing an important role in mediating bladder cancer cell-endothelial cell adhesion via interaction with ICAM-1. However, the assay provides no information on adhesion strength and forces involved by these molecules during the interaction. In recent years, single-cell force spectroscopy (SCFS) using Atomic Force Microscopy (AFM) (Zhang *et al.*, 2002; Puech *et al.*, 2005; Franz *et al.*, 2007; Friedrichs *et al.*, 2010; Laurent *et al.*, 2014) has been applied for studying adhesive interactions of cells with other cells, proteins, or functionalized surfaces. In particular, AFM is a powerful tool to identify and quantify ligand-receptor interactions (Alsteens *et al.,* 2010; Taubenberger *et al.,* 2007; Pfreundschuh *et al.,* 2015; Puech *et al.,* 2005; Sulchek *et al.,* 2005; Zhang *et al.,* 2002). In this chapter, we use the SCFS AFM mode in combination with a Gaussian mixture model (GMM) to identify and to quantify precisely the force ranges involved by MUC1 and CD43 during their interaction with ICAM-1. A detailed investigation on the rupture events (jumps and tethers) in the force curve provides some additional information regarding the interactions of receptors with the cytoskeleton.

3.1 Materials and Methods

3.1.1 Culture conditions

The cell culture medium and the conditions were already explained (refer to section 2.1.1 in chapter 2). J82 BCs were stably transfected with a plasmid expressing Lifeact-GFP to stain F-actin and these GFP transfected cells were used for AFM experiments. For AFM experiments, RPMI 1640 and endothelial growth medium were supplemented with 20 mM Hepes at pH 7.4 (Sigma-Aldrich, Lyon, France).

3.1.2 Atomic force microscopy

AFM experiments were performed using a Nanowizard II (JPK Intruments, Berlin, Germany) mounted on a Zeiss microscope (Carl Zeiss, Jena, Germany). This configuration allows us to carry out AFM measurements and simultaneously observe the cells using phase contrast or fluorescence modes. The optical microscope is necessary during the initial steps of cell selection and for attaching the cell to the cantilever as well as to follow the changes in the morphology of attached cells on the cantilever. Long range force measurements involving cell-cell interactions were performed using the CellHesion module (JPK Instruments, Berlin, Germany) which enables vertical movement of the sample holder up to 100 µm thanks to the piezo-driven movement. In addition, the objective was mounted on a vertical piezo-translator (PIFOC, PhysikInstrumente, Karlsruhe, Germany) to move the objective concurrently with the microscope stage and focus on the cells during AFM measurements. All the AFM measurements were carried out at 37°C using the Petri Dish Heater (JPK Instruments, Berlin, Germany). The AFM setup is set on a Halcyonics anti-vibration system (Halcyonics, Germany) to minimize vibrations. The AFM set up and the components are described in Appendix B.

3.1.3 Substrate preparation

For force spectroscopy experiments, HUVECs were grown on fibronectin coated coverslips for 3 days at 37°C, 5% CO_2 to achieve confluence. Prior to use, they were replaced with endothelial growth medium with 20 mM Hepes without supplements.

The monomeric form of recombinant ICAM-1-Fc (rICAM-1) was purchased from RD systems (Lille, France) and used in our experiments. To prepare rICAM-1 immobilized substrate, 20 µl of rICAM-1 (25 µg/ml) in 0.1 M $NaHCO_3$ was incubated overnight at 4°C in the Petri dish. The rIACM-1 immobilized surface mimics a HUVEC surface expressing

ICAM-1. Unbound proteins were removed by washing with PBS and then the exposed surface was blocked using 100 µg/ml of bovine serum albumin (BSA) in PBS (Sigma-Aldrich, Lyon, France). Finally, BSA was replaced by the RPMI 1640 medium without serum and used for further steps.

For the BSA immobilized substrate, 20 µl of 100 µg/ml BSA in PBS was allowed to adsorb for 30 min at 37 °C in the Petri dish. Unbound proteins were removed by washing with PBS and replaced with RPMI medium without supplements. The different substrates are sketched in Figure 3.1.

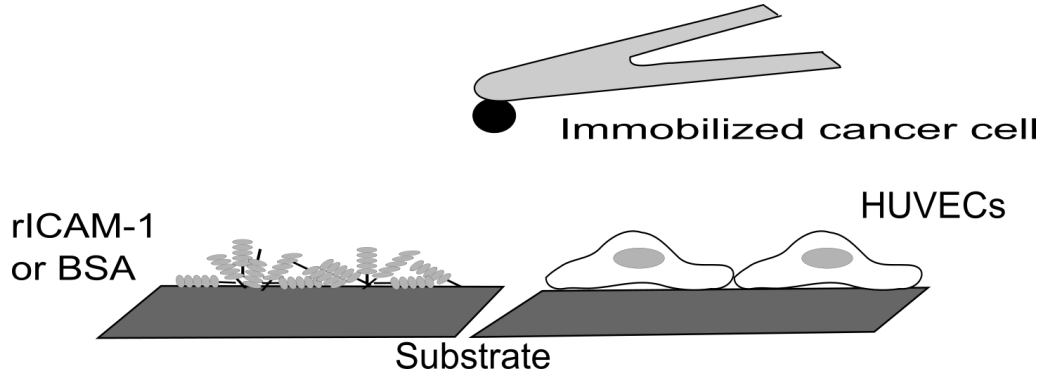

Figure 3.1: Substrates used for AFM experiments. Sketch of different substrates (rICAM-1, BSA, HUVECs) used in our SCFS experiments.

3.1.4 Cantilever preparation

V-shaped, 300 µm long tipless silicon nitride cantilevers with a nominal spring constant around 0.01 N/m (MLCT-O10, Bruker, France) were used in our experiments for force measurements. Indeed, soft cantilevers with small spring constants (~ 0.01 N/m to ~0.06 N/m) are needed to detect small forces such as the single adhesive bonds in the range 20 pN to 100 pN at the cell surface (Friedrichs *et al.*, 2013).

A single cancer cell was attached to the AFM cantilever functionalized using Concanavalin A (Con A). To prepare ConA functionalized cantilever (Figure 3.2A), the cantilever was soaked in acetone for 5 min, UV-irradiated for 15 min and incubated in biotin-BSA (0.5 mg/ml in 100 mM $NaHCO_3$, pH 8.6; Interchim, Montlucon, France) overnight at 37°C in a humidified incubator. The cantilever was then rinsed with PBS and incubated in streptavidin (0.5 mg/ml in PBS; Interchim, Montlucon, France) for 10 min at room temperature. Finally, the cantilever was rinsed with PBS and incubated in biotin-ConA (0.5 mg/ml in PBS; Interchim, Montlucon, France) for 10 min and then rinsed with PBS (Wojcikiewicz *et al.*, 2004). This protocol mediates the binding of the cancer cell to the

cantilever with a force greater than the ones occurring during the interaction between cancer cells and HUVECs (Zhang *et al.*, 2006). [Refer to Appendix B for the detailed protocol].

After functionalization, the cantilever was mounted on the AFM setup and the sensitivity and spring constant of the cantilever were determined using built-in routines from JPK Instruments as described in Appendix B. The sensitivity and spring constant are necessary to convert the cantilever deflection into volts then to its corresponding readouts in Newtons, so they are measured every time a cantilever is mounted or remounted. The sensitivity was calculated from force-distance (F-d) curve recorded by making contact of cantilever with a stiff surface (obtained by scratching in the middle of HUVECs monolayer as shown in Figure 3.2B). The sensitivity value was around 50±2.5 nm/V (5% error) for the functionalized cantilever used in the experiments. Next, the spring constant of the cantilever was determined by measuring the thermal fluctuations of the cantilever and applying equipartition theorem as previously described in the protocol (Hutter and Bechhoefer, 1993). The spring constant was around 0.01±0.001 N/m (10% error) in the experiments. An estimate of the error during sensitivity measurements and spring constant is around 15% which is much smaller than the deviation obtained within a single force curve.

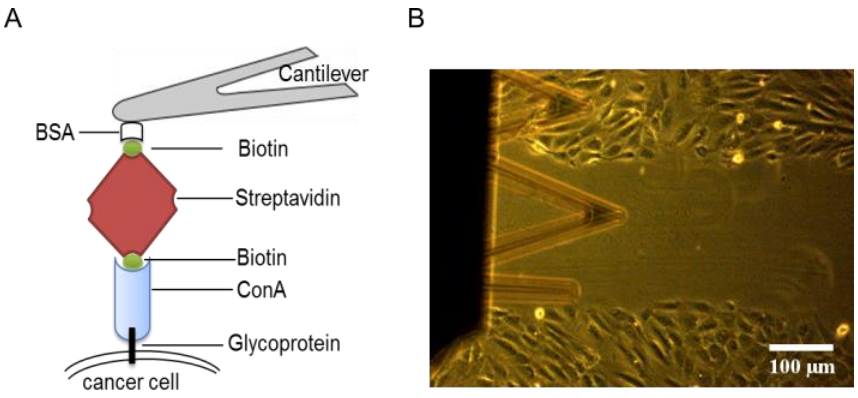

Figure 3.2: Functionalization and calibration of the cantilever. (A) The cantilever was treated with biotin-BSA, streptavidin, biotin-ConA mediating the attachment of cancer cell to the cantilever. (B) Image showing the calibration process where the sensitivity of the cantilever was measured by pressing it to the stiff surface at a location where HUVECs have been scratched.

3.1.5 Cancer cell capture

J82 cells were detached from the culture dish just before the AFM experiment using Trypsin/EDTA (Sigma-Aldrich, Lyon, France). The detached cells were recovered in complete RPMI medium, centrifuged (1200 rpm for 5 min) and resuspended in RPMI medium without serum. It has to be noted that the substrate (HUVECs or rIACM-1 or BSA)

and cancer cells were in growth medium without supplements during the attachment of cancer cells to the cantilever. As the proteins present in the supplements can bind to ConA and prevent the attachment of the cancer cell to the cantilever. J82 cells were injected into the petri dish containing a monolayer of HUVECs and allowed to settle. ConA functionalized cantilever tip was centered above a J82 cell as shown in Figure 3.3A. These cancer cells are expressing GFP-actin and can be easily distinguished from HUVECs. Then, the substrate is moved towards the cantilever (Figure 3.3A) and allowed to make contact with the cancer cell attached to the functionalized cantilever with a force of 1 nN for ten seconds (Figure 3.3B). The substrate is then retracted slowly (Figure 3.3C) and the cantilever with the cancer cell is allowed to rest for 10-15 min in the culture medium (Figure 3.3D).

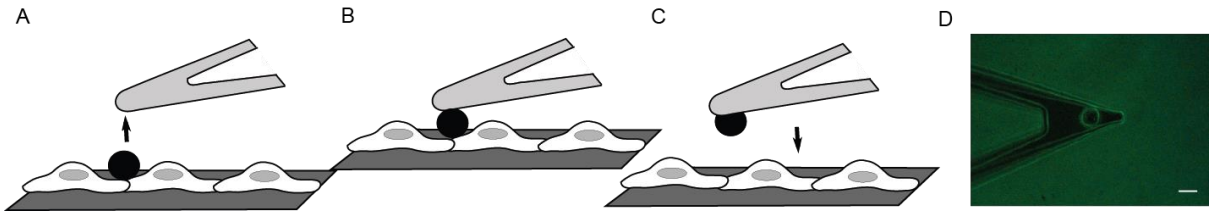

Figure 3.3: Attachment of a cancer cell to the AFM cantilever. (A) The substrate is moved towards the functionalized AFM cantilever. (B) The substrate with cancer is gently pushed (~1 nN for 10 s). (C) The substrate is retracted and the cantilever bound cell is allowed to rest. (D) Image of the AFM cantilever with cancer cell attached to it. Scale bar = 20 µm.

3.1.6 Single cell force spectroscopy (SCFS)

After the cancer cell was captured using the cantilever, 1.5 ml of complete endothelial growth medium was added and the force measurements were performed as shown in Figure 3.4A. The cancer cell one was set above the nucleus of a HUVEC (Figure 3.4C) and the HUVECs substrate was approached towards the cantilever with cancer cell at constant speed (5 µm/s) as shown in Figure 3.4A. During contact, a compression force of 500 pN was applied for 10 s and the HUVECs substrate was then retracted at constant speed of 5 µm/s (Figure 3.4A). A force-distance curve (F-d) was obtained for each approach and retraction cycle (Figure 3.4B). Typically, with a single cancer cell attached to the cantilever about 30 such F-d curves were acquired on 30 different HUVECs. The cancer cell was allowed to recover for 1 min between each force curve and 5 min between sets of 6 force curves. To block specific interactions involving cancer cells and HUVECs, cancer cells were incubated with antibodies specific for MUC1 or CD43 or MUC1+CD43 at 25 µg/ml for 15 min, prior to cell capture.

The retraction curve is characterized by the force required to separate the cancer cell from the HUVEC, referred to as the detachment force (Figure 3.4B). The detachment force corresponds mainly to the stretching of HUVEC-BC cell pair. The force jumps in the force curve correspond to the breakup of bonds involved in cell-cell interaction (Figure 3.4B).The force jumps were referred as rupture events in the text. A force jump preceded by a force plateau indicates the formation of membrane tethers. The retraction curve also provides information about the adhesion energy, which is the work that is required to detach the cancer cell. It is equal to the area under the retraction curve. This includes the work done to stretch cells as well as the work to break the molecular bonds (Figure 3.4B). All these parameters (detachment force, rupture force, adhesion energy) can be obtained from the force curve using the built-in software (JPK Instruments, Berlin, Germany).

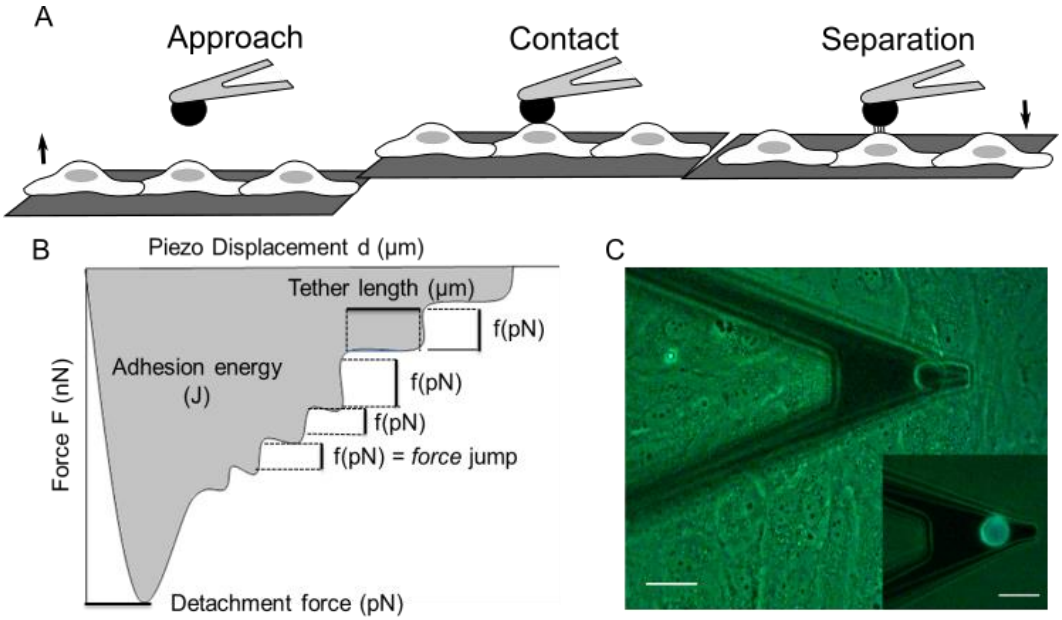

Figure 3.4: Interactions between cancer cells and ECs using SCFS. (A) Sketch of the approach-retraction method, (B) typical retraction force curve in terms of the piezo displacement. The HUVECs monolayer approaches the cancer cell at constant velocity. Then the HUVEC comes in contact with the cancer cell during 10 s (500 pN applied force) to create several bond complexes within the adhesion area. The HUVECs substrate is then retracted at constant velocity in order to detach the adhesive bonds. The retraction curve shows force jumps corresponding to the bond rupture force (f). The adhesion energy (shaded area) represents the detachment work (typically in pJ) to completely detach the cell from the substrate. The detachment force (typically in nN) is the force necessary to stretch the cancer cell and the HUVEC until bonds start to detach. Note that jumps force jumps can follow a plateau corresponding to tether formation. (C) Image of the AFM cantilever with an attached cancer cell above the HUVEC monolayer and inset showing the cantilever with fluorescent cancer cell. Scale bar = 20 µm.

3.1.7 SCFS force-distance curve analysis

The steps involved in the analysis of force curve using the JPK software are explained in Figure 3.5. First, the baseline offset and tilt was corrected by selecting the linear part of the F-d curve (Figure 3.5A, selected part is indicated with the black line) and this linear part was subtracted to the entire F-d curve as shown in Figure 3.5B. Then, the detachment force (maximum adhesive force) was determined from the F-d curve (Figure 3.5C), as well as the adhesion energy (shaded area enclosed in the curve) as shown in Figure 3.5D. The force jumps (i.e rupture events) in the F-d curve were identified (Figure 3.5E,F) by fitting a model that combines sharp steps with slowly varying background as explained (Kerssemakers *et al.*, 2006). The rupture events were identified by optimizing the values for smoothing and significance in the software and the rupture forces corresponding to each rupture events were obtained.

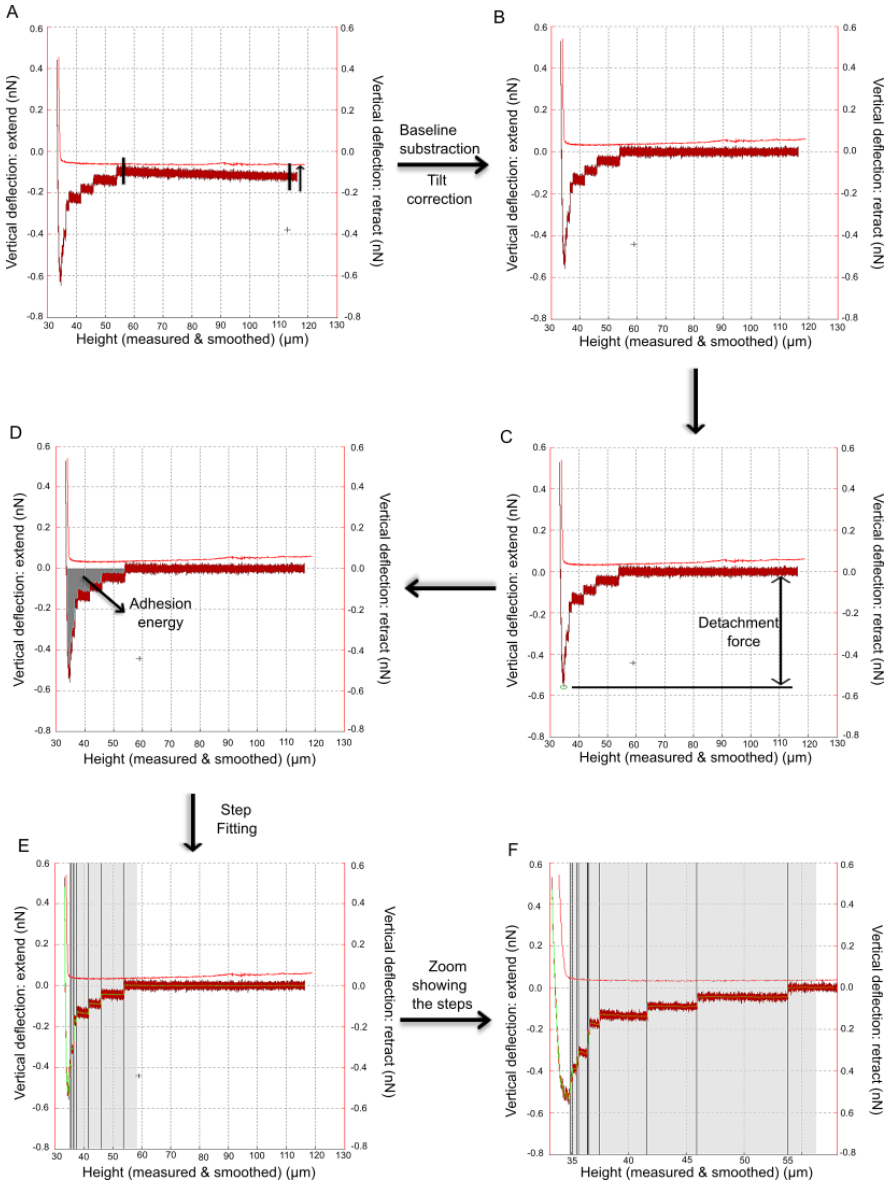

Figure 3.5: Steps involved in the analysis of F-d curves. (A) Baseline and tilt correction were used, (B) the obtained force curve obtained after correction was analyzed to find different parameters like (C) detachment force and (D) adhesion energy. Finally, the force curve (E, F) was fitted accurately to identify and to measure the magnitude of force jumps.

3.1.8 Optimizing the parameters for SCFS experiments

The number of force jumps (rupture events) in a curve depends on many parameters like velocity, applied force and contact time. It has been reported that an optimum sampling rate is necessary to identify the rupture events more precisely (Taninaka *et al.*, 2012). The values for applied force and sampling rate were optimized by performing SCFS experiments with J82 BCs attached to the cantilever and endothelial monolayer and keeping other parameters like velocity and contact time constant. The force curves from different conditions were analyzed to find the rupture events per curve and compared with each other. The rupture events recorded for the applied force 1 nN and 500 pN showed less difference between them, whereas there was a ~2 fold decrease in rupture events at 200 pN (Figure 3.6). So we used 500 pN as applied force in our experiments to obtain enough rupture events while applying less force to BCs and ECs. Changing the sampling rate did not show much difference between them for the three applied forces (Figure 3.6), yet using higher sampling rate is always recommended to discriminate the close rupture events (Taninaka *et al.*, 2012; Friedrichs *et al.*, 2013). All our AFM experiments were performed using the parameters mentioned in Table 3.1. The contact time (10 s) and velocity (5 µm/s)were used in reference with our previous publication (Laurent *et al.*, 2014).

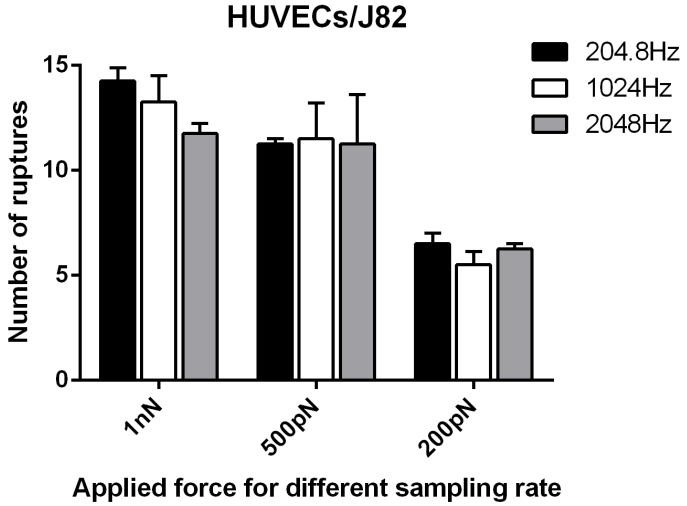

Figure 3.6: Parameters optimization for SCFS experiments. The number of bonds, Mean±SEM obtained during the adhesion of a J82 bladder cancer cells to a HUVEC monolayer for different applied forces (1 nN, 500 pN, 200 pN) and different sampling rates (204.8 Hz, 1024 Hz, 2048 Hz). The other parameters were kept constant (time of contact 10 s, velocity 5 µm/s).

Parameters	SCFS measurements
Approach velocity	5 µm/s
Retract velocity	5 µm/s
Applied force	500 pN
Contact time	10 s
Sampling rate	2048 Hz
Temperature	37°C
Contact condition	Constant force
Z loop	Open
Pulling distance	>70 µm

Table 3.1: Parameters used for SCFS measurements.

The approach and retract velocity of 5 µm/s was used in reference to our earlier publication (Laurent *et al.*, 2014). Applied force (500pN) and sampling rate (2048 Hz) was used after optimization studies as discussed before. The contact time of 10 s was selected to have a good number of rupture events in a force-curve and the piezo was maintained in constant force mode. With this mode, the same force can be maintained between the cells during the interaction time of 10 s. Open loop mode is selected to reduce the noise from the measurement so that the rupture forces can be identified at better resolution (Franz *et al.*, 2007). Studying ligand-receptor interactions between cells requires large pulling range (>70 µm) to separate two cells completely and it is made possible thanks to the CellHesion module which provides 100µm of piezo movement in z-direction (Details on CellHesion module is discussed in Appendix B).

3.1.9 Jumps and Tethers Analysis

Only force-distance curve with at least one rupture event were considered in our analysis. The rupture events followed by the force plateau with a distance higher than 2 µm were considered as tethers (membrane nanotubes) in our analysis. It has been reported that the tether length may considerably vary ranging from 1-100 µm in giant unilamellar lipidic vesicles (GUVs) and 1-20 µm in cells (Puech *et al.*, 2006). Tulla et al. considered the rupture events followed by force plateau at distances between 2 µm and 9.5 µm as membrane nanotubes or tethers in the analysis (Tulla *et al.*, 2008). In accordance with the above reference we also found that majority of tethers events had a force plateau greater than 2 µm in our force curves. The tether length was measured directly from the force-distance curve as the length of the force plateau. The mean number of jumps or tethers per curve were obtained by dividing the total numbers of jumps or tethers (>36 pN) by the number of curves and compared under different conditions.

3.1.10 Statistical Analysis

For each set of conditions, at least three independent AFM experiments were performed on three different days. All the data is reported as Mean ± SEM. With one cancer cell attached to the cantilever around ~30 F-d curves were performed on ~30 different ECs. The number of F-d curves is equal to number of endothelial cells for measurements. The number of cancer cells and endothelial cells used to obtain the data are shown in Table 3.2 for different conditions (blocking MUC1, blocking CD43 and blocking MUC1+CD43) and for two substrates (HUVECs and rICAM-1).

Conditions	**HUVECs**		**rICAM-1**	
	Number of cancer cells	**Number of ECs**	**Number of cancer cells**	**Number of ECs**
control	3	88	4	79
anti-MUC1	3	91	3	70
anti-CD43	3	89	3	86
anti-MUC1+anti-CD43	3	90	3	85

Table 3.2: Pooling of data for the analysis. The number of cancer cells and endothelial cells used for obtaining the date is indicated for each condition.

The data obtained from F-d curves were independent in terms of ECs (ECs is never the same) and on the contrary dependent in terms of cancer cells (the same cancer cell was used for around 30 measurements). Classical statistical test like ANOVA consider that the data is independent of each other and does not take random effects into account. As our data is not completely independent and it has random effects due to use of same cancer cells for multiple measurements we used a Generalized Linear Mixed Model (GLMM). This model is used to analyze the data sets in ecology and evolution that has lot of random effects (Bolker *et al.*, 2009). Statistical analysis for AFM data was performed using the R software (3.3.0 release). Differences between the data calculated on untreated BCs or by blocking MUC1 or CD43 or both on BCs were tested by the mixed function of the apex package (R software).

3.1.11 Use of a Gaussian Mixture Model

Considering that our data is comprised of rupture forces coming from different ligand-receptor interactions, a multi-component mixture model is necessary to separate the contributions of the different receptors. In order to identify and separate the different subpopulations from the overall histograms a Gaussian Mixture Model (GMM) was used. In our study we used a tri-modal GMM for control values and bi-modal GMM for data obtained while blocking MUC1 or CD43 to analyze the contributions of the different receptors. The

built-in function “fitgmdist” from Matlab was used to identify the subpopulations from our data. This function uses maximum likelihood estimations to find the parameters fitting best our experimental data and provides the overall probability density and subcomponents of each distribution.

3.2 Results

3.2.1 Quantifying the effect of blocking MUC1 and CD43 using SCFS

To measure the adhesion forces involved in bladder cancer cell-endothelial cell adhesion, we performed SCFS experiments. J82 cells were used for our AFM experiments, because they express higher levels of MUC1 and CD43 as compared to other cell lines (refer to Figure 2.1, 2.2). Initially, the rupture forces that were not mediated by molecules expressed by endothelial cells (nonspecific interactions) were quantified using BSA. A single J82 cell was attached to a functionalized tipless cantilever and put in contact with BSA on the substrate and then retracted. A single F-d curve for BSA/J82-control is shown in Figure 3.7E where no rupture events were observed. But the analysis using the JPK software detected few rupture events of low force range (~20 pN) at the beginning of the F-d curve, undetected in Figure 3.7E. Then, all the F-d curves obtained for J82/BSA interactions were analyzed to identify and measure the rupture forces corresponding to the rupture events. The rupture forces obtained from the F-d curves have to be represented in the form of an histogram with a specific bin size for the analysis. The best bin size to fit our data was selected using the Freedom-Diaconis rule (Bura *et al.*, 2009; Bizzari A.R and Cannistraro S, 2012), considering that our data is a mix of several Gaussians and therefore it does not follow the normal distribution. The analysis was performed using R and it indicated that the bin size of 2 was ideal to represent our data and so all our force histogram were constructed with the bin size of 2. The rupture force histogram obtained for J82/BSA interactions (Figure 3.8D) revealed that nonspecific interactions (forces that are not mediated by molecules expressed by endothelial cells) corresponded to the range of rupture forces <36 pN.

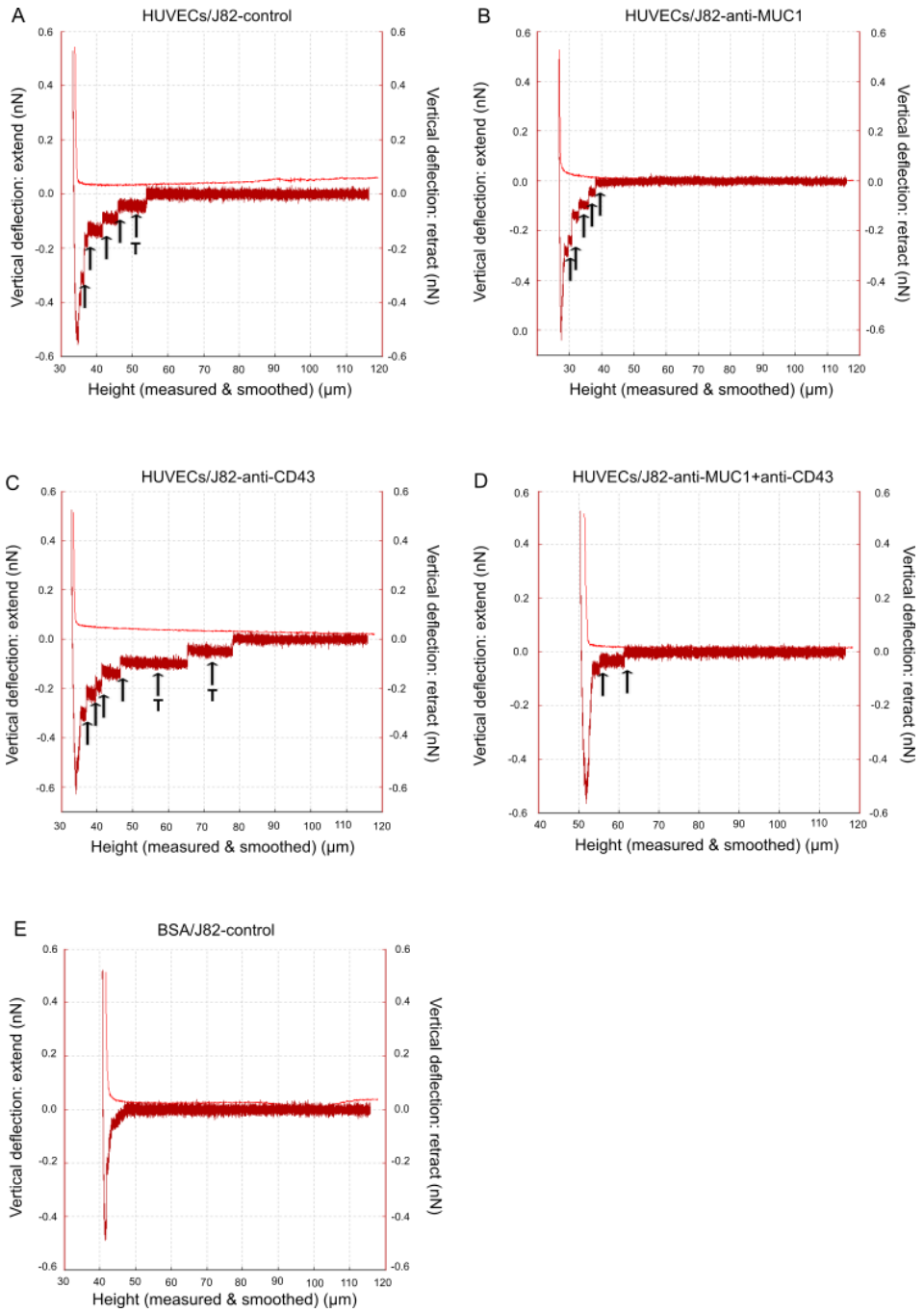

Figure 3.7: Force-distance curves. Single F-d curves with rupture events: jumps (indicated as arrows) and tethers events (indicated as T) are shown: (A) HUVEC/J82-control, (B) HUVEC/J82-anti-MUC1, (C) HUVEC/J82-anti-CD43, (D) HUVEC/J82-anti-MUC1+anti-CD43 and (E) BSA/J82-control.

AFM experiments were then performed using a HUVEC monolayer as the substrate and a J82 cell attached to the cantilever. Force curves were analyzed and the force histogram for non-treated cells (control) was obtained. Similarly AFM measurements were performed by attaching a J82 cell blocked with antibodies specific for MUC1 or CD43 or MUC1+CD43. The force histograms for anti-MUC1, anti-CD43 and anti-MUC1+anti-CD43 were obtained.

A single F-d curve for the different conditions are presented in Figure 3.7, control (Figure 3.7A), anti-MUC1 (Figure 3.7B), anti-CD43 (Figure 3.7C) and anti-MUC1+anti-CD43 (Figure 3.7D). The rupture events corresponding to jumps are indicated as arrows and tether events are indicated as T in Figure 3.7. A single F-d curve showed an almost similar number of rupture events for the control (Figure 3.7A), when blocking MUC1 (Figure 3.7B) and blocking CD43 (Figure 3.7C), while blocking both (MUC1+CD43) showed a significantly smaller number of rupture events (Figure 3.7D). Also, few tether (T) like rupture events that were observed in control and when blocking CD43 disappeared in the force curves obtained when blocking MUC1 and both (MUC1+CD43) (Figure 3.7A-D). These were our primary observations from single F-d curves and the analysis of the rupture events (jumps and tethers) on all the F-d curves obtained for different conditions are discussed in detail later (refer to section 3.2.5).

The effect of blocking the receptors (MUC1, CD43 or both) involved in the interaction was quantified by comparing their force distribution to the control. When blocking MUC1, the force histogram showed a significant decrease in the number of large rupture force events compared to the control (Figure 3.8A). This decrease in rupture events was quantified by considering the rupture events above >36 pN. The number of rupture events recorded for bins starting from 28 to 60 pN for different conditions (control, blocking MUC1, blocking CD43 and blocking MUC1+CD43) is shown in Table 3.3. For the data <36 pN, no significant decrease in the number of rupture events was observed when blocking the receptors (MUC1 or CD43 or both) as compared to control. Whereas, considering the data >36 pN, the number of rupture events significantly decreased when blocking the receptors (MUC1 or CD43 or both) as compared to control (indicated in red in Table 3.3). Although in the bin range (30-32, 32-34) we observed some decrease in number of rupture events when blocking MUC1+CD43 as compared to control (Table 3.3), a common value that fits all the different conditions was selected. This analysis indicated that the rupture events <36 pN were unresponsive when blocking the receptors (MUC1 or CD43 or both), indicating that considering the rupture events >36 pN for our quantification can be reasonable. This result also agrees with our earlier observation using BSA as the substrate (Figure 3.8D).

Bin start – Bin end (pN)	control (events)	anti-MUC1 (events)	anti-CD43 (events)	anti-MUC1+anti-CD43 (events)
28-30	70	86	84	76
30-32	90	89	83	64
32-34	87	82	73	58
34-36	74	68	68	61
36-38	**85**	**50**	**47**	**43**
38-40	**70**	**25**	**46**	**21**
40-42	**56**	**25**	**38**	**11**
42-44	**31**	**13**	**30**	**11**
44-46	**36**	**10**	**16**	**8**
46-48	**43**	**7**	**10**	**4**
48-50	**30**	**8**	**10**	**6**
50-52	**18**	**4**	**8**	**6**
52-54	**12**	**7**	**5**	**4**
54-56	**17**	**3**	**4**	**3**
56-58	**9**	**0**	**3**	**2**
58-60	**2**	**0**	**5**	**1**

Table 3.3: Rupture events <36 pN are unresponsive when blocking the receptors. Number of rupture events obtained for bins (28-60 pN) is represented for different conditions.

The analysis of the total number of rupture events showed that J82 control (4.8 events per curve) had almost 2.7 times more events than after blocking MUC1 (1.8 events per curve). The normalized inhibition in adhesion due to the blocking of MUC1 was quantified as ~64% (Table 3.4). Likewise, blocking CD43 (2.8 events per curve) showed 1.7 times less events as compared to the control (Figure 3.8B) with a ~42% normalized inhibition (Table 3.4). Blocking MUC1+CD43 (1.3 events per curve) showed 3.6 times less events as compared to the control (Figure 3.8C) with a normalized inhibition of ~72% (Table 3.4). The rupture force histogram obtained when blocking MUC1+CD43 also provides information regarding the forces that were not mediated by MUC1 and CD43. From Figure 3.8C (histogram in white), we observed that most of the rupture events were found in lower force ranges with a mean of ~30 pN which validates our inference using BSA (Figure 3.8D) and our analysis on the number of rupture events (Table 3.3). We also observed a few rupture events >36 pN (Figure 3.8C, histogram in white) which suggested that the blocking efficiency of antibodies is not 100%.

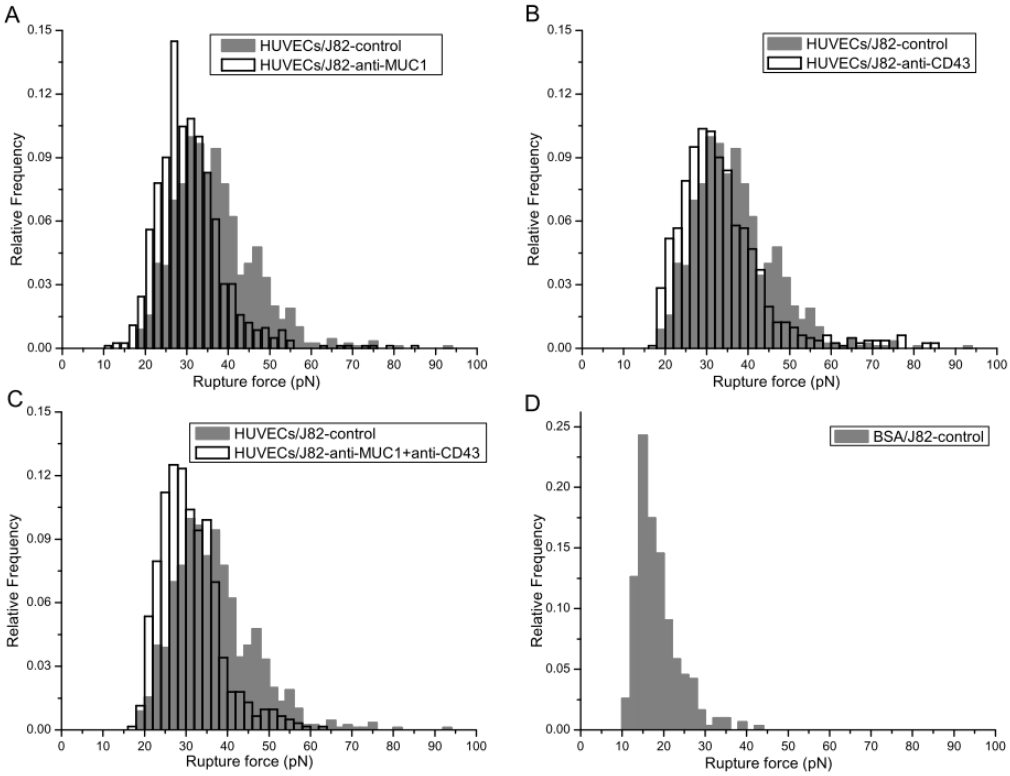

Figure 3.8: SCFS analysis of bladder cancer cell-endothelial cell adhesion. Force histograms showing the distribution of rupture events for the adhesion of HUVEC monolayer with J82 bladder cancer cells for different conditions were obtained from force curves (applied force 500 pN, time of contact 10 s, velocity 5 µm/s). Histograms obtained when (A) blocking MUC1, (B) CD43 and (C) MUC1+CD43 on J82 cells (white histogram) are compared with the control without antibody (grey histogram). (D) The Force histogram for nonspecific interactions was obtained using a BSA-coated substrate.

Substrate	J82 cell condition	% Inhibition compared to control	N	n	Mean rupture events per curve (M=n/N)
HUVECs	control		88	426	4.8
	anti-MUC1	63.9	91	159	1.8
	anti-CD43	42.2	89	249	2.8
	anti-MUC1+anti-CD43	72.2	90	121	1.3
rICAM-1	control		79	126	1.6
	anti-MUC1	56.1	70	49	0.7
	anti-CD43	40.2	86	82	0.9
	anti-MUC1+anti-CD43	76.4	85	32	0.4

Table 3.4: Analysis of rupture force distributions. The % inhibition is the number of rupture events (>36 pN) when blocking different receptors involved in the interaction. It was quantified by comparing HUVECs and rICAM-1 to the control. N represents the number of force curves, n is the total number of rupture events (>36 pN) and M represents the mean rupture events per curve. % inhibition by blocking the specific receptor was quantified using the formula $[1-(M_{Ab}/M_{cont})]*100$. M_{Ab} represents the mean rupture of events obtained while blocking MUC1, CD43 or MUC1+CD43 using specific antibodies and M_{cont} represents the mean number of rupture events for the control.

3.2.2 ICAM-1 mediates the interaction of J82 cell with HUVECs

To study the interactions of ICAM-1 alone with BCs ligands (MUC1 and CD43), we have used a rICAM-1 protein coated substrate instead of a HUVEC monolayer. SCFS experiments were performed with J82 cells attached to the cantilever and rICAM-1 adsorbed on the substrate. Force histograms obtained when blocking MUC1 (Figure 3.9A) or CD43 (Figure 3.9B) or MUC1+CD43 (Figure 3.9C) were compared to the control and the normalized inhibition was quantified (Table 3.4). Blocking MUC1 (0.7 events per curve), CD43 (0.9 events per curve) compared to the control (1.6 events per curve) showed a normalized inhibition of ~56% and ~40% respectively (Table 3.4). Blocking both MUC1 and CD43 (0.4 events per curve) showed an increase in the normalized inhibition up to ~76% (Table 3.4). The normalized inhibition obtained by blocking MUC1 or CD43 or MUC1+CD43 is similar to the one obtained using rICAM-1 and HUVECs monolayer as substrates. These results suggest that in our conditions the interaction of J82 cancer cells to ECs is mainly mediated by ICAM-1 expressed on ECs, in agreement with the results obtained from adhesion assays (refer to Figure 2.6 in chapter 2) and our previous study (Laurent et al., 2014).

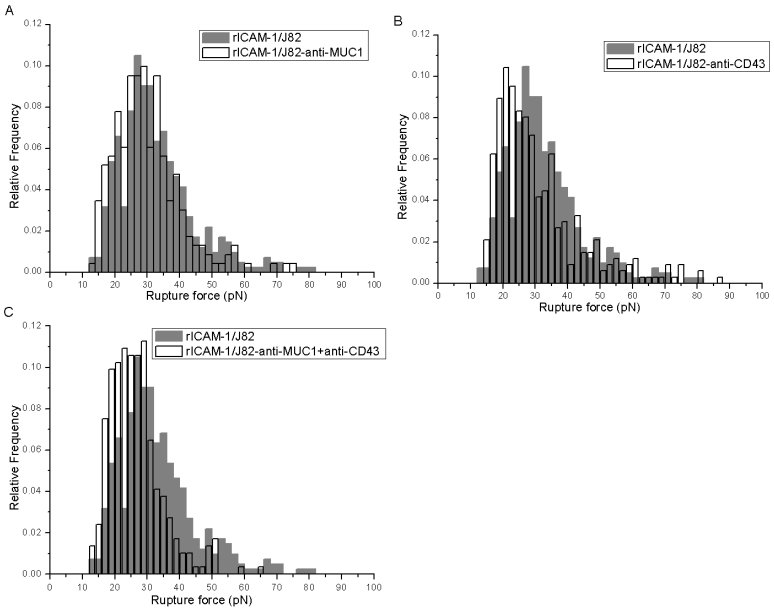

.

Figure 3.9: Quantification of J82 bladder cancer cell -rICAM-1 adhesion using SCFS when blocking MUC1, CD43 or both. Force histograms showing the distribution of rupture events for the adhesion of rICAM-1 with J82 bladder cancer cells for different conditions were obtained from force curves (applied force 500 pN, time of contact 10 s, retraction velocity 5 µm/s). Histograms obtained while (A) blocking MUC1, (B) blocking CD43 and (C) blocking MUC1+CD43 on J82 cell were compared with the control.

3.2.3 Force range involved by MUC1 and CD43 during their interaction with ICAM-1

Given the good inhibition obtained by blocking both MUC1 and CD43, we can consider that the rupture forces obtained are mainly due to the interaction between ICAM-1 (on ECs) and MUC1 or CD43 (on BCs), hence we are expecting 3 main peaks corresponding to 1) nonspecific and other interactions, 2) interaction of ICAM-1 with CD43 and 3) interaction of ICAM-1 with MUC1. To investigate the force ranges corresponding to MUC1 and CD43 during their interaction with ICAM-1, our data was analyzed using a Gaussian Mixture Model (GMM) function that identifies the subpopulations. A common approach to fix the number of gaussians is based on qualitative assessment and fitting the force histogram by changing the number of Gaussians to observe which model best fits our data (Imoukhuede and Popel, 2014; Weddell and Imoukhuede, 2014). Figure 3.10 showed that the fit obtained from three Gaussians (adjusted R-square 0.9807) represents our data better than two Gaussians (adjusted R-square 0.9745) on the HUVECs/J82 interaction force histogram. These findings from qualitative analysis also go along with our initial assumption that the force histogram obtained in the control is likely to have three subpopulations.

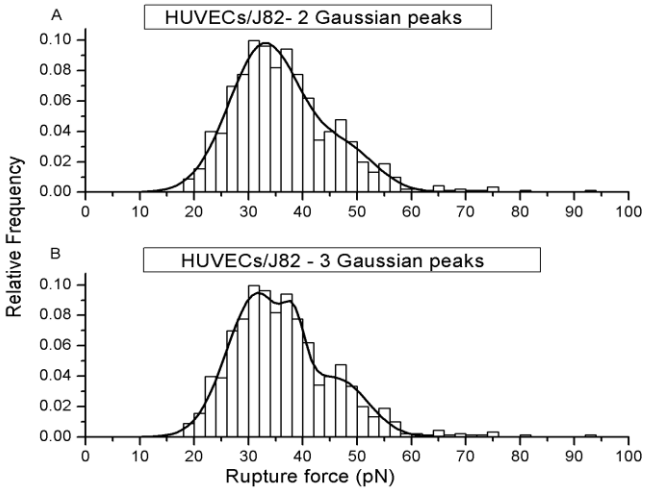

Figure 3.10: Qualitative analysis of Gaussian Mixture Model. The force histogram obtained from the adhesion of HUVEC monolayer with J82 bladder cancer cell was fitted with (A) two Gaussian model (adjusted R-square 0.9745) or (B) three Gaussian model (adjusted R-square 0.9807).

First, a tri-modal GMM function was used in our control (HUVECs/J82 cell) to identify three Gaussian peaks. The GMM analysis showed the overall probability distribution (red) and three distinctive peaks (Figure 3.11A) with mean rupture forces of ~31 pN, ~41 pN and ~50 pN (Table 3.5). The first peak at ~31 pN (green) may correspond to forces that were not mediated by MUC1 and CD43 (nonspecific interactions) in our measurements because we

already showed that forces <36 pN were unresponsive while blocking the receptors (Table 3.3). So the other two peaks at ~41 pN and ~50 pN might correspond to the interactions involving MUC1 and CD43. The specific force range corresponding to MUC1 and CD43 interactions was obtained by analyzing the force histogram obtained while blocking MUC1 or CD43. When blocking MUC1, we considered that most of the specific interactions involving MUC1 were suppressed, so the data were analyzed with bi-modal GMM to identify 2 Gaussian peaks (Figure 3.11B). The results showed a first peak (green) with a mean rupture force of ~29 pN corresponding to nonspecific interaction and a second peak (magenta) with a mean rupture force of ~43 pN that might correspond to the interaction of ICAM-1 with CD43 (Table 3.5). These results supports the idea that the second peak at ~41 pN (magenta) observed with the control (Figure 3.11A) corresponds to the interaction of ICAM-1 with CD43. Similarly, considering that most of the specific interactions involving CD43 were suppressed while blocking CD43, the data was analyzed to identify 2 Gaussian peaks (Figure 3.11C). This result also showed a first peak (green) due to nonspecific interaction at ~31 pN and a second peak (blue) with a mean rupture force of ~53 pN that might correspond to the interaction of ICAM-1 with MUC1 (Table 3.5). So the third peak at ~50 pN (blue) observed in control (Figure 3.11A) might correspond to the interaction of ICAM-1 with MUC1. The data obtained when blocking MUC1+CD43 was analyzed to identify a single Gaussian peak (Figure 3.11 D) and showed a peak (green) with a mean rupture force of ~31 pN (Table 3.5). In conclusion, the GMM analysis indicates that ICAM-1 interacts with MUC1 or CD43 with a force range centered on ~43 pN and ~53 pN respectively.

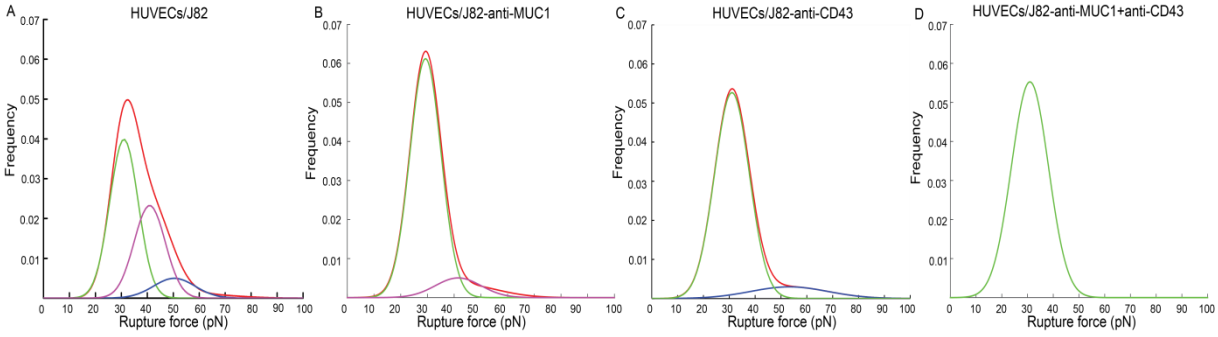

Figure 3.11: MUC1 and CD43 expressed on BCs interact with ECs with different force range. GMM function analysis on (A) control showing three different subpopulations: nonspecific interactions (green) and interaction of MUC1 (blue) and CD43 (magenta). (B) After blocking MUC1, showing two subpopulations: nonspecific interaction (green) and interaction of CD43 (magenta) and (C) after blocking CD43, showing two subpopulations, nonspecific interactions (green) and interaction of MUC1 (blue).

Substrate	J82 cell condition	Peak 1 (Green) Mean±SEM	Peak 2 (Magenta) Mean±SEM	Peak 3 (Blue) Mean±SEM
HUVECs	control	31.0±0.3	40.9±0.3	50.4±0.8
	anti-MUC1	29.3±0.2	42.9±1.4	
	anti-CD43	31.1±0.3		53.3±1.6
	anti-MUC1+anti-CD43	30.9±0.3		

Table 3.5: Force range obtained from the GMM analysis of SCFS data for the interaction of BCs with ECs. GMM analysis revealed that the interaction of CD43 is corresponds to a mean rupture force of ~43 pN and the interaction of MUC1 to a mean rupture force of ~53 pN.

3.2.4 Role of tethers on the force distribution and range

The force curves obtained by SCFS also revealed two different types of rupture events (Figure 3.7); the first type, called jump (J), is characterized by a linear increase of force before the rupture characterized by the loading rate, while for the second type, or tether (T), no force loading comes before the rupture event (i.e. it is a force plateau). Because some authors are considering only jumps in the force curves to represent the unbinding of adhesive unit (Taubenberger *et al.,* 2007; Helenius *et al.,* 2008), we analyzed the relative frequency of these events under different conditions. All rupture events preceded by a force plateau >2 µm were considered as tethers in our analysis.

The F-d curves obtained using a HUVEC monolayer as the substrate and J82 cell attached to the cantilever were analyzed and jumps and tethers in each curve were separated. The rupture forces obtained by considering only jumps were compared to force distributions obtained by considering jumps and tethers for untreated cells (Figure 3.12A), blocking MUC1 (Figure 3.12B), blocking CD43 (Figure 3.12C) and blocking MUC1+CD43 (Figure 3.12D). We did not observed significant difference in the overall force distributions. The GMM analysis of the data obtained from jumps only also showed similar force range for nonspecific interactions (~31 pN) and interactions of MUC1 (~53 pN) and CD43 (~43 pN) with ICAM-1 (Table 3.6).

Although these results indicate that the overall distribution and mean rupture force of MUC1 and CD43 are not changed much by considering tethers, further in-depth analysis revealed that for higher force ranges, the differences are not negligible. The force histogram for rupture events >40 pN were shown for control (Figure 3.13A), blocking MUC1 (Figure 3.13B), blocking CD43 (Figure 3.13C) and blocking MUC1+CD43 (Figure 3.13D). The force histogram for control shows less rupture events around 50 pN (indicated by an arrow) after removing the tether events (Figure 3.13A). Likewise, when blocking CD43, we also observed

less number of events in higher force range (>42 pN, indicated by an arrow) due to the removal of tethers. On the contrary, when blocking MUC1 and blocking MUC1+CD43 similar force distributions were obtained either in the presence or in the absence of tethers. These results indicate that removing the tether events changes the force distributions in higher force ranges especially for control and when blocking CD43 suggesting a relation between MUC1 and tether events. This relation is analyzed and discussed in the next section.

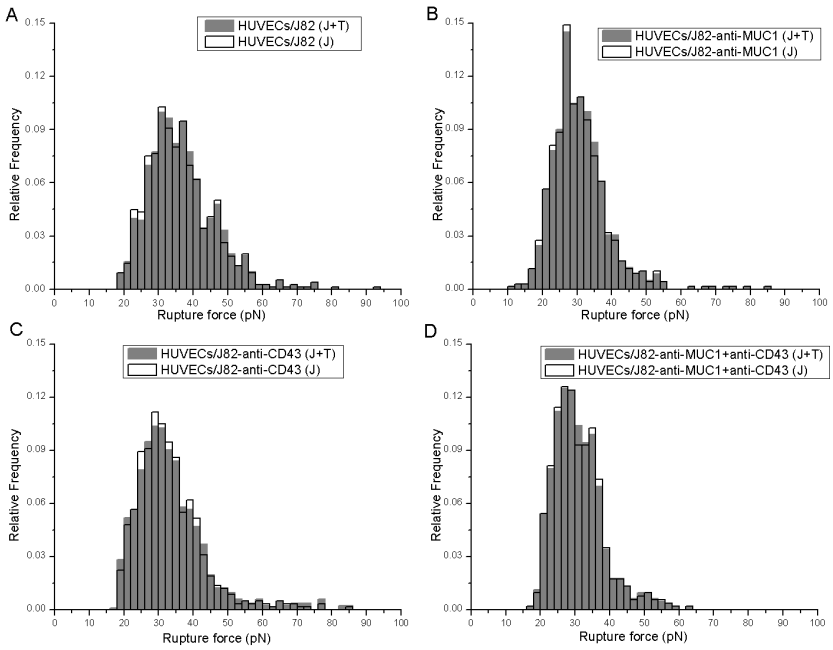

Figure 3.12: Taking into account the tethers does not alter the force distribution. Force histogram showing the distribution of rupture events for the adhesion of HUVEC monolayer with J82 bladder cancer cells for different conditions. Both jumps (J) and tethers (T) were compared with data considering only jumps. Histograms obtained while comparing (A) control, (B) blocking MUC1, (C) blocking CD43 and (D) blocking MUC1+CD43 on J82 cell were compared with the control.

Substrate	J82 cell condition	Peak 1 Mean±SEM	Peak 2 Mean±SEM	Peak 3 Mean±SEM
HUVECs	Control	30.0±0.3	39.5±0.4	53.0±1.8
	anti-MUC1	29.1±0.2	43.4±1.5	
	anti-CD43	31.0±0.3		50.4±1.8

Table 3.6: GMM analysis of SCFS data considering only jumps in the F-d curves. The GMM analysis showed that CD43 and MUC1 interact with ICAM-1 with different mean rupture forces.

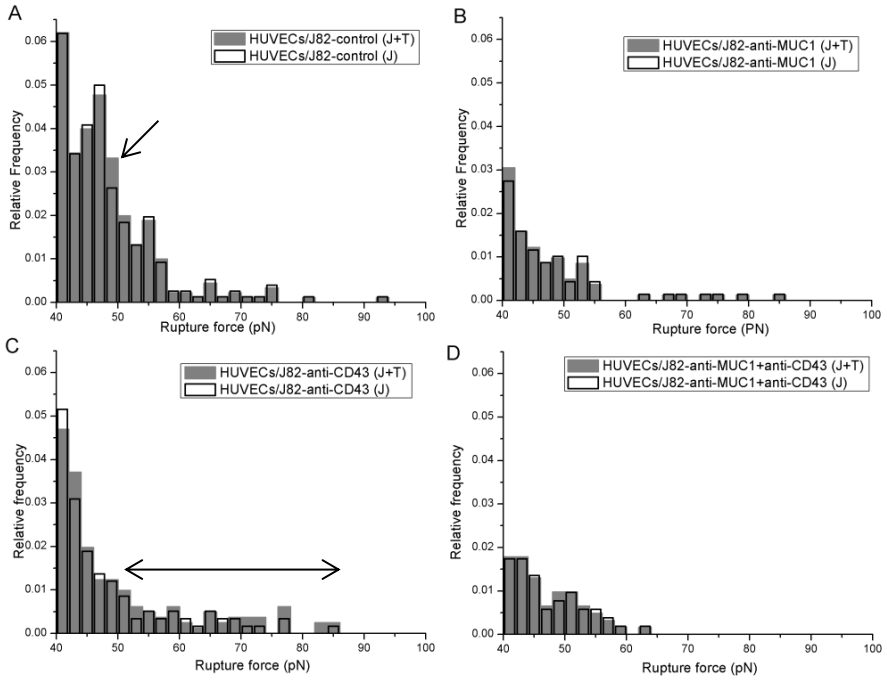

Figure 3.13: Higher force range showed some difference when removing tethers. Force histogram showing the rupture events (>40 pN) obtained from HUVEC monolayer with J82 for different conditions. The distribution obtained when considering both jumps (J) and tethers (T) were compared with jumps alone for (A) control, (B) blocking MUC1, (C) blocking CD43 and (D) blocking MUC1+CD43.

3.2.5 Attachment to the cytoskeleton is different for MUC1 or CD43

The rupture events in the F-d curves show two types of events (jumps and tethers) and it has been reported that analyzing these events can provide information on whether the receptor is connected to the cytoskeleton or not (Helenius *et al.*, 2008; Friedrichs *et al.*, 2013). Therefore, the number of jumps and tethers within the force curves were separated and analyzed under different conditions. The rupture events followed by the force plateau with a distance higher than 2 µm were considered as tethers in our analysis. Mean number of jumps or tethers per curves was obtained by dividing the total number of jumps or tethers (>36 pN) by the number of curves for each condition and the results were compared between different conditions. The analysis of the data obtained from HUVEC/J82 interactions is shown in Figure 3.14. The number of jumps decreased when blocking MUC1 or CD43 or both. The decrease in number of jumps was found non-significant when blocking MUC1 or CD43 as compared to the control (Figure 3.14A). The decrease in number of jumps showed a significant decrease ($p<0.05$) when blocking both (MUC1+CD43) as compared to the control (Figure 3.14A). The decrease in number of jumps while blocking the receptors is clearly visible in the histogram but the GLMM analysis showed non-significant difference. This

might be due to variation of number of jumps within the condition. Similar results were obtained when analyzing the number of jumps from rICAM-1/J82 under different conditions (Figure 3.15A).

The analysis of the number of tethers for different conditions revealed some interesting information (Figure 3.14A). After blocking CD43, we observed the same number of tethers as compared to the control. This result suggests that most of the MUC1 mediated interactions might be through tethers. In contrast, when blocking MUC1 and MUC1+CD43, we observed a ~64% and ~76% decrease in the number of tethers, in agreement with our early inference. Single F-d curves also showed more tethers when blocking CD43, while tether (T) events were not observed when blocking MUC1 or MUC1+CD43 (Figure 3.7B,D). These results showed that the interaction of MUC1 with ICAM-1 is mainly mediated through tethers and suggest that MUC1 on cancer cell is weakly connected to the cytoskeleton. On Figure 3.14B, Pie charts represent the relative presence of jumps and tethers for different conditions. The same proportion of jumps were observed when blocking MUC1 (~83%) as compared to control (~83%) (Figure 3.14B), on contrary when blocking CD43, the proportions of jumps decreased (~70%) indicating that CD43 might interact with ICAM-1 through jumps and CD43 on cancer cell is closely connected to cytoskeleton.

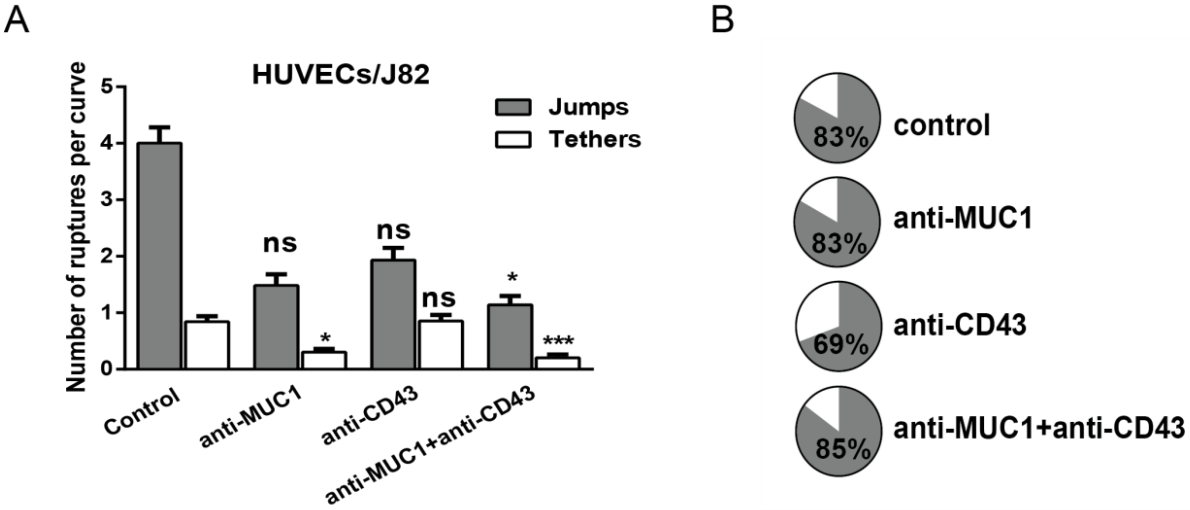

Figure 3.14: MUC1 and CD43 interact with ICAM-1 on endothelial cells through tethers and jumps: (A) Histogram showing the (Mean±SEM) number and type of ruptures (jumps and tethers) while blocking the receptors involved in the interaction using HUVECs as the substrate. GLMM (R software) was performed to check the significance with respect to the control, ***$p<0.001$, *$p<0.05$ and n.s $p>0.05$. The significance when comparing the jumps was shown in box with respect to the control. (B) Pie charts showing the relative proportion of jumps and tethers for each condition.

The analysis of the data obtained from rICAM-1/J82 is shown in Figure 3.15. The analysis of the number of tethers for different conditions showed a similar trend as compared to HUVECs/J82. After blocking CD43 (Figure 3.15A), we observed a ~34% increase in the number of tethers compared to control. When blocking MUC1 and MUC1+CD43, we observed a ~32% and ~82% decrease in the number of tethers. These results validate our early observations that the interaction of MUC1 with ICAM-1 is mainly mediated through tethers. This allows validating that the cytoskeleton of cancer cell is involved in the formation of tethers. The GLMM statistical analysis showed no significant difference between the conditions and this might be due to fewer amounts of data as compared to the HUVECs/J82 system. But qualitatively we can observe the similar trend when compared to Figure 3.15A. Likewise, from the pie chart (Figure 3.15B), we observed that the proportion of jumps slightly decreased when blocking MUC1 (63%) as compared to the control (76%), but was strongly reduced after blocking CD43 (46%), confirming that the interaction of CD43 with ICAM-1 occurs mainly through jumps.

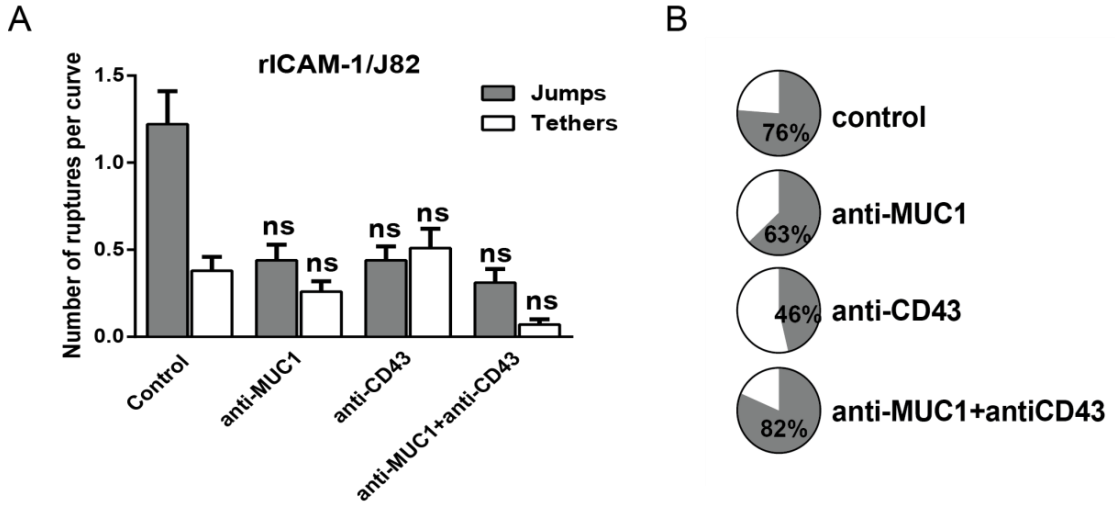

Figure 3.15: Recombinant ICAM-1 interacts with MUC1 and CD43 through tethers and jumps: (A) Histogram showing the (Mean±SEM) number and type of ruptures (jumps and tethers) while blocking the receptors involved in the interaction using rICAM-1 as the substrate. GLMM (R software) was performed to check the significance with respect to control, n.s $p>0.05$. The significance when comparing the jumps was shown in box with respect to the control. (B) Pie charts showing the relative proportion of jumps and tethers for each condition.

We also analyzed the adhesion energy obtained from F-d curves for different conditions. Adhesion energy (area under the force curve) represents the work done to stretch the cells and to break the molecules bonds and this may increase due to the presence of tethers and bonds. The mean adhesion energy was calculated for each condition and compared in

Figure 3.16, while using HUVECs or rICAM-1. The analysis showed that the mean adhesion energy decreased when blocking MUC1 or blocking both (MUC1+CD43) as compared to the control (Figure 3.16), indicating the reduced occurrence of tethers when blocking MUC1. On the contrary, the mean adhesion energy remains the same when blocking CD43 as compared to the control, indicating that blocking CD43 does not decrease tether events in the force curves (Figure 3.16). Again, the GLMM statistical analysis showed no significant difference and this might be due to high variations of adhesion energy values observed within the condition. However, we can observe the similar trend when compared to Figure 3.14A and Figure 3.15A. Taken altogether, we conclude that MUC1 on cancer cells interacts with ICAM-1 mainly through tethers and CD43 interacts with ICAM-1 through jumps.

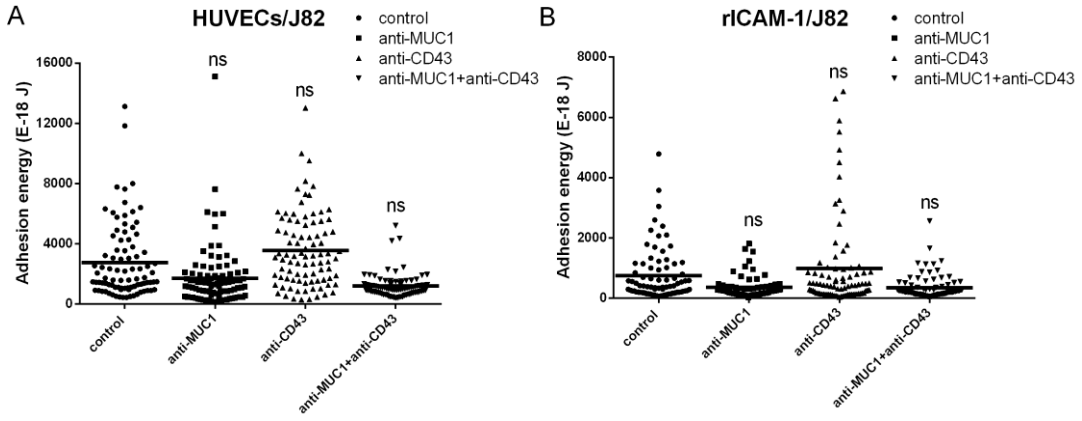

Figure 3.16: Adhesion energy obtained for different conditions. Scatter plots of the adhesion energy from each force curve with mean shown. (A) Adhesion energy obtained for the interaction of HUVEC monolayers with J82 cancer cell while blocking MUC1, CD43 or both. (B) Adhesion energy obtained during the interaction of rICAM-1 with J82 cancer cell while blocking MUC1, CD43 or both. GLMM (R software) was performed to check the significance with respect to the control, n.s $p>0.05$.

The detachment force obtained from F-d curves for different conditions while using HUVECs and rICAM-1 as substrate is shown in Figure 3.17. The detachment force is the result not only of the cell elasticity but also of the number and strength of ligand-receptor interactions. The mean detachment force was compared while blocking the receptors (MUC1 or CD43 or both) to the control. We observed that the mean detachment force decreased while blocking the receptors (MUC1 or CD43 or both) as compared to control and this decrease was found to be non-significant while using both substrates (HUVECs and rICAM-1). This might be due to high variations of detachment forces within the conditions and to fewer amounts of data.

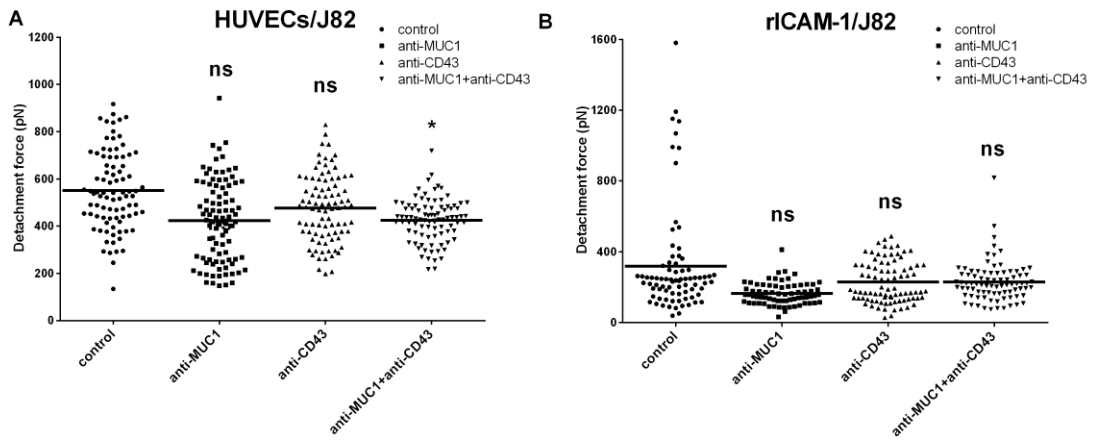

Figure 3.17: Detachment force obtained for different conditions. Scatter plots of the detachment force from each force curve with mean shown. (A) Detachment force obtained for the interaction of HUVEC monolayers with J82 cancer cell while blocking MUC1, CD43 or both. (B) Detachment force obtained during the interaction of rICAM-1 with J82 cancer cell while blocking MUC1, CD43 or both. GLMM (R software) was performed to check the significance with respect to the control, * $p<0.05$ and n.s $p>0.05$.

3.3 Discussion

SCFS has been very useful for quantifying the adhesive forces involved between cell-cell and cell-surface interactions (Taubenberger *et al.,* 2007; Fierro *et al.,* 2008). The adhesion forces involved in the interactions of leukocyte ligand (LFA-1) with ICAM-1 were studied in detail using this method (Zhang *et al.*, 2002; Wojcikiewicz *et al.*, 2003, 2006). In our previous work, we showed that ICAM-1 expressed on ECs is a key molecule in mediating the adhesion to BCs using AFM (Laurent *et al.*, 2014). We also hypothesized that MUC1 and CD43 were possible ligands expressed by BCs for mediating the adhesion with endothelial ICAM-1. In the present work, SCFS mode of AFM is applied to quantify the bladder cancer cell-endothelial cell adhesion and to unravel the different force ranges originating from the interactions of ICAM-1 with MUC1 and CD43.

SCFS studies involving cell-cell interactions were performed using HUVEC monolayers as substrate and J82 cell (invasive BCs that express strong levels of MUC1 and CD43 as compared to other cell lines) attached to a functionalized cantilever. SCFS experiments performed by blocking MUC1 and CD43 on BCs showed a significant decrease in the number of rupture events (Table 3.4) in agreement with our adhesion assays data. This quantification of rupture events from SCFS data confirmed the role of MUC1 and CD43 in bladder cancer cell-endothelial cell adhesion. We also observed that blocking MUC1 resulted in more inhibition of rupture events (>36 pN) as compared to blocking CD43, suggesting MUC1 might play a more important role in the adhesion process.

SCFS studies involving cell-protein interactions were also performed by replacing the HUVEC monolayer with rICAM-1 proteins as the substrate to specifically study the interactions mediated by ICAM-1 with the cancer cells ligands (MUC1 and CD43). This approach eliminates the other possible ligand-receptor interactions coming from the ECs. In this case we observed that the decrease in rupture events when blocking MUC1 or CD43 or both (Table 3.4) was similar to the one obtained when HUVEC monolayers were used as substrates. These results indicated that the interactions of J82 cell with ECs were mainly mediated by ICAM-1. Also, blocking MUC1 resulted in more inhibition of rupture events as compared to blocking CD43 (Table 3.4). This result validates our early inference, that MUC1 might play an important role in the adhesion process.

A GMM analysis was performed on the force histograms to unravel the force range involved by MUC1 and CD43. Through this analysis, we were able to discriminate three different force ranges, when BCs interact with ECs. The interactions that were not mediated by MUC1 and CD43 can be assigned to a mean rupture force ~30 pN (Table 3.5) definitely under 36 pN, a value in agreement with the data obtained using BSA coated substrate. GMM analysis of the force distribution when blocking MUC1 revealed that CD43 interacts with ICAM-1 with the mean rupture force ~43 pN. Similarly, GMM analysis performed on the force distribution when blocking CD43, showed that the mean rupture force of ~53 pN was involved in interaction of MUC1 with ICAM-1.

In our previous work (Laurent *et al.*, 2014), we studied the role of ICAM-1 in bladder cancer-endothelial cell adhesion using AFM. SCFS measurements were performed using normal HUVEC monolayers or HUVEC monolayers blocked with antibody specific for ICAM-1 and a J82 cell attached to the cantilever. As shown in Figure 3.18, the force histogram of normal (J82-ECs) was fitted with a double Gaussian distribution and revealed two peaks with a mean ~42 pN and ~70 pN (histogram in black). Meanwhile, the force histogram obtained when blocking ICAM-1 (J82-ECs+anti-ICAM-1) showed a single peak centered around 29 pN (histogram in red). The two peaks that were observed in the control (~42 pN and ~70 pN) disappeared when blocking ICAM-1. These results suggested that ICAM-1 interacts with at least two ligands on J82 cells with a mean rupture force ~42 pN and~70 pN and the ligands were not clearly identified in our previous study.

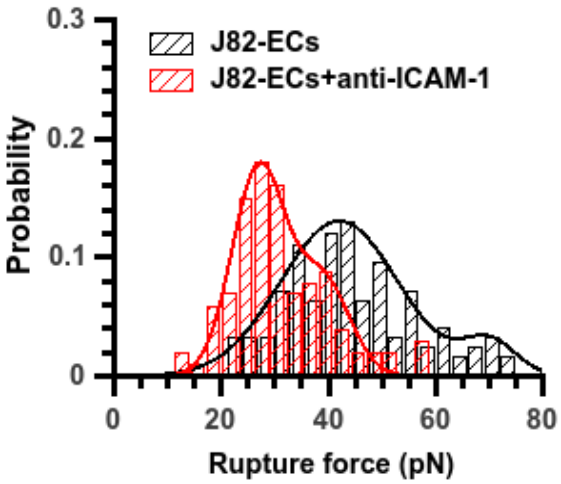

Figure 3.18: Effect of an anti-ICAM-1 antibody on Cancer-EC interactions. Rupture force distribution obtained from J82-ECs (histogram in black) and J82-ECs-anti-ICAM-1 (histogram in red) were fitted with Gaussian fits with one or two peaks revealing the presence of receptor-ligand bonds or nonspecific interactions, (Laurent *et al.*, 2014).

By correlating these results with the present study, we infer that CD43 and MUC1 are the two ligands interacting with ICAM-1. However, a slight difference in peak values was observed between both studies. This difference (~43 pN and ~53 pN in the current study *versus* ~42 pN and ~70 pN in our previous work) could be explained by the use of different parameters in both studies. In our previous study, a sampling rate of 204.8 Hz (low sampling) was used during AFM measurements. In the present work, a higher sampling rate (2048 Hz) was used to increase the resolution and to help in a better discrimination of very close rupture events like double bonds (Taninaka *et al.*, 2012; Friedrichs *et al.*, 2013). We carried out 10 times more experiments to increase our precision on mean rupture forces. Importantly, the force distributions were analyzed with a specialized GMM model to identify the mean rupture forces corresponding to the different interactions.

To see if this discrepancy between our previous study and the present work was due to the change in sampling rate or to the use of the GMM model, the data obtained from our previous study (low sampling rate 204.8 Hz) was analyzed using the GMM method. As we already guessed that there are three main interactions involved, the control data was fitted with three Gaussians. The GMM analysis showed three peaks with a mean rupture force of ~36 pN, ~46 pN and ~64 pN (Table 3.7, data in red). The first peak at ~36 pN represents the non-specific interaction and other interactions, in good agreement with the present result and with the force histogram obtained using a BSA substrate. ICAM-1 has two ligands (MUC1 and CD43) on J82 cells and blocking ICAM-1 might suppress both these interactions. Hence, the data obtained when blocking ICAM-1 was fitted with a single Gaussian and the analysis

showed a peak at ~30 pN, which corresponds to the non-specific interactions. So the peaks at ~46 pN and ~64 pN could correspond to the interaction of ICAM-1 with CD43 and MUC1 respectively. This GMM analysis on our previous data showed slightly different peak values compared to the peak values obtained in the current study. To clearly understand if this difference in the peak value arises from the use of different sampling rates, I performed some SCFS experiments to control and when blocking MUC1 and CD43 using the lower sampling rate (204.8 Hz), as in our previous study. The force histogram obtained for different conditions, control, anti-MUC1 and anti-CD43 were analyzed using the GMM. This analysis showed peaks at ~46 pN and ~60 pN corresponding to the interaction of ICAM-1 with CD43 and MUC1 respectively (Table 3.7, data in black), in agreement with the peak values obtained by GMM from our previous data (Table 3.7, Red). This strongly suggests that the differences in the peak values observed between the present work and our previous publication can be explained by the use of a different sampling rate. So higher sampling rate (2048 Hz) is recommended to distinguish the double bonds and to precisely identify the force ranges involved in ligand-receptor interactions.

Data (204.8Hz)	Substrate	J82 cell condition	Peak 1 Mean±SEM	Peak 2 Mean±SEM	Peak 3 Mean±SEM
Previous Data	HUVECs	control	36.6±1.0	46.5±1.3	64.1±1.1
		anti-ICAM-1	30.4±0.9		
Present Data	HUVECs	control	30.6±0.5	36.2±0.8	64.5±1.7
		anti-MUC1	29.1±0.4	46.7±1.9	
		anti-CD43	29.9±0.5		59.9±2.8

Table 3.7: Force range obtained from GMM analysis with low sampling rate 204.8 Hz. GMM analysis performed on our previous data (highlighted in red) and in the present data (highlighted in black) showed that MUC1 and CD43 interacts with ICAM-1 with peak value ~46 pN and ~60 pN respectively.

The force curves obtained by SCFS also revealed two different types of rupture events; the first type, called jump, is characterized by a linear increase of force before the rupture, while for the second type, or tether, no force loading comes before the rupture event (i.e. it is a force plateau). Because some authors are considering only the jumps in the force curves to represent the unbinding of adhesive units (Taubenberger *et al.*, 2007; Helenius *et al.*, 2008), we analyzed the relative frequency of these events in our data for different conditions. The rupture forces obtained by considering only jumps showed similar overall force distributions as compared to force distributions obtained by considering jumps and tethers for control as well as when blocking different receptors MUC1 or CD43 or MUC1+CD43 (Figure 3.12). GMM analysis on the data obtained by considering only jumps

also showed similar force range for nonspecific interactions and interactions of MUC1 and CD43 with ICAM-1 (Table 3.6) as compared to force range reported considering jumps and tethers (Table 3.5). These results indicated that the tether events can be considered during the analysis of ligand-receptor interactions.

It has been shown that interactions giving rise to jumps correspond to receptors attached to the cytoskeleton, and that tethers originate from receptors not or weakly anchored to the actin cell cortex (Puech *et al.*, 2005; Helenius *et al.*, 2008). This means that the relative presence of jumps and tethers in the rupture events can provide information regarding how tightly the receptors are connected with the cytoskeleton (Tulla *et al.*, 2008; Celik *et al.*, 2013; Sariisik *et al.*, 2015). In our case, a detailed analysis on the number of jumps and tethers showed that MUC1 on J82 bladder cancer cell seems to be weakly connected to the cytoskeleton as its interactions are mainly mediated through tethers. It has been reported that the cytoplasmic domain of MUC1 expressed on some breast cancer cells interacts directly with β-catenin which then binds to actin cytoskeleton through α-catenin (Yamamoto *et al.*, 1997; Li *et al.*, 1998). MUC1 also interacts with ERM proteins (erzin, radixin and moesin) that functions as membrane-cytoskeleton linkers (Bennett Jr. *et al.*, 2001). These studies indicated that MUC1 interacts with the cytoskeleton through some linkers proteins. Our results suggested that the interactions between MUC1 and the linker proteins might be weak as compared to the interaction of MUC1 with ICAM-1, thereby forming more tethers. On the other hand, we showed that CD43 could be more closely linked to the cytoskeleton and associated with the early jumps obtained on the force curve. The cytoplasmic domain of CD43 was reported to interact with the actin cytoskeleton through ERM protein linkers (Yonemura *et al.*, 1993; Serrador *et al.*, 1998). CD43 expressed on neutrophils was reported to either directly or indirectly bind microfilaments (Seveau *et al.*, 1997). These studies indicated that CD43 also interacts with cytoskeletal through linker proteins and the results obtained from our study suggest that this interaction might be stronger than for MUC1.

3.4 Conclusion

In this chapter, we analyzed the rupture events occurring during bladder cancer cell-endothelial cell interaction when blocking the receptors (MUC1, CD43 or both) using SCFS and the results clearly show that MUC1 and CD43 have an important role in bladder cancer cell-endothelial cell adhesion. The experiments comparing two different substrates HUVECs and rICAM-1 revealed that the interaction of J82 BCs with ECs is mainly mediated by ICAM-1. Through SCFS measurements and GMM analysis, we reported that CD43 and MUC1

interact with ICAM-1 with a mean rupture force of ~43 pN and ~53 pN respectively. To our knowledge, this is the first report on the force range corresponding to the interaction of MUC1 or CD43 with ICAM-1 and it is the same magnitude as the interaction of LFA-1 with ICAM-1 (Zhang *et al.*, 2002, 2006). Finally a detailed analysis of rupture events showed that MUC1 interacts with ICAM-1 mainly through tethers, whereas CD43 interacts with ICAM-1 mainly through jumps, this being related to a better attachment to the cytoskeleton in the latter case. This analysis suggested that both MUC1 and CD43 are ligands for ICAM-1 and can mediate interactions through two different processes which need to be further investigated.

Chapter 4 - Investigation of the traction stresses exerted during the transmigration of cancer cell through the endothelium

In metastasis, adhesion of cancer cells to the endothelium is followed by the transmigration of cancer cell through the endothelium. The forces involved by cancer cells during the transmigration can be studied using Traction Force Microscopy (TFM). TFM has been used to investigate the tractions in normal and cancer cell migration (Kraning-rush *et al.*, 2012; Peschetola *et al.*, 2013). Recently, this method has been applied to study the traction forces during transmigration (Rabodzey *et al.*, 2008; Liu *et al.*, 2010). In this chapter, we use TFM to study the traction stresses exerted by bladder cancer cells in contact with endothelial cells during the transmigration.

4.1 Materials and Methods

4.1.1 Preparation of polyacrylamide gels

Hydroxy-PAAm hydrogel (PAAm gel) for our experiments was prepared using the protocol of Grevesse (2013). The PAAm gel was prepared on falcon petri plates (Nunc, Saint Aubin, France). The plastic surface on the bottom of the petri dish was replaced with a glass surface that was treated with 3-(trimethoxysilyl) propyl acrylate (Sigma-Aldrich, Lyon, France) to promote strong adhesion of gels to the glass surface. 40% Acrylamide and 2% bisacrylamide solution were prepared in 50 mM Hepes and stored at 4°C. N-hydroxyethylacrylamide (N-HEA) was freshly prepared by dissolving 65 mg of N-HEA in 1 ml of 50 mM Hepes. The PAAm gel mix was prepared by mixing acrylamide, bisacrylamide, N-HEA and Hepes as mentioned in the Table 4.1. The PAAm gel mix was degassed under vacuum for 20 min. After degassing, 2.5 µl of fluorescent beads (0.2 µm, Sigma-Aldrich, Lyon, France) were mixed into the PAAm gel. The polymerization was started by adding 2.5 µl of 10% ammonium persulfate (APS) and 0.5 µl N,N,N',N'-tetramethylethylenediamine (TEMED, Sigma-Aldrich, Lyon, France). Overall the PAAm gel contains 3.2% acrylamide, 0.3% bisacrylamide and 1.3% N-HEA monomers.

Components	PAAm gel (8 kPa)
40% Acrylamide	40 µl (3.2%)
2% Bisacrylamide	75 µl (0.3%)
N-HEA	106.5 µl (1.3%)
50 mM Hepes	273 µl
Beads	2.5 µl
10% APS	2.5 µl
TEMED	0.5 µl
Final Volume	500 µl

Table 4.1: Preparation of PAAm gels (E=8 kPa)

A volume of 16 µl of this mixture was used to prepare the gel with the thickness of roughly 70 µm and it was deposited on 15 mm coverslip coated with Sigmacote (Sigmacote is a organopolysiloxane that provides hydrophobic layer on coverslip and prevents the binding of gel). The falcon petriplate with acrylate coated glass coverslip was brought down to catch the gel solution by capillary force. The PAAm gel was allowed to polymerize for 40 min and then the 15 mm upper coverslip was removed gently to obtain a gel. Finally, the PAAm gel was washed twice in PBS and stored at 4°C or used for further steps (refer to Appendix C for a detailed preparation of the solution and complete protocol).

The mechanical properties of the gels are measured by rheometry tests (Malvern rheometer, Gemini 150). Sinusoidal oscillations with a known deformation are applied within the linear regime at different angular frequencies ranging from 0.1 Hz to 10Hz. The stress response is measured and the elastic moduli (G') and viscous moduli (G'') are deduced. The elasticity is obtained using the formula E=3G'.

The rigidity of the PAAm gels was measured using a rheometer. PAAm gels with different rigidities were prepared by changing the concentration of bisacrylamide (0.1%, 0.3% and 0.6%) while keeping the concentration of acrylamide (3.2%) and N-HEA (1.3%) constant. The Young's modulus (E) is reported as the measure of rigidity (stiffness) of the gels. Young's modulus (E) of PAAm gels measured for three different concentrations of bisacrylamide (0.1%, 0.3% and 0.6%) were plotted in Figure 4.1A Young's modulus of E = 5, 8 and 28 kPa was found for the gels prepared with bisacrylamide concentration 0.1%, 0.3% and 0.6% respectively.

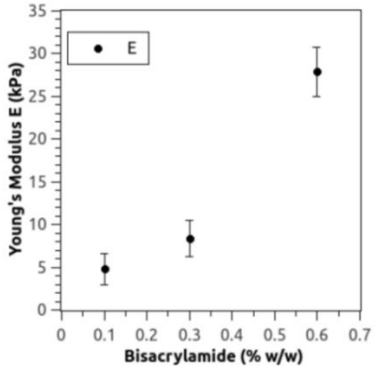

Bisacrylamide concentration (%)	E (kPa)
0.1	4.8
0.3	8.4
0.6	27.9

Figure 4.1: Young's modulus (E) is shown as a function of bisacrylamide concentration.

4.1.2 Preparation of Silicon wafer and polydimethylsiloxane microstamps

Micropatterns of 80 µm in diameter were drawn using the Inkscape software and transferred to a thin sheet of plastic (mask) as shown in Figure 4.2A. The micropatterns from the mask were transferred to the silicon wafer by soft lithography. The silicon wafer with the circular micropatterns are shown in Figure 4.2B (each circle indicates a micropattern). Microstamps were obtained by molding the silicon wafer with polydimethylsiloxane (PDMS) (Sylgard 184, silicone elastomer kit, Dow corning, Belgium) and cured for 2 h at 60°C. PDMS microstamps were obtained after curing and used for further procedures. A Cross-sectional image of the PDMS microstamp shows micropatterns of 80 µm with height 100 µm (Figure 4.2C). (See detailed protocol for silicon wafer preparation is given in Appendix C)

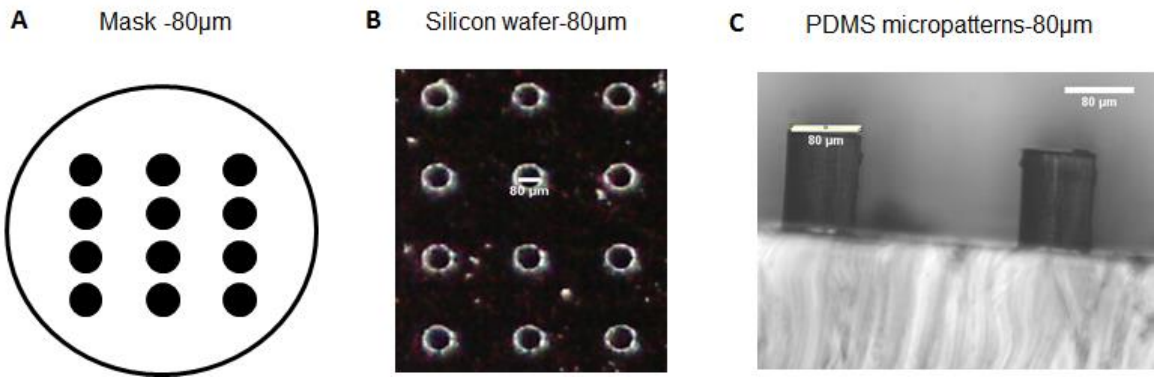

Figure 4.2: Silicon wafer and PDMS microstamps. (A) Schematic representation of mask, (B) image of silicon wafer with 80µm patterns and (C) cross-sectional image PDMS microstamp showing micropatterns of 80 µm with height 100 µm (C), Scale bar = 80µm.

4.1.3 Microcontact printing on PAAm hydrogel

The PDMS microstamp was sonicated in an ethanol: MilliQ water (1:1) mix for 15 min and dried with clean N_2 gas. The microstamp was activated using a plasma gun and then incubated with fibronectin (50 µg/ml) for 1 h. Fibronectin coated microstamps were washed twice with PBS and dried with clean N_2 gas. The PAAm gel prepared and stored in PBS (refer to section 4.1.1) was dried with clean N_2 gas and fibronectin coated microstamp was pressed gently onto the PAAm gel for 1 h. After microcontact printing, the microstamp was gently removed and the fibronectin printed PAAm gel was washed twice with PBS. The unprinted regions were passivated with a BSA solution (5 mg/ml in PBS) and incubated overnight at 4°C. After passivation with BSA, the PAAm gel was washed three times with sterile PBS and seeded with cells (refer to Appendix C for detailed protocol). It has to be noted that this step was critical and I have spent some time in optimizing the protocol to effectively transfer the fibronectin to PAAm gels.

4.1.4 Cell culture and labelling

Human Vascular Umbilical Endothelial Cells (HUVECs) were purchased from Promocell (Heidelberg, Germany) and grown on culture dishes coated with 100 µg/ml collagen I (BD Bioscience, Le Pont de Claix, France) in complete endothelial growth medium (Promocell) supplemented with 1% antibiotic/antimycotic mix. HUVEC cells were labeled with Cell Trace Far Red dye (Thermo Fischer, Courtaboeuf, France) in endothelial growth medium without supplements. HUVECs were detached using Trypsin-EDTA (Sigma-Aldrich, Lyon, France) and centrifuged. The pellet was resuspended in 1 ml of Cell Trace Far Red (30 µM concentration) and incubated at 37°C for 30 min. After incubation, 4 ml of complete medium was added to remove the unlabeled dye and centrifuged (1200 rpm/5 min). The pellet

was recovered in complete endothelial growth medium and seeded on the PAAm gel. HUVECs were allowed to adhere on the patterns by incubating at 37°C for 3-4 h. After incubation, the PAAm gel was rinsed with PBS to remove the unbound cells. Finally, a complete medium with tumor necrosis factor α (TNF-α, 10^2 TU/ml) was added to endothelial cell monolayers on PAAm gels and incubated overnight at 37°C. TNF-α was used to stimulate the expression of ICAM-1 on the surface of HUVECs. HUVECs subcultures from passage 2-6 were selected for our experiments. Cultures were grown at 37°C in a 5% CO_2 humidified atmosphere. Before imaging, fluorescent T24 bladder cancer cells (BCs) labelled with life-act GFP were added and incubated for 30 min to allow T24 cancer cells to adhere to the endothelial cell monolayers. After incubation, the PAAm gel was rinsed to remove unbound BCs and imaged (refer to Appendix C for a detailed protocol).

4.1.5 TFM imaging

The endothelial cell monolayer with one cancer cell was selected and followed in time using laser scanning confocal microscopy (Zeiss, LSM, Germany). The microscope was equipped to maintain 37°C and to supply 5% CO_2 for the cells during the measurements. Three lasers of different wavelengths were used to obtain the signals from T24 cancer cell (GFP), endothelial cell monolayer (Far red dye), fluorescent beads (red) and the images were recorded. Time lapse imaging was performed to follow the movement of T24 cancer cell, endothelial cell monolayer and beads on the surface of the PAAm gel. The relaxed position of beads was obtained at the end of the experiment after detaching the cells from the PAAm gel using Trypsin-EDTA. The data obtained from the confocal microscope were preprocessed with ImageJ (NIH, USA) and traction fields were computed in MatLab as described below. For this part, gel preparation, imaging and analysis was performed by me making use of the program to compute traction stresses that has been already used in our team in LIPhy. The program uses the Matlab code coupled with fortran and this code is constantly improved by Richard Michel for specific applications.

4.1.6 Data treatment

4.1.6.1 Determination of the displacement fields

The displacements of beads were extracted from the stack of images using ImageJ (NIH, USA). The first image of the stack corresponds to the beads in the relaxed position followed by images of gel deformed under cell tractions. The images were corrected for relative translational shifts using the StackReg plug-in (ImageJ). This plug-in was used to

align a stack of images. Each image is used as a template with respect to which the next slice is aligned. The aligned stacks of images were processed with the Particle Tracker plug-in (ImageJ). The plug-in implemented point detection and a tracking algorithm as described previously (Sbalzarini and Koumoutsakos, 2005). First, the beads in each image were localized using three parameters: radius, cut off and percentile (Figure 4.3). Then, the localized beads were linked into trajectories using two parameters, link range and displacement (Figure 4.3). The linking algorithm identifies centers corresponding to the same beads in subsequent frames and links these positions into trajectories. The contours of the HUVEC monolayer and BCs were obtained using ImageJ.

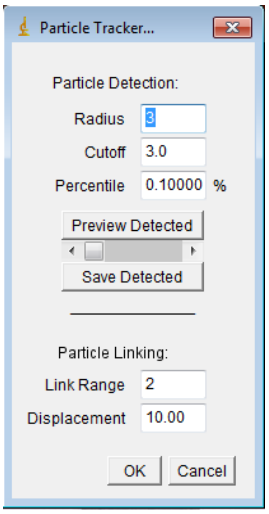

Figure 4.3: Particle detector plug-in with default values, ImageJ.

4.1.6.2 The Adjoint Method

Traction forces exerted by a cell were computed from the beads displacements using the adjoint method proposed by Ambrosi (Ambrosi *et al.*, 2009; Michel *et al.*, 2013). This method solves an inverse problem for computing the traction forces from the known displacements at the gel surface.

Let Ω be the whole domain and $\mathbf{u(x)}$ is the displacement vector field in a subset of the domain $\Omega_0 \subset \Omega$, where beads are located. The target function $\mathbf{u_0(x)}$ has support in Ω_0. The shear stress is exerted only on the portion of the region covered by the cell and this subdomain corresponds to $\Omega_c \subset \Omega$ (Figure 4.4). It is considered that the measured displacement $\mathbf{u_0}$ corresponds to beads located only at the surface of the gel. So the displacements at the bottom of the gel are considered to be zero. This method also considers that the stresses are zero outside the cell domain. It has to be noted that the micropatterned endothelial cell monolayers provide us traction free boundaries for the computation.

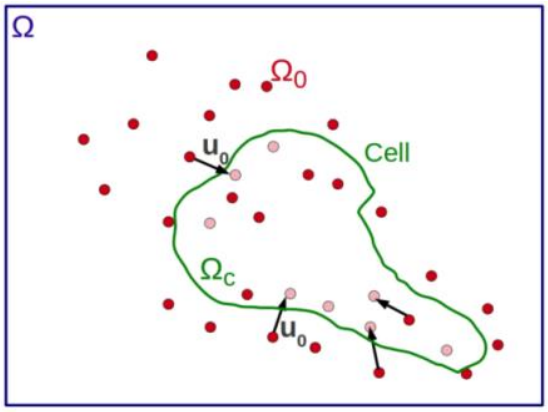

Figure 4.4: The domain Ω of the elasticity equation contains the subdomain Ω_c, the area covered by the cell and where the force is applied. The subdomain Ω_0 represents the locus of the beads where displacements are known.

The system of equations is solved using the finite element method to compute the stresses and the displacements. This method builds a mesh (with triangular elements) in order to solve the equations. The functional $J_\varepsilon = \|\mathbf{u}_\varepsilon - \mathbf{u}_0\|^2 + \varepsilon \|\mathbf{T}_\varepsilon\|^2$ measures the difference between the displacement field $\mathbf{u}_\varepsilon$ produced by $\mathbf{T}_\varepsilon$ and the experimental one $\mathbf{u}_0$. The regularization parameter ε (epsilon) is used to balance the difference. The choice of epsilon is a critical step to yield an accurate approximation of the stress field. The correct value for epsilon is chosen from the L-curve which is drawn for the range of known epsilon usually from 10^{-9} to 10^{-5} with 5 points per decade. The L-curve is obtained by plotting the stress norm $\|\mathbf{T}_\varepsilon\|$ versus the residual norm. A typical L-curve obtained from the analysis is shown in Figure 4.5. The L-curve describes the influence of ε on the stress field. Low values of epsilon lead to high values of the stress norm. On the contrary, when epsilon increases $\|\mathbf{T}_\varepsilon\|$ decreases but the error increases. In the region of higher curvature, the stability of $\|\mathbf{T}_\varepsilon\|$ and the small error are well balanced. So, the range of epsilons near the maximum curvature point is considered as the optimal value for regularization. In the L-curve shown in Figure 4.5, the optimum range of epsilon is marked and found to be around 10^{-8}.

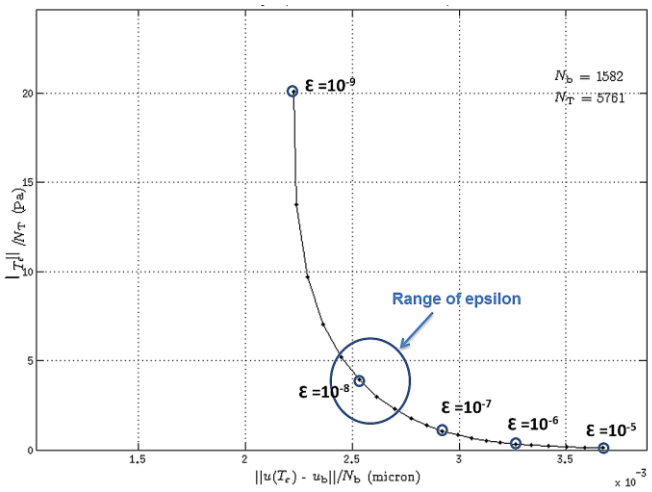

Figure 4.5: L-curve obtained from the analysis. The stress norm $||\mathbf{T}_\varepsilon||$ versus error $||\mathbf{u}_\varepsilon - \mathbf{u}_0||$ for a range of epsilon from 10^{-9} to 10^{-5} is plotted. The optimum range of epsilon near the maximum curvature is marked in light blue.

These epsilon values can also be verified from the plot J_ε as a function of log10(ε) as shown in Figure 4.6. The minimum values of the curve are selected as the optimum range of epsilon. In the plot shown, the minimum value is found to be around 10^{-8} as marked (circle). So the L-curve and minimization of J_ε suggest that epsilon values around 10^{-8} are optimal.

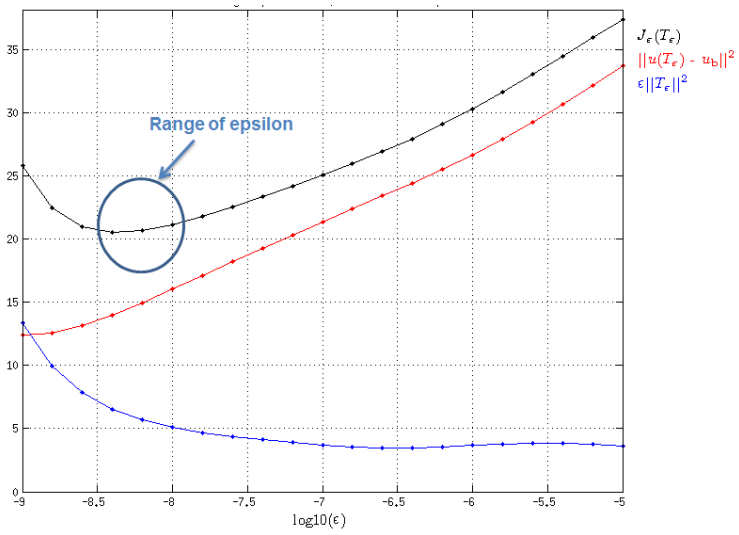

Figure 4.6: Minimization of the functional J_ε. The residual norm $||\mathbf{u}_\varepsilon - \mathbf{u}_0||^2$ (red), $\varepsilon\,||\mathbf{T}_\varepsilon||^2$ (blue) and functional J_ε (black) are plotted versus log10 (ε). The optimum range of epsilon is obtained from the plot of J_ε versus log10(ε) which corresponds to the minimum of the curve (marked in light blue).

To find a better estimate of the stresses, we used the following technique. The stress vectors corresponding to a range of epsilon near the maximum curvature point are carefully

checked. For small ε, the stress vectors point in all directions in an irregular manner (Figure 4.7A). Then as epsilon is increased, a rearrangement of the vectors orientation takes place and the direction of stresses become stable (Figure 4.7B). As epsilon is further increased, the vector patterns become over-regularized as the stress norm decreases (Figure 4.7C). Thus the optimum value of epsilon is chosen as the first ε value leading to a stabilized orientation of the directions of the stress vectors (Figure 4.7B).

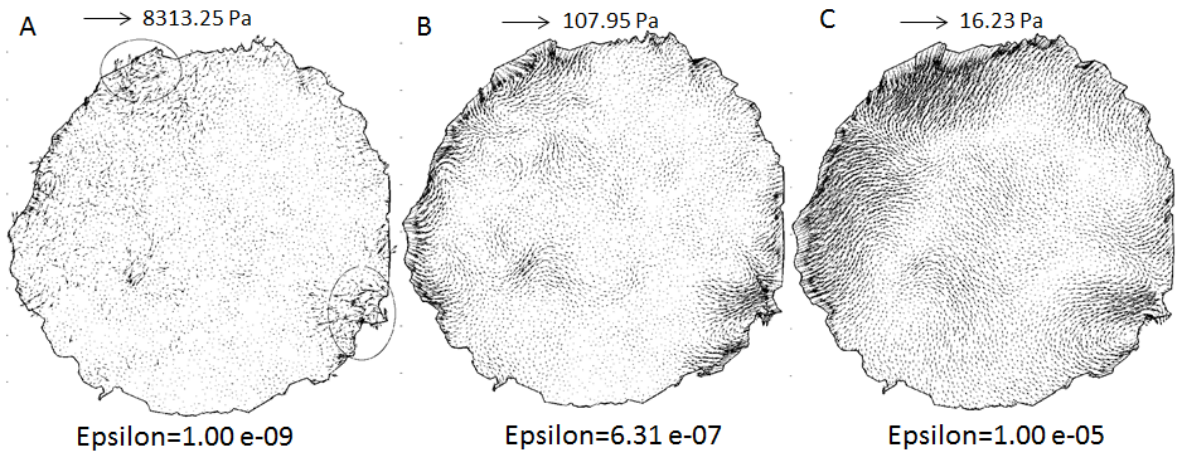

Figure 4.7: Traction vectors obtained for different values of ε. The maximum stress (Pa) is indicated by an arrow.

After visualizing the stress vectors, ε = 6.31 e-07 was chosen and finally, the traction map for the corresponding epsilon (Figure 4.8) could be analyzed to identify the maximum stress value and stress at different locations on the monolayer. Important steps involved in TFM imaging and analysis is presented in Figure 4.9.

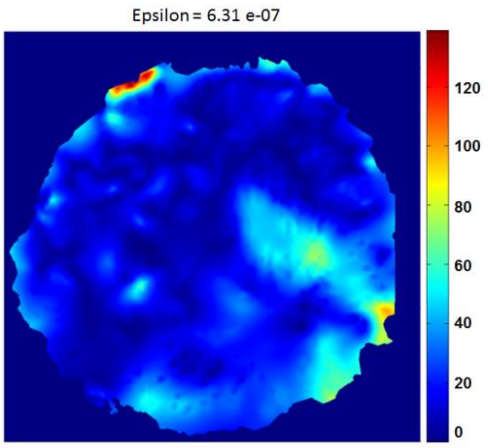

Figure 4.8: Traction map for the selected epsilon (ε = 6.31 e-07). The color bar indicates the range of traction stresses in Pa.

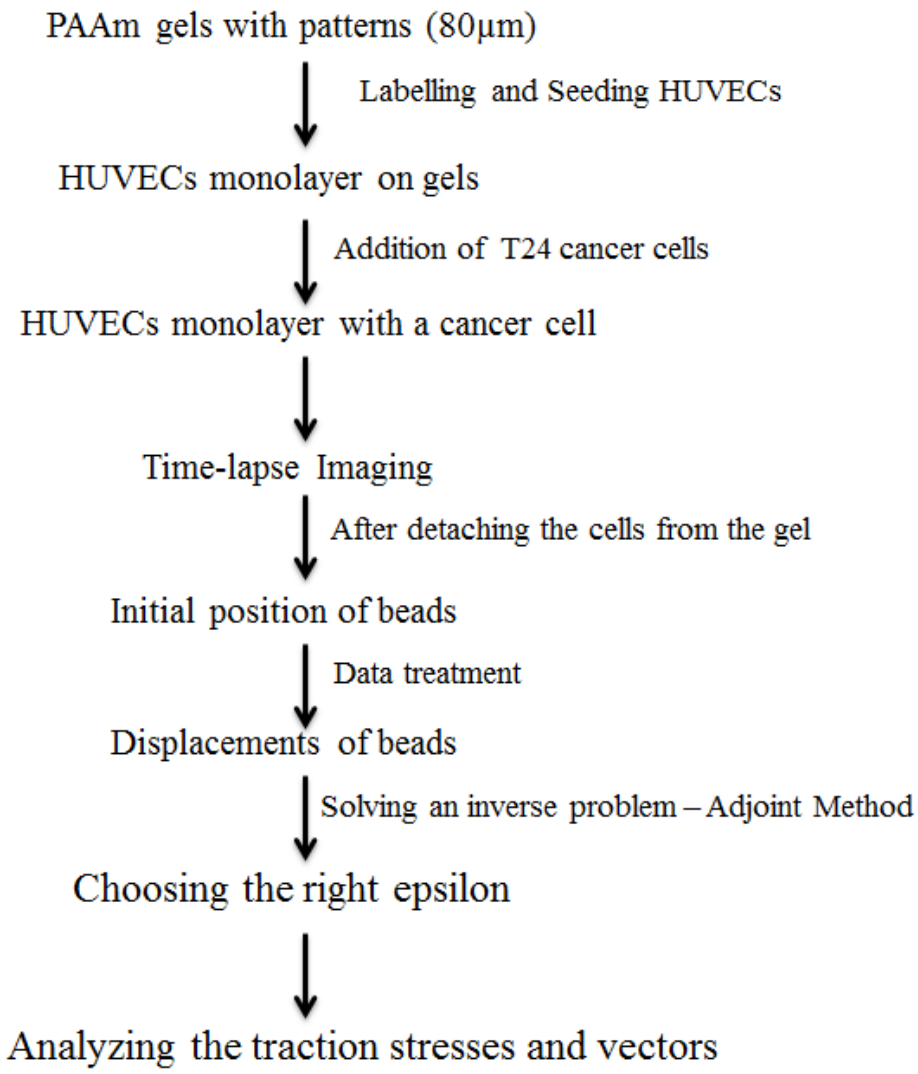

Figure 4.9: Steps involved in TFM imaging and analysis. Flow diagram explains the important steps involved in the gel preparation, TFM imaging and analysis.

4.2 Results

Time-lapse microscopy was performed to follow the migration of T24 cancer cells on an endothelial cell monolayer. Then, the traction stress maps and vectors were computed from the displacement of beads and by solving the inverse problem using the Adjoint method.

4.2.1 Traction stresses exerted by the endothelial cell monolayer

We first characterized the traction stresses exerted by the endothelial cell monolayer in the absence of cancer cell. The endothelial cell monolayer was followed in time and the images were recorded with a temporal resolution of 8 min for duration of approximately 1 h As discussed in the section 4.1.6.1 and 4.1.6.2, we determined the beads displacements and then solved an inverse problem to compute the traction stresses exerted by the endothelial cell

monolayer. Epsilon = 2.51 e-07 was chosen based on the L-curve criterion. The traction stresses corresponding to epsilon = 2.51 e-07 were analyzed at different times.

The confocal image of the endothelial cell monolayer on micropatterned PAAm gels (E = 8 kPa) is shown in Figure 4.10A. We observed 16 endothelial cells in the monolayer. The maps of traction stresses obtained at three different time points (t=0, t=32 min, t=56 min) are shown in Figure 4.10B-D. Traction stresses exerted by the endothelial cell monolayer are indicated by the color bar. By comparing the traction maps at different time points, we observed that the value of traction stresses exerted by the endothelial cell monolayer was approximately 60 Pa. From Figure 4.10B-D, it can be noted that there are few regions on the traction maps that exhibit higher traction stresses ~200 Pa (indicated as red in the traction maps). We hypothesize that these regions correspond to stronger adhesion exerted by the endothelial cell monolayer to the PAAm gel.

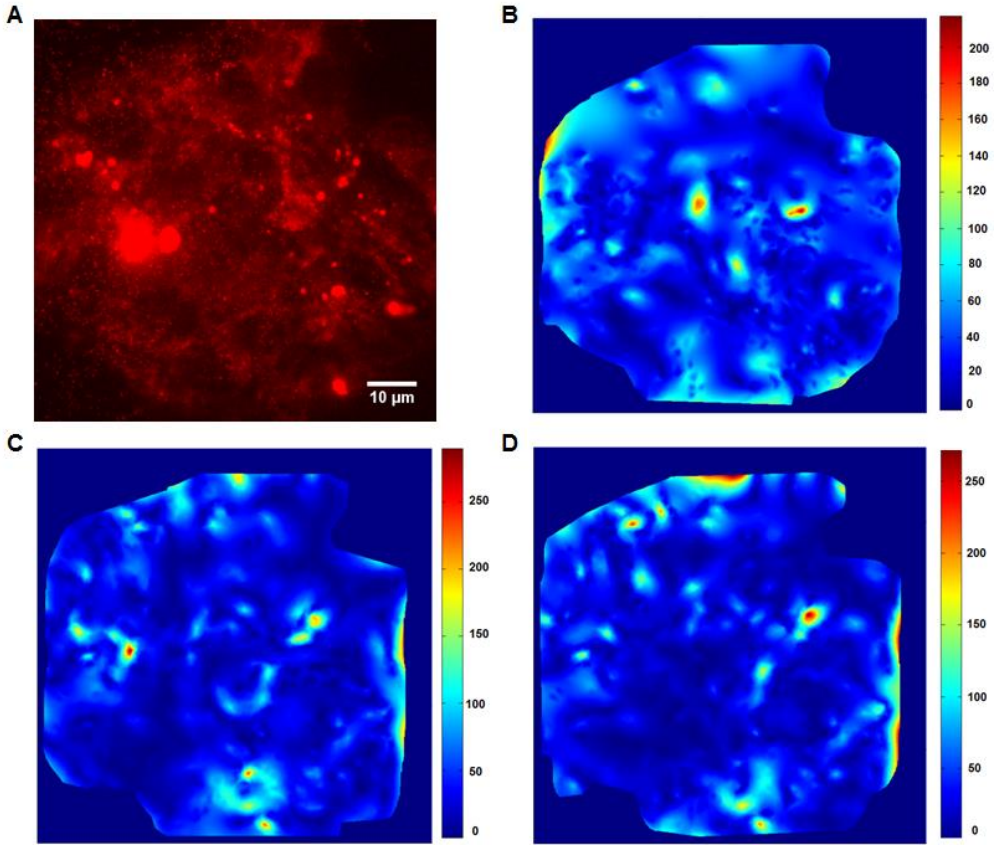

Figure 4.10: Traction stresses exerted by an endothelial cell monolayer. (A) Image of an endothelial cell monolayer on 80 µm circular micropattern, (B) tractions exerted by the endothelial cell monolayer at t=0 min, (C) t=32 min and (D) t=54 min. Scale bar = 10µm. The color bars indicate the range of traction stresses in Pa. Note that the scale of the color bar is adjusted with respect to the minimum and maximum stresses in each frame.

4.2.2 Traction stresses exerted during bladder cancer cell transmigration

An endothelial cell monolayer with aT24 bladder cancer cell was followed in time and images were recorded with a temporal resolution of 8 min for 2 h. The endothelial monolayer comprised of 12 endothelial cells. The images were analyzed to calculate the traction stresses exerted by cancer cells and the endothelial cell monolayer during transmigration. We determined the beads displacement and then solved an inverse problem as discussed before. Epsilon = 6.31 e-07 was chosen in this case and the traction stresses and vectors corresponding to epsilon = 6.31 e-07 were obtained for different time points. The same ε was kept because it was in the good region of the L-curve for all times.

Three time points corresponding to 1) beginning of the experiment (t=0), 2) transmigration of a cancer cell through the endothelial cell monolayer (t=64 min), spreading of a cancer cell on the substrate (t=72 min) and 4) end point of the experiment (t=112 min) are discussed in details. The confocal image of the endothelial cell monolayer (red) with one cancer cell (green) is shown in Figure 4.11A. An x-z slice was made through the endothelial cell monolayer with the cancer cell on the top as indicated by a blue line in Figure 4.11A. Figure 4.11B shows the cross-sectional view with the cancer cell (green), HUVEC (red) and the bottom of the PAAm gel (substrate). Similarly, the same is shown for times t = 64 min, t=72 min and t = 112 min.

At t =0 (beginning of the experiment), the cross-sectional image (Figure 4.11B) showed that the cancer cell was on top of the endothelial cell monolayer and it was not in contact with the substrate. Due to the weak fluorescence signal by labelled endothelial cells, their visualization is not clear. The contour of the cancer cell was superposed onto the map of traction stresses and vector fields to analyze and follow the stresses around the cancer cell during the process of transmigration. At this point, the traction map showed maximum value of the stresses of approximately 56 Pa. The traction map also indicated that the areas around the cancer cell showed less stresses with a mean value of 20 Pa.

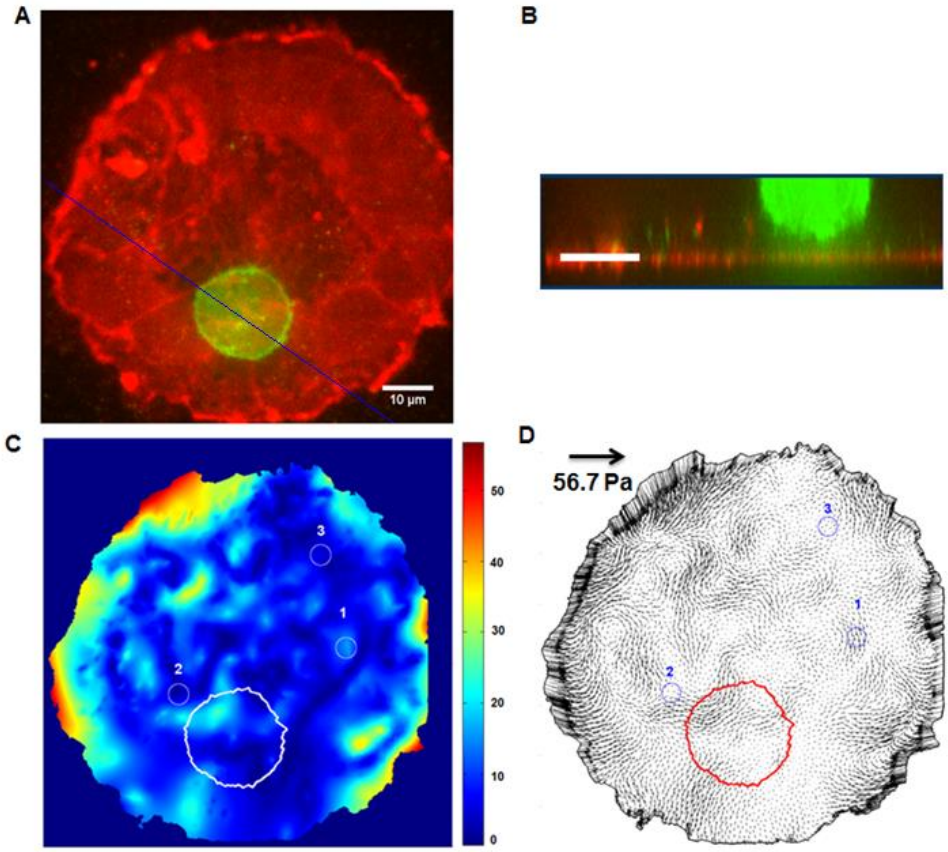

Figure 4.11: Traction stresses at the beginning of the experiment. (A) Image of an endothelial cell monolayer (red) with one cancer cell (green), (B) cross-sectional image of the monolayer, (C) map of traction stresses with contour of cancer cell in white and color bar for traction stresses and (D) vector field map with contour of cancer cells in red. Scale bar = 10µm.

By following the cancer cell on the endothelial cell monolayer, the transmigration phenomenon was observed at t=64 min. The cross-sectional view (Figure 4.12B) showed that the cancer cell comes in contact with the substrate after transmigration through the monolayer. We observed that the cancer cell is transmigrating through endothelial cells junctions (marked in yellow) as shown in Figure 4.13A. The opening of endothelial cell junctions is measured by calculating the distance between two endothelial cells (1 and 2) in time. As shown in Figure 4.13B the endothelial cell monolayer remained intact during the first 40 min and then the distance between the endothelial junctions increased during imaging. Higher values of traction stresses (70 Pa) are observed at the transmigration (location-2) as shown in Figure 4.12C. This higher stress region is also observed at early time points, so we cannot consider that the stresses correspond to the tractions exerted by cancer cells during transmigration. But, we hypothesize that these localized stresses might be due to the reorganization of neighboring endothelial cells during the transmigration process. The other locations in the monolayer showed tractions stresses with mean of approximately 20 Pa.

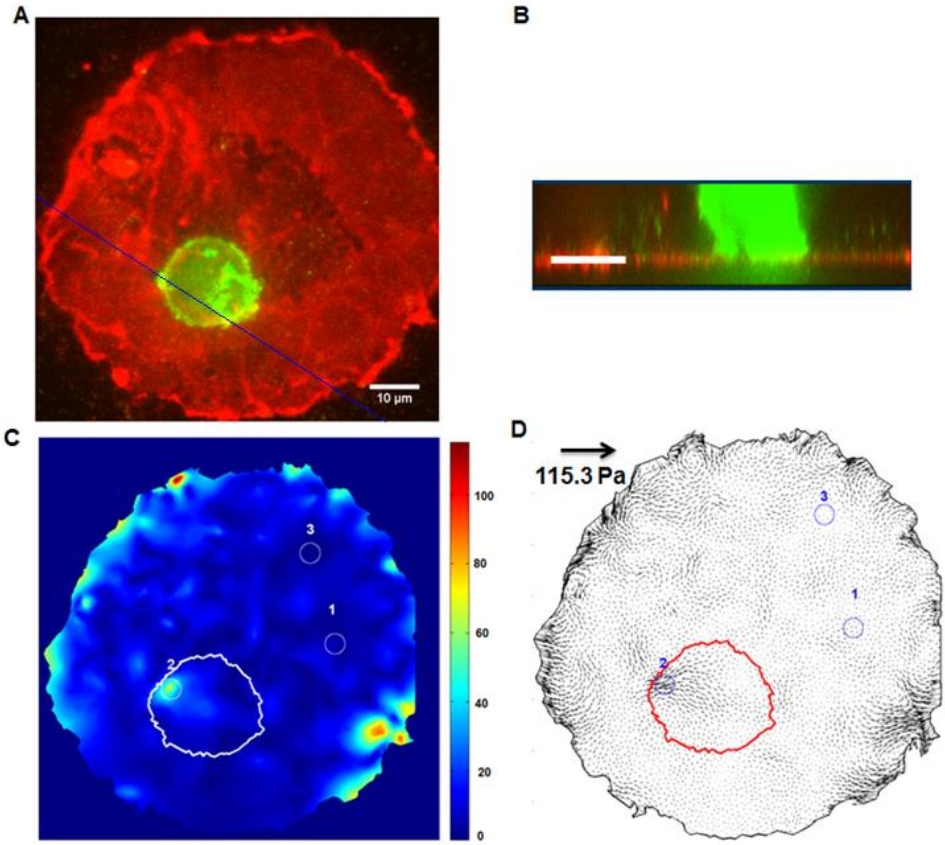

Figure 4.12: Transmigration of a cancer cell through the endothelial cell monolayer. (A) Image of an endothelial cell monolayer (red) with one cancer cell (green), (B) cross-sectional image of the monolayer, (C) map of traction stress with cancer cell contour in white and color bar for traction stresses and (D) vector field with cancer cells contour in red. Scale bar = 10 µm.

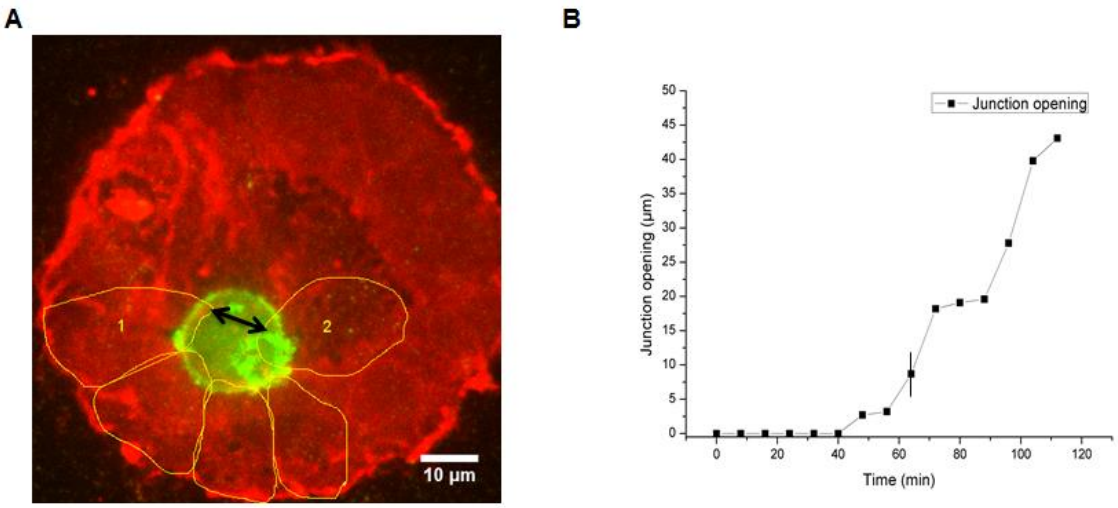

Figure 4.13: The cancer cell transmigrates through the endothelial junctions. (A) Image of an endothelial monolayer (red) with endothelial cells near the cancer cell (green) marked in yellow , (B) opening of junctions measured between endothelial cells (1 and 2 marked with arrow) over time. The black line indicates the current time point. Scale bar = 10 µm.

After transmigration, the cancer cell adheres and spreads on the gel substrate as shown in Figure 4.14A and 4.14B. Higher traction stresses (60 Pa) were observed at some locations on the edges of spreading cancer cell which corresponds to tractions exerted by the cancer cell on the substrate during spreading in Figure 4.14C. These higher stresses might correspond to tractions exerted by cancer cell on the substrate.

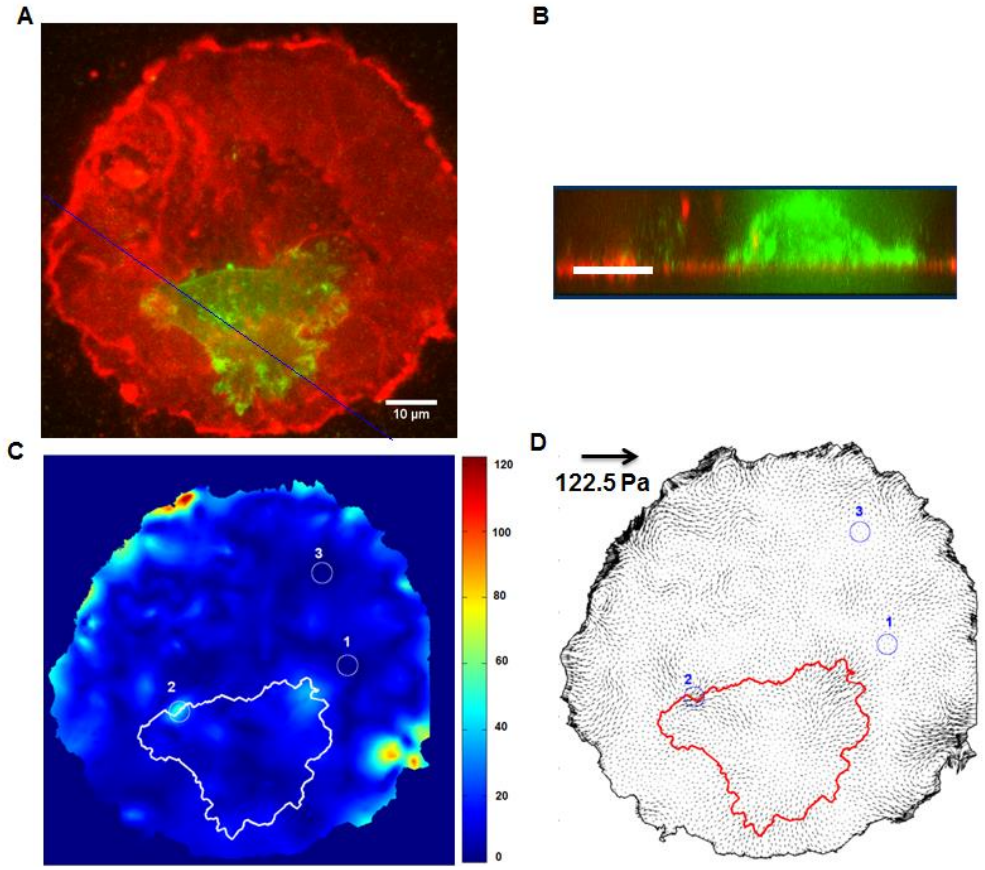

Figure 4.14: Spreading of a cancer cell on the substrate. (A) Image of an endothelial cell monolayer (red) with one cancer cell (green), (B) cross-sectional image of the monolayer, (C) map of traction stresses with contour of cancer cell in white and color bar for traction stresses and (D) vector field map with contour of cancer cells in red. Scale bar = 10µm.

The cancer cell spread on the gel substrate is shown in Figure 4.15A and 4.15B. Higher traction stresses were exerted at the edges of cancer cell (Figure 4.15 C) which was in direct contact with the substrate as shown on the confocal image in Figure 4.15B. These stress values correspond to the tractions exerted by the cancer cell on the substrate with the maximum value of approximately 125 Pa. Vectors field maps indicated that pulling forces were applied where the cancer cell is in contact with the substrate (Figure 4.15D).

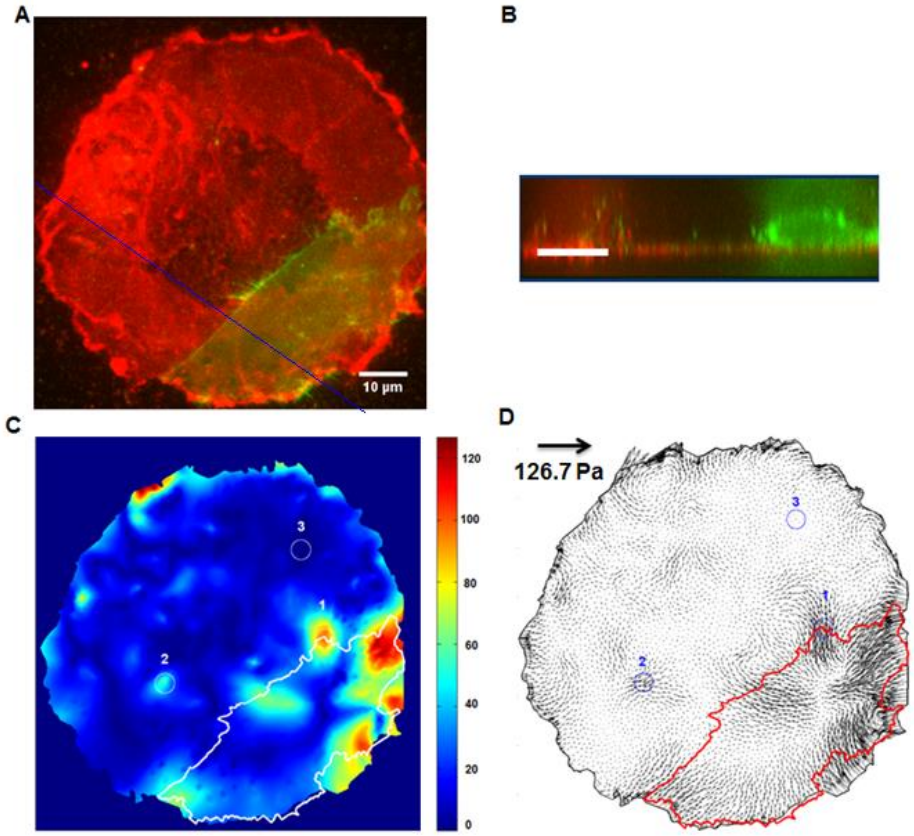

Figure 4.15: Tractions exerted a by cancer cell on the substrate. (A) Image of an endothelial cell monolayer (red) with one cancer cell (green), (B) cross-sectional image of the monolayer, (C) Map of traction stresses with cancer cell contour in white and color bar for traction stresses and (D) vector field with contour of cancer cells in red. Color bar indicates the range of traction stress. Scale bar = 10 µm.

The maximum values of traction stresses at three different locations indicated on traction map (1, 2 and 3) were obtained and plotted versus time (Figure 4.16). Traction stresses measured at location-1 remained constant at around 20 Pa for 70 min and then the increase in traction stresses was observed during the contact and spreading of cancer cell on the substrate to a maximum of 120 Pa.

In location-2, traction stresses increased initially from 20 Pa to 65 Pa and remained in the range of 60 Pa. These stresses might have been exerted by the endothelial cells that were in contact with the gel. After transmigration of the cancer cell, the traction stresses decreased to around 50 Pa as shown in Figure 4.16. The point of transmigration of cancer cell through the endothelial monolayer is indicated by a black line in Figure 4.16.

Traction stresses exerted by the endothelial cells (location-3) that were located far from the cancer cell remained almost constant with the value of approximately 20 Pa.

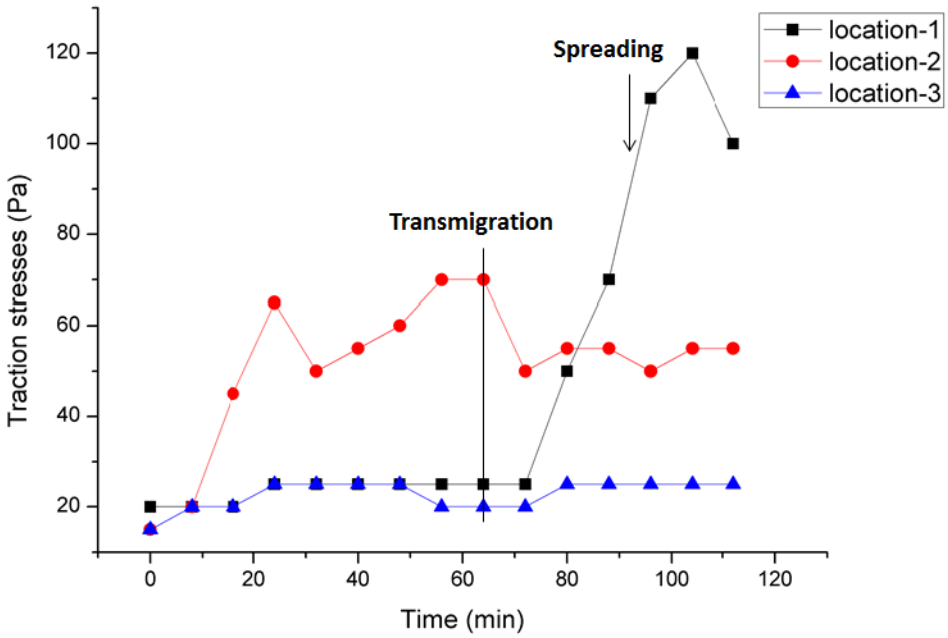

Figure 4.16: Evolution of the traction stress at three different locations. The time point corresponding to the first contact of the cancer cell with the substrate is indicated by a black line. The plot also shows the range of traction stresses during transmigration and spreading of cancer cell.

Transmigration of another cancer cell through the endothelial cell monolayer was also observed in another experiment as shown in Figure 4.17. Eleven endothelial cells were observed in the monolayer. An endothelial cell monolayer (magenta-to visualize the endothelial cell clearly) with a cancer cell (green) was followed in time and the images were recorded with a temporal resolution of 10 min for one hour. The x-z slice was made through the endothelial cell monolayer with cancer cell on the top as indicated by a blue line in Figure 4.17A for each time point. The cross-sectional view at different time points was shown in Figure 4.17B. Transmigration of the cancer cell through the endothelial cell monolayer was observed first at t=10 min (indicated by an arrow) and followed as shown in Figure 4.16B. Traction stresses were not computed for this image because the endothelial cells started retracting during the imaging.

These are the results obtained from our preliminary experiments. Further experiments need to be performed to investigate the traction stresses exerted by cancer cells and the endothelial cell monolayer during transmigration.

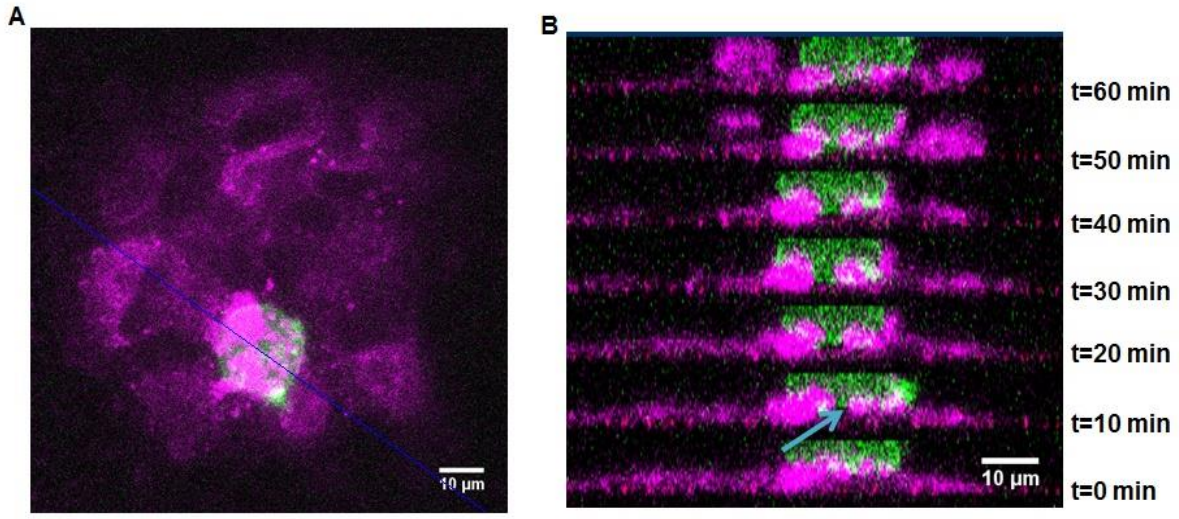

Figure 4.17: Cancer cell transmigrate through the endothelial monolayer. (A) The confocal image of endothelial monolayer (magenta) with a cancer cell (green) and (B) cross-sectional image of the monolayer at different time points.

4.3 Discussion

Polyacrylamide gel based Traction Force Microscopy has been used to study the tractions exerted by normal and cancer cells during the adhesion and migration (Dembo and Wang, 1999; Munevar *et al.*, 2001; Reinhart-King, 2008; Kraning-rush *et al.*, 2012; Peschetola *et al.*, 2013). After the development of micropatterning techniques, PA gels with adhesion islands of controlled size and shape aids us to better understand the role of the microenvironment (Théry, 2010; Rape *et al.*, 2011; Tseng *et al.*, 2011; Grevesse *et al.*, 2013; Polio and Smith, 2014).

Transmigration is an important process in cancer metastasis and this occurs through several ways: (a) cancer cell may migrate through the endothelial cell body, (b) cancer cells may migrate through the endothelial cell-cell junctions without destroying the integrity of the endothelial monolayer, (C) cancer cells may induce apoptosis in endothelial cells and (d) cancer cells may create holes in endothelial monolayer (Mierke *et al.*, 2008; Hamilla *et al.*, 2014). It has been reported that most of cancer cells transmigrate through the endothelial cell junctions and that the monolayer reseals and remains intact after transmigration. Also, the neighboring endothelial cells remain healthy without showing membrane blebbing, cell shrinkage and rounding (Mierke *et al.*, 2008). Hamilla et al. reported an additional step during cancer cell transmigration called incorporation. In this phase, cancer cells physically displace the endothelial cells and get incorporated between them. It has been reported that approximately 25% of the endothelial cells detached after the incorporation of cancer cells

and in other cases the endothelial cells remained intact (Chotard-Ghodsnia *et al.*, 2007; Hamilla *et al.*, 2014). Another study involving the transmigration of melanoma cancer cells also reported that melanoma cells can incorporate into the endothelial cell monolayer during transmigration (Onken *et al.*, 2014).

Traction forces exerted during the transmigration of neutrophils and monocyte through the endothelium have been studied using PDMS micropillar substrate (Rabodzey *et al.*, 2008; Liu *et al.*, 2010). Rabodzey et al. studied the force exerted by the neutrophils when they transmigrated through the endothelial cell-cell junctions. They reported that the traction forces increased by approximately 3 folds during the transmigration of neutrophils at cell-cell junctions and endothelial cells resealed after transmigration. They also reported that the traction forces during transmigration increased with respect to the rigidity of the substrates (Rabodzey *et al.*, 2008). The study involving the transmigration of monocytes through the endothelium reported that the average traction forces of the monolayer increases during the adhesion and transmigration of monocytes. Higher traction forces have been observed at the region where the monocyte was in contact with the endothelial cells relative to their neighbors (Liu *et al.*, 2010).

In this work, we used micropatterned PAAm gels to investigate the tractions exerted by the cancer cells during the transmigration through the endothelium. Endothelial cell monolayers formed on PAAm gels were followed in time either in the presence or absence of a cancer cell. Then, traction stresses exerted were computed from the beads displacement and by solving an inverse problem using Adjoint Method.

Traction stresses exerted by an endothelial cell monolayer in the absence of cancer cells showed no significant changes in stresses with time (Figure 4.10). We observed that the average value of traction stresses exerted by endothelial cell monolayer in 80 µm micropatterns was approximately 60 Pa which, is in the same range as previously reported by Moussus et al. They studied the stresses exerted by single endothelial cell and endothelial cell monolayers in adhesive patterns. They reported that the average stresses exerted by the endothelial cell monolayer in 100 µm micropatterns is around 50 Pa (Moussus *et al.*, 2014).

Experiments performed in the presence of cancer cell showed the transmigration of cancer cell through the endothelium cell junctions (Figure 4.13) as previously reported in the publication (Mierke *et al.*, 2008). During transmigration, higher traction stresses (70 Pa) were observed at a localized area (location-2 in Figure 4.12) where the cancer cell is in contact with

the endothelium. In 2010 Liu et al. reported the endothelial cell in contact with the monocytes show higher tractions during the transmigration of monocytes (Liu *et al.*, 2010). We suggest that these stresses might be exerted by the endothelial cells when they reorganize during transmigration or by cancer cell during transmigration which needs to be further investigated with more experiments. After transmigration, the cancer cell spread on the gel and exerted higher traction stresses at their edges while spreading (Figure 4.15). The traction stresses observed at the edges of cancer cells were in the range of 80-120 Pa. Similar values have been reported during the migration of T24 cancer cell on such gels (Peschetola *et al.*, 2013). It has been reported that the endothelial cell monolayer can be resealed after transmigration of cancer cells and neutrophils (Mierke *et al.*, 2008; Rabodzey *et al.*, 2008). Heyder et al. reported that T24 cancer cell spheroids that comprised of 5-20 cancer cells irreversibly damaged the endothelium during transmigration (Heyder *et al.*, 2002). However in our experiment we did not observe the reorganization of endothelial cells into a monolayer. Following the endothelial cell monolayer after transmigration for few hours may provide the information on reorganization of monolayer.

In the current experiment, we observed the phenomenon of transmigration of cancer cell through the endothelial cell junctions. We could not observe significant differences in the tractions stresses during the transmigration of the cancer cell. We have the following hypothesis to explain our observation: (1) endothelial cell junctions open through some mechanotransduction signals, thereby eliminating the necessity for the cancer cell to open the junctions by exerting forces, (2) weak adhesion of endothelial monolayer to the gel could have made it difficult to measure the traction exerted during the transmigration of cancer cells and (3) the number of endothelial cells and size of the patterns could have played a role in tractions exerted during transmigration. It has been reported that the stresses might vary with size of cellular assembly (Moussus *et al.*, 2014).

4.4 Conclusion

These preliminary results suggest that the tractions stresses exerted during the transmigration can be investigated with this approach. Further experiments need to be performed to measure the tractions stresses exerted by cancer cells when they migrate through the endothelial cell monolayer.

Chapter 5 - General conclusions and future perspectives

Cell adhesion and migration are involved in various biological processes like embryogenesis, wound healing, tissue formation and repair, inflammatory response and so on (Ridley *et al.*, 2003; Friedl and Wolf, 2010). The changes in cell adhesion and migration are associated with diseases such as cancer. The ability of cancer cell to spread from a primary site to a distant organ is termed as metastasis and is the primary reason for cancer-associated death (Jeon *et al.*, 2013; Reymond *et al.*, 2013). Cancer cells that are carried in the blood make contact with the endothelium and then cancer cells roll, adhere and transmigrate to complete the metastasis process. Cell adhesive molecules play an important role in cancer metastasis by mediating cell-cell interactions. Identifying the key adhesion molecules and their mechanisms involved during the multiple steps of metastasis could enable the identification of new anticancer therapies for inhibiting the adhesion and transendothelial migration of metastatic cells. The adhesion of cancer cells to endothelial cells is a vital step of metastasis that can be mediated by several cell adhesion molecules like CAMs, selectins and some integrins. We have recently showed the role of ICAM-1 in mediating the interaction of bladder cancer cells with endothelial cells using Atomic Force Microscopy (Laurent *et al.*, 2014), but the ligands for ICAM-1 on bladder cancer cells were not yet clearly identified and the forces involved by the molecules during adhesion and transmigration have not been investigated so far.

In this work, we characterized the key molecules involved in the adhesion of bladder cancer cells to the endothelium. MUC1 and CD43 expressed by some bladder cancer cells were identified as the ligands for endothelial ICAM-1. Adhesion of bladder cancer cells to endothelial cells were significantly decreased while blocking the receptors (ICAM-1 or MUC1 or CD43) indicating the role of these receptors in bladder cancer cell-endothelial cell adhesion. Invasive cells (T24 and J82) showed more inhibition in adhesion as compared to less invasive cell (RT112). These results demonstrate that MUC1 and CD43 expressed by invasive cells (T24 and J82) mediate the bladder cancer cell-endothelial cell adhesion via interacting with ICAM-1.

The forces involved in cell-cell and cell-matrix interactions can be studied using Single Cell Force Spectroscopy (SCFS) mode of Atomic Force Microscopy (AFM) (Zhang *et al.*, 2002; Puech *et al.*, 2005; Franz *et al.*, 2007; Friedrichs *et al.*, 2010; Laurent *et al.*, 2014). We used this approach to quantify the forces involved when bladder cancer cells interact with an endothelial monolayer. SCFS measurements demonstrated that the rupture events

significantly decreased when blocking MUC1 and CD43 validating our earlier observation using adhesion assays. A Gaussian mixture model was used to identify the specific force range corresponding to the interaction of MUC1 or CD43 with ICAM-1. The interaction of the receptors with its cytoskeleton can be identified by analyzing two different kinds of rupture events (jumps and tethers) (Taubenberger *et al.,* 2007; Celik *et al.,* 2013; Helenius *et al.,* 2008; Sariisik *et al.,* 2015). From the analysis, we hypothesize that MUC1 is weakly or not connected to cytoskeleton, whereas CD43 is strongly connected to cytoskeleton.

Traction Force Microscopy (TFM) has been used to study the forces exerted by the cells when they migrate on the soft substrate like polyacrylamide gels with beads (Dembo and Wang, 1999; Kraning-rush *et al.*, 2012; Grevesse *et al.,* 2013; Peschetola *et al.*, 2013). This approach can be also used to study the forces involved during transmigration (Rabodzey *et al.*, 2008; Liu *et al.,* 2010; Stroka and Aranda-Espinoza, 2011). Here, we investigated the forces exerted by cancer cells when they migrate through the endothelium. Our preliminary results suggest that traction stresses exerted by cancer cells during transmigration can be investigated with this approach.

The shRNA approach was used to knock down the expression of MUC1 on J82 BCs and we obtained stable J82 BCs showing almost negative expression for MUC1. Adhesion assays need to be performed using the knock down cells (sh-MUC1) and the percentage of inhibition will be compared with the results obtained when using antibodies. These experiments will further validate the role of MUC1 in mediating the bladder cancer cell-endothelial cell adhesion.

The association of MUC1 and CD43 with the cell cytoskeleton could be further studied using Latrunculin A that prevents the polymerization of actin filaments. Cancer cells treated with Latrunculin A can be used in SCFS measurements and the analysis on the rupture events will give further insights about the link between the MUC1 and CD43 with the cytoskeleton.

The forces exerted by cancer cells and endothelial cells during transmigration can be quantified by performing more experiments with our approach. Also the forces exerted during the adhesion of cancer cells to the endothelium, transmigration of cancer cells through the endothelium and spreading of cancer cells on the substrate can be obtained and compared. This study will provide information on forces exerted by cancer cells at different step of metastatic process.

Appendix A

Protocol for RNA extraction and Real time PCR

RNA is extracted from T24 and J82 bladder cancer cells (BCs) using RNeasy Mini Kit (Qiagen, Courtaboeuf, France). Reverse transcriptase (RT) enzyme is used to synthesize first-strand cDNA (Super Script II, Invitrogen, France). Real time PCR (BioRad CFX96, France) is performed to quantify the expression RNA. The complete protocol is described below.

A.1 Extraction of RNA from bladder cancer cells

1. BCs grown on the culture flask are detached using trypsin and the cell suspension is centrifuged at 1100 rpm for 7 min. After centrifugation, the cells are counted using neubauer chamber (Superior, Germany).

2. The extraction buffer (EB) is prepared by adding 10 µl of β-mercaptoethanol (β-ME) per 1 ml of RLT buffer (Qiagen Kit). Note: Use fume hood while working with β-ME.

3. 350 µl of EB is added if the cells are less than $5x10^6$ and 600 µl of EB if the cells are more than that. The cells in EB buffer are homogenized well by pipetting and vortex.

4. Same volume of 70% ethanol (like EB buffer) is added to the homogenized lysate and mixed well. Note: 70% ethanol is prepared by diluting the 100% ethanol with Ultra-pure water or DMPC treated RNAse free water (Sigma-Aldrich, Lyon, France).

5. The lysate is then transferred to a RNase Spin column supplied with the Qiagen kit and placed inside a 2 ml tube. Then the lysate is centrifuged for 15 s at 15000 rpm and the flow collected in the 2 ml tube is discarded.

6. 350 µl of RW1 (wash buffer 1) is added to the spin column and then the flow collected in the 2ml tube is discarded after centrifugation at 15000 rpm for 10 s.

7. DNase I recombinant enzyme (Roche, Boulogne-Billancourt, France) is used to digest the DNA so that the RNA extracted is free from DNA contamination. DNA digestion mix is prepared by adding 3 µl of DNase I with 77 µl of RDD buffer (Qiagen kit). 80 µl of this mix is added to the spin column directly on the column membrane. The column is incubated for 15 min at room temperature (RT).

8. 350 µl of RW1 buffer is then added and centrifuged (15000 rpm/15 s). The flow collected is discarded and replaced with a new 2ml collection tube for the remaining steps.

9. 500 µl of RPE buffer (wash buffer 2) is added into the column and centrifuged (15000 rpm/15 s). Again, 500 µl of RPE buffer is added into the column and centrifuged (15000 rpm/2 min).

10. Finally, the column is placed in a new 1.5 ml tube and added with 40 µl of RNase free water. The column is left undistributed for 2 min at RT and then centrifuged (15000 rpm for 1 min). The flow through now contained RNA. The concentration of the RNA is measured using Nanodrop 2000 (Thermo Scientific, Courtaboeuf, France) and then is stored at -80°C. The important steps in the extraction protocol are shown in Figure A.1.

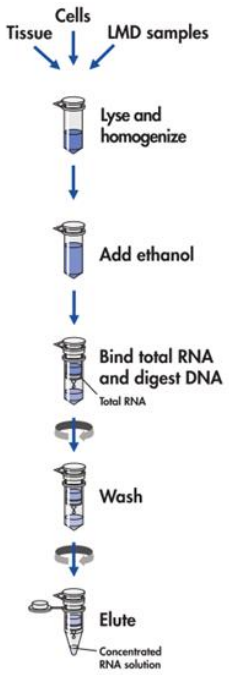

Figure A.1: RNA extraction protocol (Qiagen)

A.2 First-Strand cDNA synthesis using SuperScript II Reverse Transcriptase

1. Oligo$(dT)_{12\text{-}18}$ primers at 500 µg/ml and nucleotide mix dNTP (10 mM each) supplied with Invitrogen kit is used for cDNA synthesis.

2. The required amount of RNA in µl corresponding to 12.5 µg RNA is calculated and added with 1 µl of Oligo$(dT)_{12-18}$ and 1 µl of dNTP mix. The mix is made to 13 µl using RNase free water.

3. The mix is heated to 65°C for 5 min and chilled in ice for 5 min.

4. Then the mix is added with 4 µl of 5X first-strand buffer, 2 µl of 0.1 M DTT and 1 µl of SuperScript II Reverse Transcriptase to start the reaction.

5. cDNA synthesis is performed by incubating the mix at 45°C for 50 min. Then the mix is heated at 70°C for 15 min (to inactivate the products other than cDNA). The synthesized cDNA is stored at -20°C.

A.3 Real-Time PCR (q-PCR)

1. Real time PCR is performed to amplify the specific sequence in the cDNA template that corresponds to our protein of interest. Forward and reverse primers are used to locate the specific sequences in the cDNA and the sequences are amplified using PCR.

2. iTaq Universal SYBR Green supermix (BioRad, France) is used to quantify the amplified product using q-PCR. SYBR green is a fluorescent dye that binds to double stranded DNA. The fluorescence level can be used to quantify the amplified product in q-PCR.

3. The 10 µl of SYBR green super mix is added with 0.1 µl of forward and reverse primer each specific for the protein. Then, 2 µl of cDNA template is added and the mix is made to the final volume of 20 µl with RNase free water.
4. All the components are added in a 96 multiwell plate and sealed and centrifuged (2000 rpm for 20 s).

5. Then, the plate is transferred to Bio-Rad Thermocycler instrument and the q-PCR is performed by using a suitable program.

6. The different parameters used for q-PCR are shown in Figure A.2. The amount of DNA is doubled in each cycle through three steps such as denaturation (95°C, 10 s), annealing (60°C, 20 s) and extension (72°C, 5 min). The same cycle is repeated 40 times and the level of fluorescence is measured after extension for each cycle (indicated as camera in Figure A.2).

7. After 40 cycles, the melt-curve is performed by increasing the temperature from 60°C to 95°C by the increment of 0.5°C. The melt-curve can be used to check the specificity of our primers.

8. The program used for q-PCR is detailed below,

   1) 95.0°C for 10:00
   2) 95.0°C for 0:10 (Denaturation)
   3) 60.0°C for 0:20 + Plate Read (Annealing)
   4) 72.0°C for 0:30 (Extension)
   5) GOTO 2, 40 more times (Number of cycles)
   6) 72.0°C for 5:00
   7) 95.0°C for 0:30
   8) Melt Curve 60.0 to 95.0°C, increment 0.5°C,
   0:05 + Plate Read
   9) 8.0°C for 1:00

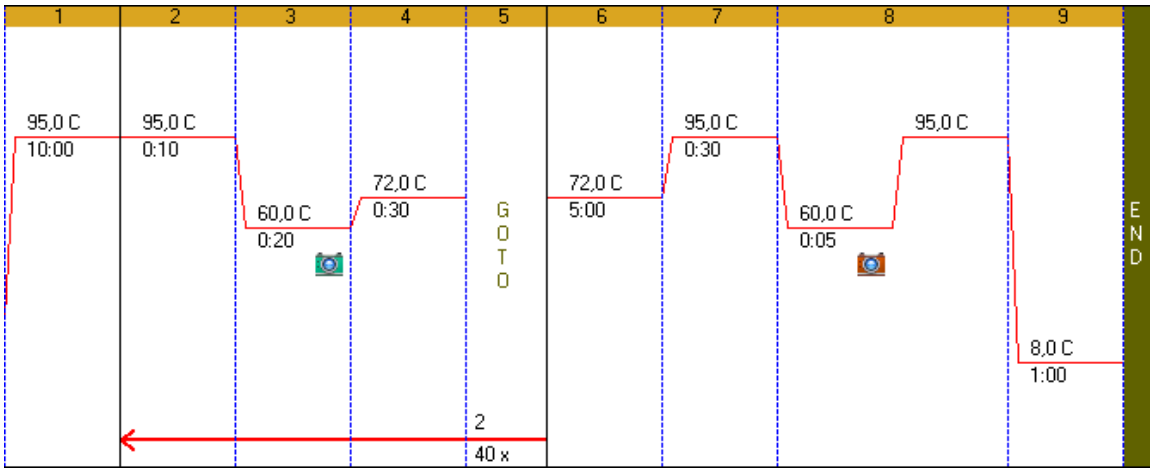

Figure A.2: The program used for q-PCR amplification.

9. The analysis is performed using Bio-Rad software that allowed us to check the amplification of specific sequence.

10. Threshold cycle (C_T) is obtained from the plots showing PCR cycle number in x-axis and fluorescence corresponding to amplified product in y-axis. The plot shows, exponential phase where product is doubled in each cycle and non-exponential phase plateau phase where the reaction components are already consumed. C_T is detected as the cycle that yields a detectable fluorescence signal (Figure A.3). C_T values are used for the analysis to quantify the expression through various methods.

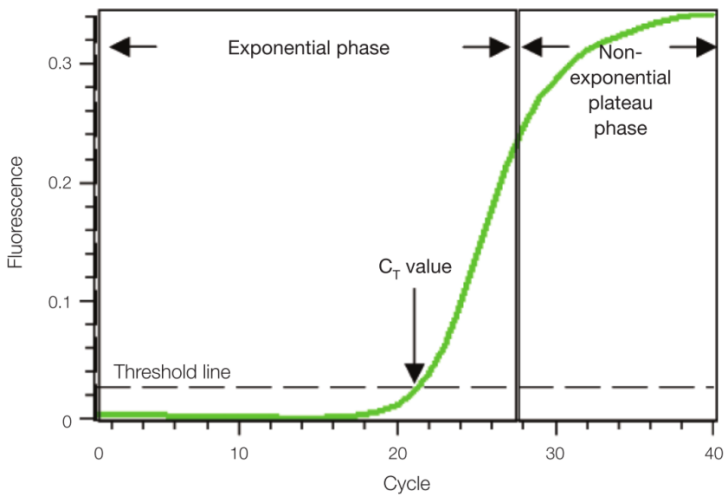

Figure A.3: Amplification plot. The two phases in DNA amplification is shown along with threshold cycle (C_T). Source: BioRad.

Appendix B

Force measurements using Atomic Force Microscopy (AFM)

B.1 AFM setup

The AFM consists of basic parts such as the optical head which is attached to a stage on inverted microscope (Zeiss) to create movement in the x,y,z directions over the sample. The complete setup of AFM used in our laboratory is shown in Figure B.1.

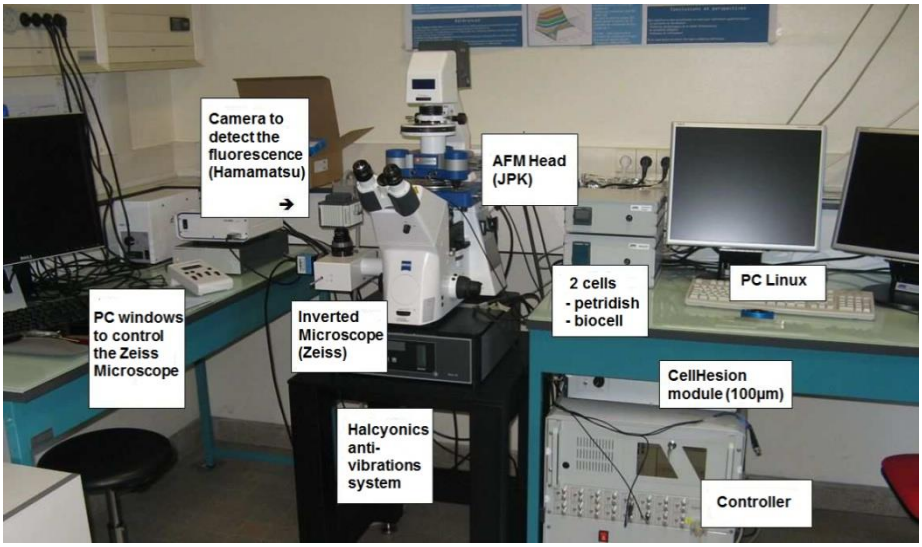

Figure B.1: AFM setup and its components at LIPhy.

The cantilever is fixed to a glass block, which is locked into the AFM head during the scanning (Figure B.2, left and inset). The laser beam embedded in the AFM head penetrates through the polished side of the glass block to hit the cantilever and is finally reflected onto a photodiode detector.

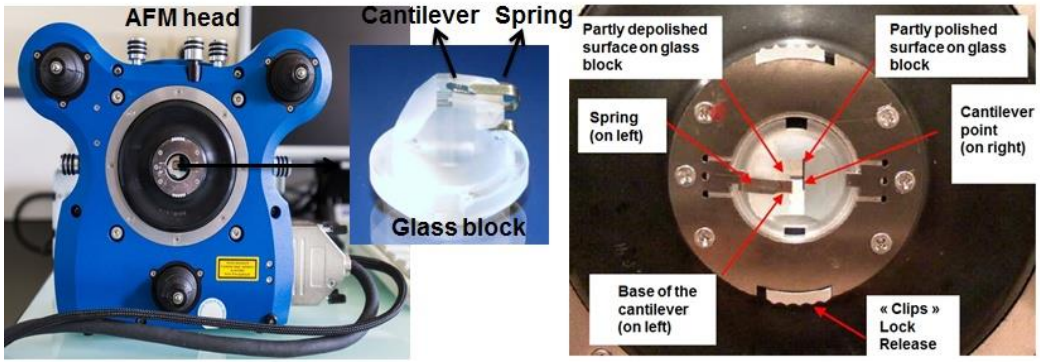

Figure B.2: AFM head (left), the glass block with cantilever attached using a spring (left, inset) and glass block attached to the head (right). (Source: NanoWizard AFM Handbook).

The AFM head of the Nanowizard II (JPK Instruments, Berlin) is equipped with a 15 µm Z-range linearized piezoelectric scanner (Puech *et al.*, 2005). This z-range is sufficient for measuring the adhesion of a cantilever-bound cell to a coated surface. However, when the cantilever bound cell is in contact with a second cell, a separation distance of more than 60 µm is required to break all the bonds between these cells due to the formation of membrane nanotubes (protrusion that extends from the plasma membrane). Long-range force spectroscopy was made possible by the use of CellHesion module (JPK instruments), that extends the z-range to 100 µm by piezo driven movement (Figure B.3). The movement of piezo is controlled by a closed feedback loop system providing sub-nanometer precision. The objective of microscope also moves on piezo device (PIFOC, PhsikInstrumente, Germany) in parallel with the sample stage allowing to observe the cell with light microscopy.

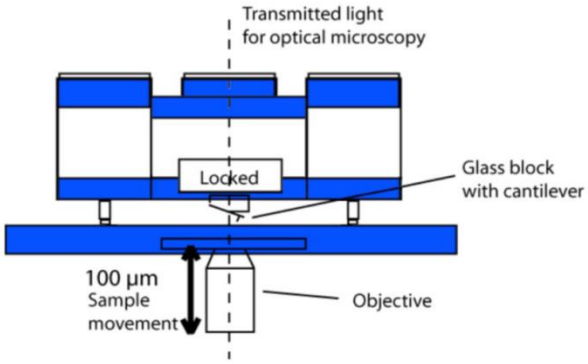

Figure B.3: Schematic of CellHesion module setup. (Source: JPK Instruments.

The photodiode detector is another important component of the AFM, detecting the angle of the reflected beam after hitting the cantilever. It contains four quadrants and the forces in two directions are measured vertically and laterally (Figure B.4). The reflected laser spot must be initially at the centre of the detector to allow maximum sensitivity for imaging and force control.

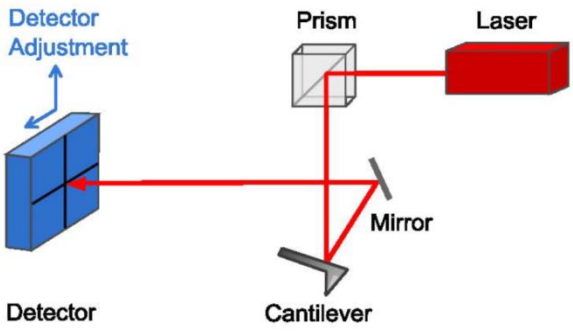

Figure B.4: Optical path of AFM setup. (Source: JPK NanoWizard II user manual).

B.2 Preparation of solutions for AFM experiments

1. Preparation of 0.1 M sodium bicarbonate buffer (pH 8.6–9.0)

4.2 g of sodium bicarbonate ($NaHCO_{3)}$ is dissolved in 500 ml of Milli-Q water. The pH of the solution is adjusted to 8.6 by adding solution of 0.1 M Na_2CO_3 buffer and stored at 4°C.

2. Biotin-BSA stock solution (0.5 mg/ml):

2 mg of biotin-BSA (Interchim, France) is dissolved in 4 ml of 0.1 M $NaHCO_3$ buffer and stored at -20°C.

3. Streptavidin stock solution (0.5 mg/ml):

5 mg of streptavidin (Interchim, France) is dissolved in 10 ml PBS and stored at -20°C.

4. Biotin-Con A stock solution (1 mg/ml):

5 mg of purified biotin-Con A reconstituted in 5 ml of distilled water (1 mg/ml) is purchased from Interchim, France. 100 µl aliquots of biotin-Con A is prepared and stored at -20°C. The stock is diluted 1:1 with PBS each time before use.

5. rICAM-1 stock solution (400 µg/ml)

50 µg of rICAM-1-Fc (RD systems, France) is mixed with 125 µl of sterile PBS (Stock: 400 µg/ml) and stored at -20°C. The rICAM-1 stock solution is diluted with 0.1 M $NaHCO_3$ to a final concentration of 25 µg/ml and used for the experiments.

B.3 AFM cantilever functionalization

1. Tipless cantilevers MLCT-O10 (Bruker AFM Probes) are used in the experiments. All the procedures are performed inside laminar hood.
2. The cantilever is placed in a glass petri plate and soaked in acetone for 5 min and then UV irradiated for 15 min.
3. The cantilever is then incubated with 50 µl of biotin-BSA (0.5 mg/ml in 0.1M $NaHCO_3$, pH 8.6) overnight at 37°C in a humidified chamber.
4. The biotin-BSA is removed from the cantilever and rinsed thrice with PBS to remove unbound proteins (The cantilever can be stored in PBS at 4°C for up to a week).

5. Then, 50 µl of streptavidin (0.5 mg/ml) is added to cover the cantilever and incubated at RT for 10 min. The cantilever is washed thrice with PBS after removing the streptavidin.

6. Finally, the cantilever is incubated with 50 µl of biotin-ConA (freshly prepared by diluting biotin-Con A in PBS in the ratio 1:1) for 10 min at RT. The cantilever is washed thrice with PBS. Then the functionalized cantilever is used for calibration and cell capture.

B.4 Cantilever calibration

The functionalized cantilever is placed on a glass block which is locked with a spring and inserted into the AFM head. The sensitivity and spring constant of the cantilever is measured using built-in routines in JPK software as described below.

Sensitivity calibration

Deflection of the cantilever detected on the photodiode is directly proportional to the interaction forces between the tip and the sample. Sensitivity and spring constant are two measurements required to convert the photodetector signal in volts to a quantitative force value in Newtons. The factor used to convert volts to nm from the deflection of the cantilever is called sensitivity. It depends on many parameters, including the type of cantilever, how the cantilever is mounted and the optical path of the AFM laser detection. So the sensitivity measurements must be repeated each time a cantilever is mounted or re-mounted.

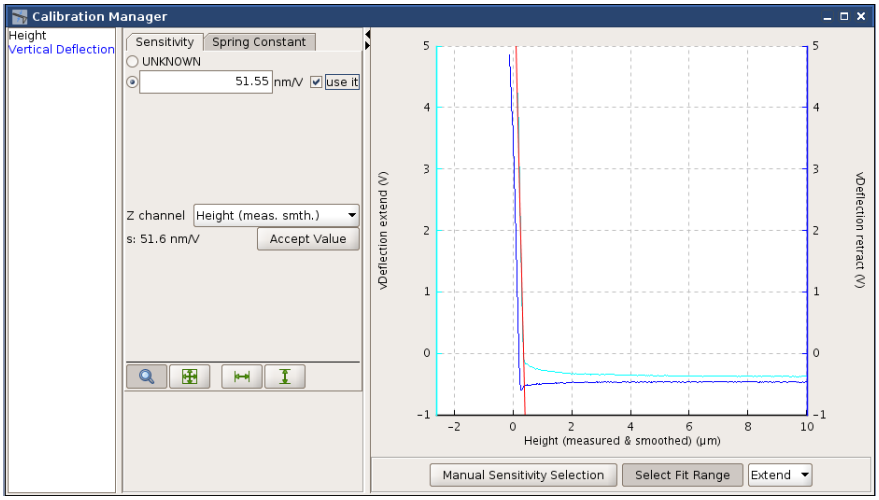

Figure B.5: Calibration of sensitivity using JPK software. (Source: JPK NanoWizard II user manual).

The sensitivity is measured by performing a force curve on a hard surface and the deflection signal is analyzed when the cantilever and surface are in contact. During the contact, deflection of the cantilever is equal to the vertical movement of the piezo, since the tip and sample move together. Figure B.5 shows the plot of vertical deflection versus distance acquired during the contact of the cantilever with a hard surface. The linear part of the blue curve is taken for sensitivity measurement and fitted (red fit).

Spring constant calibration

The nominal spring constant of the cantilever is provided by suppliers and vary usually from 0.005 N/m to 40 N/m. It is calculated in air from the cantilever shape (length, width and thickness). However, the true spring constants of the cantilevers can differ from the nominal values. The JPK software allows to measure the spring constant using the thermal noise method and equipartition theory based on the protocol given by Hutter in 1993 (Hutter and Bechhoefer, 1993). The thermal noise analysis is widely used because it can be performed in liquids and it is very accurate. The tip of the cantilever is constantly fluctuating due to thermal vibrations. The spring constant is measured by measuring the deflection of the cantilever q(f). This method is most suited to soft cantilevers, where the free fluctuations are more significant.

When the tip is far from the sample, the cantilever oscillations are only due to thermal fluctuations. Measuring these vibrations in a wide range of frequencies near to the resonant frequency allow to estimate the spring constant. Figure B.6 shows a typical resonance curve which is modelled using the perfect harmonic oscillator model,

$$q(f) = A.\frac{f_0^2}{\left(f^2 - f_0^2\right)^2 + \left(\frac{f_0 f}{Q}\right)^2} \qquad (2.1)$$

where, A = amplitude, f_0 = resonant frequency, Q = quality factor.

This curve is used to fit the measured cantilever resonance during calibration of the spring constant. Equipartition theory explains that the energy in any free mode of the system has to be equal to the thermal energy due to the absolute temperature of the system, $k_BT/2$. This measured energy is given in terms of the spring constant and the average squared vertical deflection of the cantilever (q).

$$\frac{1}{2}k_BT = \frac{1}{2}k\langle q^2\rangle \qquad (2.2)$$

where, k_B = Boltzmann constant, T = temperature, k = spring constant, q = deflection of cantilever.

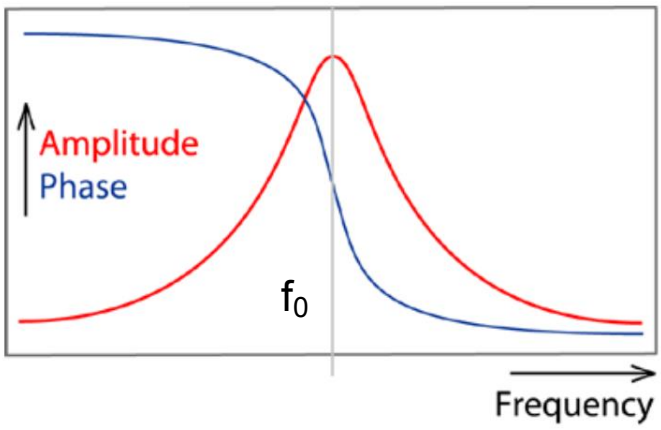

Figure B.6: The resonant curve (amplitude and phase) of the cantilever as a function of frequency. (Source: NanoWizard AFM Handbook).

The value of $\langle q^2 \rangle$ is measured from the resonance curve fit (2.1). Some correction factors are added to get more accurate value from the fit (Butt and Jackshe, Nanotechnology 1995): usually the first resonance peak of the cantilever is considered because it has large amplitude (Figure B.7) and thereby gives the best signal-to-noise ratio. However, when working with soft cantilevers in liquid, the second resonance peak is considered to give more reliable results as shown in Figure B.7. We are using soft cantilevers and so the second resonance peak is considered in our experiments. The corrections factors (c_i), 0.817 for the first mode, 0.251 for the second mode and 0.0863 for the third mode (Butt and Jaschke, 1995) are included in the equation 2.2 and the spring constant (k) of the cantilever is calculated using the formula,

$$k = c_i k_B T \frac{1}{\langle q^2 \rangle} \qquad (2.3)$$

where, c_i = correction factor, k_B = Boltzmann constant, T = temperature, $\langle q^2 \rangle$ = mean square displacement of the tip.

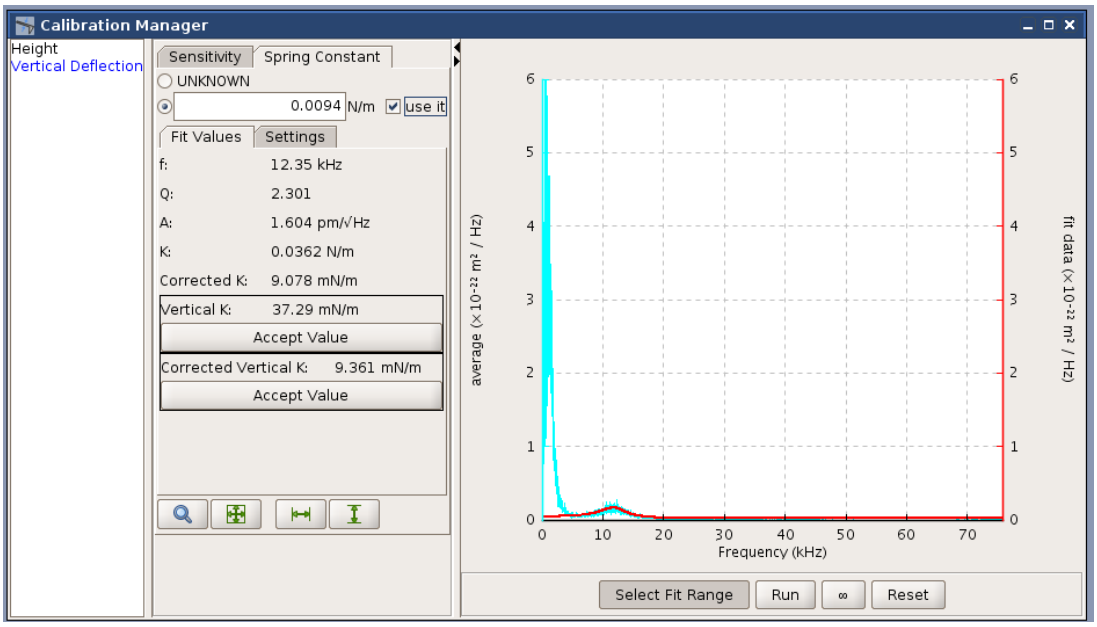

Figure B.7: Calibration of spring constant with thermal noise method using JPK software. (Source: JPK NanoWizard II user manual).

Appendix C

Preparation of Polyacrylamide Gels with micropatterns

C.1 Preparation of the Silicon master with patterns

A mask with circular patterns of 80 µm is designed using ink space and printed on plastic sheet. The mask contains an array of 80 µm patterns in black and white space surrounding them (Figure C.1). The black region blocks the UV, whereas the white allows the UV to pass through. The patterns are transferred to a silicon master by soft lithography. A negative resin (SU-8 photoresist, GM1070, GersteltecSarl, Suisse) is used in our preparations. The region exposed to UV (white region) is polymerized and remains after the development. On the contrary, the regions blocked from UV (black region) do not polymerize and is removed during the development (Figure C.1). The process is performed in the clean room as described below.

1. A 3-inch circular silicon wafer (Siltronix, France) is dehydrated by heating it at 200°C for 30 min. The wafer removed from the heating plate is allowed to cool down.

2. Then, a thin layer of SU-8 photoresist on the silicon wafer (substrate) is obtained using the spin coater. The spin coater is programmed with specific parameters to create a 100 µm height of resin on the substrate. The program for spin coating is divided as two parts, spreading of resin and creating a specified height of resin. The parameters used are given below,

   Part 1 – time 0 s, speed 5(x100) rpm and acceleration 60(x100) rpm/s.

   Part 2 – time 40 s, speed 9(x100) rpm and acceleration 1(x100) rpm/s.

3. The substrate is placed on the spin coater and added with 3 ml of SU-8 photoresist. The program is selected and performed to obtain a thin layer of resin (height 100 µm) on the substrate.

4. Then the substrate is soft baked first at 65°C for 15 min, followed by 95°C for 2 h. The substrate is allowed to cool until it reaches the RT.

5. The resin is exposed with UV for soft lithography (Karl Suss, France) as shown in Figure C.1. The lamp is switched on and allowed to stabilize for 30 min. The substrate is then placed in the setup. The mask used to transfer the pattern is placed directly on

the substrate and exposed to UV for 62 s. The time of exposure is calculated considering the power of UV lamp (P=1000 mJ/cm^2) by using the formula, t=P/16.

6. The substrate after soft lithography is kept at RT for 30 min and baked first at 65°C for 15 min, followed by 95°C for 40 min. Then, the substrate is allowed to cool.

7. Already prepared PGMEA solution (Propylene glycol monoethyl ether acetate, Sigma-Aldrich, Lyon, France) is used for the development. The substrate is placed in the holder and immersed into the PGMEA solution. During the development, the substrate is taken out of the solution and rinsed with isopropanol. The development process is continued until the patterns are visualized on the substrate.

8. Finally, the developed substrate is baked in oven at 135°C for 2 h and used for further steps.

C.2 Preparation of PDMS microstamps

1. Microstamps are obtained by molding the silicon wafer with PDMS (Sylgard 184, Dow corning, Belgium). The silicone elastomer base is mixed with curing agent in the ratio (9:1) and mixed well.

2. Then, elastomer mix is degassed under vacuum and added to the substrate with patterns and cured for 2 h at 60°C.

3. After curing, the microstamps are obtained by peeling the PDMS from the substrate (Figure C.1).

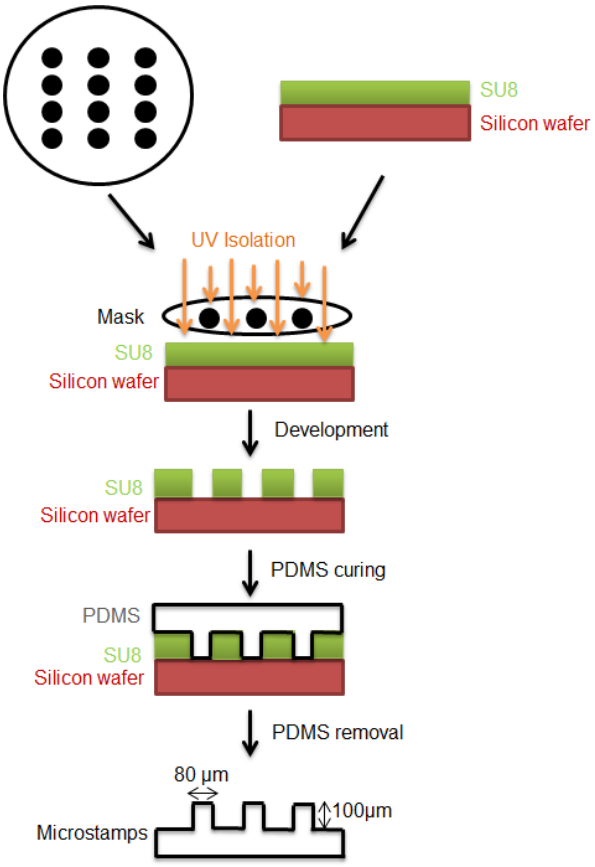

Figure C.1: Steps involved in the preparation of silicon wafer and PDMS microstamps.

C.3 Preparation of falcon petriplates

1. Coverslips of 30 mm (Knittel glass, Germany) in diameter are cleaned with plasma for 3 min.

2. After cleaning, the coverslips are treated with 3-(trimethoxysilyl) propylacrylate (100 µl per coverslip) (Sigma-Aldrich, Lyon, France) for 1 h to promote the strong adhesion of gels to the glass surface.

3. After incubation, the coverslips are washed with 70% ethanol followed by deionized water and dried with clean N_2 gas.

4. Falcon Petri plates of 35 mm (Nunc, Saint Aubin, France) are taken and drilled in the middle to make holes of 28 mm. The treated 30mm coverslips are glued to the bottom of the flacon plates with treated side facing up using UV glue (Norland Optical Adhesive 61, New Jersey). The falcon plates are placed in UV lamp for 15 min to complete the process.

C.4 Preparation of 15x15mm coverslip

1. 15 mm coverslips (Knittel glass, Germany) are washed in 50/50 ethanol-MilliQ water mixture for 5-10 min and dried with clean N_2 gas.
2. Then, few drops of Sigmacote (Sigma-Aldrich, Lyon, France) is added to cover the surface of the coverslips and incubated for 30 min at RT (inside the hood).
3. After incubation, the coverslips are rinsed with sterile water and dried with clean N_2 gas. These coverslips are used during the preparation of gels.

C.5 Preparation of hydroxy-PAAm gels (PAAm gels)

The acrylamide and bisacrylamide solutions are prepared and stored at 4°C. These solutions can be stored and used upto 3-4 months.

40% acrylamide solution: 20 g of acrylamide (Sigma-Aldrich, Lyon, France) is dissolved in 30 ml of 50 mM Hepes and stirred at 37°C for mixing. Then, the volume is made upto 50 ml by adding Hepes solution.

2% acrylamide solution: 1 g of acrylamide (Sigma-Aldrich, Lyon, France) is dissolved in 40 ml of 50 mM Hepes and stirred at 37°C for mixing. Then, the volume is made upto 50 ml by adding Hepes solution.

1. N-hydroxyethylacrylamide (N-HEA, Sigma-Aldrich, Lyon, France) is freshly prepared by dissolving 65 mg in 1 ml of 50 mM Hepes at pH 7.4.
2. The PAAm gel solution mix is obtained by adding the following components,
   40% Acrylamide–40 µl
   2% Bisacrylamide –75 µl
   50 mM Hepes –273 µl
   N-hydroxyethylacrylamide - 106.5 µl.
3. After mixing, the PAAm gel solution is degassed for 20 min under vacuum.
4. The degassed PAAm gel solution is added with 2.5 µl of sonicated beads (0.2 µm). Then the polymerization is initiated by adding 2.5 µl of 10% APS and 0.5 µl of TEMED. Overall the PAAm gel contains 3.2% Acrylamide, 0.3% Bisacrylamide and 1.3% N-HEA monomers.
5. A drop of 16 µl PAAm gel solution is added on the coverslips (15x15 mm) placed on the pipette tip as shown in Figure C.2, left.

6. The treated falcon plate is approached down slowly to catch the gel solution by capillary force (Figure C.2, right). The falcon plate (inverted/faced down) on the top of water and allowed to polymerize for 10 min.
7. Then, 1 ml of Hepes is added on the PAAm gel and incubated for 20 min at RT. The 15 mm coverslip on the top of the PAAm gel is carefully removed with scalpel.
8. Finally the PAAm gel is rinsed with water and PBS and it can be stored at 4°C for 3 days maximum by sealing the plates with parafilm.
9. Later, PAAm gel is dried and used for micro contact printing.

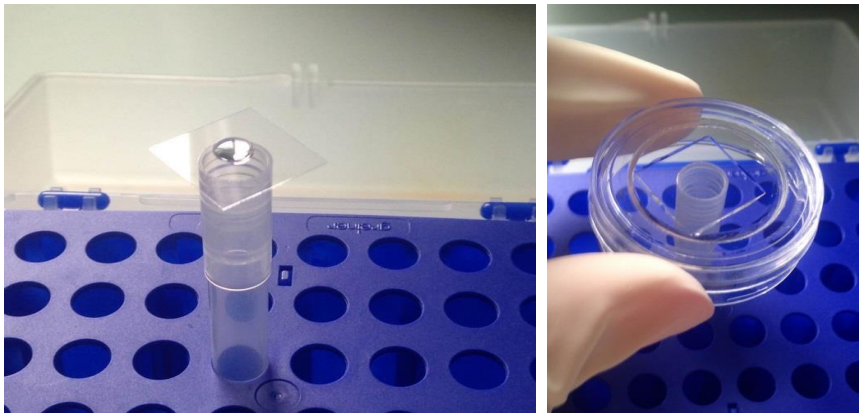

Figure C.2: Left: A drop of PA gel mix is added on 15x15 mm coverslip coated with sigmacote. Right: A flacon plate is approached and the gel is caught between the two coverslips by capillarity.

C.6 Preparation of Microstamps and Microcontact Printing

1. Microstamp obtained by molding the silicon master with PDMS is sonicated for 15 min in a 50/50 ethanol-MilliQ water mix and dried with clean N_2 gas.
2. Microstamp is activated with oxygen plasma by passing the plasma gun over the microstamps.
3. After activation, the microstamp is incubated with 100 µl of fibronectin (50 µg/ml) for 1 h at RT (Figure C.3) and protected from light with aluminum foil. From this step, all the procedures are performed inside the hood.
4. Fibronectin coated microstamp is washed twice with PBS and dried with clean N_2 gas.
5. Fibronectin coated microstamp is placed on PAAm gel surface (Figure C.3) and pressed gently on borders and in the middle. This setup is allowed for 1 h at RT to transfer the fibronectin from microstamp to PAAm gel.

6. The microstamp is removed gently by adding PBS in the falcon plate and rinsed thrice with PBS.
7. The uncoated region is blocked by incubating the PAAm gel with 1ml of BSA solution (5 mg/mL in PBS) for overnight at 4°C (Figure C.3).
8. After BSA treatment, PAAm gel is washed thrice with sterile PBS solution.
9. Then, cells are seeded on PAAm gel and imaged.

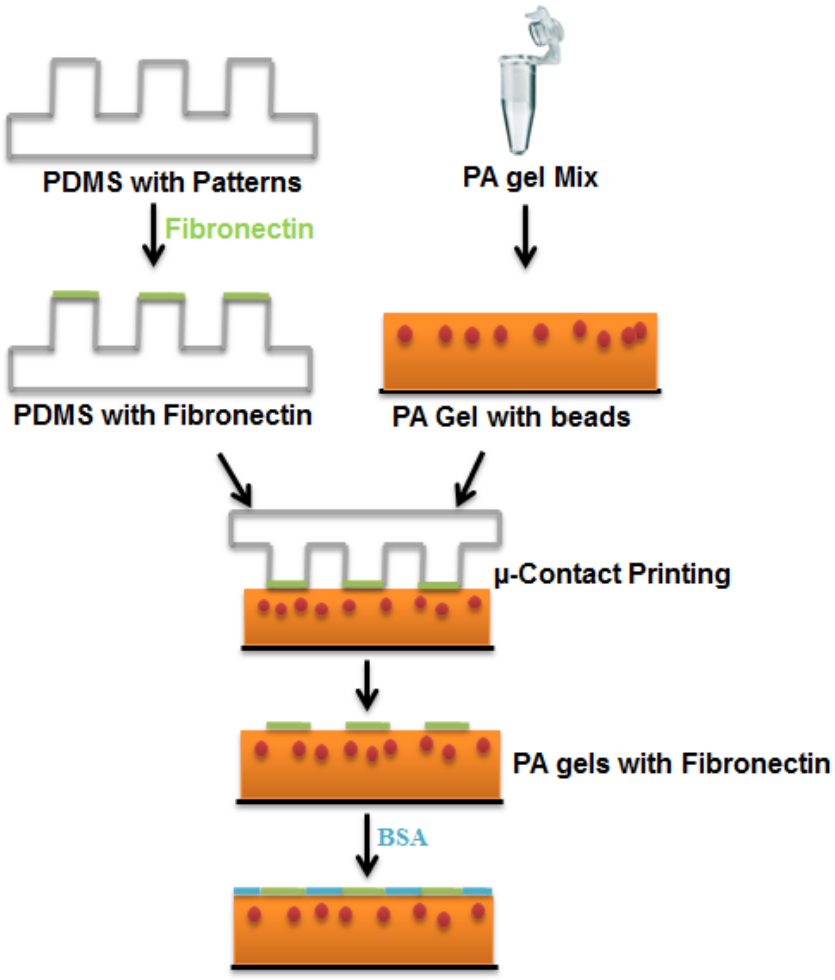

Figure C.3: Steps involved in Microcontact printing.

Appendix D
Outcomes of my PhD project

Publications

1. Atomic Force Microscopy reveals a role for endothelial ICAM-1 expression in bladder cancer cell adherence.

   Valerie M.Laurent, Alain Duperray, **Vinoth Sundar Rajan,** and Claude Verdier.

   PLOS ONE 9(5):e98034. doi:10.1371/journal.pone.0098034 (May, 2014).
2. First author paper titled "Unraveling the ligand-receptor interactions between bladder cancer cells and the endothelium using AFM" is in the process of revising and aiming to submit to Biophysical Journal.

Oral communications

1. Adhesion and transendothelial migration of cancer cells: an AFM Study.

   Vinoth SUNDAR RAJAN, Valerie Laurent, Claude Verdier and Alain Duperray.

   Mechanobiology and Physics of Life in Lyon, 12th January 2016.
2. Adhesion and transendothelial migration of cancer cells

   Vinoth SUNDAR RAJAN, Valerie Laurent, Claude Verdier and Alain Duperray.

   GDR 3570 – MECABIO, Grenoble, 2-3 th July 2015.
3. Transendothelial migration of cancer cells

   Vinoth SUNDAR RAJAN, Claude Verdier and Alain Duperray.

   Annual meeting of the doctoral school of chemistry and life science, Grenoble 24th April 2014.

Poster communications

1. Adhesion and transendothelial migration of cancer cells: an AFM Study.

   Vinoth SUNDAR RAJAN, Valerie Laurent, Claude Verdier and Alain Duperray.

   6th European Cell Mechanics Meeting, Barcelona, 13-15th May -2015.
2. Adhesion and transendothelial migration of cancer cells: an AFM Study.

   Vinoth SUNDAR RAJAN, Valerie Laurent, Claude Verdier and Alain Duperray.

   9th Nano and Micro-Environments for Cell Biology workshop, Grenoble, 8th September 2015.
3. Adhesion and transendothelial migration of cancer cells: an AFM Study.

   Vinoth SUNDAR RAJAN, Valerie Laurent, Claude Verdier and Alain Duperray.

   2nd ERC BIOMIM Meeting, Grenoble, 11-13th March 2015.

Résumé de la thèse

La migration et l'adhésion cellulaire sont impliquées dans divers processus biologiques, tels que l'embryogenèse, la cicatrisation des blessures, la formation et la réparation tissulaire, la réaction inflammatoire, etc…(Ridley *et al.*, 2003; Friedl and Wolf, 2010). Les changements relatifs à l'adhésion et la migration cellulaire sont associés aux maladies telles que le cancer. Le processus de métastatisation traduit la capacité des cellules cancéreuses à envahir un autre organe, et ce phénomène est la principale cause de décès pour 90% des cas de cancer mortel (Jeon *et al.*, 2013; Reymond *et al.*, 2013). Le caractère malin du cancer dépend très étroitement de la capacité de la tumeur à se métastaser vers les organes par les vaisseaux sanguins. Lors de ce processus, les cellules cancéreuses s'échappent de la tumeur pour pénétrer dans le flux sanguin (intravasation). Les cellules cancéreuses circulant dans le flux sanguin peuvent interagir avec le feuillet endothélial des vaisseaux sanguins, y adhérer pour finalement migrer (extravasation ou diapédèse) au travers de l'endothélium et former une tumeur à distance. Ce phénomène d'extravasation des cellules cancéreuses est très semblable à celui utilisé par les leucocytes lors de l'inflammation : 1) transport des cellules dans le flux sanguin, 2) adhésion des cellules à l'endothélium, 3) étalement et migration des cellules au travers de l'endothélium. Les molécules impliquées à chaque étape du processus sont souvent les mêmes mais les cellules cancéreuses peuvent aussi utiliser d'autres protéines adhésives (Strell and Entschladen, 2008; Mierke, 2013; Reymond *et al.*, 2013; Shenoy and Lu, 2014).

Les molécules d'adhésion cellulaire jouent un rôle important dans ce phénomène en favorisant l'interaction entre les cellules. L'identification des molécules d'adhésion impliquées, et leurs mécanismes pendant les multiples étapes de la formation des métastases, pourraient permettre de proposer de nouveaux traitements contre la dissémination tumorale, inhibant l'adhésion et la migration transendothéliale des cellules métastatiques. L'étape d'adhésion fait intervenir différentes molécules d'adhésion cellulaire (CAMs) telles que les β1 integrins (Heyder *et al.*, 2005), Vascular Cell Adhesion Molecule-1 (VCAM-1) (Klemke et al., 2006), L-selectin (Yamada *et al.*, 2006) et Intercellular Adhesion Molecule-1 (ICAM-1) (Roche *et al.*, 2003; Chotard-Ghodsnia *et al.*, 2007; Haddad *et al.*, 2010; Laurent *et al.*, 2014). Nous avons récemment démontré le rôle d'ICAM-1 exprimé par les cellules endothéliales

dans l'interaction des cellules cancéreuses de la vessie avec l'endothélium en utilisant la microscopie à force atomique (Laurent *et al.*, 2014); il restait à identifier quelles sont les molécules exprimées par les cellules cancéreuses de la vessie capables d'interagir avec ICAM-1. De plus, les forces impliquées par les interactions entre ces molécules au cours de l'adhésion et de la migration n'ont pas été examinées jusqu'à présent.

Dans cette étude, nous avons défini les molécules clefs qui sont impliquées dans l'adhésion à l'endothélium des cellules cancéreuses de la vessie, en utilisant d'abord la technique de cytométrie de flux. L'expression de MUC1 et de CD43 a été étudiées sur 5 lignées différentes, RT4, RT112, T24, J82 et TCCSUP. Ces lignées cellulaires présentent la progression d'un phénotype bien différencié au moins différencié, et l'apparition du stade superficiel au stade invasif du cancer humain épithélial de la vessie. Nous avons constaté une faible expression de MUC1 et de CD43 pour les lignées RT4, RT112 et T24 (Tableau 1). TCCSUP a montré une expression faible et modérée respectivement de MUC1 et de CD43 (Tableau 1). Comparativement aux autres BCs, J82 démontre une expression forte de MUC1 et une expression modérée de CD43 (Tableau 1).

Invasivité ↓

Cellules	MUC1 expression	CD43 expression
RT4	+	+
RT112	+	+
T24	+	+
J82	+++	++
TCCSUP	++	+

Tableau 1 : Niveau d'expression de MUC1 et de CD43 analysé en cytométrie de flux. 5 BCs ont été analysées pour l'expression de MUC1 et de CD43 en utilisant des anticorps spécifiques et les niveaux d'expression sont indiqués ainsi : + (expression faible), ++ (expression modérée), +++ (forte expression).

Comme MUC1 et CD43 sont les ligands d'ICAM-1, nous avons étudié le rôle de ces molécules dans l'adhésion des cellules endothéliales du cancer de la vessie en réalisant des tests d'adhésion. Trois BCs (RT112, T24 et J82) d'invasivité différente ont été sélectionnées pour étudier le rôle de ces molécules d'adhésion en relation avec leur capacité d'invasion (RT112<T24<J82). Le pourcentage d'inhibition obtenu par l'utilisation d'anticorps bloquants ICAM-1 sur les ECs et MUC1 ou CD43 ou MUC1+CD43 sur BCs, a été calculé et comparé à

l'adhésion obtenue en utilisant un contrôle isotypique. Les résultats sont présentés dans le Tableau 2.

Cellules	anti-ICAM-1 Mean±SEM	anti-MUC1 Mean±SEM	anti-CD43 Mean±SEM	anti-MUC1+anti-CD43 Mean±SEM
RT112	**18.0±3.7**	**25.4±1.4**	**28.7±1.8**	**41.2±4.6**
T24	**36.4±1.7**	**47.3±4.8**	**62.1±5.5**	**61.0±2.0**
J82	**35.6±6.6**	**49.3±3.2**	**45.0±1.5**	**59.4±3.4**

Tableau 2 : Quantification de l'adhésion cellulaire des cellules tumorales sur des cellules endothéliales. Le pourcentage d'inhibition de l'adhésion (Mean±SEM) est indiqué après blocage de différents récepteurs des cellules endothéliales (ICAM-1) et des cellules cancéreuses (MUC1, CD43 ou les deux) pour 3 différentes cellules du cancer de la vessie (RT112, T24 et J82).

L'adhésion des cellules du cancer de la vessie aux cellules de l'endothélial décroît significativement après blocage des récepteurs (ICAM-1 ou MUC1 ou CD43 ou les deux) indiquant le rôle de ces récepteurs dans l'adhésion des cellules du cancer de la vessie sur les cellules endothéliales. La diminution de l'adhésion pendant le blocage est deux fois plus faible pour la lignée RT112 comparativement aux lignées T24 et J82 (Tableau 2). Ces résultats suggèrent que l'adhésion des cellules invasives du cancer de la vessie (T24 et J82) aux cellules endothéliales est principalement due à l'interaction de MUC1 et de CD43 avec ICAM-1 exprimée par l'endothélium. Par contre, l'adhésion de la lignée moins invasive RT112 sur le ECs est moins dépendante d'ICAM-1.

Récemment la spectroscopie de force d'une cellule (SCFS) utilisant la microscopie à force atomique (AFM) (Zhang *et al.*, 2002; Puech *et al.*, 2005; Franz *et al.*, 2007; Friedrichs *et al.*, 2013; Laurent *et al.*, 2014) a été appliquée pour étudier les interactions adhésives des cellules avec d'autres cellules, protéines, ou surfaces fonctionnalisées. La microscopie à force anatomique est un outil puissant permettant d'identifier et de quantifier les interactions récepteur ligand (Zhang *et al.*, 2002; Puech *et al.*, 2005; Sulchek *et al.*, 2005; Taubenberger *et al.*, 2007; Alsteens *et al.*, 2010; Pfreundschuh *et al.*, 2015). Nous avons utilisé la SCFS AFM pour quantifier les forces impliquées lorsque les cellules du cancer de la vessie interagissent avec une monocouche endothéliale. Les événements de rupture < 36 pN ont été définis comme étant du bruit de fond (interactions non spécifiques) en utilisant de la sérum albumine bovine comme substrat et seuls les événements de rupture > 36 pN ont été pris en compte dans l'analyse.

Le pourcentage d'inhibition après blocage de MUC1 ou de CD43 ou des deux par rapport au témoin est indiqué dans le Tableau 3. Les mesures montrent que la force de rupture

décroît significativement après blocage de MUC1 ou CD43 ou des deux (Tableau 3) ce qui valide nos observations antérieures utilisant des tests d'adhérence.

Les résultats montrent clairement que MUC1 et CD43 ont un rôle important lors de l'adhésion des cellules tumorales du cancer de la vessie aux cellules endothéliales. De plus, des expériences comparant 2 substrats différents (cellules endothéliales HUVECs et protéine recombinante ICAM-1 rICAM-1) ont révélé que l'interaction de J82 avec les ECs est principalement médiée par ICAM-1 (Tableau 3)

Substrat	J82 état de cellules	% d'inhibition par rapport au contrôle	N	n	Moyenne des événements de rupture par courbe (M=n/N)
HUVECs	control		88	426	4.8
	anti-MUC1	63.9	91	159	1.8
	anti-CD43	42.2	89	249	2.8
	anti-MUC1+anti-CD43	72.2	90	121	1.3
rICAM-1	control		79	126	1.6
	anti-MUC1	56.1	70	49	0.7
	anti-CD43	40.2	86	82	0.9
	anti-MUC1+anti-CD43	76.4	85	32	0.4

Tableau 3 : Analyse de la distribution des forces de rupture. Le pourcentage d'inhibiton est le nombre des événements de rupture (<36 pN) après blocage de différents récepteurs impliqués dans l'interaction. Cela a été quantifié en comparant HUVECs et rICAM-1 pour le contrôle. N représente le nombre de courbes de force, n est le nombre total des événements de rupture (<36pN) et M représente l'événement de rupture moyen par courbe. Le pourcentage d'inhibition dans le blocage d'un récepteur spécifique est quantifié par la formule $[1-(M_{Ab}/M_{cont})]*100$. $M_{Ab,}$ représentant le principal événement de rupture obtenu pendant le blocage du MUC1, CD43 ou MUC1+CD43, utilisant des anticorps spécifiques, et M_{cont} représente le nombre principal des événements de rupture pour le contrôle.

Un modèle de mélange Gaussien (GMM) a été utilisé pour identifier la plage de force spécifique correspondant à l'interaction de MUC1 ou de CD43 avec ICAM-1. L'analyse montre que les interactions non spécifiques ont une force de rupture moyenne de ~30 pN (Tableau 4). L'analyse GMM a également montré que l'interaction de CD43 et de MUC1 avec ICAM-1 est médiée par une force de rupture moyenne de respectivement ~43 pN et ~53 pN (Tableau 4).

Substrat	J82 état de cellules	Peak 1 (Green) Mean±SEM	Peak 2 (Black) Mean±SEM	Peak 3 (Blue) Mean±SEM
HUVECs	control	31.0±0.3	40.9±0.3	50.4±0.8
	anti-MUC1	29.3±0.2	42.9±1.4	
	anti-CD43	31.1±0.3		53.3±1.6

Tableau 4 : Plage de force obtenue par l'analyse GMM, des données SCFS pour l'interaction du BCs avec les ECs. L'analyse GMM a révélé que l'interaction de CD43 correspond à une rupture de force moyenne de ~43 pN et l'interaction de MUC1 à une la rupture de force moyenne de ~53 pN.

L'interaction des récepteurs avec le cytosquelette peut être identifiée en analysant deux différents types d'événements de rupture (sauts et « tethers »), observés dans les courbes de force (Taubenberger *et al.*, 2007; Helenius *et al.*, 2008; Celik *et al.*, 2013; Sariisik *et al.*, 2015) Il a été démontré que les interactions donnant lieu à des sauts, correspondent aux récepteurs attachés au cytosquelette, et que les « tethers » proviennent de récepteurs ancrés faiblement au cortex cellulaire d'actine. (Puech *et al.*, 2005; Helenius *et al.*, 2008).

Cette analyse détaillée du nombre de sauts et de « tethers » montre que MUC1 exprimé par la lignée J82 peut être faiblement connecté au cytosquelette puisque ses interactions sont principalement médiées par les «tethers ». D'un autre côté nous avons démontré que CD43 doit être plus étroitement lié au cytosquelette et correspond aux premières ruptures obtenues sur les courbes de force.

La TFM est utilisée pour étudier les forces émises par les cellules lorsqu'elles migrent sur un substrat souple tel que les gels de polyacrylamides contenant des billes fluorescentes. (Dembo and Wang, 1999; Kraning-rush *et al.*, 2012; Grevesse *et al.*, 2013; Peschetola *et al.*, 2013). Cette approche peut aussi être utilisée pour étudier les forces impliquées lors de la transmigration. (Rabodzey *et al.*, 2008; Liu *et al.*, 2010; Stroka and Aranda-Espinoza, 2011). Dans cette étude, nous utilisons des gels de polyacrylamide décorés avec des îlots de fibronectine pour étudier les forces de traction exercées par les cellules du cancer de la vessie pendant la transmigration au travers de l'endothélium. Les images des monocouches de cellules endothéliales cultivées sur ces gels et des billes sont enregistrées à différents intervalles de temps en présence ou en absence de cellules cancéreuses. Ensuite, les contraintes de tractions exercées sont calculées à partir du déplacement des billes en résolvant un problème inverse, utilisant la méthode adjointe. Notre étude préliminaire montre que les contraintes de tractions exercées par les cellules du cancer de la vessie pendant la transmigration peuvent être étudiées grâce à cette approche.

Bibliography

Abidine, Y., Laurent, V. M., Michel, R., Duperray, A., and Verdier, C. (2015). Local mechanical properties of bladder cancer cells measured by AFM as a signature of metastatic potential. Eur. Phys. J. Plus *130:202*, 1–13.

Acres, B., Lacoste, G., and Limacher, J. M. (2015). Targeted Immunotherapy Designed to Treat MUC1-Expressing Solid Tumour. Curr. Top. Microbiol. Immunol, 1-19.

Alberts et al., 2002 (2002). Molecular Cell Biology. Mol. Biol. Cell. 4th Ed. *The Self-A*, http://www.ncbi.nlm.nih.gov/books/NBK26862/.

Alkhamesi, N. A., Roberts, G., Ziprin, P., and Peck, D. H. (2007). Induction of Proteases in Peritoneal Carcinomatosis, the Role of ICAM-1/CD43 Interaction. Biomark. Insights *2*, 377–384.

Alkhamesi, N. A., Ziprin, P., Pfistermuller, K., Peck, D. H., and Darzi, A. W. (2005). ICAM-1 mediated peritoneal carcinomatosis, a target for therapeutic intervention. Clin. Exp. Metastasis *22*, 449–459.

Alsteens, D., Garcia, M. C., Lipke, P. N., and Dufrêne, Y. F. (2010). Force-induced formation and propagation of adhesion nanodomains in living fungal cells. Proc. Natl. Acad. Sci. U. S. A. *107*, 20744–20749.

Ambrosi, D., Duperray, A., Peschetola, V., and Verdier, C. (2009). Traction patterns of tumor cells. J. Math. Biol. *58*, 163–181.

Ananthakrishnan, R., and Ehrlicher, A. (2007). The forces behind cell movement. Int. J. Biol. Sci. *3*, 303–317.

Apostolopoulos, V., Stojanovska, L., and Gargosky, S. E. (2015). MUC1 (CD227): a multi-tasked molecule. Cell. Mol. Life Sci. *72*, 4475–4500.

Balaban, N. Q. *et al.*(2001). Force and focal adhesion assembly: a close relationship studied using elastic micropatterned substrates. Nat. Cell Biol. *3*, 466–472.

Barthel, S. R. *et al.*(2014). Definition of molecular determinants of prostate cancer cell bone extravasation. Cancer Res. *73*, 942–952.

Barthel, S. R., Gavino, J. D., Descheny, L., and Dimitroff, C. J. (2008). Targeting selectins and selectin ligands in inflammation and cancer Steven. Expert Opin. Ther. Targets *11*, 1473–1491.

Bella, J., Kolatkar, P. R., Marlor, C. W., Greve, J. M., and Rossmann, M. G. (1998). The structure of the two amino-terminal domains of human ICAM-1 suggests how it functions as a rhinovirus receptor and as an LFA-1 integrin ligand. Proc Natl Acad Sci U S A *95*, 4140–4145.

Bennett Jr., R., Jarvela, T., Engelhardt, P., Kostamovaara, L., Sparks, P., Carpen, O., Turunen, O., and Vaheri, A. (2001). Mucin MUC1 is seen in cell surface protrusions together with ezrin in immunoelectron tomography and is concentrated at tips of filopodial protrusions in MCF-7 breast carcinoma cells. J Histochem Cytochem *49*, 67–77.

Berrier, A. L., and Yamada, K. M. (2007). Cell-matrix adhesion. J. Cell. Physiol. *213*, 565–573.

Bersini, S., Jeon, J. S., Moretti, M., and Kamm, R. D. (2014). In vitro models of the metastatic cascade: from local invasion to extravasation. Drug Discov. Today *19*, 735–742.

Binnig, G., Quate, C.F., and Gerber, Ch. (1986). Atomic Force Microscope. Phys. Rev. Lett. *56*, 930–933.

Bizzari, A. R, and Cannistraro, S (2012). Dynamic Force Spectroscopy and Biomolecular recognition. CRC Press *ebook* 978-1-4398-6238-4.

Bolker, B. M., Brooks, M. E., Clark, C. J., Geange, S. W., Poulsen, J. R., Stevens, M. H. H., and White, J. S. S. (2009). Generalized linear mixed models: a practical guide for ecology and evolution. Trends Ecol. Evol. *24*, 127–135.

Boyden, S. (1962). The chemotactic effect of mixtures of antibody and antigen on polymorphonuclear leukocytes. J Exp Medicine, *115*, 453–466.

Brown, M., and Wittwer, C. (2000). Flow cytometry: Principles and clinical applications in hematology. Clin. Chem. *46*, 1221–1229.

Buckley, C. D., Rainger, G. E., Bradfield, P. F., Nash, G. B., and Simmons, D. L. (1998). Cell adhesion: more than just glue (review). Mol. Membr. Biol. *15*, 167–176.

Bura, E., Zhmurov, A., and Barsegov, V. (2009). Nonparametric density estimation and optimal bandwidth selection for protein unfolding and unbinding data. J. Chem. Phys. *130*, 1-15.

Burridge, K., and Wennerberg, K. (2004). Rho and Rac Take Center Stage. Cell *116*, 167–179.

Butt, H. J., and Jaschke, M. (1995). Calculation of thermal noise in atomic force microscopy. Nanotechnology *6*, 1-7.

Cardillo, M. R., Castagna, G., Memeo, L., De Bernardinis, E., and Di Silverio, F. (2000). Epidermal growth factor receptor, MUC-1 and MUC-2 in bladder cancer. J Exp Clin Cancer Res *19*, 225–233.

Carman, C.V., and Springer, T.A (2008). Trans-cellular migration: cell–cell contacts get intimate. Curr. Opin. Cell Biol. *20*, 533–540.

Celik, E., Faridi, M. H., Kumar, V., Deep, S., Moy, V. T., and Gupta, V. (2013). Agonist leukadherin-1 increases CD11b/CD18-dependent adhesion via membrane tethers. Biophys. J. *105*, 2517–2527.

Chambers, A. F., Groom, A. C., and MacDonald, I. C. (2002). Dissemination and growth of cancer cells in metastatic sites. Nat. Rev. Cancer *2*, 563–572.

Champelovier, P., Simon, A., Garrel, C., Levacher, G., Praloran, V., and Seigneurin, D. (2003). Is interferon gamma one key of metastatic potential increase in human bladder carcinoma? Clin Cancer Res *9*, 4562–4569.

Chang, K. C., Chiang, Y. W., Yang, C. H., and Liou, J. W. (2012). Atomic force microscopy in biology and biomedicine. Tzu Chi Med. J. *24*, 162–169.

Cheung, G., Sahai, A., Billia, M., Dasgupta, P., and Khan, M. S. (2013). Recent advances in the diagnosis and treatment of bladder cancer. BMC Med. *11*, 1-8.

Chotard-Ghodsnia, R., Haddad, O., Leyrat, A., Drochon, A., Verdier, C., and Duperray, A. (2007). Morphological analysis of tumor cell/endothelial cell interactions under shear flow. J. Biomech. *40*, 335–344.

Connors, W. L., and Heino, J. (2005). A duplexed microsphere-based cellular adhesion assay. Anal. Biochem. *337*, 246–255.

Cooper, G. (2000). The Cell: A Molecular Approach. Cell A Mol. Approach. 2nd Ed., http://www.ncbi.nlm.nih.gov/books/NBK9932/.

Damljanovic, V., Lagerholm, B. C., and Jacobson, K. (2005). Bulk and micropatterned conjugation of extracellular matrix proteins to characterized polyacrylamide substrates for cell mechanotransduction assays. Biotechniques *39*, 847–851.

Delanoe-Ayari, H., Rieu, J. P., and Sano, M. (2010). 4D traction force microscopy reveals asymmetric cortical forces in migrating dictyostelium cells. Phys. Rev. Lett. *105*, 1–4.

Dembo, M., and Wang, Y.L (1999). Stresses at the Cell-to-Substrate Interface during Locomotion of Fibroblasts. Biophys. J. *76*, 2307–2316.

Elangbam, C. S., Quallis, C. W., and Dahlgren, R. R (1997). Cell Adhesion Molecules - Update. Vet. Pathol. *34*, 61–73.

Engler, A. J., Sen, S., Sweeney, H. L., and Discher, D. E. (2006). Matrix Elasticity Directs Stem Cell Lineage Specification. Cell *126*, 677–689.

Evans, E ., and Ritchie, K. (2000). Dynamic Strength of Molecular Adhesion Bonds. Biophys. J. *72*, 1541–1555.

Even-Ram, S., and Yamada, K. M. (2005). Cell migration in 3D matrix. Curr. Opin. Cell Biol. *17*, 524–532.

Fernandez-Rodriguez, J., Andersson, C. X., Laos, S., Baeckström, D., Sikut, A., Sikut, R., and Hansson, G. C. (2002). The Leukocyte Antigen CD43 Is Expressed in Different Cell Lines of Nonhematopoietic Origin. Tumor Biol. *23*, 193–201.

Fierro, F. A., Taubenberger, A., Puech, P. H., Ehninger, G., Bornhauser, M., Muller, D. J., and Illmer, T. (2008). BCR/ABL Expression of Myeloid Progenitors Increases β1-Integrin Mediated Adhesion to Stromal Cells. J. Mol. Biol. *377*, 1082–1093.

Franz, C. M., Taubenberger, A., Puech, P. H., and Muller, D. J. (2007). Studying integrin-mediated cell adhesion at the single-molecule level using AFM force spectroscopy. Sci. STKE *2007*, 1–16.

Friedl, P., and Brocker, E. B. (2000). The biology of cell locomotion within three-dimensional extracellular matrix. Cell. Mol. Life Sci. *57*, 41–64.

Friedl, P., Sahai, E., Weiss, S., and Yamada, K. M. (2012). New dimensions in cell migration. Nat. Rev. Mol. Cell Biol. *13*, 743–747.

Friedl, P., and Wolf, K. (2003). Tumour-cell invasion and migration: diversity and escape mechanisms. Nat. Rev. Cancer *3*, 362–374.

Friedl, P., and Wolf, K. (2010). Plasticity of cell migration: A multiscale tuning model. J. Cell Biol. *188*, 11–19.

Friedrichs, J., Helenius, J., and Muller, D. J. (2010). Quantifying cellular adhesion to extracellular matrix components by single-cell force spectroscopy. Nat. Protoc. *5*, 1353–1361.

Friedrichs, J., Legate, K. R., Schubert, R., Bharadwaj, M., Werner, C., Müller, D. J., and Benoit, M. (2013). A practical guide to quantify cell adhesion using single-cell force spectroscopy. Methods *60*, 169–178.

Fu, J., Wang, Y. K., Yang, M. T., Desai, R. A., Yu, X., Liu, Z., and Chen, C. S. (2010). Mechanical regulation of cell function with geometrically modulated elastomeric substrates. Nat. Methods *7*, 733–736.

Fujii, T., Shimada, K., Anai, S., Fujimoto, K., and Konishi, N. (2013). ALKBH2, a novel AlkB homologue, contributes to human bladder cancer progression by regulating MUC1 expression. Cancer Sci. *104*, 321–327.

Galbraith, C. G., and Sheetz, M. P. (1997). A micromachined device provides a new bend on fibroblast traction forces. Proc. Natl. Acad. Sci. U. S. A. *94*, 9114–9118.

Gendler, S. J. (2001). MUC1, the renaissance molecule. J. Mammary Gland Biol. Neoplasia *6*, 339–353.

Geng, Y., Yeh, K., Takatani, T., and King, M. R. (2012). Three to tango: MUC1 as a ligand for both E-selectin and ICAM-1 in the breast cancer metastatic cascade. Front. Oncol. *2*, 1-8.

Glinsky, V. V, Glinsky, G. V, Rittenhouse-olson, K., Huflejt, M. E., Glinskii, O. V, Deutscher, S. L., and Quinn, T. P. (2001). The Role of Thomsen-Friedenreich Antigen in Adhesion of Human Breast and Prostate Cancer Cells to the Endothelium. Cancer Res. *61*, 4851–4857.

Grevesse, T., Versaevel, M., Circelli, G., Desprez, S., and Gabriele, S. (2013). A simple route to functionalize polyacrylamide hydrogels for the independent tuning of mechanotransduction cues. Lab Chip *13*, 777–780.

Haddad, O., Chotard-Ghodsnia, R., Verdier, C., and Duperray, A. (2010). Tumor cell/endothelial cell tight contact upregulates endothelial adhesion molecule expression mediated by NFkappaB: differential role of the shear stress. Exp. Cell Res. *316*, 615–626.

Haddon, L., and Hugh, J. (2015). MUC1-mediated motility in breast cancer: a review highlighting the role of the MUC1/ICAM-1/Src signaling triad. Clin. Exp. Metastasis *32*, 393–403.

Hamilla, S. M., Stroka, K. M., and Aranda-Espinoza, H. (2014). VE-Cadherin-Independent Cancer Cell Incorporation into the Vascular Endothelium Precedes Transmigration. PLoS One *9*, e109748

Hanisch, F. G., and Müller, S. (2000). MUC1: the polymorphic appearance of a human mucin. Glycobiology *10*, 439–449.

Harris, A. K., Wild, P., and Stopak, D. (1980). Silicone rubber substrata: A New Wrinkle in the Study of Cell Locomotion. Science, New Series. 208, 177–179.

Hayashi, T., Takahashi, T., Motoya, S., Ishida, T., Itoh, F., Adachi, M., Hinoda, Y., and Imai, K. (2001). MUC1 mucin core protein binds to the domain 1 of ICAM-1. Digestion *63*, 87–92.

Hayes, D. F., Sekine, H., Ohno, T., Abe, M., Keefe, K., and Kufe, D. W. (1985). Use of a murine monoclonal antibody for detection of circulating plasma DF3 antigen levels in breast cancer patients. J. Clin. Invest. *75*, 1671–1678.

Helenius, J., Heisenberg, C. P., Gaub, H. E., and Muller, D. J. (2008). Single-cell force spectroscopy. J. Cell Sci. *121*, 1785–1791.

Heyder, C., Gloria-Maercker, E., Entschladen, F., Hatzmann, W., Niggemann, B., Zänker, K., and Dittmar, T. (2002). Realtime visualization of tumor cell/endothelial cell interactions during transmigration across the endothelial barrier. J. Cancer Res. Clin. Oncol. *128*, 533–538.

Heyder, C., Gloria-Maercker, E., Hatzmann, W., Niggemann, B., Zänker, K. S., and Dittmar, T. (2005). Role of the β1-integrin subunit in the adhesion, extravasation and migration of T24 human bladder carcinoma cells. Clin. Exp. Metastasis *22*, 99–106.

Hirohashi, S., and Kanai, Y. (2003). Cell adhesion system and human cancer morphogenesis. Cancer Sci. *94*, 575–581.

Huang, S., and Ingber, D. E. (1999). The structural and mechanical complexity of cell-growth control. Nat. Cell Biol. *1*, 131–138.

Hulkower, K. I., and Herber, R. L. (2011). Cell migration and invasion assays as tools for drug discovery. Pharmaceutics *3*, 107–124.

Hurford, M. T., Gujral, S., Schuster, S. J., and Schwarting, R. (1999). Extramedullary myeloid cell tumor of the urinary bladder in a patient with myelodysplastic syndrome. Pathol. Res. Pract. *195*, 699–703.

Huttenlocher, A., and Horwitz, A. R. (2011). Integrins in cell migration. Cold Spring Harb. Perspect. Biol. *3*, 1–16.

Hutter, J. L., and Bechhoefer, J. (1993). Calibration of atomic-force microscope tips. Rev. Sci. Instrum. *64*, 1868–1873.

Ibbotson, G. C., Doig, C., Kaur, J., Gill, V., Ostrovsky, L., Fairhead, T., and Kubes, P. (2001). Functional alpha4-integrin: a newly identified pathway of neutrophil recruitment in critically ill septic patients. Nat. Med. *7*, 465–470.

Imoukhuede, P. I., and Popel, A. S. (2014). Quantitative fluorescent profiling of VEGFRs reveals tumor cell and endothelial cell heterogeneity in breast cancer xenografts. Cancer Med. *3*, 225–244.

Ivanov, D. B., Philippova, M. P., and Tkachuk, V. A. (2001). Structure and functions of classical cadherins. Biochem. *66*, 1174–1186.

Jeon, J. S., Zervantonakis, I. K., Chung, S., Kamm, R. D., and Charest, J. L. (2013). In vitro model of tumor cell extravasation. PLoS One *8*, e56910.

Jonckheere, N., and Van Seuningen, I. (2008). The membrane-bound mucins: how large O-glycoproteins play key roles in epithelial cancers and hold promise as biological tools for gene-based and immunotherapies. Crit. Rev. Oncog. *14*, 177–196.

Jonckheere, N., Skrypek, N., and Van Seuningen, I. (2010). Mucins and pancreatic cancer. Cancers. *2*, 1794–1812.

Karsten, U., Diotel, C., Klich, G., Paulsen, H., Goletz, S., Müller, S., and Hanisch, F. G. (1998). Enhanced binding of antibodies to the DTR motif of MUC1 tandem repeat peptide is mediated by site-specific glycosylation. Cancer Res. *58*, 2541–2549.

Karsten, U., Serttas, N., Paulsen, H., Danielczyk, A., and Goletz, S. (2004). Binding patterns of DTR-specific antibodies reveal a glycosylation-conditioned tumor-specific epitope of the epithelial mucin (MUC1). Glycobiology *14*, 681–692.

Kaur, S., Momi, N., Chakraborty, S., Wagner, D. G., Horn, A. J., Lele, S. M., Theodorescu, D., and Batra, S. K. (2014). Altered expression of transmembrane mucins, MUC1 and MUC4, in bladder cancer: pathological implications in diagnosis. PLoS One *9*, e92742.

Keiper, T., Santoso, S., Nawroth, P. P., Orlova, V., and Chavakis, T. (2005). The role of junctional adhesion molecules in cell-cell interactions. Histol. Histopathol. *20*, 197–203.

Kerssemakers, J. W. J., Munteanu, E. L., Laan, L., Noetzel, T. L., Janson, M. E., and Dogterom, M. (2006). Assembly dynamics of microtubules at molecular resolution. Nature *442*, 709–712.

Khaldoyanidi, S. K., Glinsky, V. V., Sikora, L., Glinskii, A. B., Mossine, V. V., Quinn, T. P., Glinsky, G. V., and Sriramarao, P. (2003). MDA-MB-435 human breast carcinoma cell homo- and heterotypic adhesion under flow conditions is mediated in part by Thomsen-Friedenreich antigen-galectin-3 interactions. J. Biol. Chem. *278*, 4127–4134.

Khalili, A.A., and Ahmad, M.R (2015). A Review of Cell Adhesion Studies for Biomedical and Biological Applications. Int. J. Mol. Sci. *16*, 18149–18184.

Knowles, M. A., and Hurst, C. D. (2015). Molecular biology of bladder cancer : new insights into pathogenesis and clinical diversity. Nat. Rev. Cancer. *15*, 25–41.

Kramer, N., Walzl, A., Unger, C., Rosner, M., Krupitza, G., Hengstschläger, M., and Dolznig, H. (2013). In vitro cell migration and invasion assays. Mutat. Res. *752*, 10–24.

Kraning-rush, C. M., Califano, J. P., and Reinhart-king, C. A. (2012). Cellular Traction Stresses Increase with Increasing Metastatic Potential. PLoS One *7*, e32572.

Ladoux, B., and Nicolas, A. (2012). Physically based principles of cell adhesion mechanosensitivity in tissues. Reports Prog. Phys. *75*, 1–25.

Lam, V. M., Beerepoot, P., Angers, S., and Salahpour, A. (2013). A Novel Assay for Measurement of Membrane-Protein Surface Expression using a β-lactamase Reporter. Traffic *14*, 778–784.

Languino, L. R., Duperray, A., Joganic, K. J., Fornaro, M., Thornton, G. B., and Altieri, D. C. (1995). Regulation of leukocyte-endothelium interaction and leukocyte transendothelial migration by intercellular adhesion molecule 1-fibrinogen recognition. Proc. Natl. Acad. Sci. U. S. A. *92*, 1505–1509.

Lauffenburger, D. A., and Horwitz, A. F. (1996). Cell migration: a physically integrated molecular process. Cell *84*, 359–369.

Laurent, V. M., Duperray, A., Sundar Rajan, V., and Verdier, C. (2014). Atomic force microscopy reveals a role for endothelial cell ICAM-1 expression in bladder cancer cell adherence. PLoS One *9*, e98034.

Lawson, C., and Wolf, S. (2009). ICAM-1 signaling in endothelial cells. Pharmacol. Reports *61*, 22–32.

Lee, J., Ishihara, A., and Jacobson, K. (1993). How do cells move along surfaces? Trends Cell Biol. *3*, 366–370.

Lee, J., Leonard, M., Oliver, T., Ishihara, A., and Jacobson, K. (1994). Traction Forces Generated by Locomting Keratocytes. J. Cell Biol. *127*, 1957–1964.

Lekka, M. (2016). Discrimination Between Normal and Cancerous Cells Using AFM. Bionanoscience *6*, 65–80.

Lekka, M., Laidler, P., Gil, D., Lekki, J., Stachura, Z., and Hrynkiewicz, A. Z. (1999). Elasticity of normal and cancerous human bladder cells studied by scanning force microscopy. Eur. Biophys. J. *28*, 312–316.

Ley, K. (2003). The role of selectins in inflammation and disease. Trends Mol. Med. *9*, 263–268.

Li, M., Liu, L., Xi, N., and Wang, Y. (2015). Nanoscale monitoring of drug actions on cell membrane using atomic force microscopy. Acta Pharmacol. Sin., 1–14.

Li, Y., Bharti, A., Chen, D., Gong, J., and Kufe, D. (1998). Interaction of glycogen synthase kinase 3beta with the DF3/MUC1 carcinoma-associated antigen and beta-catenin. Mol. Cell. Biol. *18*, 7216–7224.

Linden, S. K., Sutton, P., Karlsson, N. G., Korolik, V., and McGuckin, M. A (2008). Mucins in the mucosal barrier to infection. Mucosal Immunol. *1*, 183–197.

Liu, Z., Sniadecki, N. J., and Chen, C. S. (2010). Mechanical forces in endothelial cells during firm adhesion and early transmigration of human monocytes. Cell. Mol. Bioeng. *3*, 50–59.

Lo, C. M., Wang, H. B., Dembo, M., and Wang, Y. L. (2000). Cell movement is guided by the rigidity of the substrate. Biophys. J. *79*, 144–152.

Lodish et al. (2000). Molecular Cell Biology. Mol. Cell Biol. 4th Ed. *Section 22*, http://www.ncbi.nlm.nih.gov/books/NBK21599/.

Lukas, Z., and Dvorak, K. (2004). Adhesion molecules in biology and oncology. Acta Vet. Brno *73*, 93–104.

Luo, B.H., Carman, C. V, and Springer, T. A (2007). Structural basis of integrin regulation and signaling. Annu. Rev. Immunol. *25*, 619–647.

Maître, J. L., and Heisenberg, C. P. (2013). Three functions of cadherins in cell adhesion. Curr. Biol. *23*, 626–633.

Klemke, M., Weschenfelder, T., Konstandin, M. H ., and Samstag, Y (2006). High affinity interaction of integrin alpha4beta1 (VLA-4) and vascular cell adhesion molecule 1 (VCAM-1) enhances migration of human melanoma cells across activated endothelial cell layers. J. Cell. Physiol. *207*, 12–22.

Masters, J. R. W., Hepburn, P. J., Walker, L., Highman, W. J., Trejdosiewicz, L. K., Povey, S., Parkar, M., Hill, B. T., Riddle, P. R., and Franks, L. M. (1986). Tissue Culture Model of Transitional Cell Carcinoma : Characterization of Twenty-two Human Urothelial Cell Lines. Cancer Res. *46*, 3630–3636.

Matsumoto, M., Atarashi, K., Umemoto, E., Furukawa, Y., Shigeta, A., Miyasaka, M., and Hirata, T. (2005). CD43 functions as a ligand for E-Selectin on activated T cells. J. Immunol. *175*, 8042–8050.

Maver, U., Velnar, T., Gaberšček, M., Planinšek, O., and Finšgar, M. (2016). Recent progressive use of atomic force microscopy in biomedical applications. TrAC Trends Anal. Chem. *80*, 96–111.

Michel, R., Peschetola, V., Vitale, G., Etienne, J., Duperray, A., Ambrosi, D., Prezoisi, L., and Verdier, C. (2013). Mathematical framework for traction force microscopy. ESAIM Proceedings, 42, 61-83.

Mierke, C. T. (2013). Physical break-down of the classical view on cancer cell invasion and metastasis. Eur. J. Cell Biol. *92*, 89–104.

Mierke, C. T., Zitterbart, D. P., Kollmannsberger, P., Raupach, C., Schlötzer-Schrehardt, U., Goecke, T. W., Behrens, J., and Fabry, B. (2008). Breakdown of the endothelial barrier function in tumor cell transmigration. Biophys. J. *94*, 2832–2846.

Mierke, C. T., Röse, D., Fabry, B., and Brabek, J. (2008a). Contractile forces in tumor cell migration Claudia. Eur. J. Cell Biol. *87*, 669–676.

Miles, F. L., Pruitt, F. L., van Golen, K. L., and Cooper, C. R. (2008). Stepping out of the flow: capillary extravasation in cancer metastasis. Clin. Exp. Metastasis *25*, 305–324.

Mitra, A. P., and Cote, R. J. (2009). Molecular pathogenesis and diagnostics of bladder cancer. Annu. Rev. Pathol. *4*, 251–285.

Moussus, M., der Loughian, C., Fuard, D., Courçon, M., Gulino-Debrac, D., Delanoë-Ayari, H., and Nicolas, A. (2014). Intracellular stresses in patterned cell assemblies. Soft Matter *10*, 2414–2423

Munevar, S., Wang, Y.L., and Dembo, M. (2001). Traction Force Microscopy of Migrating Normal and H-ras Transformed 3T3 Fibroblasts. Biophys. J. *80*, 1744–1757.

Nakamori, S., Ota, D. M., Cleary, K. R., Shirotani, K., and Irimura, T. (1994). MUC1 Mucin Expression As a Marker of Progression and Metastasis of Human Colorectal-Carcinoma. Gastroenterology *106*, 353–361.

Nath, S., and Mukherjee, P. (2014). MUC1: A multifaceted oncoprotein with a key role in cancer progression. Trends Mol. Med. *20*, 332–342.

Nelson, C. M., Jean, R. P., Tan, J. L., Liu, W. F., Sniadecki, N. J., Spector, A. A, and Chen, C. S. (2005). Emergent patterns of growth controlled by multicellular form and mechanics. Proc. Natl. Acad. Sci. U. S. A. *102*, 11594–11599.

Nieto, M. A. (2011). The ins and outs of the epithelial to mesenchymal transition in health and disease. Annu Rev Cell Dev Biol *27*, 347–376.

Oliver, T., Dembo, M., and Jacobson, K. (1995). Traction forces in locomoting cells. Cell Motil. Cytoskeleton *31*, 225–240.

Onken, M. D., Li, J., and Cooper, J. A. (2014). Uveal Melanoma Cells Utilize a Novel Route for Transendothelial Migration. PLoS One *9*, e115472.

Orr, F. W., Wang, H. H., Lafrenie, R. M., Scherbarth, S., and Nance, D. M. (2000). Interactions between cancer cells and the endothelium in metastasis. J. Pathol. *190*, 310–329.

Ostermann, G., Weber, K. S. C., Zernecke, A., Schröder, A., and Weber, C. (2002). JAM-1 is a ligand of the beta(2) integrin LFA-1 involved in transendothelial migration of leukocytes. Nat. Immunol. *3*, 151–158.

Park, H. K., and Seov, U. H. (2009). MUC1 from the Mucin Family as Potential Tools in Breast Cancer Immunotherapy. J. Breast Cancer *12*, 125–133.

Park, W. S., Kim, H. J., Lee, G. K., Son, H. S., and Bae, Y. (2012). Anti-adhesive functions of CD43 expressed on colon carcinoma cells through the modulation of integrins. Exp. Mol. Pathol. *92*, 82–89.

Paszek, M. J. *et al.* (2005). Tensional homeostasis and the malignant phenotype. Cancer Cell *8*, 241–254.

Pelham, R. J., and Wang, Y. L. (1998). Cell locomotion and focal adhesions are regulated by substrateflexibility. Proc. Natl. Acad. Sci. U. S. A. *94*, 13661–13665.

Perinpanayagam, H., Zaharias, R., Stanford, C., Brand, R., Keller, J., and Schneider, G. (2001). Early cell adhesion events differ between osteoporotic and non-osteoporotic osteoblasts. J. Orthop. Res. *19*, 993–1000.

Peschetola, V., Laurent, V. M., Duperray, A., Michel, R., Ambrosi, D., Preziosi, L., and Verdier, C. (2013). Time-Dependent Traction Force Microscopy for Cancer Cells as a Measure of Invasiveness. Cytoskeleton. *70*, 201–214.

Pfreundschuh, M., Alsteens, D., Wieneke, R., Zhang, C., Coughlin, S. R., Tampé, R., Kobilka, B. K., and Müller, D. J. (2015). Identifying and quantifying two ligand-binding sites while imaging native human membrane receptors by AFM. Nat. Commun. *6*, 1–7.

Ploeg, M., Aben, K. K. H., and Kiemeney, L. A. (2009). The present and future burden of urinary bladder cancer in the world. World J. Urol. *27*, 289–293.

Pochampalli, M. R., el Bejjani, R. M., and Schroeder, J. A (2007). MUC1 is a novel regulator of ErbB1 receptor trafficking. Oncogene *26*, 1693–1701.

Polio, S. R., and Smith, M. L. (2014). Patterned hydrogels for simplified measurement of cell traction forces, Methods in Cell Biology. 121, 17-31.

Polio, S. R., Rothenberg, K. E., Stamenović, D., and Smith, M. L. (2012). A micropatterning and image processing approach to simplify measurement of cellular traction forces. Acta Biomater. *8*, 82–88.

Psaila, B., and Lyden, D. (2009). The metastatic niche: adapting the foreign soil. Nat. Rev. Cancer *9*, 285–293.

Puech, P.H., Taubenberger, A., Ulrich, F., Krieg, M., Muller, D. J., and Heisenberg, C.P. (2005). Measuring cell adhesion forces of primary gastrulating cells from zebrafish using atomic force microscopy. J. Cell Sci. *118*, 4199–4206.

Puech, P. H., Poole, K., Knebel, D., and Muller, D. J. (2006). A new technical approach to quantify cell-cell adhesion forces by AFM. Ultramicroscopy *106*, 637–644.

Rabodzey, A., Alcaide, P., Luscinskas, F. W., and Ladoux, B. (2008). Mechanical forces induced by the transendothelial migration of human neutrophils. Biophys. J. *95*, 1428–1438.

Rahman, A., and Fazal, F. (2009). Hug tightly and say goodbye: Role of endothelial ICAM-1 in leukocyte transmigration. Antioxid. Redox Signal. *11*, 823–839.

Rahn, J. J., Chow, J. W., Horne, G. J., Mah, B. K., Emerman, J. T., Hoffman, P., and Hugh, J. C. (2005). MUC1 mediates transendothelial migration in vitro by ligating endothelial cell ICAM-1. Clin. Exp. Metastasis *22*, 475–483.

Rahn, J. J., Shen, Q., Mah, B. K., and Hugh, J. C. (2004). MUC1 initiates a calcium signal after ligation by intercellular adhesion molecule-1. J. Biol. Chem. *279*, 29386–29390.

Ramos, J. R., Pabijan, J., Garcia, R., and Lekka, M. (2014). The softening of human bladder cancer cells happens at an early stage of the malignancy process. Beilstein J. Nanotechnol. *5*, 447–457.

Rape, A. D., Guo, W.H., and Wang, Y.L. (2011). The regulation of traction force in relation to cell shape and focal adhesions. Biomaterials *32*, 2043–2051.

Regimbald, L. H., Pilarski, L. M., Longenecker, B. M., Reddish, M. A., Zimmermann, G., and Hugh, J. C. (1996). The Breast Mucin MUC1 as a Novel Adhesion Ligand for Endothelial Intercellular Adhesion Molecule 1 in Breast Cancer. Cancer Res. *56*, 4244–4249.

Reig, G., Pulgar, E., and Concha, M. L. (2014). Cell migration: from tissue culture to embryos. Development *141*, 1999–2013.

Reinhart-King, C. A (2008). Endothelial cell adhesion and migration. Methods Enzymol. *443*, 45–64.

Retz, M., Lehmann, J., Röder, C., Ret, M., Roder, C., Eggers, J., Pauluschke, J., Kalthoff, H., and Stã, M. (1998). Differential Mucin MUC7 Gene Expression in Invasive Bladder Carcinoma in Contrast to Uniform MUC1 and MUC2 Gene Expression in Both Normal Urothelium and Bladder Carcinoma. Cancer Res. *58*, 5662–5666.

Reymond, N., D'Água, B. B., and Ridley, A. J. (2013). Crossing the endothelial barrier during metastasis. Nat. Rev. Cancer *13*, 858–870.

Ridley, A. J., Schwartz, M. A., Burridge, K., Firtel, R. A., Ginsberg, M. H., Borisy, G., Parsons, J. T., and Horwitz, A. R. (2003). Cell migration: integrating signals from front to back. Science. *302*, 1704–1709.

Rieu, J. P., Delanoë-Ayari, H., Takagi, S., Tanaka, Y., and Nakagaki, T. (2015). Periodic traction in migrating large amoeba of Physarum polycephalum. J. R. Soc. Interface *12*, 1-10.

Rivalland, G., Loveland, B., and Mitchell, P. (2015). Update on Mucin-1 immunotherapy in cancer: a clinical perspective. Expert Opin. Biol. Ther. *15*, 1773–1787.

Roche, Y., Pasquier, D., Rambeaud, J. J., Seigneurin, D., and Duperray, A. (2003). Fibrinogen mediates bladder cancer cell migration in an ICAM-1-dependent pathway. Cell. Proteolysis Oncol. *89*, 1089–1097.

Roland, C. L., Harken, A. H., Sarr, M. G., and Barnett, C. C. (2007). ICAM-1 expression determines malignant potential of cancer. Surgery *141*, 705–707.

Rosenstein, Y., Park, J. K., Hahn, W. C., Rosen, F. S., Bierer, B. E., and Burakoff, S. J. (1991). CD43, a molecule defective in Wiskott-Aldrich syndrome, binds ICAM-1. Nature *354*, 233–235.

Ruppert, M., Aigner, S., Hubbe, M., Yagita, H., and Altevogt, P. (1995). The L1 adhesion molecule is a cellular ligand for VLA-5. J. Cell Biol. *131*, 1881–1891.

Sabass, B., Gardel, M. L., Waterman, C. M., and Schwarz, U. S. (2008). High Resolution Traction Force Microscopy Based on Experimental and Computational Advances. Biophys. J. *94*, 207–220.

Sans, E., Delachanal, E., and Duperray, A. (2001). Analysis of the roles of ICAM-1 in neutrophil transmigration using a reconstituted mammalian cell expression model: implication of ICAM-1 cytoplasmic domain and Rho-dependent signaling pathway. J. Immunol. *166*, 544–551.

Santamaría, M., López-beltrán, A., Toro, M., Pena, J., and Molina, I. J. (1996). Specific Monoclonal Antibodies against Leukocyte-restricted Tumor Cells React with Nonhematopoietic Tumor. Cancer Res. *56*, 3526–3529.

Sarafian, V., Jadot, M., Foidart, J. M., Letesson, J. J., Van den Brule, F., Castrunovo, V., Wattiaux, R., and Wattiaux De Coninck, S. (1998). Expression of Lamp-1 and Lamp-2 and their interactions with galectin-3 in human tumor cells. Int. J. Cancer *75*, 105–111.

Sariisik, E., Popov, C., Müller, J. P., Docheva, D., Clausen-Schaumann, H., and Benoit, M. (2015). Decoding Cytoskeleton-Anchored and Non-Anchored Receptors from Single-Cell Adhesion Force Data. Biophys. J. *109*, 1330–1333.

Sbalzarini, I. F., and Koumoutsakos, P. (2005). Feature point tracking and trajectory analysis for video imaging in cell biology. J. Struct. Biol. *151*, 182–195.

Seller, Z. (2001). Cellular Adhesion and Adhesion Molecules. Turkish J. Biol. *25*, 1–15.

Senapati, S., Das, S., and Batra, S. K. (2010). Mucin-interacting proteins: From function to therapeutics. Trends Biochem. Sci. *35*, 236–245.

Serrador, J. M. *et al.* (1998). CD43 interacts with moesin and ezrin and regulates its redistribution to the uropods of T lymphocytes at the cell-cell contacts. Blood *91*, 4632–4644.

Seveau, S., Lopez, S., Lesavre, P., Guichard, J., Cramer, E. M., and Halbwachs-Mecarelli, L. (1997). Leukosialin (CD43, sialophorin) redistribution in uropods of polarized neutrophils is induced by CD43 cross-linking by antibodies, by colchicine or by chemotactic peptides. J. Cell Sci. *110*, 1465–1475.

Shelley, C. S., Donnell, E. R., Rosen, S., and Whiteheadtt, A. S. (1990). Structure of the human sialophorin (CD43) gene. Biochem. J. *270*, 569–576.

Shenoy, A. K., and Lu, J. (2014). Cancer cells remodel themselves and vasculature to overcome the endothelial barrier. Cancer Lett. *3835*, 1–9.

Simms, M. S., Hughes, O. D., Limb, M., Price, M. R., and Bishop, M. C. (1999). MUC1 mucin as a tumour marker in bladder cancer. BJU Int. *84*, 350–352.

Simon, S. I., Burns, A. R., Taylor, A. D., Gopalan, P. K., Lynam, E. B., Sklar, L. A, and Smith, C. W. (1995). L-selectin (CD62L) cross-linking signals neutrophil adhesive functions via the Mac-1 (CD11b/CD18) beta 2-integrin. J. Immunol. *155*, 1502–1514.

Simon, S. I., and Green, C. E. (2005). Molecular mechanics and dynamics of leukocyte recruitment during inflammation. Annu Rev Biomed Eng *7*, 151–185.

Simon, S. I., Hu, Y., Vestweber, D., and Smith, C. W. (2000). Neutrophil tethering on E-selectin activates beta 2 integrin binding to ICAM-1 through a mitogen-activated protein kinase signal transduction pathway. J. Immunol. *164*, 4348–4358.

Sokolov, I. (2007). Atomic force microscopy in cancer cell research. Cancer Nanotechnol., 1–17.

Stephen Paget (1889). The Distribution of Secondary Growths in Cancer of the Breast. Cancer Metastasis Rev. *8*, 98–101.

Strell, C., and Entschladen, F. (2008). Extravasation of leukocytes in comparison to tumor cells. Cell Commun. Signal. *6*, 1-13.

Strell, C., Lang, K., Niggemann, B., Zaenker, K. S., and Entschladen, F. (2007). Surface molecules regulating rolling and adhesion to endothelium of neutrophil granulocytes and MDA-MB-468 breast carcinoma cells and their interaction. Cell. Mol. Life Sci. *64*, 3306–3316.

Stroka, K. M., and Aranda-Espinoza, H. (2011). Endothelial cell substrate stiffness influences neutrophil transmigration via myosin light chain kinase-dependent cell contraction. Blood *118*, 1632–1640.

Sulchek, T. a, Friddle, R. W., Langry, K., Lau, E. Y., Albrecht, H., Ratto, T. V, DeNardo, S. J., Colvin, M. E., and Noy, A. (2005). Dynamic force spectroscopy of parallel individual Mucin1-antibody bonds. Proc. Natl. Acad. Sci. U. S. A. *102*, 16638–16643.

Szekanecz, Z., and Koch, A. E. (2000). Cell-cell interactions in synovitis. Endothelial cells and immune cell migration. Arthritis Res *2*, 368–373.

Takai, Y., Kitano, K., Terawaki, S. ichi, Maesaki, R., and Hakoshima, T. (2008). Structural Basis of the Cytoplasmic Tail of Adhesion Molecule CD43 and Its Binding to ERM Proteins. J. Mol. Biol. *381*, 634–644.

Tan, J. L., Tien, J., Pirone, D. M., Gray, D. S., Bhadriraju, K., and Chen, C. S. (2003). Cells lying on a bed of microneedles: an approach to isolate mechanical force. Proc. Natl. Acad. Sci. U. S. A. *100*, 1484–1489.

Taninaka, A., Hirano, Y., Takeuchi, O., and Shigekawa, H. (2012). Force measurement enabling precise analysis by dynamic force spectroscopy. Int. J. Mol. Sci. *13*, 453–465.

Taubenberger, A. V, Hutmacher, D. W., and Muller, D. J. (2014). Single-Cell Force Spectroscopy , an Emerging Tool to Quantify Cell Adhesion to Biomaterials. Tissue Eng, 20, 40-55.

Taubenberger, A., Cisneros, D. A., Friedrichs, J., Puech, P. H., Muller, D. J., and Franz, C. M. (2007). Revealing Early Steps of α2β1 Integrin-mediated Adhesion to Collagen Type I by Using Single-Cell Force Spectroscopy. Mol. Biol. Cell *18*, 1634–1644.

Théry, M. (2010). Micropatterning as a tool to decipher cell morphogenesis and functions. J. Cell Sci. *123*, 4201–4213.

Thiery, J. P., Acloque, H., Huang, R. Y. J., and Nieto, M. A. (2009). Epithelial-Mesenchymal Transitions in Development and Disease. Cell *139*, 871–890.

Tréhoux, S., Duchêne, B., Jonckheere, N., and Van Seuningen, I. (2015). The MUC1 oncomucin regulates pancreatic cancer cell biological properties and chemoresistance. Implication of p42–44 MAPK, Akt, Bcl-2 and MMP13 pathways. Biochem. Biophys. Res. Commun. *456*, 757–762.

Tremblay, P. L., Huot, J., and Auger, F. A. (2008). Mechanisms by which E-selectin regulates diapedesis of colon cancer cells under flow conditions. Cancer Res. *68*, 5167–5176.

Trepat, X., Wasserman, M. R., Angelini, T. E., Millet, E., Weitz, D. A., Butler, J. P., and Fredberg, J. J. (2009). Physical forces during collective cell migration. Nat. Phys. *5*, 426–430.

Tse, J. R., and Engler, A. J. (2010). Preparation of hydrogel substrates with tunable mechanical properties. Curr. Protoc. Cell Biol., 1–16.

Tseng, Q., Wang, I., Duchemin-Pelletier, E., Azioune, A., Carpi, N., Gao, J., Filhol, O., Piel, M., Théry, M., and Balland, M. (2011). A new micropatterning method of soft substrates reveals that different tumorigenic signals can promote or reduce cell contraction levels. Lab Chip *11*, 2231–2240.

Tuccillo, F. M. *et al.*(2014a). Aberrant glycosylation as biomarker for cancer: focus on CD43. Biomed Res. Int. *742831*, 1–13.

Tuccillo, F. M. *et al.* (2014b). Cancer-associated CD43 glycoforms as target of immunotherapy. Mol. Cancer Ther. *13*, 752–762.

Tulla, M., Helenius, J., Jokinen, J., Taubenberger, A., Müller, D. J., and Heino, J. (2008). TPA primes alpha2beta1 integrins for cell adhesion. FEBS Lett. *582*, 3520–3524.

Vahabi, S., Nazemi Salman, B., and Javanmard, A. (2013). Atomic force microscopy application in biological research: A review study. Iran. J. Med. Sci. *38*, 76–83.

Valster, A., Tran, N. L., Nakada, M., Berens, M. E., Chan, A. Y., and Symons, M. (2005). Cell migration and invasion assays. Methods *37*, 208–215.

Versaevel, M., Grevesse, T., Riaz, M., Lantoine, J., and Gabriele, S. (2014). Micropatterning hydroxy-PAAm hydrogels and sylgard 184 silicone elastomers with tunable elastic moduli. Methods Cell Biol. *121*, 33–48.

Vestweber, D. (2012). Relevance of endothelial junctions in leukocyte extravasation and vascular permeability. Ann. N. Y. Acad. Sci. *1257*, 184–192.

Vignaud, T., Ennomani, H., and Théry, M. (2014). Polyacrylamide hydrogel micropatterning. Methods Cell Biol. *120*, 93–116.

Weddell, J. C., and Imoukhuede, P. I. (2014). Quantitative characterization of cellular membrane-receptor heterogeneity through statistical and computational modeling. PLoS One *9*, e97271.

Wickstead, B., and Gull, K. (2011). The evolution of the cytoskeleton. J. Cell Biol. *194*, 513–525.

Wojcikiewicz, E. P., Abdulreda, M. H., Zhang, X., and Moy, V. T. (2006). Force spectroscopy of LFA-1 and its ligands, ICAM-1 and ICAM-2. Biomacromolecules *7*, 3188–3195.

Wojcikiewicz, E. P., Zhang, X., Chen, A., and Moy, V. T. (2003). Contributions of molecular binding events and cellular compliance to the modulation of leukocyte adhesion. J. Cell Sci. *116*, 2531–2539.

Wojcikiewicz, E. P., Zhang, X., and Moy, V. T. (2004). Force and Compliance Measurements on Living Cells Using Atomic Force Microscopy (AFM). Biol. Proced. Online *6*, 1–9.

Xu, W., Mezencev, R., Kim, B., Wang, L., McDonald, J., and Sulchek, T. (2012). Cell Stiffness Is a Biomarker of the Metastatic Potential of Ovarian Cancer Cells. PLoS One *7*, e46609.

Yamada, M. *et al.* (2006). Regulation of local and metastatic host-mediated anti-tumour mechanisms by L-selectin and intercellular adhesion molecule-1. Clin. Exp. Immunol. *143*, 216–227.

Yamamoto, M., Bharti, A., Li, Y., and Kufe, D. (1997). Interaction of the DF3/MUC1 breast carcinoma-associated antigen and beta-catenin in cell adhesion. J. Biol. Chem. *272*, 12492–12494.

Yang, E., Hu, X. F., and Xing, P. X. (2007). Advances of MUC1 as a target for breast cancer immunotherapy. Histol. Histopathol. *2*, 905–922.

Yonemura, S., Nagafuchi, A., Sato, N., and Tsukita, S. (1993). Concentration of an integral membrane protein, CD43 (leukosialin, sialophorin), in the cleavage furrow through the interaction of its cytoplasmic domain with actin-based cytoskeletons. J Cell Biol *120*, 437–449.

Yu, L. G. (2007). The oncofetal Thomsen-Friedenreich carbohydrate antigen in cancer progression. Glycoconj J. 24, 411-420.

Zhang, X., Chen, A., De Leon, D., Li, H., Noiri, E., Moy, V. T., and Goligorsky, M. S. (2004). Atomic force microscopy measurement of leukocyte-endothelial interaction. Am. J. Physiol. Heart Circ. Physiol. *286*, 359–367.

Zhang, X., Wojcikiewicz, E., and Moy, V. T. (2002). Force Spectroscopy of the Leukocyte Function-Associated Antigen-1/Intercellular Adhesion Molecule-1 Interaction. Biophys. J. *83*, 2270–2279.

Zhang, X., Wojcikiewicz, E. P., and Moy, V. T. (2006). Dynamic Adhesion of T Lymphocytes to Endothelial Cells Revealed by Atomic Force Microscopy. Exp. Biol. Med. *231*, 1306–1312.

Ziprin, P., Alkhamesi, N. A., Paul, F., Peck, D. H., and Darzi, A. W. (2004). Tumour-expressed CD43 (sialophorin) mediates tumour- mesothelial cell adhesion. Biol. Chem. *385*, 755–761.